UNIMORE
UNIVERSITÀ DEGLI STUDI DI
MODENA E REGGIO EMILIA

UNIVERSITÀ DEGLI STUDI
DI MODENA E REGGIO EMILIA

Dottorato di ricerca in
Ingegneria Industriale e del territorio

Ciclo XXXVIII

Biomaterials: Design, Production, And Characterization of Novel Alternatives for Tissue Engineering

Biomateriali: Design, Produzione e Caratterizzazione di Nuove Alternative per l'Ingegneria Tissutale

Candidato Andrea Martelli

Relatore (Tutor): Prof. Valeria Cannillo

Correlatore (Co-Tutor): Prof. Devis Bellucci

Coordinatore del Corso di Dottorato: Prof. Alberto Muscio

Abstract

The growing incidence of chronic and degenerative diseases associated with ageing and population growth, such as osteoarthritis and non-healing wounds (e.g. diabetic ulcers), has intensified the need for advanced materials capable of supporting tissue regeneration. Biomaterials play a central role in this context, as they can provide structural frameworks while interacting beneficially with biological systems. This thesis explores the design, fabrication, and characterization of advanced biomaterials that integrate inorganic, polymeric, and composite systems to address current challenges in tissue engineering.

The first part of the work focuses on the development of novel bioactive glass compositions. Bioactive glasses, thanks to their specific composition and inherent amorphous nature, can interact with biological tissue and promote regeneration. By incorporating strontium and magnesium as dopants, new silicate-based glasses with improved thermal stability, sintering behaviour, and bioactivity were obtained. The influence of these dopants on structure, mechanical performance, and cellular response was systematically investigated. The obtained glass compositions demonstrated enhanced sinterability compared to the main commercial compositions (Bioglass® 45S5 and S53P4), along with promising biological outcomes for potential scaffold fabrication. Building on these findings, fused deposition modeling was employed to design and fabricate polymer–bioactive glass composite scaffolds. Mechanical testing, finite element simulations, and biological evaluations confirmed the potential suitability of these 3D-printed structures for bone tissue regeneration, highlighting the synergy between material composition and manufacturing process.

In parallel, the research explored sustainable natural polymer systems derived from three Theobroma biomass sources (cacao, cupuaçu, and macambo). These fruits generate large amounts of waste in South American countries, as approximately 70% of their mass corresponds to the pod husk, which is rich in bioactive molecules and polysaccharides. To exploit these underused resources, pectin-rich polysaccharides were isolated via ultrasound-assisted extraction and characterized in terms of chemical composition, rheological properties, and bioactive compound content. The extracted polymers exhibited higher antioxidant activity than commercial pectin, along with promising functional properties. This section highlights both the potential of naturally derived materials for tissue engineering and the importance of circular economy principles in developing functional biomaterials.

Finally, the thesis discusses the emerging role of artificial intelligence in biomaterials science, highlighting limits and how machine learning algorithms and data-driven modelling can accelerate material discovery, optimize composition-property relationships, and predict biological performance.

Overall, this research provides a multidisciplinary framework for the rational design of multifunctional biomaterials, offering promising pathways for next-generation solutions in tissue engineering.

Keywords: Biomaterials; Tissue Engineering; Bioactive glass; Biopolymers; Bioactivity.

Riassunto

L'incidenza crescente di malattie croniche e degenerative associate all'invecchiamento e all'aumento della popolazione, come l'osteoartrite e le ferite croniche (es. ulcere da diabete), ha messo in risalto la necessità di materiali avanzati in grado di supportare la rigenerazione tissutale. I biomateriali svolgono un ruolo centrale in questo ambito, poiché forniscono una struttura di supporto interagendo in modo favorevole con i sistemi biologici. La presente tesi esplora la progettazione, la fabbricazione e la caratterizzazione di biomateriali avanzati che integrano sistemi inorganici, polimerici e compositi per affrontare le sfide attuali dell'ingegneria tissutale.

La prima parte del lavoro è dedicata allo sviluppo di nuove composizioni di vetri bioattivi. I vetri bioattivi, grazie alla loro specifica composizione e alla loro intrinseca natura amorfa, possono interagire con i tessuti biologici e promuoverne la rigenerazione. Attraverso l'incorporazione di stronzio e magnesio come dopanti, sono stati ottenuti nuovi vetri silicatici con migliore stabilità termica, miglior sinterizzazione e bioattività. L'influenza di questi dopanti sulla struttura, sulle proprietà meccaniche e sulla risposta cellulare è stata studiata in modo sistematico. Le nuove composizioni di vetro hanno mostrato una sinterizzabilità superiore rispetto alle principali composizioni commerciali (Bioglass® 45S5 e S53P4), insieme a promettenti risultati biologici per la potenziale fabbricazione di scaffold. Basandosi su queste evidenze, sono stati progettati e realizzati scaffold compositi polimero–vetro bioattivo attraverso la stampa 3D. Le prove meccaniche, le simulazioni agli elementi finiti e le valutazioni biologiche hanno confermato la potenziale idoneità di questi dispositivi per la rigenerazione ossea, evidenziando la sinergia tra composizione del materiale e processo di produzione.

Parallelamente, la ricerca ha esplorato sistemi polimerici naturali sostenibili derivati da tre fonti di biomassa di Theobroma (cacao, cupuaçu, and macambo). Questi frutti producono grandi quantità di scarti nei paesi sudamericani, poiché circa il 70% della loro massa corrisponde alla buccia del frutto, ricca di molecole bioattive e polisaccaridi. Per sfruttare queste risorse sottoutilizzate, tramite l'estrazione assistita da ultrasuoni, sono stati isolati polisaccaridi ricchi in pectina e caratterizzati in termini di composizione chimica, comportamento reologico e contenuto di composti bioattivi. I polisaccaridi estratti hanno mostrato un'attività antiossidante superiore rispetto alla pectina commerciale, insieme a promettenti proprietà funzionali. Questa sezione evidenzia sia il potenziale dei materiali di origine naturale per l'ingegneria tissutale, sia il valore dei principi di economia circolare nello sviluppo di biomateriali funzionali.

Infine, la tesi discute il ruolo emergente dell'intelligenza artificiale nella scienza dei biomateriali, evidenziandone i limiti e come questa possa accelerare la scoperta di nuovi materiali, ottimizzare le relazioni composizione-proprietà e prevedere le prestazioni biologiche.

Nel complesso, questa ricerca propone un quadro multidisciplinare per la progettazione razionale di biomateriali multifunzionali, indicando prospettive promettenti per soluzioni di nuova generazione nell'ingegneria tissutale.

Parole chiave: Biomateriali; Ingegneria Tissutale; Vetri Bioattivi; Biopolimeri; Bioattività.

Table of Contents

Abstract 3

Riassunto 4

Table of Contents 6

1. Introduction 9

1.1. Biomaterials: classification and clinical relevance 10

1.2. Bioactive glasses: structure, properties, and doping strategies 12

1.3. Polymers: synthetic and natural approaches 15

1.4. Scaffolds for tissue engineering: roles and alternatives 18

1.5. Challenges and aims of the thesis 20

2. Bioactive glasses: novel compositions 22

2.1. Introduction 22

2.2. Enrichment of strontium and magnesium improves the physical, mechanical and biological properties of bioactive glasses undergoing thermal treatments: new cues for biomedical applications 25

2.2.2. Materials and Methods 25

2.2.3. Results and Discussion 29

2.2.4. Conclusions 56

2.1.5. Supplementary 58

2.3. An enhanced bioactive glass composition with improved thermal stability and sinterability 60

2.3.2. Materials and Methods 60

2.3.3. Results and Discussion 63

2.3.4. Conclusion 70

3. Additive Manufacturing and Composite Scaffolds 71

3.1. Additive Manufacturing of Polymer/Bioactive Glass Scaffolds for Regenerative Medicine: A Review 71

3.1.1. Introduction 71
3.1.1. Extrusion-based 3D printing 74
3.1.2. Lithography-based 3D printing 83
3.1.3. Laser-based 3D printing 87
3.1.4. Conclusions 94
3.2. Mechanical, Computational, and Biological Evaluation of 3D-Printed PLA-Bioglass Scaffolds for Bone Tissue Regeneration 96
3.2.1. Introduction 96
3.2.1. Materials and methods 98
3.2.3. Results and discussion 103
3.2.4. Conclusions 112
3.2.5. Supplementary 114
4. Natural Polymers from Biomass 115
4.1. Valorization of metabolite-enriched carbohydrates from Theobroma biomass via ultrasound-assisted alkaline extraction 115
4.1.1. Introduction 115
4.1.2. Materials and methods 118
4.1.3. Results 124
4.1.4. Conclusion 144
4.1.5. Supplementary 146
5. Future Perspectives: Artificial Intelligence in Biomaterials 149
5.1. The role of artificial intelligence in biomaterials science: a review 149
5.1.1. Introduction 149
5.1.2. Methodology 150
5.1.3. Artificial Intelligence: from data science to machine learning 150
5.1.4. Machine learning for biomaterials 162
5.1.5. Challenges and future perspectives 178
5.1.6. Conclusions 179

6. Conclusions and future challenges 180

7. List of publications 182

8. References..... 184

1. Introduction

Over the past few decades, the progressive ageing of the global population has led to a rising incidence of age-related diseases. Advances in biomedical science and technology have enabled the replacement of damaged tissues with grafts aimed at restoring physiological function. Grafts are generally classified according to their origin (**Figure 1**).

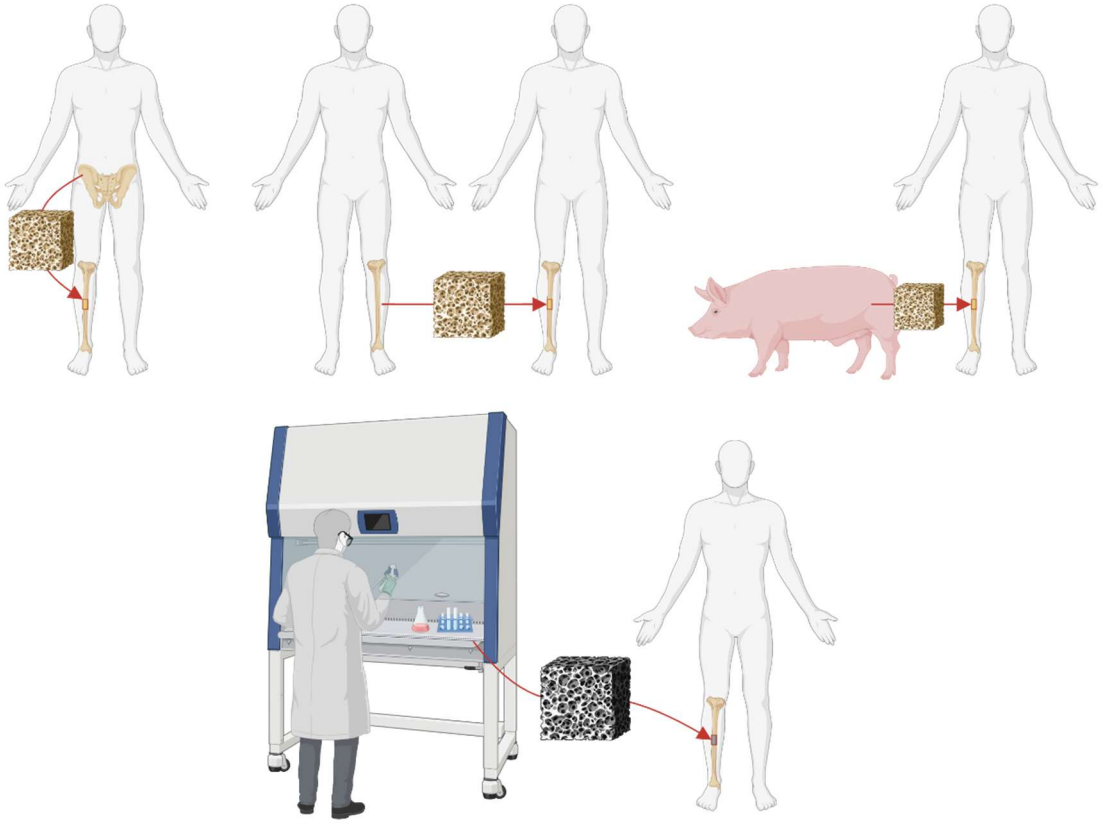

Figure 1. *Schematic representation of autograft, allograft, xenograft and synthetic graft. Created in https://BioRender.com.*

Autografts, which involve transplantation of the patient's own tissue, remain the clinical gold standard because they inherently provide osteoinductive factors, osteogenic cells, and an osteoconductive matrix. Nonetheless, their use is constrained by donor site morbidity and limited tissue availability. To address these drawbacks, allografts - tissues obtained from human donors other than the recipient - have been introduced, though they are associated with risks of immune rejection and disease transmission (Betz, 2002; Giannoudis et al., 2005). Xenografts, obtained from non-human species such as porcine or bovine sources, are more readily available and less costly than allografts; however, their use is limited by strong immunological rejection (Amini and Lari, 2021; Azimzadeh et al., 1996; Carvalho et al., 2021). Synthetic grafts, by contrast, decrease immune-related complications through their

non-biological origin, yet they have not fully achieved the regenerative capacity of natural tissues (Betz, 2002; Giannoudis et al., 2005).

Regenerative medicine (RM) focuses on restoring or replacing human cells, tissues, or organs to reestablish normal physiological function (Mason and Dunnill, 2008). Within RM, tissue engineering (TE) specifically addresses the design and fabrication of synthetic grafts. TE employs two primary strategies for tissue regeneration: *ex vivo* and *in situ* approaches. In *ex vivo* TE, cells and bioactive molecules are combined with temporary, porous scaffolds outside the body to produce tissue constructs suitable for implantation (Stevens et al., 2005). Although this method can closely replicate native tissue properties, it faces several drawbacks, including donor tissue limitations, the requirement for large numbers of compatible cells, and difficulties in expanding cells *in vitro*. Moreover, replicating natural autocrine and paracrine signalling pathways remains challenging. Conversely, *in situ* TE exploits the body's intrinsic regenerative capacity, thereby eliminating the need for external cell handling. This strategy involves biomaterials embedded with bioactive cues that direct tissue repair at the injury site (Gaharwar et al., 2020). Such techniques are generally simpler, impose fewer regulatory constraints, and avoid the complex cell culture conditions necessary for *ex vivo* constructs. Additionally, synthetic scaffolds used in *in situ* methods typically exhibit longer shelf lives than their cell-laden counterparts, making them particularly advantageous for clinical applications (Gaharwar et al., 2020).

While TE provides a framework for restoring tissue function, its success relies heavily on the selection of appropriate biomaterials. These materials support cell attachment, proliferation, and differentiation. Therefore, understanding biomaterials, their classifications, properties, and biological interactions, is fundamental to advancing regenerative medicine.

1.1. Biomaterials: classification and clinical relevance

The use of exogenous materials to enhance tissue healing or to restore lost functions largely anticipated the born of the term biomaterial, with the first examples of applications that can be collocated around 2000 B.C. with use of linen by Ancient Egyptians, or with the use of bamboo in China (Todros et al., 2021).

Defining biomaterials is challenging, as the concept has evolved over time in response to advances in technology and scientific knowledge. The European Society for Biomaterials first formalized a definition in 1986: "*A nonviable material used in a medical device,*

intended to interact with biological systems" (Williams and Zhang, 2019). However, this definition did not describe the mechanisms of interaction with host tissues. Additionally, technological developments, including the incorporation of living cells into implantable materials, necessitated a broader definition. Consequently, the definition was modified as follow in 2018: "*A substance that has been engineered to take a form which, alone or part a complex system, is used to direct, by control of interactions with components of living systems, the course of any therapeutic or diagnostic procedure, in human or veterinary medicine*" (Williams and Zhang, 2019). This updated definition emphasizes both the intentional design of biomaterials and their capacity to modulate biological responses, and it remains the most widely accepted today.

Beyond definitions, biomaterials can be grouped according to their material type, an approach that helps predict their key properties and potential applications. Within this framework, biomaterials are generally categorized as:

- Metals, known for their exceptional mechanical strength and toughness, metals are ideal for load-bearing applications such as joint replacements. Certain alloys also display shape-memory effects, which are advantageous in devices like stents (Prasad et al., 2017).
- Ceramics, characterized by high stiffness, hardness, and wear resistance, ceramics exhibit good to excellent biocompatibility. These attributes make them valuable in orthopaedic implants, dental restorations, and tissue engineering scaffolds (Boccaccini et al., 2021; Vaiani et al., 2023).
- Polymers, offer high tuneable mechanical and biological properties. Their ease shapeability allows the fabrication of diverse medical products, from suture threads to complex tissue-engineering matrices (Asghari et al., 2017; Joseph et al., 2017).
- Composites, combining two or more material classes, they integrate the advantages of their constituents to achieve tailored performance, such as enhanced mechanical strength or controlled degradation. Their versatility enables a wide range of biomedical uses (Boccaccini and Blaker, 2005; Khanna et al., 2021).

Alternatively, biomaterials can be classified according to their degree of interaction with the biological environment (Darvell and Smith, 2022; Marin et al., 2020; Montoya et al., 2021):

- Inert biomaterials can be defined as materials that do not exert any biological function and do not induce adverse effects. Examples of inert biomaterials are titanium-alloys, zirconia or polyethylene.
- Bioresorbable materials are able to degrade under physiological conditions without producing toxic by-products. Typical examples of this material class are suture materials, such as polyglycolic acid or polydioxanone.
- Bioactive materials are able to react under physiological conditions, stimulating the healing process. Examples for this class include bioactive glass or hydroxyapatite.
- Bioresponsive materials react to internal or external stimuli, such as pH variation or magnetic fields, and may deliver therapeutics compounds or cells (Lu et al., 2016; Zhao et al., 2016). Typical examples for responsive biomaterials are the hydrogels (Karati, 2023).

1.2. Bioactive glasses: structure, properties, and doping strategies

Among the wide variety of biomaterials developed for clinical applications, bioactive glasses (BGs) have emerged as one of the most versatile and effective systems for hard tissue regeneration. Their ability to bond chemically with bone and stimulate cellular responses distinguishes them from conventional inert ceramics. BGs are amorphous solids, characterized by the absence of long-range order and by bioactivity. They are typically composed of network formers, network modifiers, and intermediate oxides. Network formers are essential for constructing the glass framework and include silica (SiO_2) in silicate glasses, boron trioxide (B_2O_3) in borate glasses, and phosphorus pentoxide (P_2O_5) in phosphate glasses. Network modifiers, such as alkali or alkaline-earth oxides (e.g., Na_2O, K_2O, CaO), disrupt the glass network by breaking Si–O–Si bonds and converting bridging oxygen atoms (BO) into non-bridging oxygen atoms (NBO), thereby increasing ion release and reactivity. Intermediate oxides (e.g., Al_2O_3, TiO_2, ZrO_2, ZnO) occupy a dual role within the glass structure. Unlike network formers, they cannot independently create a glassy network, but they can enter the network as partial formers when charge-balanced or behave as modifiers when present in higher concentrations (Jones, 2015; Kaur et al., 2014).

The first BG was invented by Professor Larry Hench in the early 1970s, and it is a silicate glass known as 45S5 or Bioglass® (composition in mol%: 46.1% SiO_2, 26.9% CaO, 24.4% Na_2O, 2.6% P_2O_5) (Hench et al., 1971). Thanks to its intrinsic amorphous structure and unique chemical composition, this glass can interact with biological tissue and form a bond

with bone so strong that it cannot be removed without fracturing the bone itself. 45S5 not only bonds rapidly to bone but also stimulates bone growth away from the bone-implant interface. The mechanism for bone bonding is attributed to two mechanisms: (i) the formation of a layer of hydroxyl-carbonate apatite (HCA), and (ii) the interactions with collagen fibrils of damaged bone to form a bond (Hench and Paschall, 1973). While the HCA mechanism is now well understood, the latter process remains under debate (Jones, 2015).

The mechanism of bonding to living bone tissue involves a sequence of 12 steps. The first five stages, illustrated in **Figure 2**, occur quickly on the surface through ion exchange, network dissolution, silica-gel polymerization, and chemisorption of ions (e.g. Ca^{2+}, PO_4^{3-}, CO_3^{2-}). These reactions lead to the crystallization of an HCA layer whose composition and structure closely resemble those of biological apatite, the mineral phase of bone. Subsequent steps, including the adsorption of growth factors and a synchronized sequence of cellular events, result in the formation of new bone tissue (Hench, 1998).

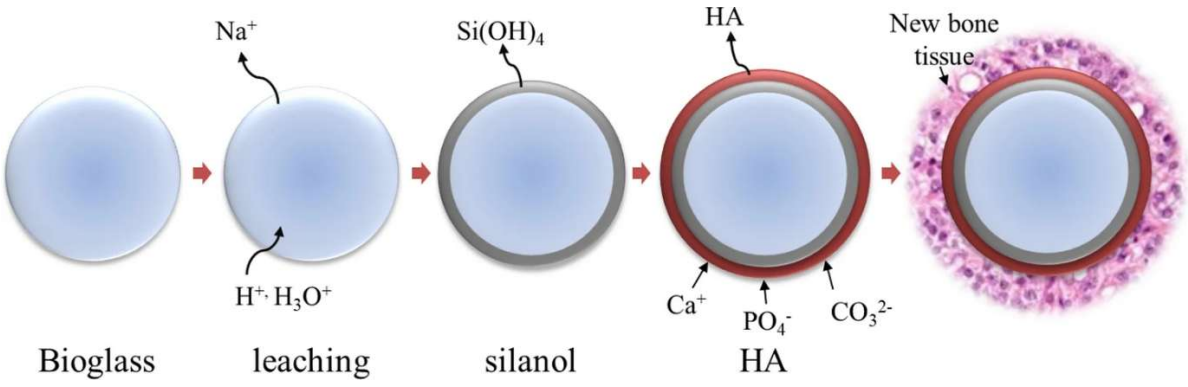

Figure 2. *Schematic illustration of the surface stages (1–5) reactions on bioactive glass, forming double SiO2 rich and Ca, P-rich layers. This figure is reproduced from (Farag, 2023) under an open access license.*

Since their discovery, numerous BG compositions have been developed. BGs can be classified into three categories according to their primary network former: silicate (Si^{4+}), borate/borosilicate (B^{3+}), and phosphate glasses (P^{5+}) (Kaur et al., 2014). Changes in the network former significantly affect glass properties. For example, borate glasses exhibit faster reaction kinetics and more rapid conversion rates into hydroxyapatite than their silicate counterparts (Huang et al., 2006; Yao et al., 2007). Furthermore, ion doping can tailor the physical and biological responses of BGs, enhancing their suitability for specific applications (Hoppe et al., 2011; Pantulap et al., 2022; Rabiee et al., 2015; Zhang et al., 2022). Examples of such ions include Sr, which enhances osteoblast activity and modifies bioactivity, and Ag, which influences both antibacterial activity and bioactivity (Rabiee et al., 2015). **Figure 3** summarizes the key dopants and their associated biological functions.

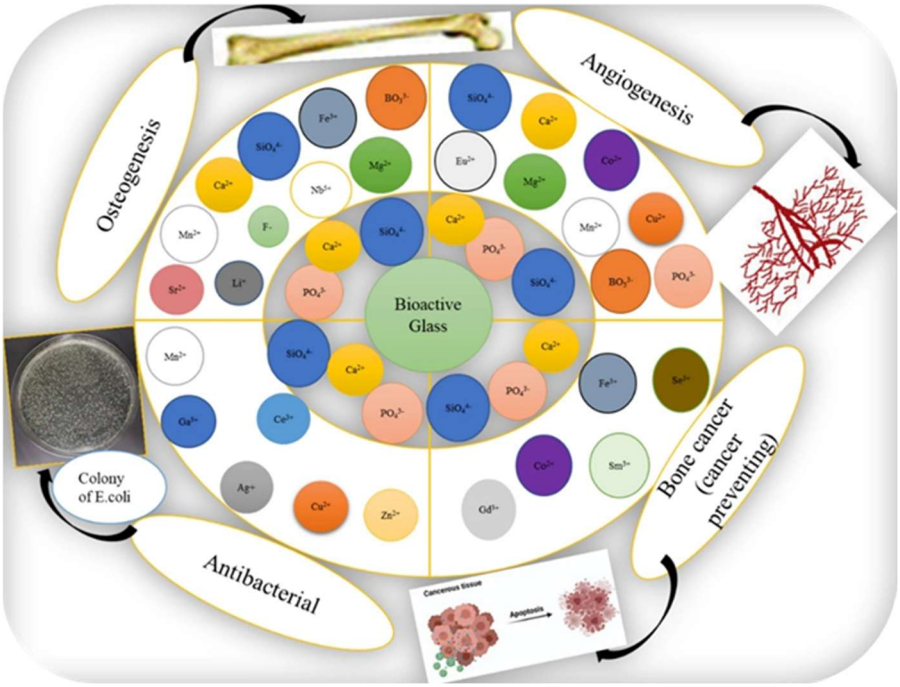

Figure 3. Schematic representation of the biological effects of different ions incorporated in BG composition. Reproduced with license from (Taye, 2022).

Controlling the dissolution rate remains a non-trivial challenge, as it influences both bioactivity and the resulting biological response. One strategy to modulate dissolution is to exploit the mixed-alkali effect, introducing multiple alkali ions (e.g., K^+) rather than relying solely on sodium in the BG composition (Brückner et al., 2016). Alternatively, the dissolution rate can be predicted using molecular dynamics simulations or machine-learning models, which employ structural descriptors such as network connectivity parameters (Montazerian et al., 2020). Network connectivity (NC) is directly related to glass properties, such as dissolution rates or thermal properties (Akunna and Cerruti, 2024). In silicate glasses, NC represents the average number of BOs on each silica tetrahedron $(SiO_4)^{4-}$ and reflects the degree of crosslinking within the silica network (Jones and Clare, 2012; Shelby, 2005). It can be calculated as:

$$NC = \frac{4[SiO_2] - 2[M_2^I O + M^{II} O] + 6[P_2O_5]}{[SiO_2]}$$

Where M_2^IO and $M^{II}O$ are the mono- and divalent modifier oxides in the glass (Hill and Brauer, 2011). As example, NC for 45S5 is:

$$NC = \frac{4 \times [46.1] - 2 \times [24.4 + 26.9] + 6 \times [2.6]}{[46.1]} = 2.11$$

Notably, NC is inversely correlated with the onset of apatite formation (Hill and Brauer, 2011). Glasses with an NC greater than 2.6 are generally considered non-bioactive due to their limited dissolution (Jones, 2015).

The unique properties of bioactive glasses have led to several clinical applications with the first human use of Bioglass® approved by Food and Drug Administration (FDA) in the 1980s for middle-ear ossicular implant and periodontal bone repair. Another application of 45S5, under the commercial name of Novamin®, is its incorporation as a desensitizing agent in toothpastes for the treatment of dentin hypersensitivity (Baino et al., 2018). Nowadays, along with 45S5, the most commonly used and FDA approved BGs are S53P4, commercially known as Bonalive® (composition in mol%: 53.8% SiO_2, 21.8% CaO, 22.7% Na_2O, 1.7% P_2O_5), and 13-93 (composition in mol%: 54.6% SiO_2, 22.1% CaO, 6.0% Na_2O, 1.7% P_2O_5, 7.9% K_2O, 7.7% MgO) (Brink, 1997; Jones, 2015; Massera et al., 2012).

BG compositions have also been used as porous glass-ceramic sintered block. However, crystallization negatively influences BG bioactivity, due to the reduced ionic release once implanted in the body. Moreover, the different degradation rates of the amorphous and crystalline phases introduced by partial crystallization may undermine the mechanical properties of sintered scaffold (Chen et al., 2006; Jones, 2015). Consequently, one of the main challenges in the use of BG lies in their tendency to crystallize during heat processing. To widen the working window of BGs - defined as the temperature difference between the glass transition temperature and the crystallization temperature, that allows sintering without unwanted crystallization (Jones, 2015) - various new compositions have been developed over the years, e.g. 13-93, ICIE6, and BGMS10 (Bellucci and Cannillo, 2018; Brink, 1997; Elgayar et al., 2005). However, although the results are promising, the current proposals have not yet achieved the optimal compromise between physical and biological behaviour. **Chapter 2** is dedicated to addressing this challenge, with novel compositions proposed to overcome the issue.

1.3. Polymers: synthetic and natural approaches

Despite the remarkable bioactivity of glass-based materials, their brittleness and limited flexibility constrain their use in load-bearing or soft tissue applications. To overcome these limitations, polymers have gained increasing attention due to their tuneable mechanical and biological properties.

Polymers are large macromolecules formed by the repetition of smaller structural units known as monomers. Two main structural types of polymers exist: linear and crosslinked. Linear polymers consist of long molecular chains connected end to end. These chains can also exhibit branching, meaning that side chains extend from the main polymer backbone (**Figure 4**). Typically, linear polymers are thermoplastic (Dyson, 1987). Thermoplastics are materials that soften or melt when heated and can be reshaped repeatedly without significant chemical change. Examples of thermoplastic polymers used in tissue engineering include polylactic acid (PLA) and polyethylene (PE) (Hall, 1981), that can be easily shaped by additive manufacturing techniques.

Crosslinked polymers consist of various polymer chains joined by covalent or non-covalent bonds (**Figure 4**), and their properties depend on the type and degree of crosslinking (Dyson, 1987). In general, a higher degree of crosslinking results in lower elasticity, higher stiffness, lower viscosity, and enhanced mechanical strength (Maitra and Shukla, 2014). Thermosetting polymers belong to this category; they undergo irreversible cross-linking during treatment, and subsequent heating causes degradation rather than melting. Examples of thermosetting polymers include methacrylic resins (Hall, 1981). Additionally, crosslinked polymers are insoluble but can absorb solvents and swell until reaching a gel state (Maitra and Shukla, 2014). This hydrogel-like behaviour is particularly valuable in soft tissue regeneration, where flexibility, water uptake, and biocompatibility are essential.

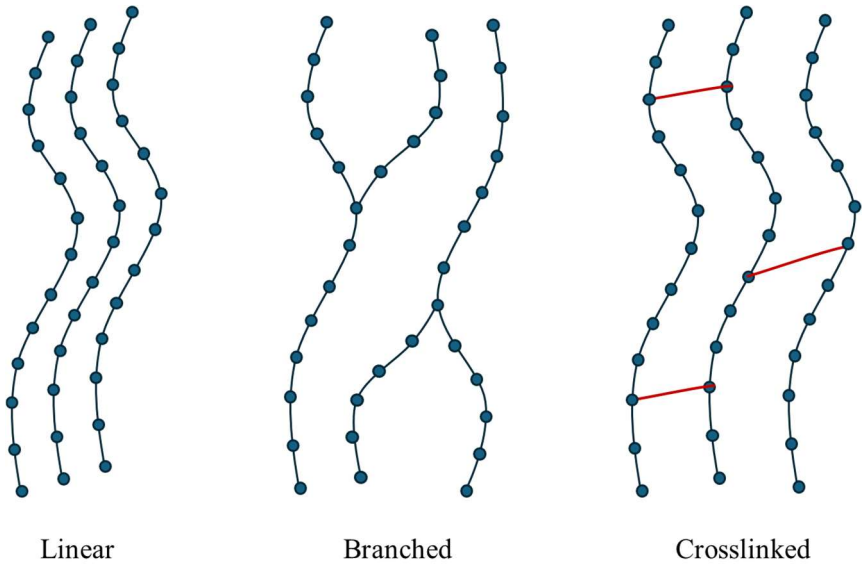

Figure 4. *Schematic representation of polymer structures.*

Various types of crosslinkers and crosslinking techniques are employed depending on the type of biopolymer to be crosslinked and the desired improvement in material properties.

Chemical crosslinking forms covalent and irreversible bonds. It can be triggered by chemical reactions, such as condensation, or by irradiation, such as UV exposure. The resulting polymer networks exhibit high stability; however, their biocompatibility depends on the reagents involved. Physical crosslinking arises from non-covalent interactions, such as hydrogen bonding or ionic interactions. It can be triggered by ionic exchange or temperature changes, and in some cases is reversible. This approach is commonly used in hydrogel gelation processes, as no chemical reagents are required. Enzymatic crosslinking is catalysed by specific enzymes and occurs under physiological conditions. This method offers high biocompatibility, although the reaction rate and kinetics can be difficult to control (Gao et al., 2021; Maitra and Shukla, 2014; Reddy et al., 2015; Xue et al., 2022).

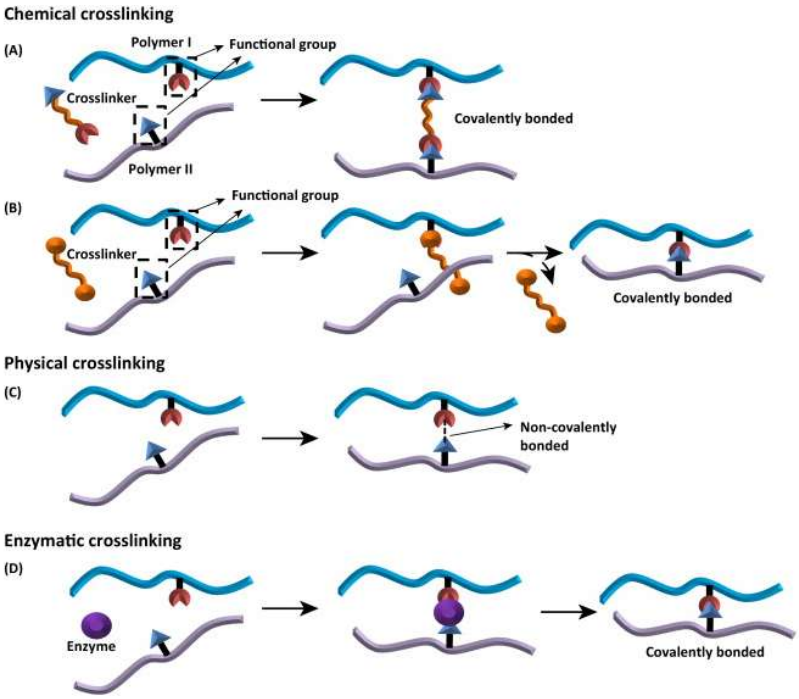

Figure 5. *Schematic representation of different crosslinking methods: (A) chemical crosslinking with the crosslinker incorporated into the bond, (B) chemical crosslinking with the crosslinker not incorporated into the bond, (C) physical crosslinking, (D) enzymatic crosslinking. Reproduced with license from (Reddy et al., 2015)*

Another classification is based on their origin, distinguishing synthetic from natural polymers. Synthetic polymers offer numerous advantages, such as tuneable mechanical properties (ranging from soft elastomers to stiff thermoplastics), less immunogenic, adjustable chemical and physical characteristics, high processability, and cost-effectiveness (Kalirajan et al., 2021; Terzopoulou et al., 2022). On the other hand, natural polymers are generally biocompatible, biodegradable, and environmentally friendly. However, due to their biological origin, they may exhibit batch-to-batch variability, potential immunogenicity, and complex extraction or purification processes, which can be time- and resource-intensive.

Common examples of natural polymers include chitosan, pectin, and alginate (Asghari et al., 2017; Terzopoulou et al., 2022).

The potential of polymers in tissue engineering also lies in their ability to deliver drugs, helping to maintain constant therapeutic levels and thus minimize dosing frequency. Polymers can be used as membranes for drug encapsulation, where diffusion is determined by the membrane's composition and thickness (Klojdová et al., 2023; Martelli et al., 2025). Alternatively, drugs can be dissolved within the polymer matrix, with the release rate governed by the geometry of the system. The introduction of additive manufacturing enables more precise control over geometry and, consequently, the drug release profile (Borandeh et al., 2021). Another approach, which offers several advantages - including enhanced drug solubilization, controlled delivery, increased efficacy, and improved pharmacokinetics - involves the covalent conjugation of drugs to polymers. In this case, drug release mainly depends on the degradation rate of the polymer and the geometry of the construct (Borandeh et al., 2021; Ekladious et al., 2019).

Overall, polymers represent a versatile class of materials widely used in medicine due to their broad range of properties, ease of processing, and lower cost compared to metals or ceramics.

1.4. Scaffolds for tissue engineering: roles and alternatives

Scaffolds are fundamental tools in tissue engineering, providing mechanical and biological support to facilitate host tissue healing. The ideal scaffold should mimic as closely as possible the structure and function of the tissue it aims to restore. In particular, it should:

- Be biocompatible, allowing cell attachment and proliferation without inducing adverse immune or inflammatory responses (Dave and Gomes, 2019);
- Have an interconnected pore structure with controlled pore size, which is crucial for nutrient transport, waste removal, and tissue growth. The optimal pore size may vary depending on the target tissue (Hollister, 2005; Poh et al., 2019);
- Have mechanical properties that resemble those of the target tissue, to prevent complications such as mechanical mismatch or bone resorption (Hollister, 2005; Poh et al., 2019);
- Be biodegradable when tissue substitution or regeneration is required, allowing gradual replacement by newly formed tissue;

- Be capable of withstanding sterilization procedures and maintain structural integrity after sterilization, as proper sterilization is essential to prevent infections (Suamte et al., 2023).

Scaffolds can be broadly classified into two main categories: two-dimensional (2D) and three-dimensional (3D) structures (**Figure 6**).

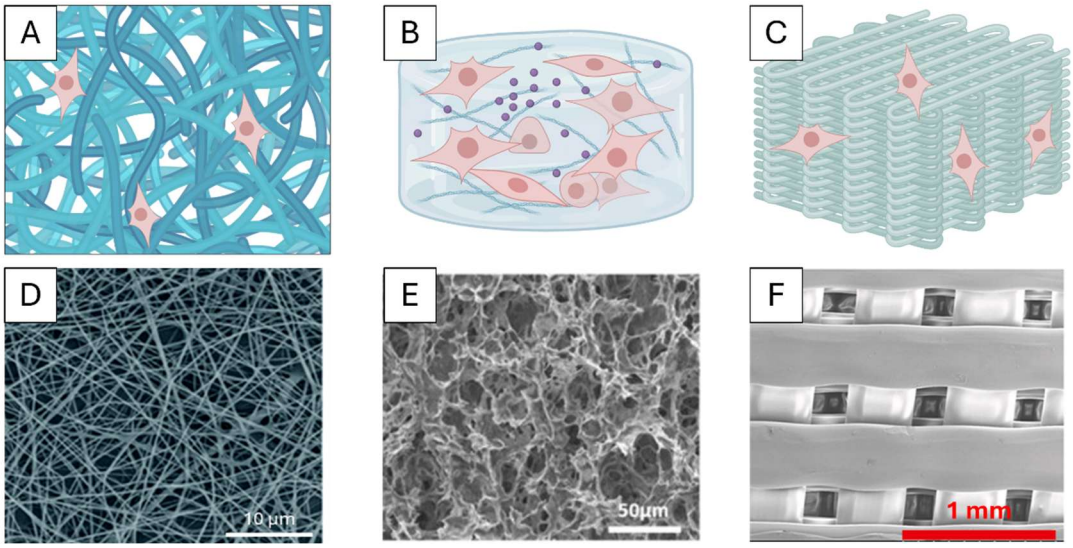

Figure 6. *Representative structures of 2D and 3D scaffolds for tissue engineering. Schematic illustrations of (A) electrospun fibrous scaffolds, (B) hydrogel-based scaffolds, and (C) 3D-printed scaffolds showing encapsulated or attached cells. Created in https://BioRender.com. Corresponding scanning electron microscopy (SEM) images demonstrating the microstructural features of (D) electrospun nanofibers, (E) porous hydrogel networks, and (F) layer-by-layer 3D-printed architectures. Reproduced under the terms of the CC BY license (Jadbabaei et al., 2021; Scalzone et al., 2019) and with permission from the publisher (Wang et al., 2021).*

2D scaffolds, which are thin, surface-like materials with a high surface-to-volume ratio and controllable topography, are suitable for applications requiring high flexibility and intensive cell–surface interactions, such as nerve regeneration, skin repair, and vascular grafts (Flores-Rojas et al., 2023; Liu et al., 2020; Yeo and Kim, 2020). Typically, these structures are fabricated by electrospinning, a technique that uses an electric field to produce nano- and microfibrous mats from polymer solutions (Flores-Rojas et al., 2023). Electrospun 2D mats can also be shaped into tubular forms for nerve grafts (Hou et al., 2023; Kim et al., 2016). Moreover, recent research has expanded the use of 2D scaffolds for advanced biomedical applications such as biosensing, drug delivery, and cancer therapy (Flores-Rojas et al., 2023; Liu et al., 2020).

3D scaffolds, on the other hand, possess a volumetric porous architecture that enables cell infiltration, proliferation, and extracellular matrix deposition throughout the structure. They can exhibit either a random architecture, as seen in hydrogels or sponges, or a highly

organized geometry, such as grid-like or lattice structures. Organized 3D scaffolds are often fabricated using additive manufacturing (3D printing) techniques, which allow precise control over pore size, interconnectivity, and mechanical properties. For a more detailed discussion on fabrication approaches, please refer to **Chapter 3**.

Ultimately, the choice between 2D and 3D scaffolds depends on the specific tissue target, desired mechanical behaviour, and the extent of cell–material interactions required for functional tissue regeneration.

1.5. Challenges and aims of the thesis

Regenerative medicine relies on the synergy between materials science and biological systems to restore or replace damaged tissues and organs. Biomaterials, ranging from inorganic glasses to organic polymers, provide the essential foundation for designing scaffolds capable of supporting cell adhesion, proliferation, and tissue regeneration. Despite significant advances, achieving an optimal balance among bioactivity, mechanical strength, and manufacturability remains a persistent challenge.

The primary aim of this thesis is to investigate and develop novel biomaterials that can address existing limitations in the field, building upon the existing expertise of Cannillo's research group while introducing new methodological and application-oriented perspectives, and contributing to the design of next-generation scaffolds for regenerative medicine applications.

Specifically, **Chapter 2** focuses on bioactive glasses and the challenges related to their thermal processing, which often affect structural integrity and bioactivity. This topic represents a core research area within Cannillo's group. Compared to the current state of the art, the novelty of this work lies in a systematic investigation across multiple compositions and thermal treatment conditions, enabling a deeper understanding of the role of dopants in governing processing windows and functional properties.

Chapter 3 explores the use of additive manufacturing technologies for the fabrication of BG-based scaffolds, combining a comprehensive literature review with experimental investigations. While additive manufacturing has previously been explored within Cannillo's group, this thesis expands and strengthens this research line through the application of fused deposition modelling. Compared to the existing literature, the experimental approach proposes a simple strategy to address the low wettability typically associated with PLA, improving material compatibility and potential biomedical performance.

Chapter 4, developed through an international collaboration, investigates the extraction of natural polymers with a high content of antioxidants from biowaste, with potential application in scaffold production for tissue engineering. This topic had not previously been explored within Cannillo's group and introduces new expertise related to sustainable biomaterials and circular economy strategies. The work systematically analyses and compares polymers extracted from three different biowaste sources, providing insight into their potential functional performance and applicability.

Finally, **Chapter 5** discusses emerging perspectives in regenerative medicine driven by artificial intelligence and data-informed materials design, positioning the thesis within broader future research directions and highlighting opportunities for integrating computational approaches with experimental biomaterials development.

2. Bioactive glasses: novel compositions

2.1. Introduction

45S5 Bioglass® (composition: 46.1 mol% SiO_2, 26.9 mol% CaO, 24.4 mol% Na_2O, 2.6 mol% P_2O_5) stands as the pioneering bioactive glass (BG) developed in the 1970s due to the visionary work and serendipity of L.L. Hench (Hench et al., 1971). Presently, it finds extensive use in orthopaedic and dental applications. However, 45S5 is not the only contender in the market. Indeed, extensive BG research in Finland resulted in the commercialization of the S53P4 formulation (53.8 mol.% SiO_2, 21.8 mol.% CaO, 22.7 mol.% Na_2O, 1.7 mol.% P_2O_5), known as Bonalive®.

The significance of BGs lies in their remarkable propensity to elicit a positive response within the body, particularly in fostering bonding and/or interactions with host tissues (Jones, 2015). This groundbreaking discovery led to the development of various BG types: conventional silicates, exemplified by 45S5, alongside phosphate-based and borate-based glasses. Essential characteristics for BG suitability in the human body encompass biocompatibility, non-cytotoxicity, immunogenicity, and bioactivity, ensuring they do not induce fibrous tissue formation or implant rejection at the application site.

A notable limitation of 45S5 and S53P4 is their challenge in being formed into amorphous bioactive glass scaffolds and, more broadly, in being sintered without experiencing significant crystallization. This issue arises from their tendency to crystallize during sintering, mainly because of a limited sintering window (called also processing window), which is defined as the difference between the crystallization onset temperature and the glass transition temperature (Jones, 2015). Indeed, typical applications require thermal treatments to obtain products, such as sintered parts, scaffolds, and coatings (Baino and Verne, 2017; Henao et al., 2019).

In this context, understanding the crystallization behaviour holds crucial significance, as it is widely acknowledged that crystallization can hinder or reduce bioactivity (Jones, 2015). In certain cases, it may even jeopardize the stability of the implant after it has been placed in the body, given that the residual amorphous phase of the material and the crystalline phase exhibit different reactivity and dissolution rates (Filho et al., 1996). Consequently, extensive efforts have been devoted to the identification of BG compositions with broader sintering windows, exemplified by formulations like 13-93, Bio_MS, and BGMS10 (Bellucci et al., 2020; Bellucci and Cannillo, 2018; Brink, 1997). Among these glasses, Bio_MS (46.1 mol%

SiO_2, 31.3 mol% CaO, 5 mol% Na_2O, 2.6 mol% P_2O_5, 5 mol% MgO, 10 mol% SrO) has exhibited an exceptionally high crystallization temperature (T_C) while showcasing outstanding biological performance (Bellucci et al., 2020).

These distinct properties are attributed to the lower content of alkaline elements and the presence of magnesium (Mg) or strontium (Sr) in the BG composition, recognized for their positive biological effects and their ability to modify thermal and mechanical properties (Bellucci et al., 2017b; Diba et al., 2012; Leite et al., 2018; Verné et al., 2009). In particular, Mg is regarded as functioning both as a network former and as an intermediate oxide (Shimoda et al., 2007; Stebbins, 1998). It acknowledged that Mg decreases the glass transition temperature (T_G) of BGs (Diba et al., 2012; Watts et al., 2010) due to the lower strength of Si-O-Mg bond compared to Si-O-Si bond. Moreover, Mg doping can influence mechanical properties (Jha and Singh, 2016; Magallanes-Perdomo et al., 2012; Pedone et al., 2009) because of its higher ionic field strength (Magallanes-Perdomo et al., 2012). Additionally, Mg-doped BG presents optimal biocompatibility, osteogenic and cell differentiation effects (Moghanian et al., 2018; Schmitz et al., 2020), despite a possible reduction in hydroxyapatite (HA) precipitation *in vitro* on the material, compared to the case of undoped BG (Kanzaki et al., 2000) – HA precipitation is typically taken as an indicator of bioactivity for bioactive glasses.

Similarly, excellent biological behaviour has also been found in Sr-doped BGs (Isaac et al., 2011), although the effect of Sr on HA formation remains controversial (Bahati et al., 2023; O'Donnell and Hill, 2010). Additionally, the impact of Sr doping on the physical properties of BGs is also a subject of debate (Fujikura et al., 2012; Kargozar et al., 2019; O'Donnell et al., 2010), as is the case for K-doped BGs (Cannillo and Sola, 2009; Tylkowski and Brauer, 2013). In fact, when K_2O is added to BG, it acts as a network modifier, and a high content of this oxide can significantly weaken the glass structure (Marikani et al., 2008; Rabiee et al., 2015). Conversely, partially substituting Na with K results in a significantly improved sintering window and a reduced tendency to crystallize compared to undoped glass (Devis Bellucci et al., 2011; Tylkowski and Brauer, 2013). Furthermore, K doping can influence dissolution behaviour, affecting both apatite formation and the biological response (Brink et al., 1997; Hupa et al., 2016).

Different studies suggest promising results from the combined effects of Mg and Sr. Although the recognized beneficial effects of Mg and Sr doping on both physical and biological properties (Bellucci et al., 2020; Bellucci and Cannillo, 2018), a significant gap

in the literature remains regarding systematic studies on co-doping with Mg and Sr in silicate BG composition and corresponding thermal treatments. Similarly, nonetheless the combined effects of Mg, Sr, and K demonstrated excellent thermal stability, bioactivity, and biological performance both *in vitro* and *in vivo* (Anesi et al., 2023; Bellucci and Cannillo, 2018) only few studies focused on the combined effects of these elements. Considering this knowledge gap, our research focuses on a set of BGs to elucidate on the non-trivial relationships between composition, sintering, crystallization, and biological responses.

The chosen reference BGs for this investigation include two widely known commercial variants, namely 45S5 and S53P4, as well as the previously presented patented BG Bio_MS. Furthermore, our study extends its exploration by introducing doped versions of the commercial BGs. Specifically, Mg, Sr (named as MS), and K (named as MSK) are introduced as substitutes for sodium (Na). This research focuses on two interconnected aims. The primary goal is to investigate the impact of sintering and crystallization on BGs. Simultaneously, it aims to assess how doping influences the processes of sintering and crystallization, and the biological response of these BGs.

2.2. Enrichment of strontium and magnesium improves the physical, mechanical and biological properties of bioactive glasses undergoing thermal treatments: new cues for biomedical applications

(This section has been published in: Bellucci, D.; Mazzilli, A.; Martelli, A.; Mecca, F.G.; Bonacorsi, S.; Lofaro, F.D.; Boraldi, F.; Quaglino, D.; Cannillo, V. Enrichment of strontium and magnesium improves the physical, mechanical and biological properties of bioactive glasses undergoing thermal treatments: New cues for biomedical applications, Ceramics International, 2024, 50, Issue 24, Part A, Pages 52819-52837, https://doi.org/10.1016/j.ceramint.2024.10.135. *Reproduced in accordance with the publisher's copyright policy.)*

The candidate performed the experimental work, in particular crystallization assessment, phases analysis, and mechanical characterization. Additionally, the candidate contributed to data analysis and manuscript preparation.

2.2.2. Materials and Methods

2.2.2.1. Preparation of the bioactive glass

This study aims to comprehensively investigate and characterize the effects of thermal treatment on the physical, chemical, and biological properties of BGs. The production of the glasses in this study utilized a well-established melt-quenching method, which has previously been employed for the production of other BGs (Hench et al., 1971). High-quality raw materials in powder form (Carlo Erba Reagenti, Rodano-Milano, Italy) were accurately weighed and mixed for 2 hours in a laboratory rotary mixer. The mixture was melted in a platinum crucible following this thermal treatment: heated from room temperature to 1100 °C at 10 °C/min; decarbonated at 1100 °C for 1.5 hours; then heated from 1100 °C to 1450 °C at 10 °C/min and held for 1 hour at 1450 °C to obtain a homogeneous melt. The molten glass was subsequently quenched in water to achieve rapid cooling, resulting in the formation of a frit. The frit was then dried at 110 °C for 12 hours.

A portion of each frit was then ground in a porcelain jar and sieved to obtain powders with a particle size below 63 μm. Another portion was ground and sieved to produce granules with a grain size ranging between 250 and 500 μm. This specific grain size was chosen to optimize the *in vitro* biological response, based on insights from prior studies (Jones, 2015; Tainio et al., 2020).

The compositions of the BGs employed for the present study, expressed in mol%, are detailed in **Table** 1. Please note that the MgO and SrO contents in 45S5_MS and S53P4_MS were chosen to be comparable to that of Bio_MS.

***Table 1**. Composition in mol% of the five BGs.*

Sample	**SiO_2**	**P_2O_5**	**Na_2O**	**CaO**	**MgO**	**SrO**
45S5	46,1	2,6	24,4	26,9	-	-
S53P4	53,8	1,7	22,7	21,8	-	-
Bio_MS	46,1	2,6	5	31,3	5	10
45S5_MS	46,1	2,6	9,4	26,9	5	10
S53P4_MS	53,8	1,7	7,7	21,8	5	10

2.2.2.2. Thermal analysis

The thermal behaviour of the produced BGs, in both powder and granule form, was investigated via Differential Thermal Analysis (DTA) using a Differential Thermal Analyzer (STA 429 CD, Netzsch-Gerätebau GmbH, Selb, Germany). In this analysis, 30 mg of glass was placed in a platinum crucible and heated from room temperature to 1200 °C at a rate of 20 °C/min. The DTA curve obtained allowed for the determination of characteristic temperatures of the BGs, which are the glass transition temperature (T_G), onset crystallization temperature (T_{C_onset}), and peak crystallization temperature (T_C). Additionally, a heating microscope (HM) was employed to examine the behaviour of the glass powders over a broader temperature range, from room temperature to 1600 °C, with a heating rate of 10 °C/min. This was conducted using a Misura 3.32 equipment (Expert System Solutions, Modena, Italy). The purpose of this analysis was to identify the sintering temperature (T_S) and the melting temperature (T_M) of the BGs.

2.2.2.3. Sintering behaviour

To explore the impact of temperature on sintering, the glass powders were used to create disks that underwent heat treatment for three hours at five arbitrarily chosen temperatures: 650 °C, 750 °C, 850 °C, 950 °C, and 1050 °C. The evaluation of sintering quality was based on the observed degree of shrinkage. The process to create the green bodies involved subjecting the glass powders to uniaxial pressing at a pressure of 7 bar for 10 seconds. Subsequently, five green bodies of each BG were placed in a muffle furnace (AWF 13/12, Lenton - Laboratory Scientific Equipment, Randburg, South Africa) and subjected to heat treatment at the specified temperatures, employing a heating rate of 10 °C/min. Following

the thermal treatment, the samples were air-cooled to reach room temperature. To assess the changes in size resulting from shrinkage, the diameters of the samples were measured using a digital calliper (LTF 327.09, LTF S.p.A., Antegnate, Italy). The temperature associated with the maximum observed shrinkage was considered the best sintering temperature (T_{BS}).

2.2.2.4. Phases analysis

To compare the impact of heat treatment on the five BG compositions, granules were subjected to heat treatment at two specific temperatures: T_C determined via DTA analysis, and T_{BS} determined as previously described. Both treatments lasted three hours. The phase composition of both untreated and treated granules, along with the potential formation of crystalline phases, was examined using X-Ray Diffractometry (XRD: X'Pert PRO; Panalytical, Almelo, the Netherlands). Data collection was obtained by a 2θ scan method in the range of 10–90° using Cu-kα X-ray line (step size: 0.017° 2θ).

2.2.2.5. Physical and mechanical properties

To determine the density of the samples treated at T_{BS}, cross-sectional analysis was conducted using image analysis techniques. The Environmental Scanning Electron Microscope (ESEM) (Quanta 2000, Fei Co., Eindhoven, Netherlands) was employed to capture images of the samples, and ImageJ software was used to assess the porosity from the images. Following the density evaluation, the mechanical properties were examined using Open Platform equipment (CSM Instruments, Peseux, Switzerland) with a Vickers indenter tip. A load of 1000 mN was applied during indentation, with a loading/unloading rate of 2000 mN/min and a hold time of 15 s. Each sample was tested at least 15 times, and the load-penetration depth curve was automatically recorded for each indentation. Young's modulus was automatically calculated using the method proposed by Oliver and Pharr (Oliver and Pharr, 1992).

2.2.2.6. SBF testing

The assessment of the bioactivity of the BG granules involved their immersion in Simulated Body Fluid (SBF), following the Kokubo protocol (Kokubo et al., 1990; Ohtsuki et al., 1991). Specifically, 1.5 g of BG granules were submerged in 50 ml of SBF and incubated at 37 °C for durations of 3, 7, and 14 days. The pH of the solution was monitored, and the SBF was replaced every 48 hours. The starting pH of the solution was 7.4 as specified by the Kokubo protocol (Kokubo et al., 1990; Kokubo and Takadama, 2006). After each time interval, the granules were collected via filtration and washed with distilled water. At the end of the test the samples were air-dried at room temperature for 24 hours.

The apatite-forming ability of both heat treated and untreated glasses was assessed using XRD and micro-Raman spectroscopy (LabRAM, Horiba Jobin-Yvon, Villeneuve D'Aseq, France). The spectrometer was equipped with a diode laser operating at a wavelength of 632.8 nm and delivering 20 mW of power to the sample. The scattered photons were dispersed using a grating monochromator with a resolution of 1800 lines/mm and then captured by a CCD camera. An optic with a 100X Ultra Long Working Distance (ULWD) objective was utilized. The spectral data were collected through a series of 15 acquisitions, each lasting 20 seconds. Lastly, the microstructure of the samples was examined using ESEM equipped with X-ray energy dispersive spectroscopy (EDS) (Inca, Oxford Instruments, UK), conducted under low-vacuum conditions (~ 0.5 Torr).

2.2.2.7. Cytotoxicity according to ISO 10993

To prepare the eluates, BGs were incubated with Dulbecco Modified Eagle Medium (DMEM) (Thermo Fisher Scientific, MA, USA) at 37°C for 16 hours, as recommended by ISO 10993-12 procedures (International Standard Organization, n.d.). Eluates were sterilised using 0.22 μm filters (Merck-Life Science, Darmstadt, Germany).

Balb/3T3 embryonic mouse fibroblast cell line (American Type Culture Collection, ATCC) is widely used for testing cytotoxicity. Cells were seeded at a density of 10^3 cells/well in 96-well plates and cultured in DMEM supplemented with 10% foetal bovine serum, 1% penicillin-streptomycin and 1% non-essential amino acids (Thermo Fisher Scientific). After 24 hours, the culture medium was replaced with eluates at different concentrations (i.e., 100%, 50%, 25% and 12.5%). Negative and positive controls were set using the culture medium only, or the culture medium plus 0.1% sodium dodecyl sulphate (SDS, Merck-Life Science), respectively. After additional 24 hours, cell morphology was evaluated under a phase-contrast microscope (DIAPHOT-TMD, Nikon, Japan) and cytotoxicity was assessed with the MTT assay as recommended by the ISO 10993-5 protocol (Biological Evaluation of Medical Devices - Part 5: Tests for In Vitro Cytotoxicity). Briefly, tetrazolium salts (1mg/mL in DMEM) were added to the cell culture and incubated at 37°C in humidified atmosphere (95% air and 5% CO_2) for 2 hours, then the medium was removed, and 200 μL of dimethyl sulphoxide were added to each well to dissolve formazan crystals. The optical density (O.D.) was measured at 540 nm using a multiplate reader (Multiskan FC, Thermo Fisher Scientific). Data were expressed as percentage of O.D. values of metabolically active living cells in cultures with the presence of eluates compared to cells incubated in the

absence of eluates set at 100%. Blank absorbance was represented by the medium alone. MTT assay was performed in sextuplicate.

2.2.2.8. Cell viability and cell adhesion

Human dermal fibroblasts (HDFs) from adult donors (Cat #C-013-5C, Invitrogen, USA) were cultured and maintained according to Boraldi et al. (Boraldi et al., 2015) . BGs were sterilised by UV light and placed into 96-well ultra-low adhesion plates (Cat #3474, Corning, USA) without washing. HDFs were seeded onto BG ($1.5x10^5$ cells/50 mg of BG) and cultured in standard cell culture conditions for 7 days. The culture medium was changed every two days. At different times of culture (i.e., 1h, 4 and 7 days), cell viability and cell morphology were evaluated by MTT assay and by optical digital microscopy (VHX-7000, Keyence, Japan), respectively. For cell morphology, the cells were fixed with 20% cold methanol and stained with 0.5% crystal violet (Feoktistova et al., 2016). Area (total area of each cell), perimeter, aspect ratio (the ratio between the major and minor axis of a cell) were evaluated using the Image software (v.1.53t) on approximately 80 cells/sample.

2.2.2.9. Cell growth

For cell growth assessment, 12-well plates (Falcon) were prepared with a cell density of 6.0×10^4 cells/well in 1 mL of complete DMEM or in 1 mL of 100% eluate obtained from BG 45S5 T_{BS} (for the preparation of the eluate see paragraph 2.7). Cells were cultured for 7 days with changes of the medium (DMEM or eluate) on the fifth day of culture. Cell counts were performed at day 1, 4 and 7 after seeding using the Neubauer chamber.

2.2.2.10. Statistical analysis

One-way analysis of variance (ANOVA) was used for multiple comparisons and a Tukey post-hoc test was applied. Statistical analyses were performed using GraphPad Prism 8.0 software (San Diego, CA). Values are reported as mean ± standard deviation (SD). Differences were considered significant for $p < 0.05$.

2.2.3. Results and Discussion

2.2.3.1. Thermal analysis

Figure 7 (A-E) presents the DTA curves of the BGs, acquired while heating at a rate of 20 °C/min using fine powders (<63 μm). The observed glass transition temperatures T_G for 45S5 and S53P4, measuring 520 °C and 530 °C, respectively, are consistent with data documented in existing literature (Arstila et al., 2007; Boccaccini et al., 2007; Bretcanu et al., 2009; Massera et al., 2012; Strömberg et al., 2023). Similarly, the data obtained for

Bio_MS aligns with the analysis conducted in prior research (Bellucci et al., 2020), thereby establishing a foundational platform for comparing with other MS-doped BGs. However, it's important to note that while the findings concerning the crystallization temperature T_C of 45S5 and Bio_MS align with literature (Arstila et al., 2007; Bellucci et al., 2020; Boccaccini et al., 2007; Bretcanu et al., 2009; Massera et al., 2012), the data for S53P4 contradicts existing studies. Specifically, the recorded T_C is 648 °C, unlike the range found in other studies, which report a T_C between 730 °C and 805 °C (Fabert et al., 2017; Strömberg et al., 2023). This discrepancy could potentially be attributed to the granulometry used for the DTA analysis or the heating rate employed during evaluation. Further DTA analyses on BG granules confirmed the effect of granulometry size on thermal behaviour. Comparative data between powders and granules for each composition are provided in the Supplementary Materials (**Supplementary 1**), highlighting an increase in T_C with increasing granulometry size, consistent with literature findings (Massera et al., 2012).

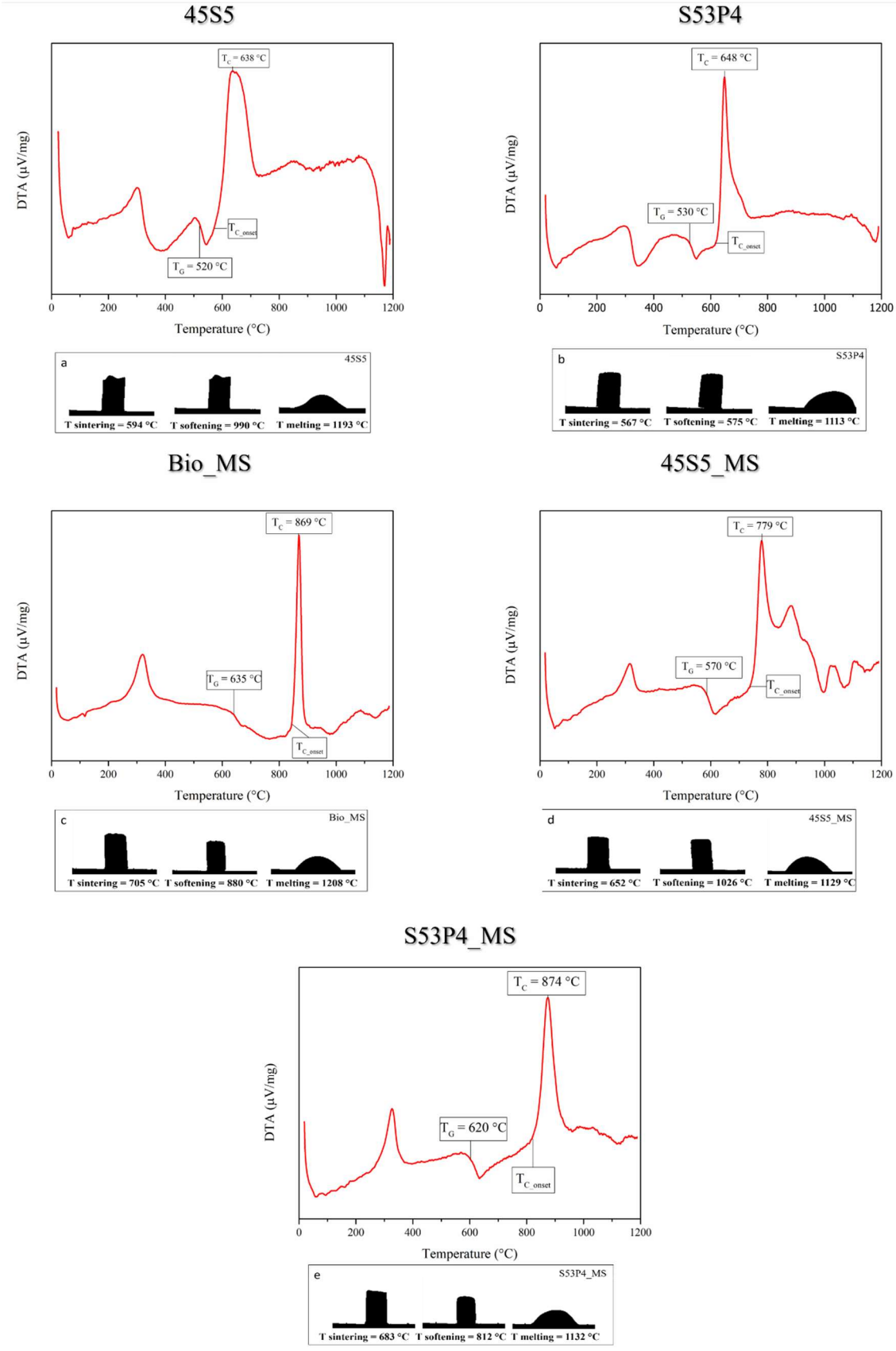

Figure 7. *DTA and HM analyses of: (A) 45S5, (B) S53P4, (C) Bio_MS, (D) 45S5_MS and (E) S53P4_MS. Characteristic temperatures TG, TC_onset and TC are highlighted on the DTA curves.*

Figure 7 also illustrates the results of the HM analysis, delineating the sintering, softening (marking the initiation of BG collapse owing to viscous flow), and melting temperatures of the samples. The data highlighted that the "MS" samples exhibit higher sintering temperature compared to their parent glass, with Bio_MS showing to have the highest sintering temperature. However, this analysis alone does not comprehensively reveal the optimal sintering conditions for BGs but rather indicates the temperature at which the glass begins to contract. Therefore, additional studies were conducted to explore BGs behaviour under various sintering conditions.

2.2.3.2. Sintering behaviour

Table 2. Values of shrinking (expressed as percentages) of the BG disks after heat treatment for 3 hours at different temperatures. The highlighted values represent the highest value of shrinkage measured for each BG. showcases the results obtained from a shrinkage assessment conducted at different temperatures, highlighting the best sintering temperature T_{BS} in green. For 45S5, as observed by Bretcanu et al. (Bretcanu et al., 2009) and Lefebvre et al. (Lefebvre et al., 2008), the sintering process reveals two distinct stages: an initial phase followed by a more prolonged and marked stage. Densification initiates at 650 °C during the first step, while the second densification phase starts at 950 °C, peaking at 1050 °C. The shrinkage associated with the first step measures approximately 2%, whereas a higher shrinkage rate of around 10% was recorded during the subsequent phase of densification. Remarkably, the T_{BS} identified in this study aligns with findings reported by Chen et al. (Chen et al., 2006).

In the case of the S53P4, the glass exhibited the highest level of shrinkage at 650 °C, suggesting this temperature as potentially ideal for the sintering process. However, this observation contradicts other studies that identified 720 °C as the optimal sintering temperature (Björkenheim et al., 2021; Strömberg et al., 2023). It is worth noting that in these studies, the determination of the optimal sintering temperature relied on manually testing the fragility of BG-scaffolds produced at different temperatures. It is noteworthy to mention that the S53P4 samples encountered difficulty in being sintered at 1050 °C due to glass softening, thus making the measurement of shrinkage impossible in those conditions.

Regarding Bio_MS, its identified T_{BS} aligns with the findings of a previous study (Bellucci et al., 2020). Similarly, for other MS-doped bioactive glasses, the maximum densification occurred at 750 °C, diverging from the sintering temperatures suggested by the

HM analysis, which were 50-100 °C lower. Notably, Bio_MS, 45S5_MS, and S53P4_MS also exhibit superior sinterability compared to commercial BGs.

Table 2. *Values of shrinking (expressed as percentages) of the BG disks after heat treatment for 3 hours at different temperatures. The highlighted values represent the highest value of shrinkage measured for each BG.*

	Shrinkage % at the respective temperatures				
Sample	650 °C	750 °C	850 °C	950 °C	1050 °C
45S5	2% (± 0.48)	2% (± 0.91)	3% (± 0.52)	7% (± 0.96)	10% (± 1.21)
S53P4	10% (± 0.68)	7% (± 1.81)	7% (± 0.96)	8% (± 1.51)	-
Bio_MS	0% (± 0.40)	13% (± 0.55)	13% (± 1.24)	10% (± 0.62)	10% (± 1.30)
45S5_MS	13% (± 0.62)	14% (± 0.96)	13% (± 1.44)	9% (± 1.02)	9% (± 0.35)
S53P4_MS	8% (± 1.33)	14% (± 1.08)	11% (± 1.30)	7% (± 2.41)	14% (± 1.07)

Table 3 summarizes the characteristic temperatures found for the five glass compositions. The processing window, defined as the difference between the temperature of crystallization onset and T_G, and the sinterability parameter ($S_C = T_{C\_onset} - T_{BS}$) are reported as well. The sinterability parameter S_C of a glass is an estimate of its sintering ability versus its crystallization trend. In particular, if T_{C_onset} is lower than the sintering temperature, then $Sc < 0$ and the glass is likely to crystallize before it can sinter; this usually results in non-optimal densification. On the other hand, if $Sc > 0$, the glass can sinter without crystallizing, and thus compaction is promoted.

It is crucial to highlight the beneficial effect of reducing the alkaline content and doping with Mg-Sr on the sintering behaviour of BGs. This leads to increased sample shrinkage and widens the processing window of doped BGs. This observed trend likely results from various factors contributing to higher T_C: lower Na content in doped BGs, potentially reducing glass network mobility (H. Arstila et al., 2008), enhanced stability of MgO-doped glasses due to MgO's inhibitory effect on crystallization (Verné et al., 2009), higher entropy supporting the preservation of the BG network's amorphous structure, and the possible augmentation of flow viscosity owing to the presence of Sr^{2+} (Lotfibakhshaiesh et al., 2010).

Table 3. *Characteristic temperatures of the five BGs, obtained through various techniques: TG glass transition temperature; TC_onset onset crystallization temperature; TC peak crystallization temperature; TBS best sintering temperature; processing window (TC_onset - TG), and sinterability parameter (SC = TC_onset - TBS).*

	T_G	T_{C_onset}	T_C	T_{BS}	Processing window	S_C
45S5	520 °C	560 °C	638 °C	1050 °C	40 °C	< 0
S53P4	530 °C	615 °C	648 °C	650 °C	85 °C	< 0
Bio_MS	635°C	830 °C	869 °C	750 °C	195 °C	80 °C
45S5_MS	570 °C	740 °C	779 °C	750 °C	170 °C	< 0
S53P4_MS	620 °C	810 °C	874 °C	750 °C	190 °C	60 °C

2.2.3.3. Phases analysis

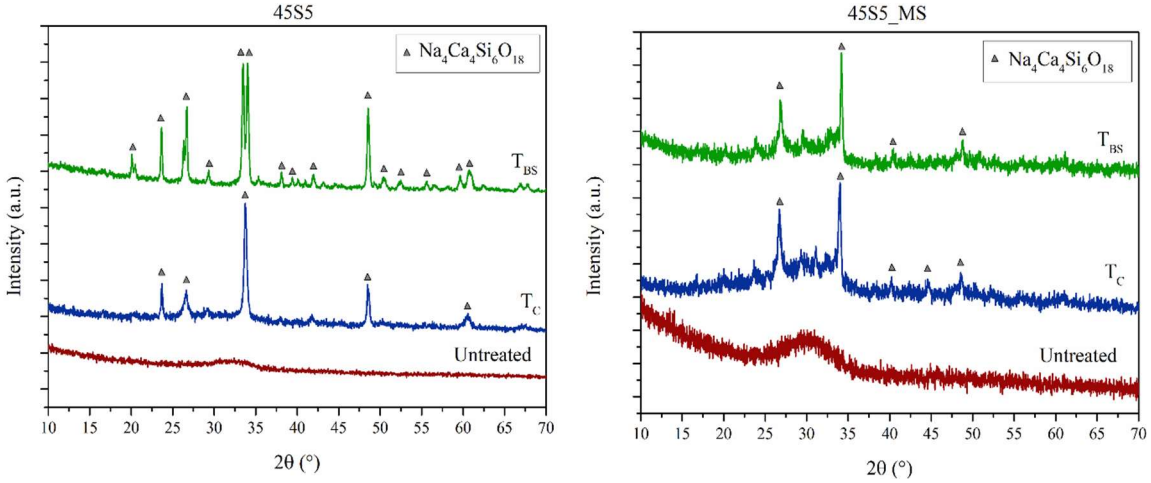

Figure 8. *XRD spectra of 45S5 and 45S5_MS samples in different conditions: untreated (red curve), after heat treatment at TC for 3 hours (blue curve), and after heat treatment at TBS for 3 hours (green curve).*

Figure 8 presents XRD analysis results of 45S5 and 45S5_MS subjected to different heat treatments: untreated and heated at T_C and T_{BS} for 3 hours. Our analysis indicates that after post-thermal treatment, the primary crystalline phase identified is combeite ($Na_4Ca_4Si_6O_{18}$, JCPSD no. 01-079-1086). This aligns with previous studies on the crystallization of 45S5 (Berbecaru et al., 2010; Volzone and Stábile, 2013), although other crystalline phases have also been identified (Boccaccini et al., 2007; Clupper and Hench, 2003). Moreover, XRD analyses confirmed the behaviour observed by Boccaccini et al. (Boccaccini et al., 2007), which identified the variation in lattice parameters, rather than a phase change, as a possible reason for the peak separation in 45S5.

The influence of Mg and Sr on the crystallization behaviour must be considered. Notably, the doped glass exhibits a lower degree of crystallization compared to pure 45S5. This

finding suggests the potential for significant control over the crystallization of doped BG, enabling regulation of the crystalline-to-amorphous BG ratio. Such control could potentially dictate the mechanical and bioactive properties of the BG (Montazerian et al., 2023). It is important to note that the analysed samples do not display any peak associated with crystalline phases of Mg and/or Sr, as confirmed in previous studies (Gavinho et al., 2023).

Figure 9 displays the XRD analysis of the five BG compositions treated at T_{BS} for 3 hours. The analysis indicated the formation of combeite (Na4Ca4Si6O18, JCPSD no. 01-079-1086) in thermally treated S53P4, as reported elsewhere (Stiller et al., 2024). The impact of Mg-Sr doping and the concurrent reduction in the alkaline element content on crystallization is readily apparent, as the doped BGs exhibit minimal to no crystallization. Specifically, a lower tendency to crystallize is observed in Bio_MS and S53P4_MS. This tendency could be attributed to their lower sodium content, resulting in reduced diffusion coefficients and slower rates of crystal growth (C. Yang et al., 2023).

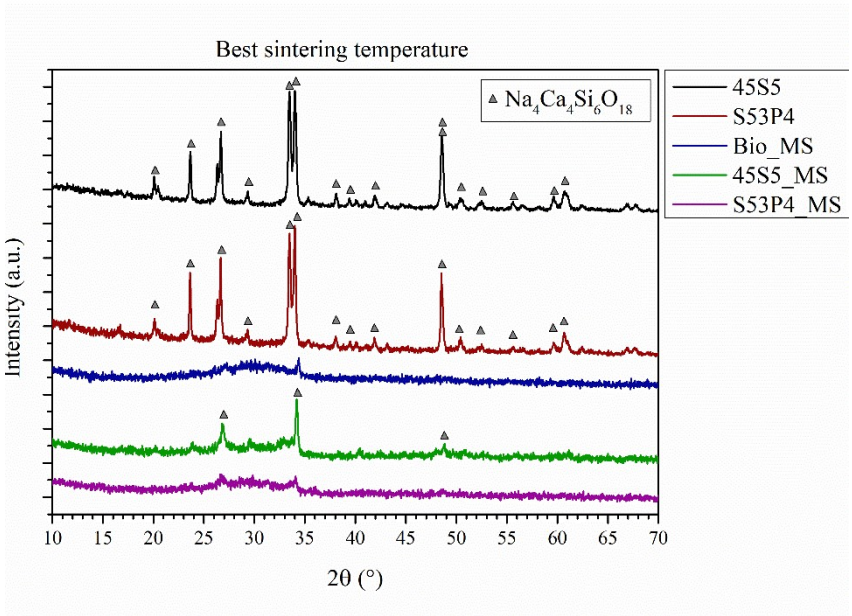

Figure 9. *XRD spectra of the five BGs after heat treatment at TBS for 3 hours.*

2.2.3.4. Physical and mechanical properties

Figure 10 presents the cross-section images of BG samples heat treated at their respective T_{BS}. The diagram in **Figure 11** illustrates the density obtained through image analysis. Notably, all examined BG compositions demonstrate exceptional density levels, surpassing 95%. While Bio_MS exhibits higher shrinkage compared to the commercial BGs, its density is slightly lower. This discrepancy in density may be attributed to larger pore dimensions observed in Bio_MS compared to those of other BG compositions. Regarding other MS-

doped BG compositions, the higher shrinkage aligns with the increased density found by image analysis, confirming the superior sinterability of these BG compositions.

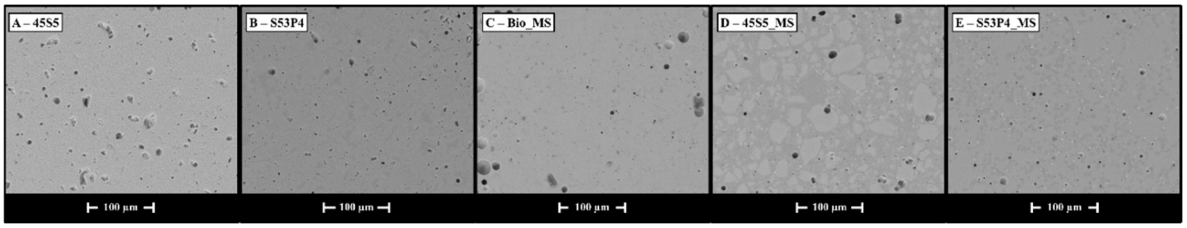

Figure 10. *SEM micrographs of the cross-sections of the five BGs disks samples heat treated at their respective TBS.*

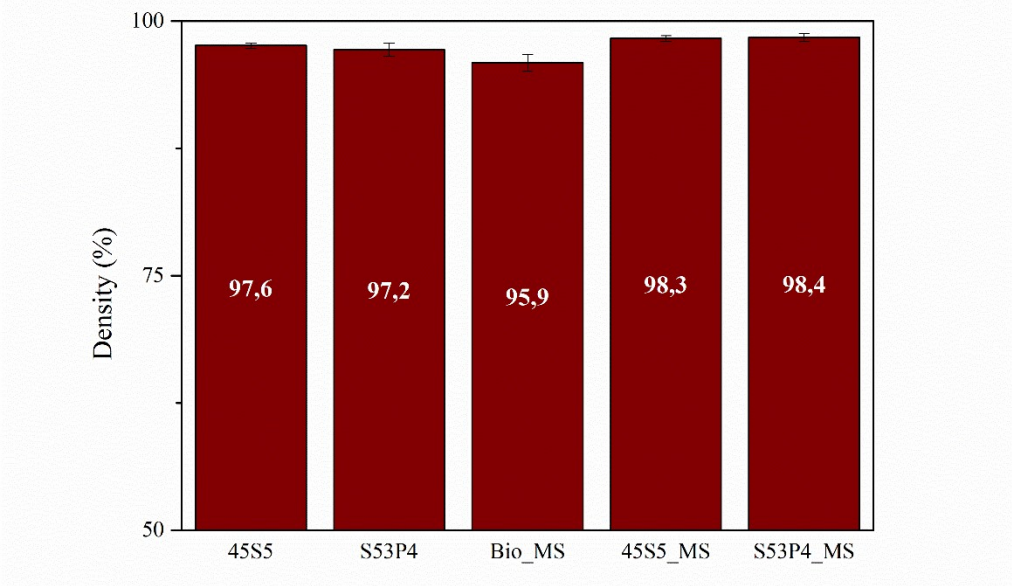

Figure 11. *Calculated density of the BG disks after sintering at TBS. Results were obtained analysing the cross-section images.*

The chart depicted in **Figure 12** provides the results of the mechanical properties of the BGs analysed in the present study. Consistently, the hardness values obtained for 45S5 and S53P4 align with established literature sources (El Damrawi et al., 2021; Hench, 1998). However, there is a noticeable scarcity of studies specifically investigating the hardness of Bio_MS or the MS-doped compositions, although the results presented here indicate higher values compared to other Mg or Sr doped BGs (Bellucci et al., 2017; Sharifianjazi et al., 2020b). The impact of Mg and Sr on the hardness of 45S5_MS is clearly discernible from the data, as it results higher than the reference commercial BG. In contrast, data suggest a marginal reduction in hardness within the S53P4_MS sample. This distinct behaviour might be linked to the different Mg-Sr/Si ratios. Notably, the effects of Mg are still debated, as it exhibits dual characteristics as both a network modifier and a network former (Cacciotti, 2017). The formation of Si–O–Mg linkages may locally increase network connectivity and

contribute to composition-dependent improvements in mechanical properties (Sharifianjazi et al., 2020). Nevertheless, because Mg–O bonds are weaker than Si–O bonds, the overall effect of Mg addition can still result in a mechanically weaker glass network, depending on composition and Mg content (Watts et al., 2010).

In the case of Sr-doped BGs, the potential weakening of the glass structure is attributed to the small but significant expansion of the glass network as a consequence of the substitution of Ca by Sr (Fredholm et al., 2010). This expansion occurs due to the larger size of the Sr^{2+} cation compared to Ca^{2+}. The impact of doping on the elastic modulus (E) appears to be minimal, aligning with findings similar to those reported by Sharifianjazi et al. (Sharifianjazi et al., 2020). Nonetheless, direct comparisons with existing literature present challenges due to the scarcity of studies specifically addressing the mechanical properties of bulk BG.

It's important to note that the presence of residual pores and variations in powder granulometry might significantly impact the mechanical properties of sintered BGs (Bellucci et al., 2017b; Cannillo et al., 2009). This aspect warrants further investigation and consideration in interpreting the presented results. Finally, it is important to note that BGs are intrinsically brittle materials and therefore, in load bearing applications, are used as coatings, e.g. on metallic prostheses. In this case, besides the fact that the BGs are thermally treated, it is important to pay attention to the mismatch of the coefficient of thermal expansion of the BG and the metallic substrate. In fact, due to such mismatch, thermal stresses may arise (Cannillo et al., 2006, 2002).

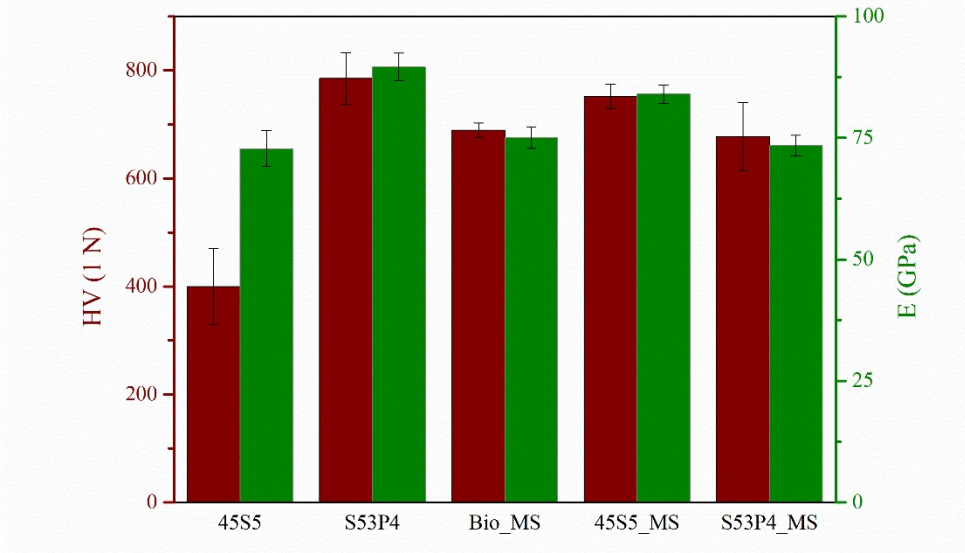

Figure 12. *Mechanical properties (specifically, microhardness and elastic modulus) of the sintered BG disks.*

2.2.3.5. SBF assesment

Figure 13 compares the effects of different composition on the pH of the SBF, to show the pH variation in the same heat treatment conditions. Results show that the heat treatment can influence the reactivity of BG compositions, as reported in other studies (Mecca et al., 2023). In the same figure, the optimal pH range for tissue regeneration has been added (Zarur et al., 2023). Indeed, it has been demonstrated that a weakly alkaline environment, up to pH 8, can enhance osteogenic activities and promote antibacterial effects without toxic effects on cells (Allan et al., 2001; El-Ghannam et al., 1997; Ramp et al., 1994a; Zhang et al., 2010a).

Taking this into account, a delayed and lower reactivity of BG can be seen positively, considering the need for a controlled, slower reaction while retaining bioactivity. This result was achieved with BGs doped with Mg and Sr and a lower alkali content. Although no direct ion-release or dissolution measurements were performed, the observed pH evolution suggests a moderated reaction kinetics consistently with literature, which reports that Mg and Sr influence the reactivity of BG *in vitro* (Diba et al., 2012; Rabiee et al., 2015). Therefore, the differences in reactivity discussed here should be interpreted as qualitative trends rather than as quantitative dissolution behaviour.

Notably, it can be seen how the doped samples heat treated at T_{BS} are able to maintain a lower pH than the samples heat treated at T_C. This finding is promising for glasses containing Mg and Sr, since it may point to a greater propensity of these compositions for the application as sintered BGs, allowing a simpler and more successful development of sintered parts.

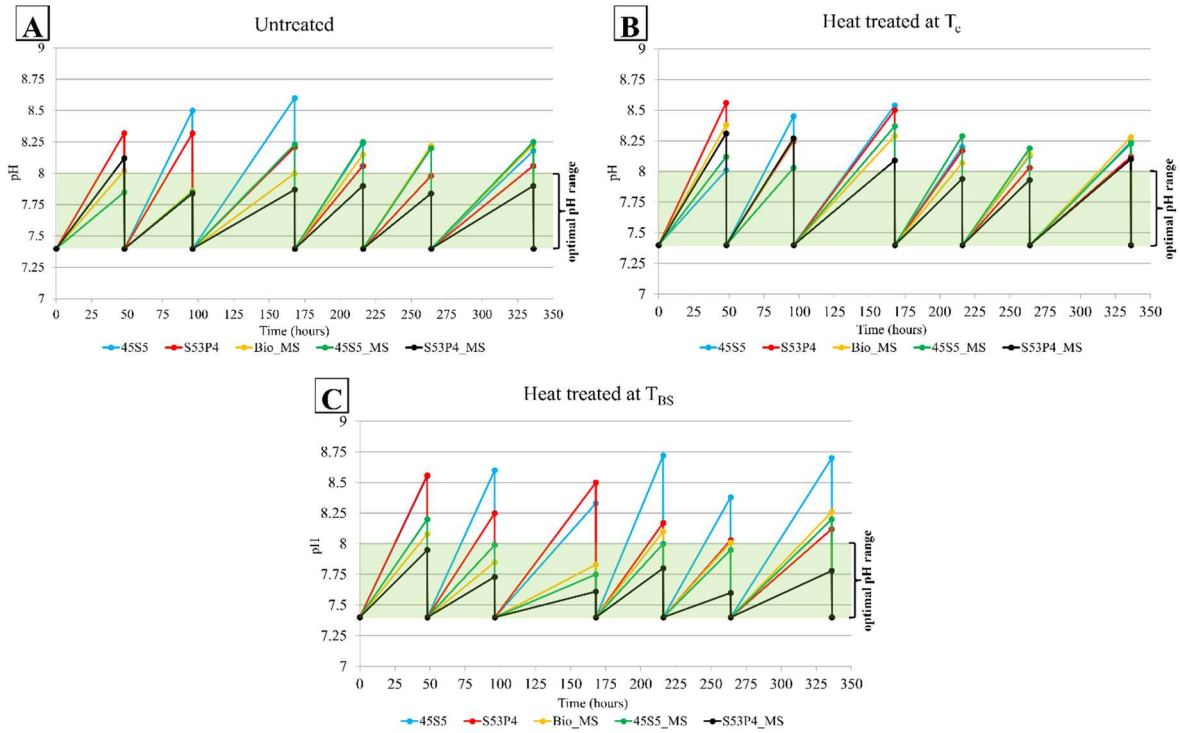

Figure 13. *pH variation induced by the untreated samples (A), and by the heat-treated samples at T_c (B), and T_{BS} (C). The green area represents the optimal pH for osteoblast activity (Brandao-Burch et al., 2005).*

The *in vitro* bioactivity of a BG, specifically its ability to induce an HA precipitation, can be assessed using Raman spectroscopy. The results of the analysis are depicted in **Figure 14**, illustrating the Raman spectra of untreated granules of 45S5, S53P4, Bio_MS, 45S5_MS and S53P4_MS after soaking in SBF for 7 days. Analogous results were obtained from the analyses of crystals grown on the surfaces of heat-treated BG granules. A representative Raman spectrum acquired on the precipitates on the surface of a heat treated sample in reported in the Supplementary Materials (**Supplementary 2**).

Examination of the spectra reveals the presence of typical peaks attributable to *in vitro* precipitated HA: one around 430 cm^{-1}, another at 590 cm^{-1}, and a prominent narrow peak at about 960 cm^{-1}. These peaks can be attributed to the bond stretching of the $(PO_4)^{3-}$ groups (Antonakos et al., 2007; Penel et al., 1998). Moreover, a peak at 1070 cm^{-1}, related to the stretching of the carbonate groups, confirms that the HA formed is carbonated, as reported in the literature (Awonusi et al., 2007). These observations apply to all untreated samples following a 7-day immersion in SBF, thus confirming their bioactivity. However, the kinetics of HA deposition on the surface of the granules varies among the samples due to their composition, which can modify glass solubility and reactivity.

The diminished reactivity of BGs containing Mg and Sr, which may ultimately lead to less HA precipitation, can be observed through the analysis of the Raman spectra. An

example of this behaviour is illustrated in **Figure 15**, which shows the Raman spectra of untreated S53P4 and S53P4_MS granules, both as-fritted and after soaking in SBF for 3 and 7 days. Examination of the spectra of both samples before immersion in SBF reveals a broad peak at 625 cm^{-1}, corresponding to the vibration of the Si-O-Si silicate groups (Ziemath and Aegerter, 1994). Additionally, a broad peak around 940 cm^{-1} is due to the vibration of the $(PO_4)^{3-}$ groups present in the BG structure (Bellucci et al., 2012). After 3 days S53P4_MS exhibits result similar to those at time 0 day (**Figure 15 B**), whereas the spectrum of S53P4 showed peaks at 430 cm^{-1}, 590 cm^{-1}, 960 cm^{-1} and at 1070 cm^{-1} (**Figure 15 A**). Similar results were obtained for untreated 45S5 and 45S5_MS granules soaked in SBF; the Raman spectra observed for Bio_MS granules closely resemble those seen in glasses that contain strontium and magnesium (data not shown).

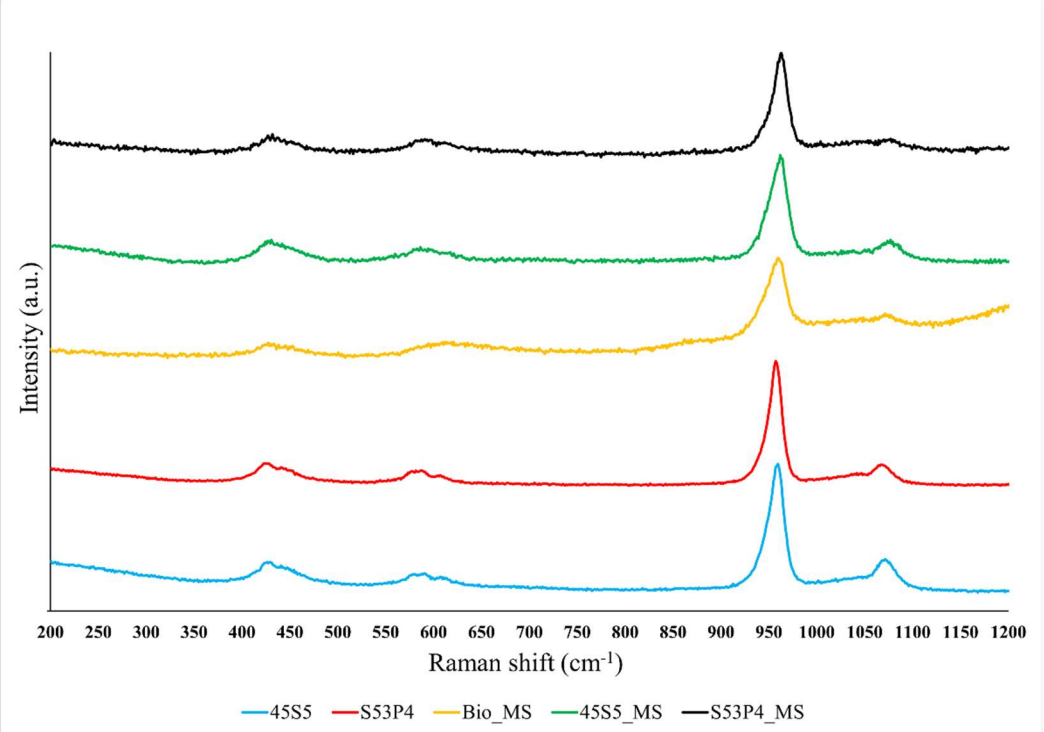

Figure 14. *Raman spectra acquired on untreated BG granules after immersion for 7 days in SBF.*

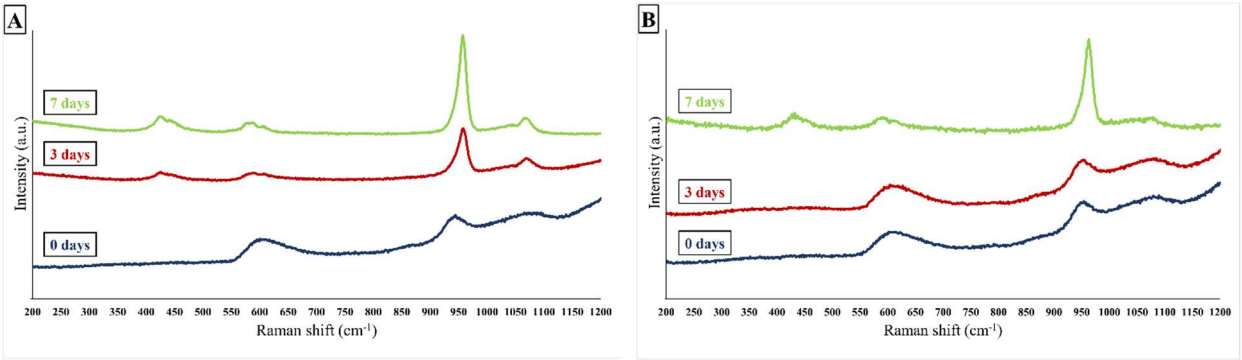

Figure 15. *Raman spectra acquired on S53P4 (A) and S53P4_MS (B) untreated granules after immersion for different times in Simulated Body Fluid.*

The surfaces of the samples after immersion in SBF were observed using SEM. A qualitative chemical analysis was conducted by means of EDS. **Figure 16** and **Figure 17** present the results of the SEM/EDS analysis of the surfaces of some representative BGs after soaking in SBF. Specifically, **Figure 16** shows the SEM/EDS of the S53P4 (A-B) and S53P4_MS (C-D) samples after 3 days of soaking in SBF solution, respectively. Results show that the surface of S53P4 is covered by spherical particles with a cauliflower-like structure, which is typical of the HA formed *in vitro*. However, these kinds of deposits cannot be detected on the surface of the S53P4_MS samples, apart from local formations, supporting the previous hypothesis of the slower reactivity of this composition compared to its counterpart that does not contain strontium and magnesium.

Additional considerations can be made based on the EDS analysis. In fact, in the EDS spectrum of S53P4_MS, a pronounced presence of silicon is observed, indicative of the formation of a superficial silica gel layer. The gel formation is an essential part of the reactions leading to the precipitation of HA and dehydrates after extraction from SBF, resulting in the typical cracked surface visible in in **Figure 16** (C) (Bellucci et al., 2012; Hench, 1991). Furthermore, the EDS analysis shows an increase in the phosphorus peak, attributable to the formation of localized precipitates rich in phosphorus and calcium, precursors of HA (H. Liu et al., 2008). It can therefore be concluded that the HA formation process on S53P4_MS is at a less advanced stage. The presence of small amounts of magnesium and chlorine on the S53P4 sample (**Figure 16** A) is likely due to the deposition of salts precipitating from the SBF, as reported by the literature (Padilla et al., 2006). Similar observations can be made for the 45S5 and 45S5_MS samples. Regarding Bio_MS, after 3 days, it tends to behave *in vitro* like the other glasses containing magnesium and strontium (data not shown).

Figure 17 shows the EDS analysis for the 45S5_MS (A-B) and S53P4_MS (C-D) samples after heat treatment at T_C and 7 days of immersion in SBF. This analysis aims to highlight the different effects of Mg and Sr, as well as a lower alkali content, on two different BG compositions. On the surface of the 45S5_MS (**Figure 17 A**) some globular precipitates are clearly visible. EDS analysis confirms that these precipitates have high concentrations of Ca and P, supporting the hypothesis of HA formation on the surface (further confirmed by Raman investigation – data not shown). **Figure 17** (C-D) shows the results of S53P4_MS after heat treatment at T_C. Some HA precipitates are visible, but the surface is less covered compared to the 45S5_MS samples, indicating lower bioactivity of the S53P4_MS sample, even after 7 days of exposure to SBF. Nevertheless, both experimental compositions are bioactive after heat treatment at T_C.

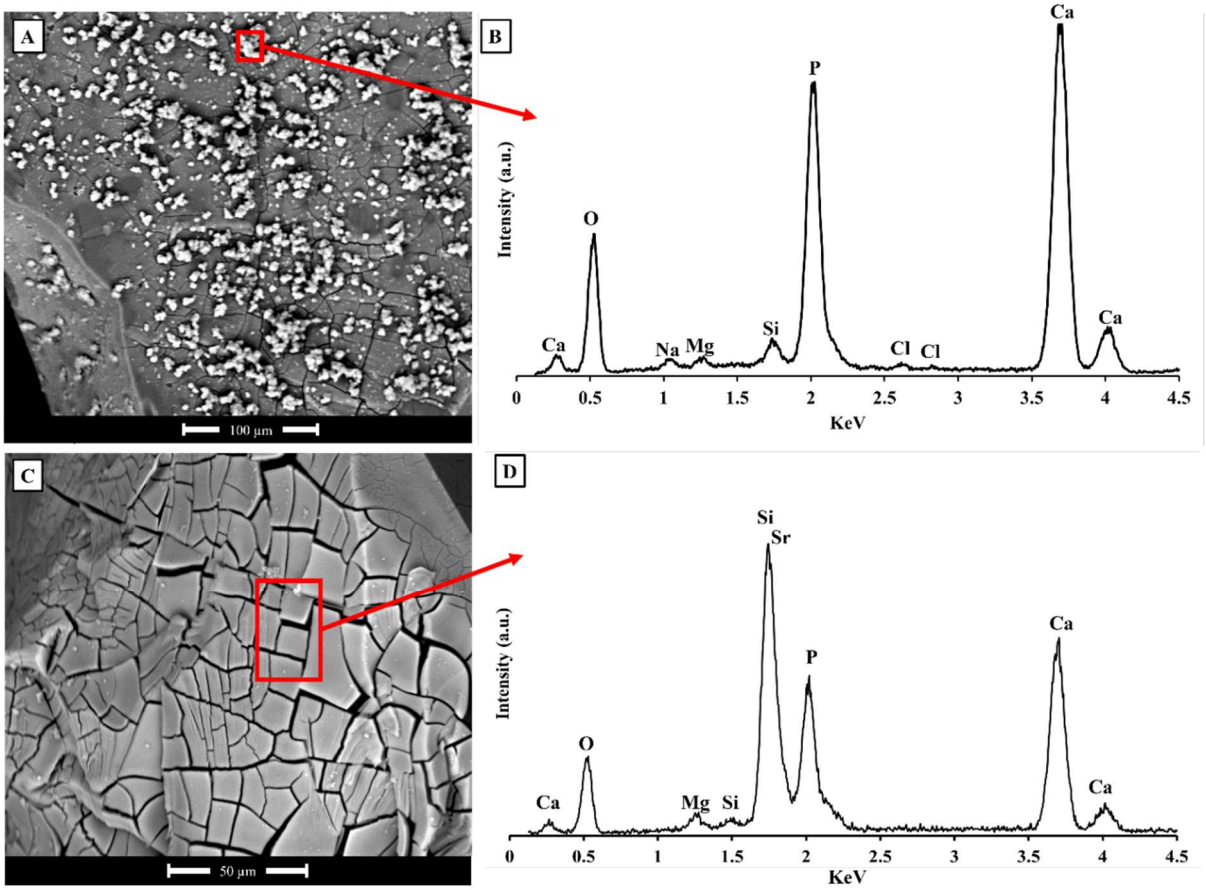

Figure 16. *(A) SEM micrograph of S53P4 sample after 3 days of soaking in SBF, and (B) EDS analysis of the highlighted (red) area in micrograph (A). (C) SEM micrograph of S53P4_MS sample after 3 days of soaking in SBF, and (D) EDS analysis of the highlighted (red) area in micrograph (C).*

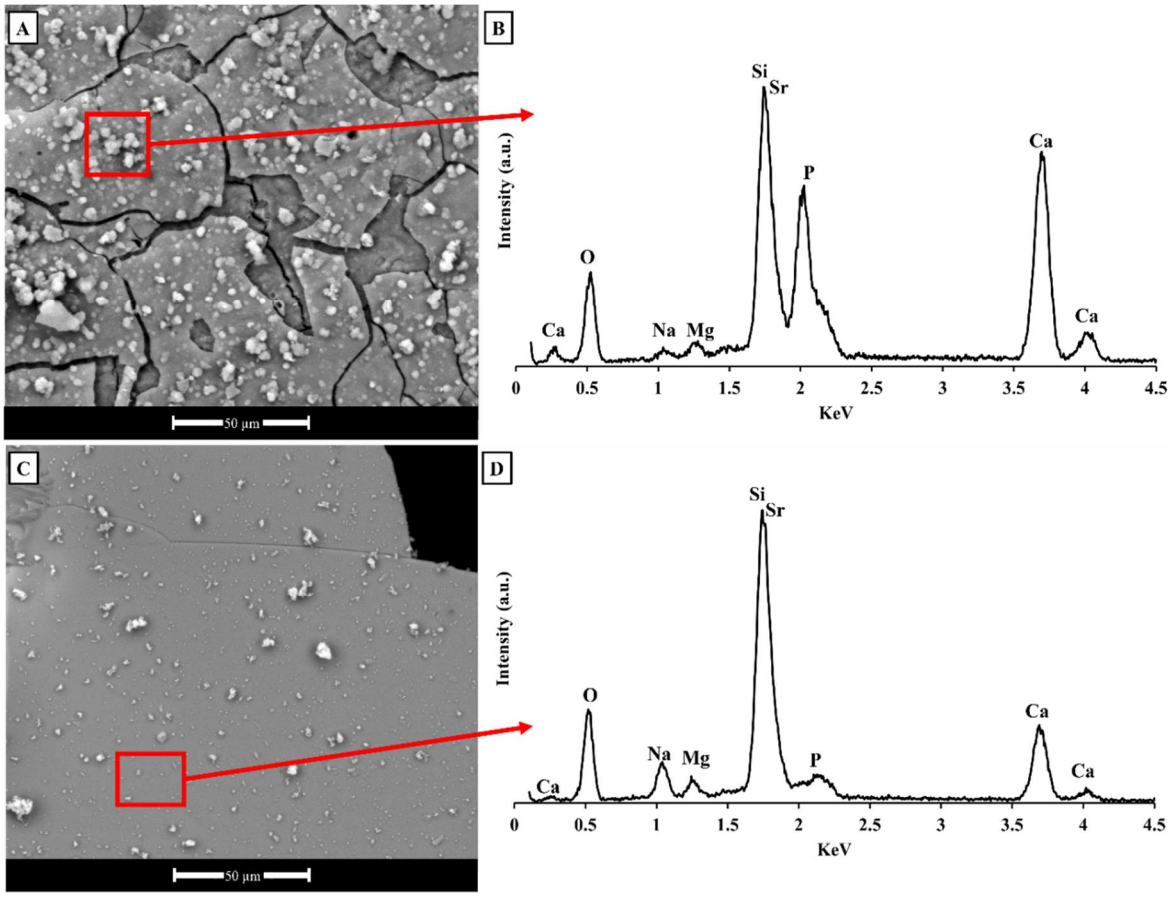

Figure 17. *(A) SEM micrograph of 45S5_MS sample, heat treated at TC after 7 days of soaking in SBF, and (B) EDS analysis of the highlighter (red) area in micrograph (A). (C) SEM micrograph of S53P4_MS sample, heat treated at TC after 7 days of soaking in SBF, and (D) EDS analysis of the highlighter (red) area in micrograph (C).*

These results are further supported by **Figure 18**, which illustrates SEM images comparing the temporal evolution of the surfaces of untreated BG samples containing Mg and Sr after 3, 7, and 14 days of soaking in SBF. It is evident that, after 3 days, the samples containing Mg and Sr present few to none deposits with the typical morphology of HA, thus confirming, as previously discussed, that the Mg/Sr doped compositions are less reactive than the undoped counterparts (Rabiee et al., 2015). In particular, the delayed HA formation has been attributed primarily to Sr, whereas Mg is reported to have beneficial effects on reaction kinetics (Bellucci et al., 2017b; Rabiee et al., 2015). However, after 14 days of immersion, all surfaces are covered with a layer of HA, confirming the bioactivity of all BGs and the abundant deposition of HA on their surfaces after 14 days of immersion.

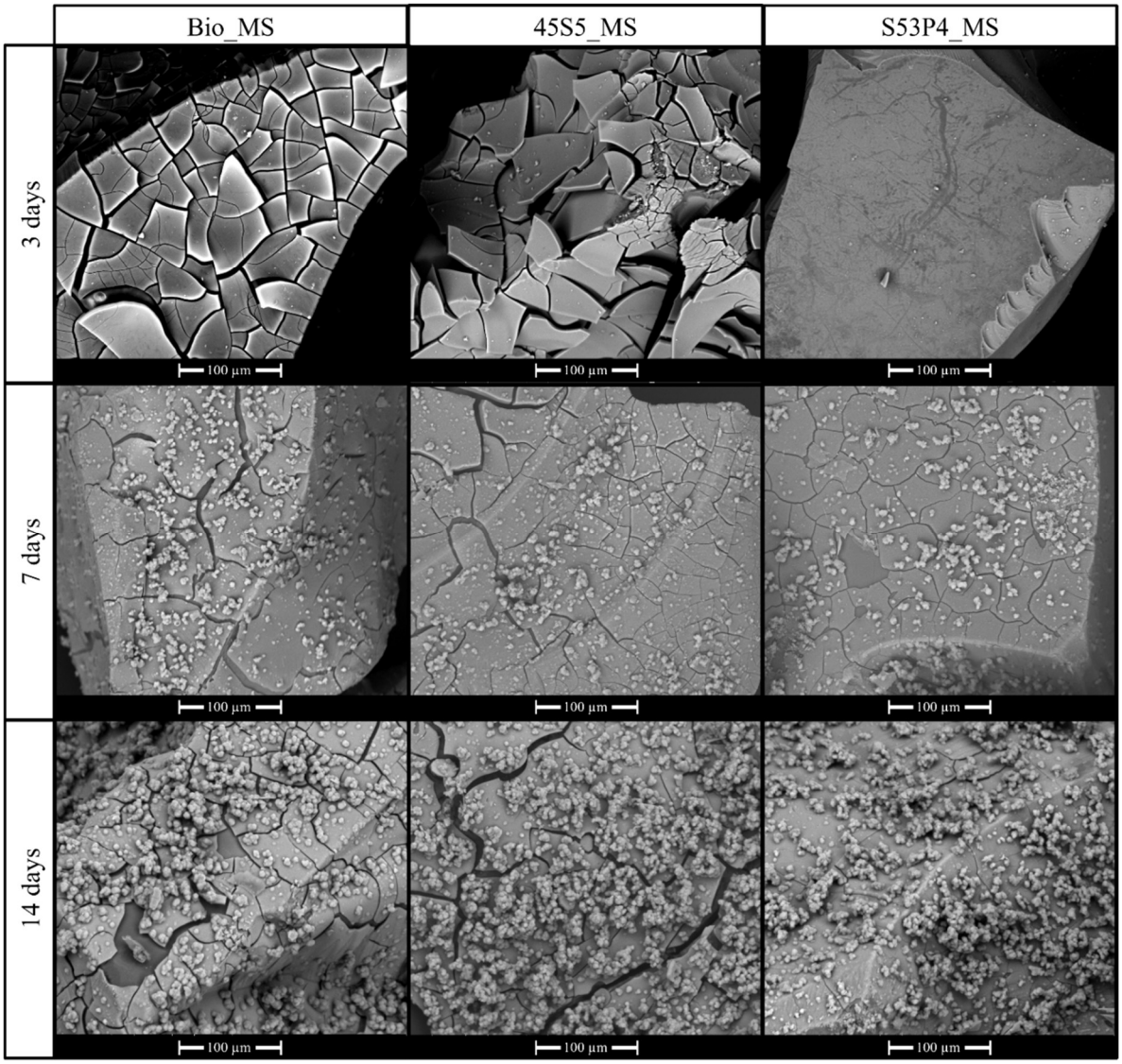

Figure 18. *Grid of SEM micrograph of Bio_MS, 45S5_MS and S53P4_MS untreated samples after 3, 7 and 14 days of soaking in SBF.*

Finally, **Figure 19** (A-J) presents SEM images of BGs, both non-heat-treated and heat-treated at T_C, after 14 days of soaking in SBF. These images demonstrate that all the samples are highly bioactive after 14 days in SBF, as they exhibit HA globular precipitates on their surfaces. This further supports the high reactivity of these BGs, even after thermal treatment.

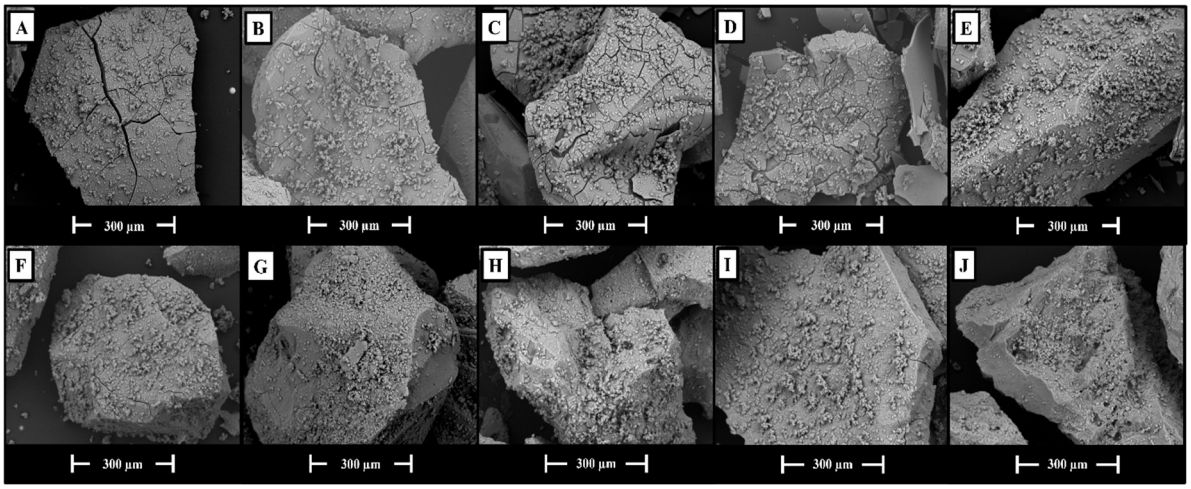

Figure 19. *SEM micrographs of: 45S5 (A), S53P4 (B), Bio_MS (C), 45S5_MS (D), and S53P4_MS (E) untreated granules after 14 days of soaking in SBF, and 45S5 (F), S53P4 (G), Bio_MS (H), 45S5_MS (I), and S53P4_MS (J) granules heat treated at Tc after 14 days of soaking in SBF.*

2.2.3.6. Biological assessment

Cytotoxicity test

MTT test is routinely used to evaluate the possible cytotoxicity of biomaterials and other medical devices, before conducting more detailed analyses on more complex experimental models (Liu et al., 2018). MTT is a yellow tetrazolium salt that is metabolized by mitochondrial dehydrogenases leading to the formation of purple formazan crystals (Ciapetti et al., 1993). The intensity of the purple colour is representative of the number of metabolically active cells capable of converting MTT, as an indicator of cell proliferation, viability and cytotoxicity. According to ISO 10993-5, samples are considered noncytotoxic when the cell viability is never below the threshold value of 70% compared to cells cultured in the absence of eluates (set at 100%) (**Figure 20**) Balb 3T3 fibroblasts were incubated with different concentrations (*i.e.,* 100%, 50%, 25% and 12.5%) of eluates from the different BGs untreated and treated at different temperatures (**Figure 20**). Only the positive control (*i.e.,* cells in DMEM+SDS) shows cytotoxicity, while all tested BGs, regardless of their different composition, heat treatment and eluates' concentration, do not exhibit any cytotoxic effect.

Notably, lower cell viability was observed for BGs thermally treated at Tc. This behaviour may be associated with surface modifications induced by thermal treatment, such as reduced surface roughness and changes in surface charge following partial crystallization. These surface alterations can negatively affect protein adsorption, thereby hindering initial cell adhesion and spreading, and ultimately impacting cell viability (El-Ghannam et al., 2001; Levy et al., 2007).

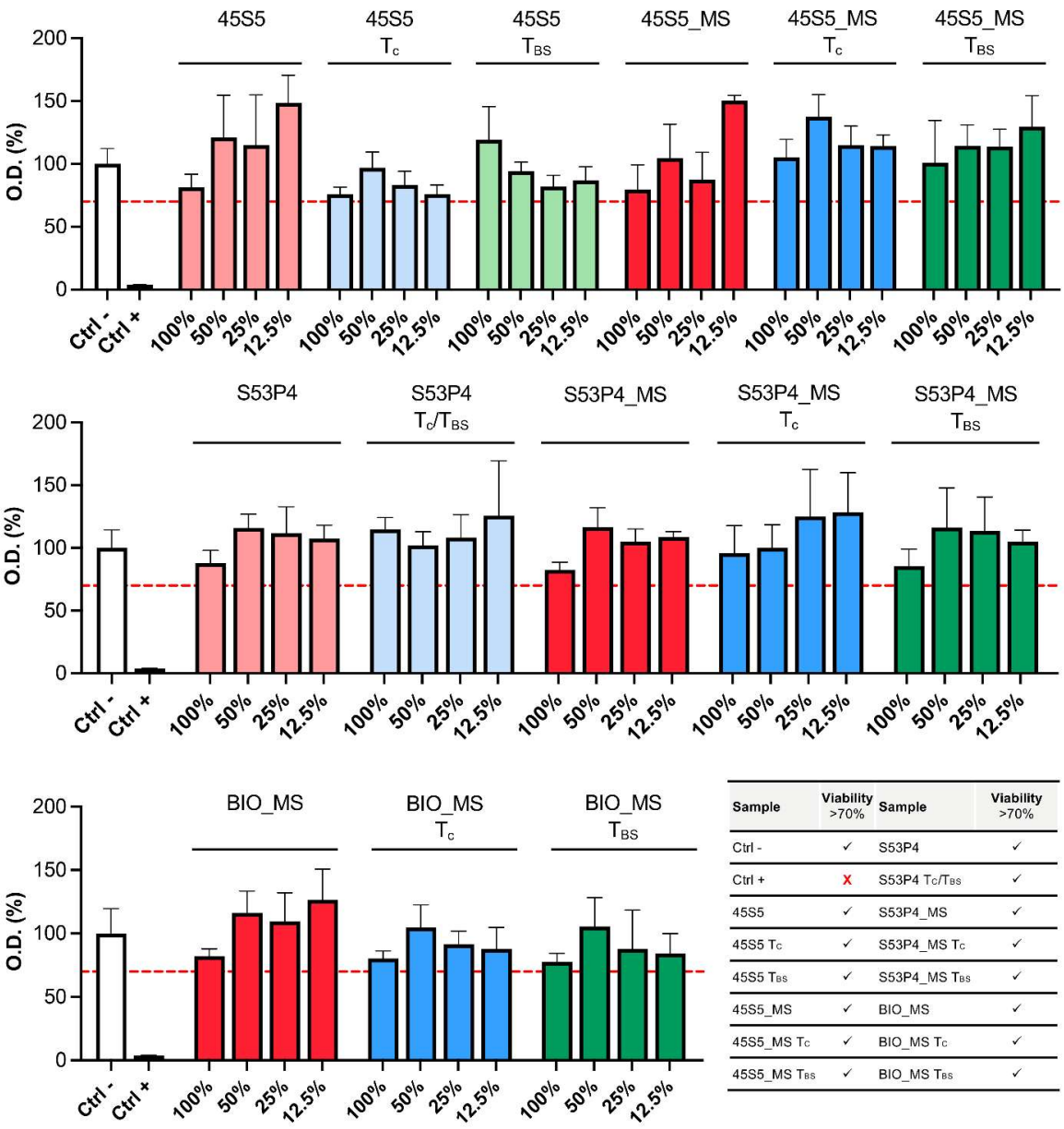

Sample	Viability >70%	Sample	Viability >70%
Ctrl -	✓	S53P4	✓
Ctrl +	X	S53P4 Tc/TBS	✓
45S5	✓	S53P4_MS	✓
45S5 Tc	✓	S53P4_MS Tc	✓
45S5 TBS	✓	S53P4_MS TBS	✓
45S5_MS	✓	BIO_MS	✓
45S5_MS Tc	✓	BIO_MS Tc	✓
45S5_MS TBS	✓	BIO_MS TBS	✓

Figure 20. *ISO 10993-5 cytotoxicity test. The viability of the Balb 3T3 cell line was evaluated by the MTT test after 24 hours in the absence (DMEM, Ctrl-) or in the presence of different concentrations (100%, 50%, 25% and 12.5%) of eluates from the BGs. The positive control was represented by cells treated for 24 hours with DMEM plus 0.1% SDS (Ctrl +). Optical density (O.D.) from cells cultured in DMEM was set at 100%. The dotted line represents the threshold value of 70%, compared to Ctrl-, that, according to the ISO 10993-5 guidelines, is required to demonstrate the absence of cytotoxicity. Values represent the mean ± SD of two independent experiments. (TC = crystallization temperature; TBS= best sintering temperature).*

Viability and adhesion of human dermal fibroblasts grown onto BGs

BGs have several well-known clinical applications in dental or orthopaedic areas as scaffolds promoting bone regeneration (Arcos Navarrete and Vallet-Regí, n.d.; Salinas et al., 2018). Data reported in previous sections have already highlighted the ability of BGs to favour the deposition of hydroxyapatite due to ion exchange on the BGs' surface, even in the absence of cells.

Therefore, we aimed at widening the spectrum of possible applications of BGs also in the field of soft connective tissue repair, given the clinical impact of defective wound healing (Liu et al., 2023). In this study we have evaluated cell viability and the interactions between BGs and human dermal fibroblasts (HDFs) in primary culture as a prototype of soft connective tissue mesenchymal cells producing the different components of the extracellular matrix (Boraldi et al., 2024; Viennet and Muret, 2015).

Since, we have previously demonstrated that a novel patented BG, Bio_MS (Anesi et al., 2023), due to the integration of Mg and Sr (MS) in its composition, has promising applicative perspectives and improved thermal properties, we included in our biological evaluations also two commercially available BGs (i.e., 45S5 and S53P4) modified with the addition of MS.

Furthermore, to better investigate the behaviour of cells directly interacting with BGs, HDFs were seeded on the surface of BGs and cell viability, adhesion properties and morphology of cells at different time points, up to 7 days, were evaluated.

Data reported in **Figure 21** for Bio_MS indicate that cell viability is affected by the treatment at $\mathbf{T_C}$ but not at $\mathbf{T_{BS}}$. To be noted, however, that reduction of cell viability at 4 and 7 days, compared to 1h, was always less than 20%.

Time	BIO_MS	BIO_MS T_C	BIO_MS T_{BS}
1 h	**100±5**	80±4	94±5
4 d	82±10§	69±11	83±13
7 d	85±7§	67±8	95±14

1 h	BIO_MS	BIO_MS T_C	BIO_MS T_{BS}
BIO_MS		**	
BIO_MS T_C			
BIO_MS T_{BS}			

4 d	BIO_MS	BIO_MS T_C	BIO_MS T_{BS}
BIO_MS			
BIO_MS T_C			
BIO_MS T_{BS}			

7 d	BIO_MS	BIO_MS T_C	BIO_MS T_{BS}
BIO_MS		*	
BIO_MS T_C			***
BIO_MS T_{BS}			

Figure 21. *Cell viability of human dermal fibroblasts grown for 1 hour (1h), 4 and 7 days (4d and 7d) on Bio_MS untreated or treated at different temperatures (TC = crystallization temperature; TBS= best sintering temperature). Data are expressed as mean values ± SD. Values obtained with Bio_MS at 1h without any treatment were set at 100%. § p value < 0.05 of 4 or 7 days vs 1h in the same experimental condition; * p value < 0.05, ** p value < 0.01, *** p value < 0.001 between BGs untreated or treated at different temperatures at the same time point.*

Morphological observations and morphometrical analyses performed on HDFs grown on Bio_MS at different temperatures of treatment demonstrated good adhesion properties (see

Figure 22). A consistent number of cells adhered to the surface of BGs independently of treatments. As expected, cells were round after 1 hour but appeared well spread and elongated after 4 and 7 days from seeding. At 7 days, fibroblasts on Bio_MS T_c appeared slightly, but significantly smaller compared to Bio_MS, suggesting that changes in the characteristics of the BG's surface, such as roughness and surface charge, may influence the way cells interact with the BG (El-Ghannam et al., 2001; Levy et al., 2007). In this case, the bioactivity of Bio_MS treated at T_{BS} is not influenced by the sintering temperature. Indeed, as demonstrated in previous studies, one of the advantages of the Bio_MS formulation is the wide processing window with regards to heat treatment. Developing formulations that can be sintered without forming crystals and that are able to maintain good cell viability is an essential requirement for biomedical perspectives (Bellucci et al., 2020). Since thermal treatments are necessary for the manufacturing of composite materials, porous scaffolds or coatings (Bellucci et al., 2020), Bio_MS treated at T_{BS} emerges as a possible candidate capable of maintaining high biocompatibility even after treatment at high temperatures.

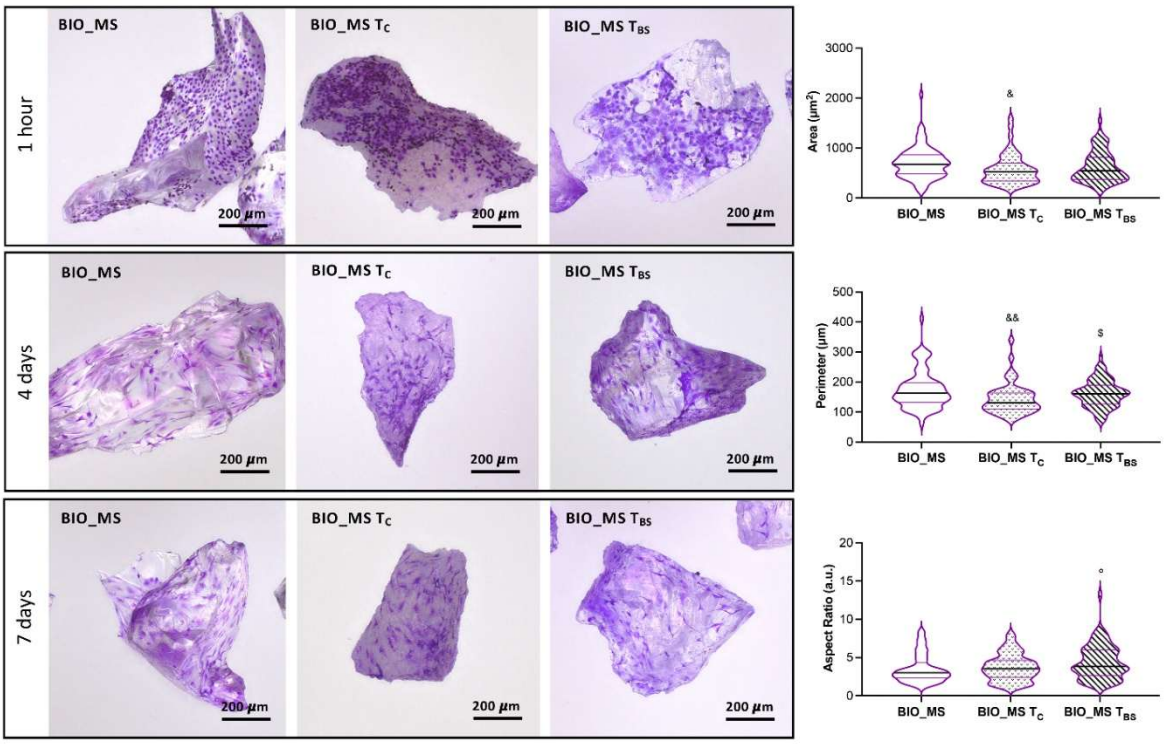

***Figure 22**. Representative images of HDFs seeded for 1 hour, 4 and 7 days on Bio_MS untreated and treated at different temperatures (TC = crystallization temperature; TBS= best sintering temperature). Violin plot representing area, perimeter and aspect ratio evaluated after 7 days of culture. & p<0.05, && p<0.01 MS TC vs MS; $ p<0.05 MS TBS vs MS TC; ° p<0.05 MS TBS vs MS.*

The same type of analyses described for Bio-MS, were performed on BGs used as reference standards and on the same commercial BGs also supplemented with MS.

Figure 23 indicates that cell viability is progressively reduced on 45S5 without addition of MS and that these effects are particularly evident after treatment at T_{BS}. Data seem in contrast with the well-known properties of this BG, that represents the gold standard for implants, for supporting structures to be used in bone tissue regeneration (Rodrigues et al., 2019) or for the re-mineralization of tooth enamel (Bakry et al., 2014, 2011). However, its applicability and usability in the regeneration of loose connective tissues or in wound repair have been poorly investigated (Handel et al., 2013; Naseri et al., 2017; Yu et al., 2016). Within this context, it is worth mentioning that most of the data in the literature concerns the use of bone-related cells. For instance, 45S5 does not interfere with osteoblast viability, since these cells are well adapted to the extra- and intracellular alkalinization exerted by the BG (Silver et al., 2001).

Interestingly, a previous study by Day and coworkers (Day et al., 2004), using a fibroblast cell line (208F) cultured on surfaces coated with 45S5, demonstrated a reduced cell proliferation depending on the time of culture (48 and 72 h) and/or on the concentration (0.01-0.2%wt/vol) of 45S5. In the light of these data we can suggest that HDFs in primary culture, compared to other cells, may have different interactions with the BG and that even local changes in the pH, without any pre-treatment of the BG (e.g., with serum components, simulated body fluid - SBF, or with adhesive glycoproteins) (Detsch et al., 2015), can influence cell adhesion (Cerruti et al., 2005) and cell proliferation, possibly mimicking *in vitro* what can happen *in vivo*, i.e. when the BGs are implanted.

Time	45S5	45S5 T_C	45S5 T_{BS}	45S5_MS	45S5_MS T_C	45S5_MS T_{BS}
1 h	**100±11**	93±1	91±2	112±14	114±8	98±8
4 d	56±10§§§§	93±20	9±1§§§§	83±15§§§	75±5§§§§	93±9
7 d	67±10§§§	69±13$^{§§\#}$	8±2§§§§	96±10§	104±20$^{\#\#}$	113±12$^{§\#\#}$

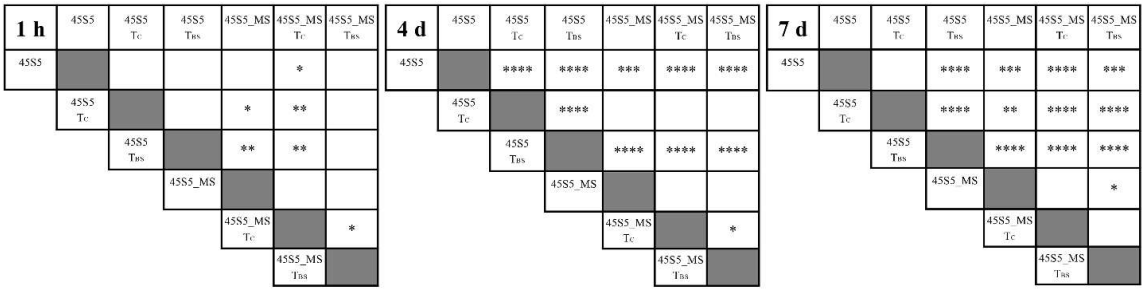

Figure 23. *Cell viability of human dermal fibroblasts grown for 1 hour (1h), 4 and 7 days (4d and 7d) on 45S5 and 45S5_MS untreated or treated at different temperatures (TC = crystallization temperature; TBS= best sintering temperature). Data are expressed as mean values ± SD. Values obtained with 45S5 without any treatment at 1 h were set at 100%. § p value < 0.05, §§ p value < 0.01, §§§ p value < 0.001, §§§§ p value < 0.0001 of 4 or 7 days vs 1h in the experimental condition; # p value < 0.05, ## p value < 0.01 of 7 vs 4 days; *p value < 0.05, ** p value < 0.01, *** p value < 0.001, ****p value < 0.0001 between BGs untreated or treated at different temperatures at the same time point.*

It is well known that the adsorption of proteins on the BG is influenced by numerous factors, both external (e.g., pH and temperature) and internal (e.g., surface charges and topography of the BG surface) (Rabe et al., 2011).

Interestingly, MS-doped BG showed significantly improved cell viability, and this effect appeared to be independent of the treatment temperature. At 7 days of culture, the viability of cells grown on doped BGs was greater than on BGs. Noteworthy data obtained with the 45S5_MS T_{BS} vs 45S5 T_{BS} since addition of MS completely abolished the cytotoxic effect of the thermal treatment. In doped-BGs cell viability showed a general decrease at day 4 and an increase at day 7. These data suggest that 45S5_MS, regardless of treatment, induces an initial selection within the cell population in favour of a subpopulation capable of better adapting to the microenvironment, as already observed in the literature (Xynos et al., 2000).

The better performance observed for the doped 45S5 is associated with the addition of MS. This result is not surprising, as it has been already demonstrated that the addition of Mg to BGs promotes the adhesion of bone-derived cells (de Araujo Bastos Santana et al., 2021). Indeed, previous studies demonstrated that Mg promotes cell adhesion favouring the synthesis of collagen type I, vitronectin, fibronectin and the activation of kinases associated with focal adhesions in osteoblasts (Schlaepfer et al., 1994; Zreiqat et al., 2002) as well as in human fibroblasts (Amberg et al., 2018). Furthermore, also Sr can act as an inducer of cell

adhesion and proliferation, as shown on BGs subjected to treatments at temperatures that can compromise the bioactivity of the biomaterial (Kargozar et al., 2019), and can promote both osteogenesis and angiogenesis when added to BG nanoparticles (Leite et al., 2018). Furthermore, Sr can maintain an optimal pH in the surrounding environment, thus ensuring good cell viability (Dash et al., 2023).

The interactions between cells and BGs were also assessed by evaluating the morphology of HDFs grown up to 7 days on 45S5 and 45S5_MS at different temperatures. Morphometric analyses were also performed at 7 days to quantitate differences in the spreading of the cells.

HDFs adhered well on all BGs at 1h, although, as expected, they are still round. Over time in culture, cells acquired a more elongated shape except for 45S5 T_{BS}. Due to the low number of cells on 45S5 T_{BS}, morphometric analyses on these samples were not performed.

MS-doped BG allowed to maintain the number of adhered cells that exhibited a more spread morphology compared to cells on 45S5 (**Figure 24**) confirming the beneficial role of MS addition.

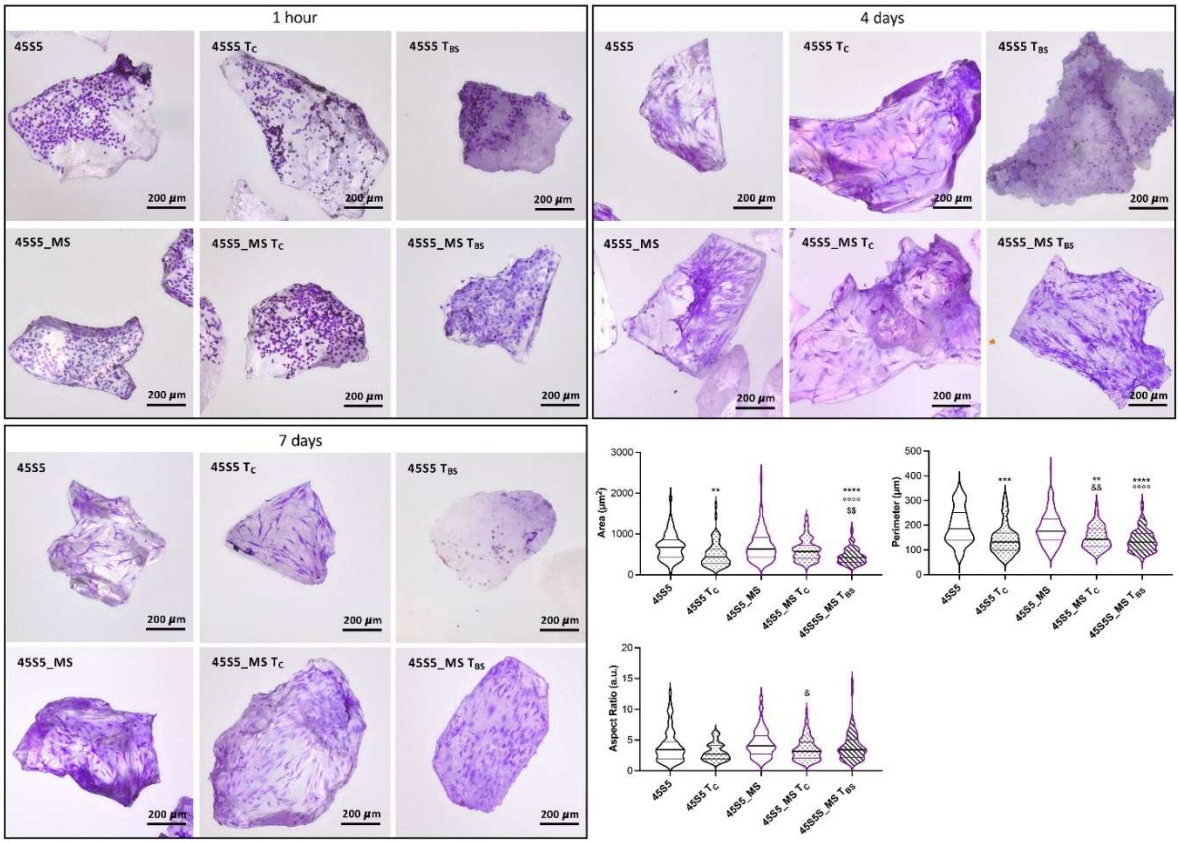

Figure 24. *Representative images of HDFs seeded for 1 hour, 4 and 7 days on 45S5 and 45S5_MS untreated and treated at different temperatures (TC = crystallization temperature; TBS= best sintering temperature). Violin plot representing area, perimeter and aspect ratio evaluated after 7 days of culture. **p<0.01, ***p<0.001, ****p<0.0001 all conditions vs 45S5; &p<0.05, &&p<0.01 MS TC vs MS; °°°°p<0.0001 MS TBS vs MS; $$p<0.01 MS TBS vs MS TC.*

Since cell viability and adhesion were severely affected on 45S5 T_{BS}, we wanted to test if the observed effects were due to the release of specific components affecting cell behaviour or if the cells negatively responded to changes of the surface of the BGs. Therefore, HDFs were cultured on standard multiwell plates in the presence of DMEM or of 100% eluates from 45S5T_{BS}. Fibroblasts, in the presence of 100% 45S5 T_{BS} eluates, exhibited good proliferation capabilities (see **Figure 25**).

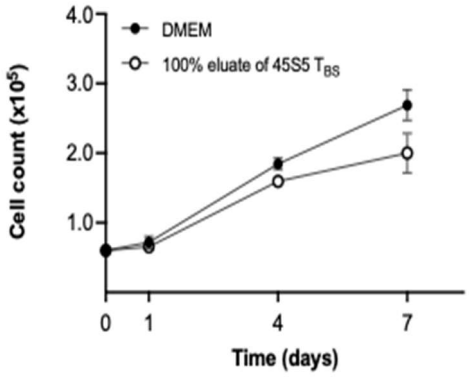

Figure 25. *Cell proliferation. HDF were grown in DMEM or in DMEM+ 100% eluate from 45S5 TBS (TBS= best sintering temperature) and cell number evaluated at different time points after seeding. There are no significant differences between the two experimental conditions. Data are expressed as mean values ± SD.*

Data demonstrate that the reduced cell viability observed with 45S5 T_{BS} is not due to cytotoxic components released by the BG but could be linked to modifications of the microstructure of the BG following heat treatment, as suggested by previous studies (Lefebvre et al., 2007). The operating conditions adopted during the sintering process for the consolidation of the powders, can modify the compositional and structural characteristics of the BG, which in turn influence mechanical and biological properties. Indeed, it has been observed that, as the temperature increases, the surface of 45S5 goes from smooth to wrinkled with consequences on the bioactivity of the BG (Lefebvre et al., 2007). Therefore, cell viability is not influenced by ions and/or toxic components released by the BG, but more likely by changes occurring on the surface of the BG after treatment at sintering temperature.

In **Figure 26** data show the viability of cells grown on the S53P4, that was developed and mainly used in clinical applications related to bone healing, vascularization, and cartilage repair (Lindfors, 2011; McAndrew et al., 2013). Although there are several data in the literature related to the effect of BG S53P4 on bone-derived cells (osteoblasts and osteoclasts) (Pérez-Tanoira et al., 2015; Todaro and Green, 1963; van Gestel et al., 2019), to our knowledge, there are no studies on the use of dermal fibroblasts.

Time	S53P4	S53P4 T_C/T_{BS}	S53P4_MS	S53P4_MS T_C	S53P4_MS T_{BS}
1 h	**100±11**	86±8	127±11	110±5	125±9
4 d	82±6§§	79±14	104±11§	82±10§§	107±11
7 d	67±14§§§§	55±5§§§##	79±10§§§§#	97±10	120±19

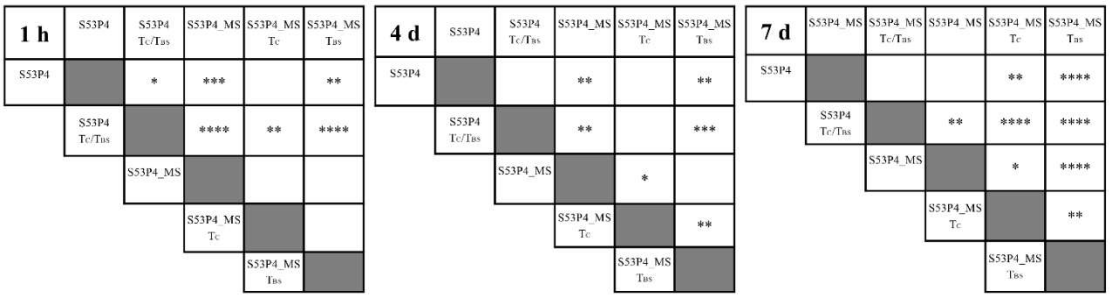

Figure 26. *Cell viability of human dermal fibroblasts grown for 1 hour (1h), 4 and 7 days (4d and 7d) on S53P4 and S53P4_MS untreated or treated at different temperatures (TC = crystallization temperature; TBS= best sintering temperature). Data are expressed as mean values ± SD. Values obtained with S53P4 were set at 100%. § p value < 0.05, §§ p value < 0.01, §§§ p value < 0.001, §§§§ p value < 0.0001 of 4 or 7 days vs 1h in the same experimental condition; # p value < 0.05, ## p value < 0.01 of 7 vs 4 days; * p value < 0.05, ** p value < 0.01, *** p value < 0.001, ****p value < 0.0001 between BGs untreated or treated at different temperatures at the same time point.*

In the present study, cell viability is progressively reduced on the BG both without any heat treatment or at temperatures T_C/T_{BS}. Similarly, to 45S5_MS, also S53P4_MS showed significantly improved cell viability, effects being independent on temperatures.

The interactions between cells and S53P4 BGs were assessed by evaluating the morphology of HDFs grown up to 7 days on the BGs. Morphometric analyses were also performed at 7 days to quantitate differences in the spreading of cells.

When HDFs were grown on S53P4, after 1h, cell behaviour was similar to that on 45S5. By contrast after 4 and 7 days, the number of adhered cells was reduced on BG treated at T_C/T_{BS}, thus underlining the effect of treatment on adhesion and cell viability of cells in contact with BGs. On the contrary, S53P4_MS exhibited nicely spread and typically elongated HDFs. Data, once more, clearly demonstrated the positive effect of the addition of Mg and Sr to the BG (**Figure 27**).

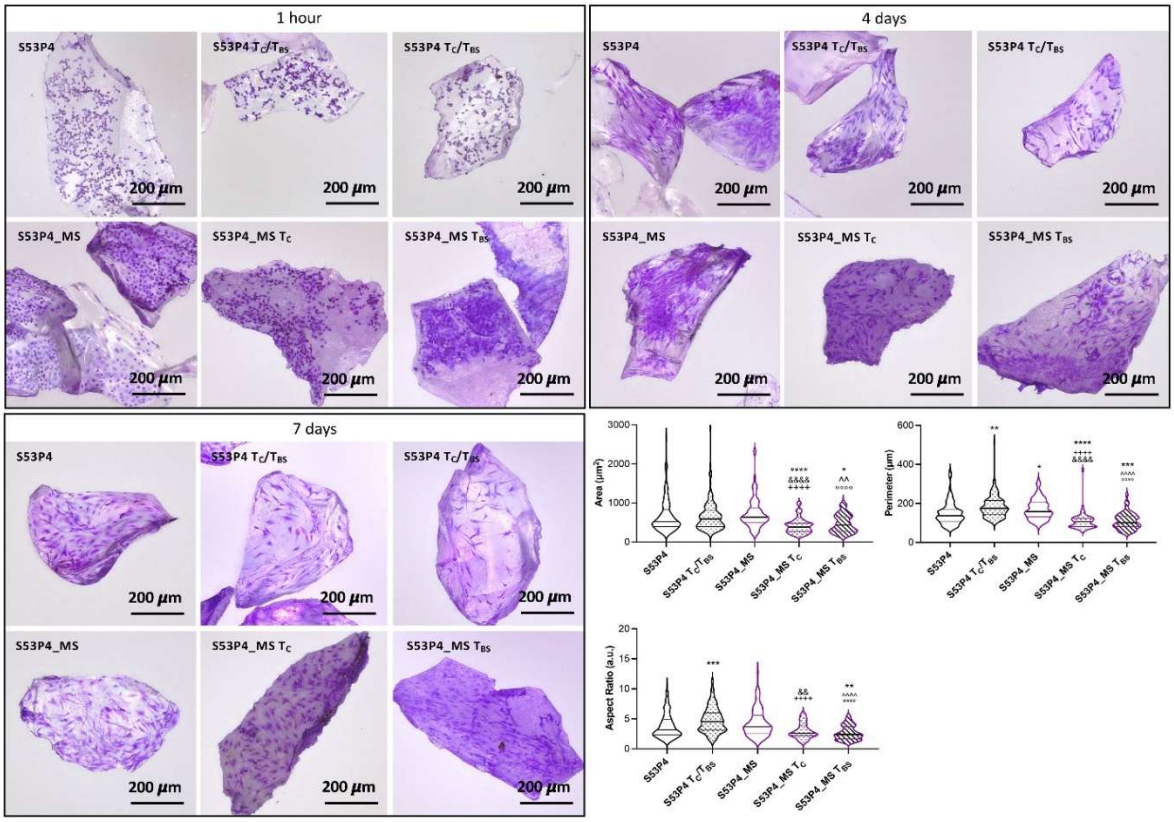

Figure 27*. Representative images of HDFs seeded for 1 hour, 4 and 7 days on S53P4 and S53P4_MS untreated and treated at different temperatures (TC = crystallization temperature; TBS= best sintering temperature). Violin plot representing area, perimeter and aspect ratio evaluated after 7 days of culture. * p< 0.05, ** p< 0.01, *** p< 0.001, **** p< 0.0001 all conditions vs S53P4; && p< 0.01, &&&& p< 0.0001 MS TC vs MS; °°°° p< 0.0001 MS TBS vs MS; ++++ p< 0.0001 TC/TBS vs MS TC; ^^ p< 0.01, ^^^^ p< 0.0001 TC/TBS vs MS TBS.*

Finally, to better evaluate cell viability of HDFs in the different experimental conditions, BGs were compared to each other based on their formulation, regardless of the heat treatment. In particular, cell viability was evaluated on BGs without heat treatment (NHT), on BGs treated at crystallization temperatures (Tc) and on BGs treated at best sintering temperatures (T_{BS}). The cell viability data were compared with results of the non-thermally treated 45S5, considered the gold standard of BGs currently on the market (Rodrigues et al., 2019).

In group NHT, cell viability on 45S5_MS and Bio_MS was higher than on standard BG (45S5) (**Figure 28**).

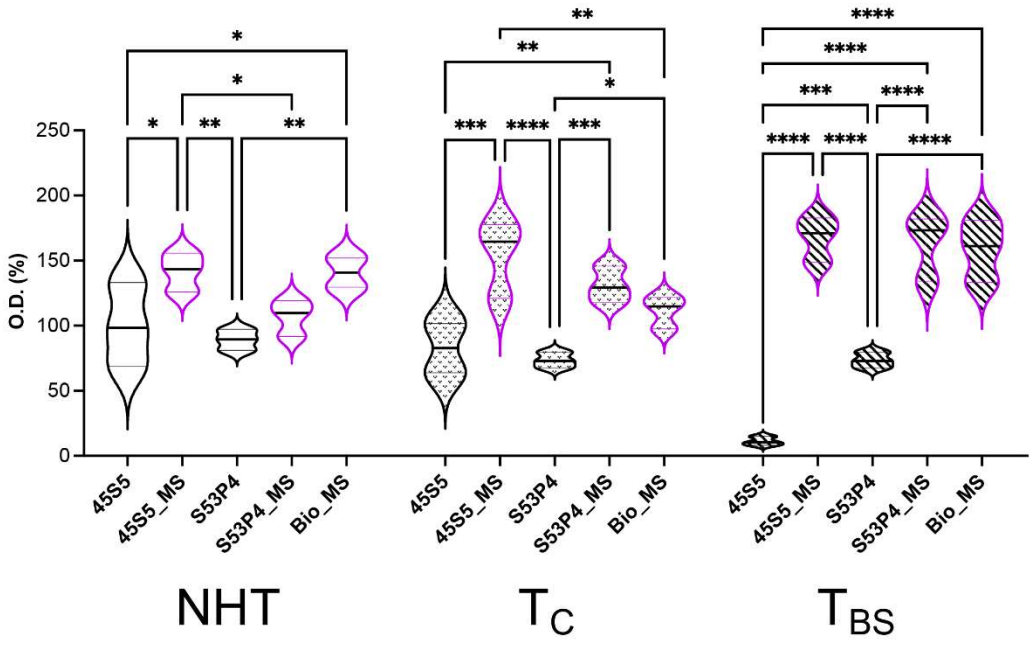

Figure 28. *Violin plot representation of the cell viability of HDFs grown on non-heat-treated (NHT) or heat-treated bioglasses (BGs) for 7 days. TC = crystallization temperature; TBS= best sintering temperature. Values of optical density (O.D.) obtained with 45S5 at 7 days were set to 100%. * p value < 0.05; ** p value < 0.01; *** p value < 0.001; **** p value < 0.0001*

In group Tc, cell viability was significantly higher for all BGs with MS compared to the same BGs without MS (**Figure 28**).

In group T_{BS} it clearly emerges that the addition of MS to the BGs significantly increased the cell viability of HDFs compared to formulations without MS. Furthermore, cell viability was similar among the three MS-containing BGs (**Figure 28**).

2.2.4. Conclusions

The results show several positive effects of the substitution of Mg^{2+} and Sr^{2+} ions in the "MS" BG compositions. Specifically:

- Both T_G and T_C show a significant increase in value in MS-doped BGs, while also showcasing a wider sintering window. This may allow for low temperature sintering of the BGs.
- Heat treating the MS-doped BGs resulted in quasi-amorphous or low-crystallites-containing structures. Lower temperatures were able to create sintered BG samples while retaining a mostly amorphous structure. Densification was also higher for the MS-doped BGs.

- 45S5_MS showed better mechanical properties after sintering heat treatment compared to sintered 45S5. Meanwhile S53P4_MS showed mechanical properties similar to other BGs in this study.
- The MS-doped BGs resulted bioactive after SBF testing. Although they presented a slower reaction kinetic. This can also prove beneficial, as the pH of the solution increased less compared to the undoped BGs.
- A good interaction between bioglasses and HDF suggesting their possible use in soft connective tissues, in addition to what has already been demonstrated for bone and cartilaginous tissues. Future studies will investigate the potential therapeutic effects, e.g. angiogenesis, of these novel compositions.
- Treatment at high temperatures can modify the surface of BGs with consequences on cellular adhesion as highlighted in the case of 45S5 T_{BS}.
- Bio_MS, a recently formulated BG, confirms its excellent biocompatibility also using HDF.
- The integration of MS in two BGs which, in the standard formulation, are already widely used for orthopaedic and dental applications, further improves the performance of BGs;
- The positive effect of MS is particularly evident when BGs are treated at T_C and T_{BS}.

2.1.5. Supplementary

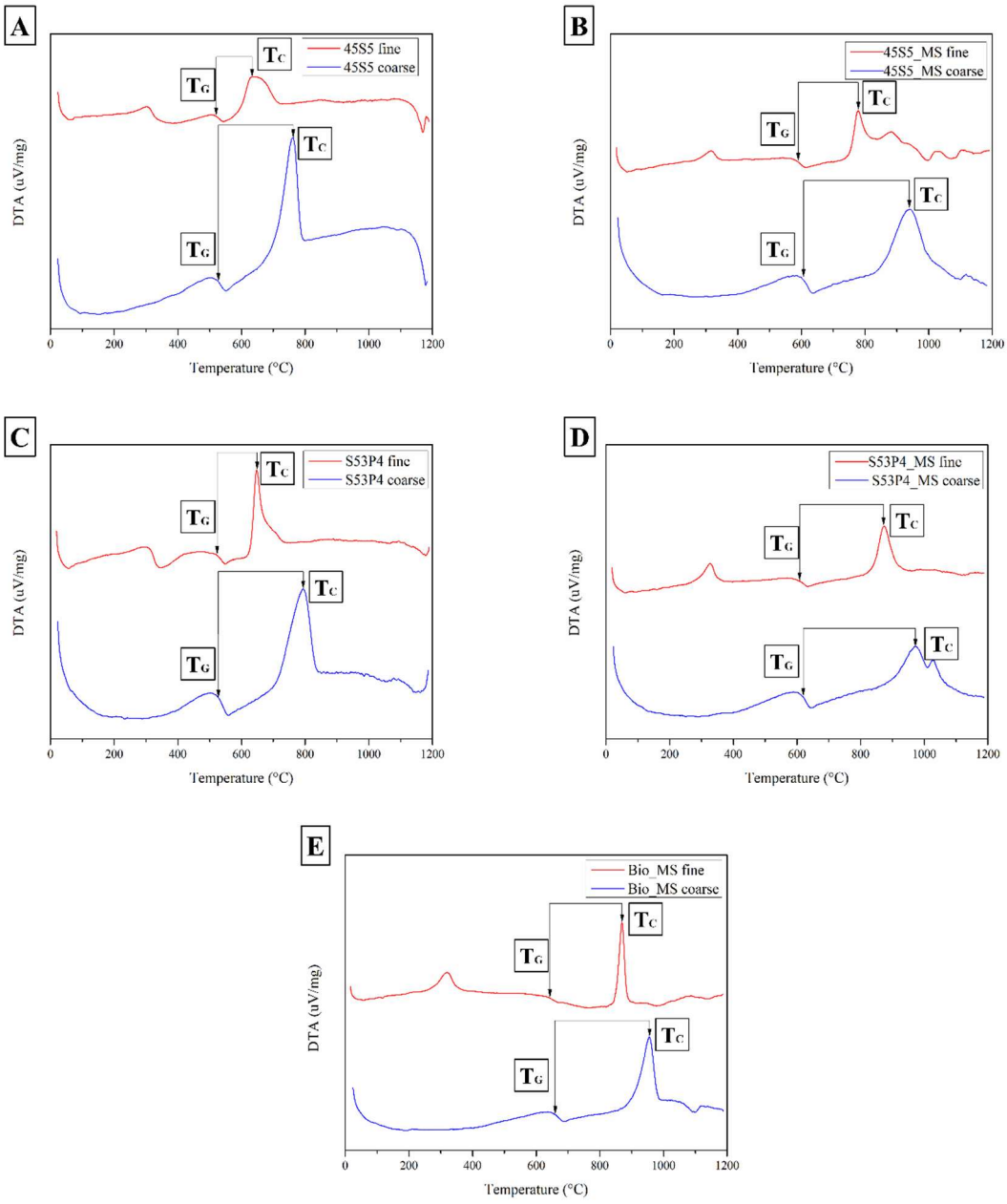

Supplementary 1. *Comparative DTA curves of (A) 45S5, (B) 45S5_MS, (C) S53P4, (D) S53P4_MS, (E) Bio_MS samples, each displaying two granulometries: fine (red) and coarse (blue).*

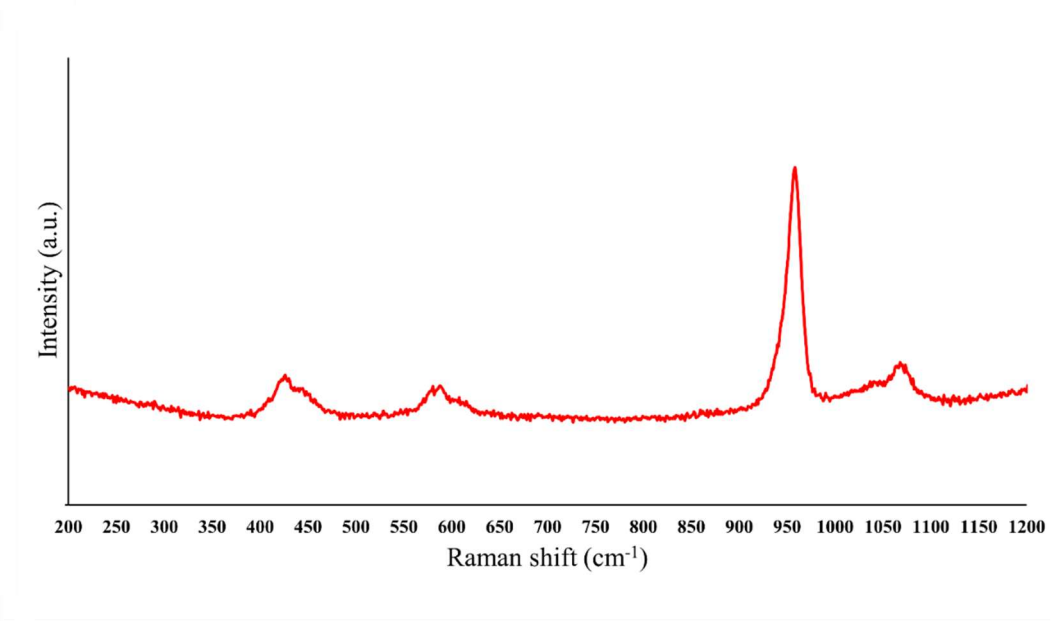

Supplementary 2. *Raman spectrum acquired on a precipitate on the surface of a heat-treated BG sample after immersion in SBF for 7 days.*

2.3. An enhanced bioactive glass composition with improved thermal stability and sinterability

(This section has been published in: Martelli, A.; Bellucci, D.; Cannillo, V. An Enhanced Bioactive Glass Composition with Improved Thermal Stability and Sinterability. Materials, 2024, 17, 6175. https://doi.org/10.3390/ma17246175. *Reproduced in accordance with the publisher's copyright policy.)*

2.3.2. Materials and Methods

The analyses described in the following paragraphs evaluate the physical and mechanical properties of S53P4_MSK, as well as its sintering and bioactivity behaviours. **Figure 29** presents a flowchart summarizing the experimental characterizations conducted.

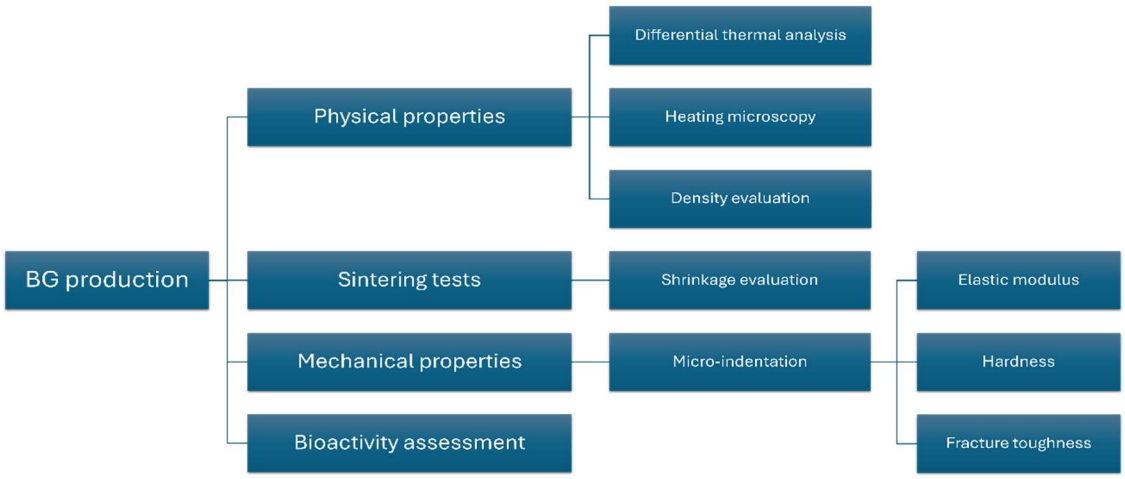

Figure 29. *Flow chart of the experimental characterizations.*

Bioactive glass production

S53P4_MSK (composition, in mol%: 5.4 Na_2O; 21.8 CaO; 2.3 K_2O; 10.0 MgO; 10.0 SrO; 1.7 P_2O_5; 48.8 SiO_2), was produced using a classical melt-quenching route as described elsewhere (Bellucci et al., 2020). High-quality raw materials in powder form (Carlo Erba Reagenti, Rodano-Milano, Italy) were carefully weighted and mixed for 2 hours using a laboratory rotary mixer. The resulting mixture was melted in a platinum crucible following this thermal process: heating from room temperature to 1100 °C at a rate of 10 °C/min, decarbonation at 1100 °C for 1.5 hours, further heating from 1100 °C to 1450 °C at 10 °C/min, and holding at 1450 °C for 1 hour to achieve a homogeneous melt. The molten glass was rapidly quenched in water to form a frit, which was subsequently dried at 110 °C for 12 hours. The obtained glass frit was grinded in a ceramic jar and sieved under 63 μm for subsequent thermal analysis and sintering evaluation.

Physical properties

Thermal properties were evaluated on BG powders using differential thermal analysis (DTA, Netzsch Differential Thermal Analyzer STA 429 CD, Netzsch-Gerätebau GmbH, Selb, Germany), heating the sample from room temperature to 1200 °C at a rate of 20°C/min. Additionally, heating microscopy (HM, Misura 3.32; Expert System Solutions, Modena, Italy) was conducted from room temperature to 1600 °C, with a heating rate of 10 °C/min. The processing window was calculated as the difference between the onset crystallization (T_{c_onset}) and the glass transition (T_g) (Jones, 2015; Tylkowski and Brauer, 2013), while the sintering behaviour of S53P4_MSK was estimated by the sinterability parameter (S_c) (Lara et al., 2004):

$$S_c = T_{c\_onset} - T_s \quad (1)$$

where T_s is the sintering temperature.

The density of the BG powder was measured using a gas pycnometer (AccuPyc II 1340, Micromeritics Instrument Corp., Norcross, USA). Helium with a total purity > 99.999% mol was used as the dispersion medium.

Sintering tests

Once the characteristic temperatures of S53P4_MSK were established, sintering evaluations were conducted on glass powder pressed in disk form. The green bodies were obtained by pressing the powder in a mould using a hydraulic press (Mignon S, Nannetti, Faenza, Italy). These green bodies were then thermally treated for three hours at 600 °C, 700 °C, 800 °C, and 900 °C in a muffle furnace (AWF 13/12, Lenton - Laboratory Scientific Equipment, Randburg, South Africa) with a heating rate of 10 °C/min. The sintering behaviour of S53P4_MSK was investigated through volume shrinkage ($\Delta_{\%}$) after thermal treatment. The following equation

$$\Delta_{\%} = \frac{d_0 - d_s}{d_0} \cdot 100 \quad (2)$$

was used to calculate $\Delta_{\%}$, where d_0 and d_s are the nominal diameter of the mould and the measured diameter of the glass disks after sintering, respectively. All diameters were measured using a digital calliper (LTF 327.09, LTF S.p.A., Antegnate, Italy). Additionally, image analysis using ImageJ software (NIH, Bethesda, MA, USA) was performed on the cross-sections of the disks to quantify residual porosity. The images were acquired using scanning electron microscopy (SEM) (Quanta 2000, FEI Co., Eindhoven, The Netherlands)

(micrographs are not presented for brevity). Furthermore, the disks were ground and subjected to X-Ray Diffraction (XRD) analysis (X'Pert Pro, Panalytical, Almelo, Netherlands) to detect any crystallization resulting from the thermal treatment. XRD scanning was conducted with Cu-Kα radiation over the range of 2θ = 10° - 70° with increments of 0.017°.

Mechanical properties

The elastic modulus and hardness (HV) of the sintered sample were assessed using the micro-indentation technique on the cross-section of glass disks sintered at 700 °C. This temperature was chosen because it represents the temperature at which full sintering occurs with no crystallization. The evaluations were conducted utilizing the Open Platform equipment (CSM Instruments, Peseux, Switzerland), employing a Vickers indenter tip. The indentation process applied a 0.5 N load with a loading/unloading rate of 1 N/min, and the maximum load was sustained for 15 s. 15 measurements were taken and an automatic recording of the load-penetration depth curve was made for each indentation. The elastic modulus was determined using the Oliver and Pharr method, which relies on the indentation load-unloading curves (Oliver and Pharr, 1992). Additionally, fracture toughness was evaluated using a load of 1 N in order to make cracks propagate from the indent tips. Fracture toughness (K_{Ic}) was then calculated based on the crack lengths according to widely used equations here reported (EC: Evans and Charles; LF: Lawn and Fuller; EW: Evans and Wilshaw; L: Lankford) (Ponton and Rawlings, 1989a, 1989b).

$$K_{Ic,EC} = 0.0824 \cdot \frac{P}{c^{3/2}} \quad (3)$$

$$K_{Ic,LF} = 0.0515 \cdot \frac{P}{c^{3/2}} \quad (4)$$

$$K_{Ic,EW} = 0.079 \cdot \frac{P}{a^{3/2}} \cdot log\left(\frac{4.5\,a}{c}\right) \quad (5)$$

$$K_{Ic,L} = 0.0363 \cdot \left(\frac{E}{HV}\right)^{2/5} \cdot \left(\frac{P}{a^{1.5}}\right) \cdot \left(\frac{a}{c}\right)^{1.56} \quad (6)$$

Where ***P*** is the applied load, ***c*** is the average crack length measured from the indentation centre (in μm), ***a*** is the average indentation half-diagonal (in μm), ***E*** is the elastic modulus (in GPa), ***HV*** is the Vickers hardness (in GPa).

Bioactivity assessment

In vitro bioactivity assessments were conducted following the Kokubo's protocol (Kokubo and Takadama, 2006) on untreated BG granules ranging in size from 250 to 500

μm in Simulated Body Fluid (SBF) at a concentration of 4 %w/v. This specific grain size was chosen to control both the dissolution rate and ion release, in order to optimize the potential *in vitro* biological response (Tainio et al., 2020). The bioactivity tests were conducted at 37°C, with time points set at 1, 3, 7, and 14 days. pH measurements of the SBF were taken every 48 hours, with fluid renewal occurring at the same interval. Once extracted, the granules were gently rinsed with distilled water to stop further reaction and dried at room temperature. Hydroxyapatite formation was evaluated by Raman spectroscopy (LabRAM Odissey, Horiba Jobin-Yyon, Villeneuve D'Aseq, France) equipped with a 632.8 nm-wavelength laser. The surface morphology of the granules before and after immersion in SBF was examined using SEM and field emission gun (FEG) – SEM (Nova NanoSEM 450, FEI Co., Eindhoven, The Netherlands). Further characterization of apatite precipitation was performed using X-ray energy dispersive spectroscopy (EDS) (Inca, Oxford Instruments, Abingdon, UK).

2.3.3. Results and Discussion

Physical properties

The data obtained from DTA and HM are shown in **Figure 30**. The HM output consists of a series of images acquired during the sample's heat treatment. Using geometric calculations, HM can determine temperatures critical for sintering, softening, and melting (Venturelli, 2011). These values, along with the results from the density analysis for S53P4_MSK, are summarized in **Table 4.** Characteristic temperatures and density of S53P4_MSK glass compared to those of S53P4 and 45S5.alongside those of commercially available 45S5 and S53P4 (Venturelli, 2011), provided for comparison.

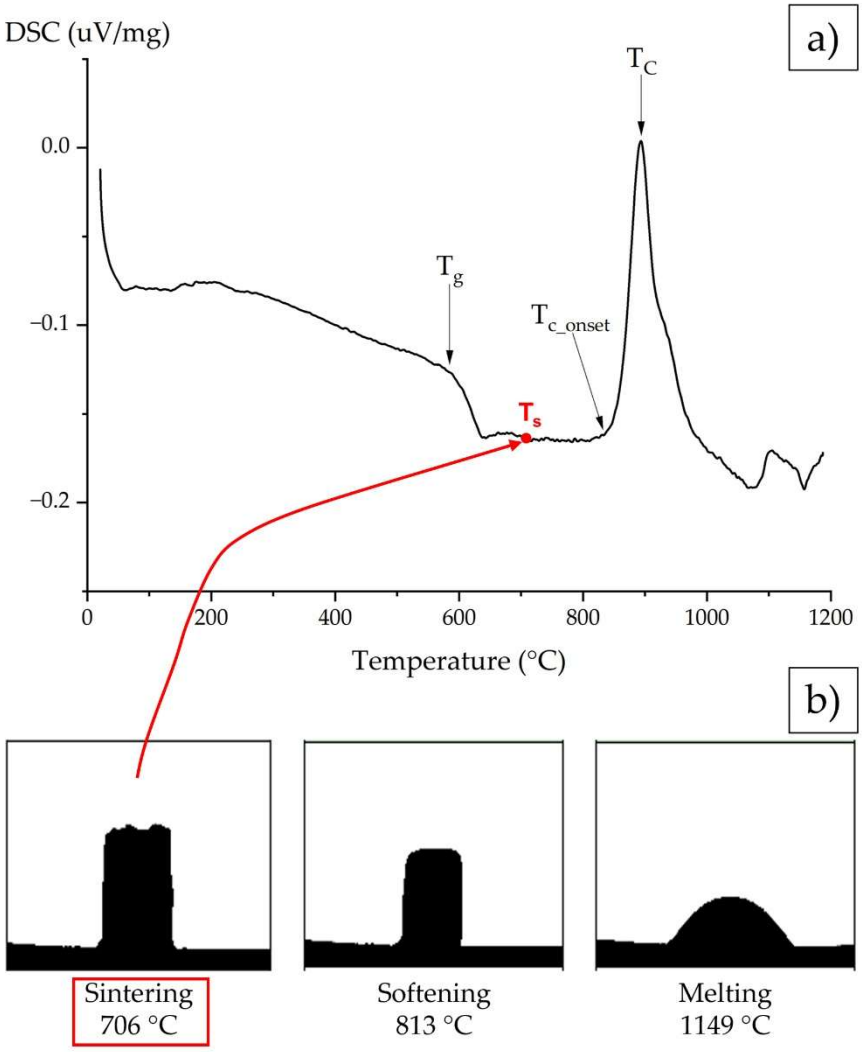

Figure 30. *a) DTA graph and b) HM of S53P4_MSK glass. The characteristic temperatures T_g, T_s, T_{c_onset} and T_c are shown on the DTA curves.*

Table 4. *Characteristic temperatures and density of S53P4_MSK glass compared to those of S53P4 and 45S5.*

	Tg (°C)	Ts (°C)	Tc_onset (°C)	Tc (°C)	Tm (°C)	Sc (°C)	Processing window (°C)	Density (g/cm3)
S53P4_MSK	600	706	835	894	1149	129	235	2.957 ± 0.001
S53P4 (Massera and Hupa, 2014; Strömberg et al., 2023)	520	700	650	730	1100	<0	130	2.66
45S5 (Boccaccini et al., 2007; Bretcanu et al., 2009; Chen et al., 2006)	549	1050	610	676	1165	<0	61	2.70

S53P4_MSK begins crystallization above 835 °C, reaching its peak at 894 °C. This high crystallization temperature shows promise for tissue engineering applications that require thermal treatments like scaffolds or coatings, due to the wider processing window it offers. In contrast, the two most commonly used BGs for comparison exhibit lower crystallization temperatures and narrower processing windows. Specifically, 45S5 has a crystallization temperature (T_c) of 676 °C (Bretcanu et al., 2009), and S53P4 has a T_c of 730 °C (Strömberg et al., 2023). Furthermore, as indicated in Table 1, both the commercial BGs exhibit negative S_c values, highlighting their tendency to crystallize during the sintering process. The enhanced thermal stability of S53P4_MSK could be attributed to i) the lower content of Na_2O, which is known to induce crystallization (H. Arstila et al., 2008); ii) the potential inhibitory effect of MgO on devitrification (Ma et al., 2010); and iii) the increased entropy of the system favouring the amorphous condition (Lotfibakhshaiesh et al., 2010).

Sintering tests

To further evaluate the sintering behaviour of S53P4_MSK, both volumetric shrinkage and the density of disk cross-sections treated at different temperatures were analyzed. The results are summarized in **Table 5**. The sintering process identified from the data reveals that densification begins between 600 °C and 700 °C, reaching its maximum at this point, and continues up to 800 °C. Afterward, densification decreases in terms of both shrinkage and density, possibly due to crystal nucleation and growth.

***Table 5**. Sintering behaviours of S53P4_MSK at different temperatures.*

Temperature (°C)	600	700	800	900
Shrinkage (%)	0.10 ± 0.06	14.78 ± 0.12	14.55 ± 0.12	6.66 ± 0.09
Density (%)	NA	99.68 ± 0.05	99.48 ± 0.08	95.58 ± 0.17

XRD diffractograms (**Figure 31**) acquired from samples treated at different temperatures confirmed the crystallization of S53P4_MSK at temperature about 800 °C, while showing the typical pattern of an amorphous glass at temperature below 700 °C. The impact of ion doping with Mg, Sr, and K, coupled with the concurrent reduction in Na content, is readily apparent, as no signs of crystallization are detectable at sintering temperature. This outcome can be attributed to the previously reported effects of composition on thermal stability (H. Arstila et al., 2008; Lotfibakhshaiesh et al., 2010; Ma et al., 2010). Typically, heat treatment of S53P4 leads to the formation of sodium-calcium silicate, although the stoichiometry of the formed crystalline phase remains a subject of debate (Aalto-Setälä et al., 2021; Massera et al., 2012). Despite the reduced sodium content, the analogous formation of sodium-

calcium silicate (Na_2CaSiO_4) was detectable in S53P4_MSK at 800 °C. Moreover, the crystallization of the novel S53P4_MSK composition resulted in the formation of other phases at T_c, whose identification was challenging due to peak overlap. Among these, diopside ($CaMgSi_2O_6$, JCPDS no. 01-078-1390) could be identified, as reported elsewhere for crystallization of Mg-doped BGs (Elsayed et al., 2017).

It is important to note that DTA and XRD results may appear contradictory. While DTA indicated a T_{c_onset} of 835 °C, XRD detected crystallization at 800 °C. This apparent discrepancy can be explained by the different holding times used during thermal treatments. In fact, prolonged exposure to temperatures slightly below T_{c_onset} can trigger crystallization like treatments performed above T_{c_onset}. In DTA analyses, the sample was subjected to a constant heating rate until melting occurred, while the samples analysed by XRD were held at a temperature slightly below T_{c_onset} for a long period.

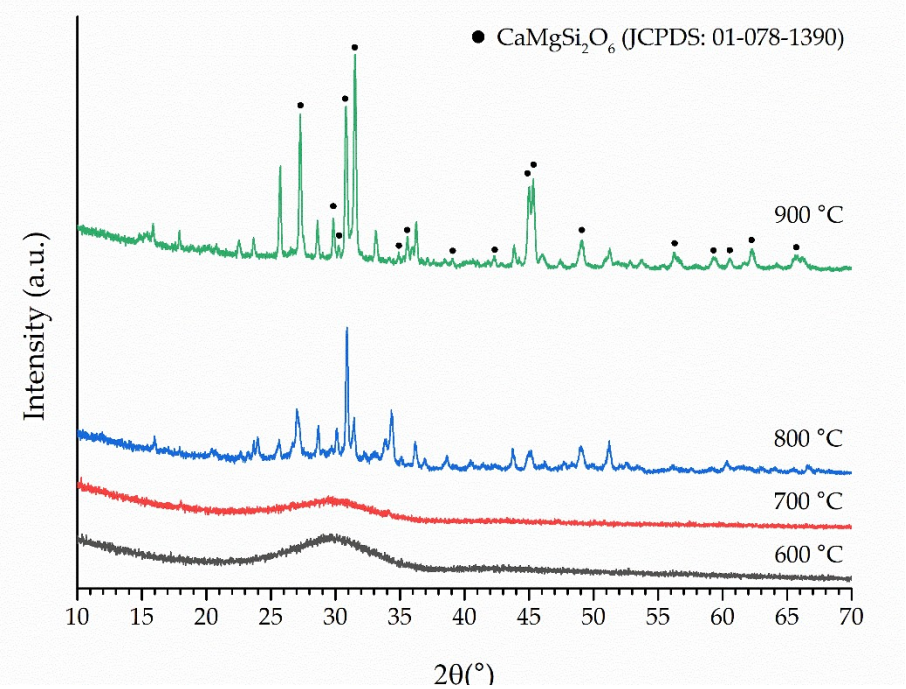

Figure 31. *XRD diffractograms of S53P4_MSK after thermal treatment for 3 h at different temperature ranging from 600 °C to 900 °C. The primary crystalline phase identified is diopside (CaMgSi2O6, JCPDS no. 01-078-1390).*

Mechanical properties

The mechanical properties of S53P4_MSK were evaluated on samples thermally treated at 700 °C, the temperature at which full sintering with no crystallization occurs. The results derived from the indentation are reported in **Table 6**. The findings revealed that the elastic modulus and hardness of the S53P4_MSK are slightly higher than those reported in analogous studies (Jones, 2015; Loh et al., 2023; Sharifianjazi et al., 2020). This can be

attributed to the addition of Mg, Sr and K ions and the lower content of Na ions. In fact, these ions can occupy the interstitial sites within the ceramic-glass networks, improving the mechanical properties of the BGs (Sharifianjazi et al., 2020). Moreover, the fracture toughness results are consistent with the range reported for BGs in literature (Fu et al., 2011). However, despite the large number of measurements (n = 56), a significant scatter is observed, with standard deviations on the order of 15–20% depending on the adopted model. This highlights the intrinsic limitations of indentation-based methods, which are highly sensitive to crack length measurement and model assumptions. Therefore, the fracture toughness values obtained in this study should be interpreted cautiously and considered as comparative indicators rather than absolute material properties.

Table 6. *Mechanical properties of S53P4_MSK. EC: Evans and Charles; LF: Lawn and Fuller; EW: Evans and Wilshaw; L: Lankford.*

Elastic modulus (GPa)	HV (GPa)	K_{IC} (MPa $m^{1/2}$)			
		EC	LF	EW	L
91.38 ± 2.81	6.91 ± 0.35	0.70 ± 0.11	0.44 ± 0.07	0.65 ± 0.13	0.79 ± 0.13

Bioactivity assessment

The bioactivity of S53P4_MSK was assessed *in vitro* using simulated body fluid solution (SBF) over a period of up to 14 days. SEM analysis shown that the surface of S53P4_MSK granules begins to convert into HA within one day (**Figure 32** a), marked by the formation of a silica gel (Kaur et al., 2014). The silica gel appears cracked due to the drying of the samples (D. Bellucci et al., 2011). Globular precipitates were observed after three days (**Figure 32** b). This morphology is characteristic of in vitro-formed apatite (Ebrahimi et al., 2023; Murimadugula et al., 2024). High-magnification acquisition shows the typical cauliflower-like structure of apatite formation after 14 days of soaking in SBF (**Figure 33**). The high concentration of calcium and phosphorus found in the EDS analysis of these structures support the hypothesis that apatite formation is occurring on the surface of the granules (H. Liu et al., 2008).

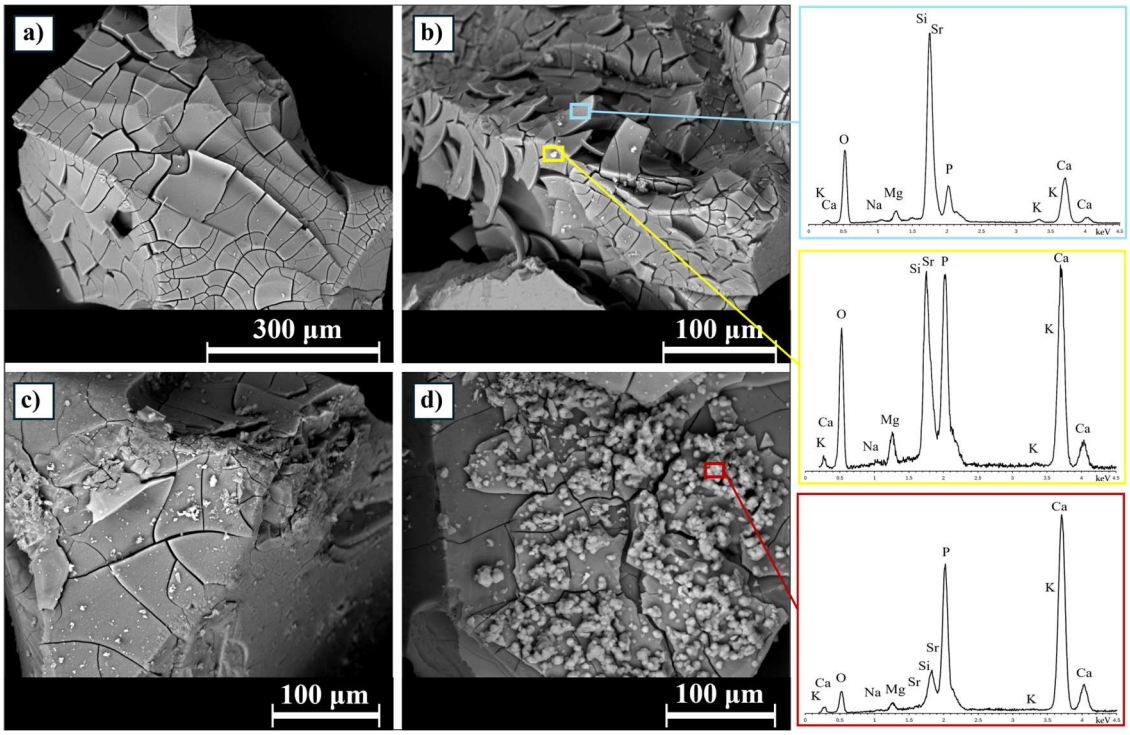

Figure 32. *SEM micrographs of S53P4_MSK granules after a) 1, b) 3, c) 7, and d) 14 days of soaking in SBF. On the right there are the EDS analyses of the highlighted areas in the micro-graphs.*

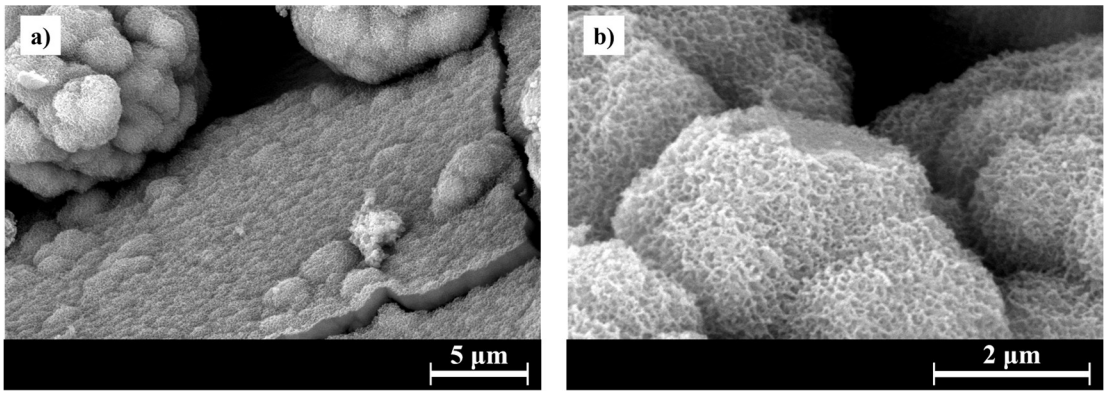

Figure 33. *FEG-SEM micrographs of S53P4_MSK granules after 14 days of soaking in SBF.*

The *in vitro* bioactivity of the novel glass has been further confirmed using Raman spectroscopy. **Figure 34** presents the spectra acquired on BG granules after 1 and 14 days of soaking in SBF. The spectrum after 1 day revealed the presence of peaks associated with silicate groups (Ziemath and Aegerter, 1994) and phosphate groups present in the original structure of the BG (Bellucci et al., 2012). In particular, the broad peak around 635 cm^{-1} is attributed to the Si-O-Si bond, while the partially obscured peak at 860 cm^{-1}, appearing as a shoulder due to the main peak around 950 cm^{-1}, represents the monomer SiO_4^{4-}. The main peak around 950 cm^{-1} is commonly associated with the symmetrical stretching of the PO_4^{3-} group (D. Bellucci et al., 2011). Finally, the peak around 1075 cm^{-1} can be attributed to the

asymmetrical stretching of the Si-O-Si group (González et al., 2003). These features are commonly associated with a BG that has not yet reacted (D. Bellucci et al., 2011).

Conversely, the spectra acquired after 14 days of soaking show peaks commonly associated with in vitro-formed HA. The peaks related to silicate groups become less intense, yielding to increased intensity of the phosphate and carbonate group peaks. Specifically, the peaks associated with the phosphate group, which indicate PO_4^{3-} bending, are observed around 430 and 590 cm^{-1} (Antonakos et al., 2007; Penel et al., 1998), accompanied by a shift of the main peak from 950 to 960 cm^{-1} (D. Bellucci et al., 2011). Additionally, the peak at 1070 cm^{-1} signifies the stretching of a carbonate group (Awonusi et al., 2007), suggesting the formation of hydroxyl-carbonate apatite (HCA) (Bellucci and Cannillo, 2018). HCA is a compound chemically and structurally similar to HA that represents a preliminary step for bio-integration (D. Bellucci et al., 2011; J. Liu et al., 2008; Shah, 2020).

Alongside its bioactivity, the novel composition exhibits optimal reactivity *in vitro*, as indicated by pH measurements ranging from 7.75 to 8.1 throughout the duration of the experiments. This finding is highly promising, as mildly alkaline environments are widely recognized for promoting tissue regeneration by stimulating osteogenic activity and inducing the antibacterial effects of BGs (Allan et al., 2001; Ramp et al., 1994b; Zhang et al., 2010b). Moreover, such minor pH fluctuations are expected to minimize potential cytotoxic effects. Significant pH changes can indeed damage cells, underscoring the necessity to precondition certain BG compositions before cell exposure (Ciraldo et al., 2018).

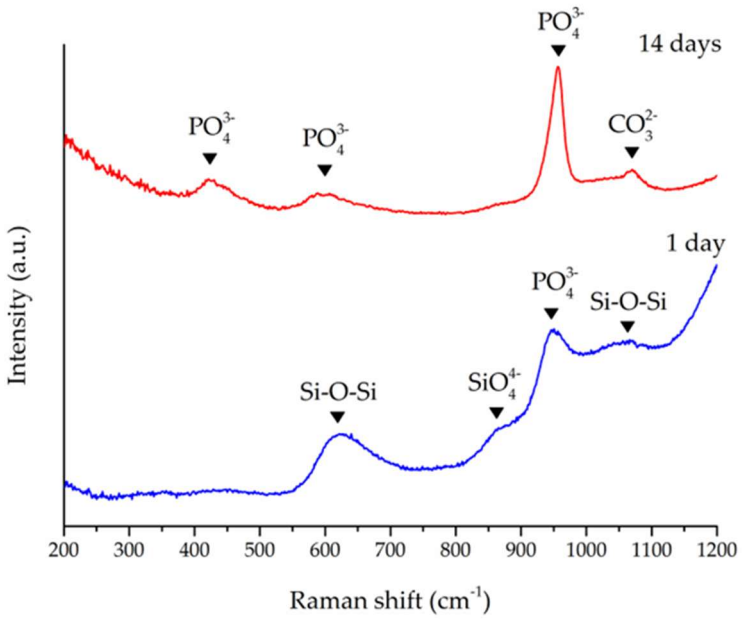

Figure 34. *S53P4_MSK Raman spectra of granules soaked in SBF for 1 and 14 days.*

2.3.4. Conclusion

One of the main challenges for BGs lies in their low thermal stability, which often results in crystallization during thermal treatments required for coating or sintering processes. While using a high heating rate can partially mitigate this issue, it cannot completely prevent crystallization (Stiller et al., 2024). An alternative approach involves doping agents to expand the sintering window. In this context, S53P4_MSK is a new BG composition doped with Mg, Sr, and K, retaining the same P_2O_5 content as its "parent" glass, the commercial S53P4.

The main advantages of S53P4_MSK include:

- High sinterability at 700 °C with no crystallization.
- High bioactivity, with HA formation observed after 3 days in SBF.
- Good mechanical properties.
- The presence of biologically significant ions.

The combination of these physical properties with potential biological benefits makes this novel BG particularly promising for applications requiring thermal treatments. Future studies will focus on the biological performance of this new composition, including investigations into its potential angiogenic, osteogenic, and antibacterial properties. Additionally, the production of sintered scaffolds will be explored to further evaluate the biological performance of 3D structures made with S53P4_MSK.

3. Additive Manufacturing and Composite Scaffolds

3.1. Additive Manufacturing of Polymer/Bioactive Glass Scaffolds for Regenerative Medicine: A Review

(This section has been published in: Martelli, A.; Bellucci, D.; Cannillo, V. Additive Manufacturing of Polymer/Bioactive Glass Scaffolds for Regenerative Medicine: A Review. Polymers, 2023, 15, 2473. https://doi.org/10.3390/polym15112473. *Reproduced in accordance with the publisher's copyright policy.)*

N.B. The introductory section is an updated and revised version of the article published. The changes concern the introduction only, aimed at avoiding repetition and ensuring consistency with the preceding chapters. Additionally, new figures have been added for clarity.

3.1.1. Introduction

Scaffolds are one of the main tools available in TE, and provide a 3D porous structure for the regeneration of damaged tissue, for example in critical-sized defects. In fact, such defects cannot be expected to heal spontaneously without additional intervention. Even if the dimensions and size of a critical-sized defect depend on the specific location within the body and various patient-related factors, they are usually defined as bone voids that are larger than twice the diameter of the affected bone or involve more than 50% circumferential bone loss (Haines et al., 2016; Sanders et al., 2014). Scaffolds mimic the functions of native extracellular matrix (ECM) in human tissue, which provides a supportive environment for cells to attach, migrate, and differentiate to create new tissue (Chan and Leong, 2008). Moreover, scaffolds are designed to mimic the shape, microstructure, and mechanical properties of the damaged tissue, which affect effective tissue regeneration. The scaffold's porosity and surface properties must be optimized to facilitate cell attachment, migration, and differentiation (Chan and Leong, 2008; Muschler et al., 2004).

Scaffolds must satisfy some features, as summarized in **Figure 35**, to be safe and promote tissue regeneration, such as cyto- and tissue compatibility, mechanical, architecture property and bioactivity (Chan and Leong, 2008; Ferreira, 2017). Scaffolds are considered bioactive when they can achieve a controlled interaction and reaction with the surrounding tissue in a physiological environment (Hench and Thompson, 2010). Moreover, scaffolds can be used as a delivery vehicle for bioactive molecules, e.g. drugs, antibiotics, etc., or contain cells (Arinzeh et al., 2005; Matsuno et al., 2010; Willerth and Sakiyama-Elbert, 2019; Y. Zhang et al., 2020). Scaffolds can be realized with different materials, e.g., metals, polymers,

ceramics, and composites, and by means of different protocols, obtaining disparate results (Koons et al., 2020).

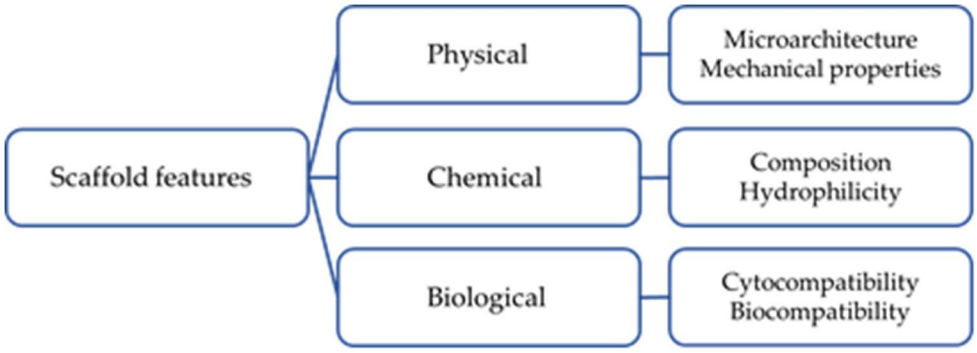

***Figure 35**. Schematic representation of scaffold features and requirements.*

Ceramic implants have excellent bioactivity and biocompatibility, meaning they are capable of interacting favourably with the body and eliciting an appropriate physiological response in specific applications (Williams, 1999). In particular, bioactive glass gained a lot of attention among the bioceramics for the properties presented in previous chapters. However, ceramics are brittle, in contrast to polymers and metallic implants that have higher mechanical properties but lower bioactivity and biocompatibility. To combine the best properties of both ceramics and other materials, two alternative approaches have emerged in the last two decades. The first approach involves using a bioceramic scaffold as a matrix and coating it with polymer (Bretcanu et al., 2007; Mohamad Yunos et al., 2008). The second approach involves adding bioceramics as coating or filler to a polymer matrix (Mohamad Yunos et al., 2008). This method has led to the development of a new generation of biomaterials that are composite materials (Baino et al., 2015; Shekhawat et al., 2021), and properly benefit from unique properties of their constituents.

On the other hand, polymers can be categorized into two main types: natural and synthetic. Examples of natural polymers include collagen, gelatine, and alginates, which are known for their good to excellent biocompatibility and biodegradability but often have poorer mechanical properties compared to synthetic polymers. Some commonly used synthetic polymers in TE include polycaprolactone (PCL), polylactic acid (PLA), and polyethylene glycol (PEG) (Echeverria Molina et al., 2021). These materials offer a wide range of mechanical and degradation properties that can be tailored for specific tissue engineering applications. Moreover, some polymers can be photosensitive, meaning their physical or chemical properties can change upon exposure to light (Wu et al., 2022). Photopolymers, unlike thermoplastic polymers, have a cross-linked molecular structure that

does not melt and exhibit much less creep and stress relaxation (Davoudinejad, 2021). This property allows the production of scaffolds by lithography, which is a promising technique of additive manufacturing (AM) that will be covered in depth in the following paragraphs.

The combination of BGs' bioactivity and the versatility of polymers creates a strong potential for polymer/BGs scaffolds to achieve exceptional regeneration rates compared to mono-material scaffolds (Joshi et al., 2020). As a result, there is significant interest and ongoing research aimed at developing and optimizing these composite materials.

As previously mentioned, scaffolds can be made with different methods. Conventional protocols for scaffold production are defined as processes that result in a homogenous, continuous pore structure without any long-range channeling microarchitecture (Sachlos et al., 2003). This non-specific microarchitecture leads to limitations in terms of finely controlling the geometry, pore size, and pore interconnectivity of the scaffold structure (A. Kumar et al., 2019).

One of the most representative examples of conventional methods is the foam replica method. This method involves replicating the porous structure of a sacrificial template to obtain a positive replica made of glass or glass-ceramic particles, which are then sintered around the organic strut. This method is versatile as it allows for the use of a wide variety of sacrificial templates of both synthetic and natural origin. It is also relatively inexpensive and requires no special equipment (Fiume et al., 2021). However, this technique has some limitations, including the lack of reproducibility and control of architecture in large or complex samples due to the formation of slurry gradients and pore occlusion in a confined portion of the volume, resulting in variable porosity between different samples (Baino et al., 2019). As a result, the operator's skill level strongly influences the final outcome, making it difficult to standardize the manufacturing process (Fiume et al., 2021). Moreover, it is not possible to achieve pore architecture and porosity tailored to the specific patient's needs (El-Rashidy et al., 2017).

The limitations of conventional manufacturing methods have been overcome using AM. AM is a layer-by-layer deposition process that can be performed with or without a substrate. Compared to traditional methods, AM offers improved material utilization, reduced waste, and greater design freedom (Ngo et al., 2018). AM is based on advanced computer modelling, enabling for the creation of complex shapes and internal structures. This capability allows for the production of scaffolds with precise control over their hierarchical pore structure, which can be tailored to meet the specific needs of individual patients (A.

Kumar et al., 2019). Moreover, bioprinting, a subcategory of AM, enables the printing of structures using viable cells and biological molecules. This approach addresses the issue of cell homogeneity, resulting in faster integration with the host tissue, lower risk of rejection, and most importantly, uniform tissue growth in vivo (Kačarević et al., 2018).

A lot of reviews about AM technique for scaffolding have been written, however most of them focus on a specific tissue or material (Arifin et al., 2022; A. Kumar et al., 2019; Santos et al., 2013; Yang et al., 2019). In particular, just few authors have discussed scaffolds containing BG: for example, Dukle et al. highlighted the bottlenecks in 3D printing of BG (Dukle et al., 2022), while Simorgh et al. reviewed the application of BGs for the fabrication of 3D-printed and bioprinted scaffolds and their usability in TE (Simorgh et al., 2023). Therefore, the aim of this review is to give an overview on the main AM techniques able to produce polymeric composites scaffold containing BG, emphasizing the potentials and limitations of each specific protocol.

3.1.1. Extrusion-based 3D printing

Extrusion-based 3D printing involves depositing layers of materials, such as polymers, onto a baseplate using a movable nozzle. The feedstock can come in various forms, including filaments, granules, or pastes (Dukle et al., 2022). Examples of this technology include Fused Deposition Modeling (FDM), Powder Extrusion Deposition (PED), and Direct Ink Writing (DIW).

Fused deposition modelling

Fused deposition modelling (FDM) is a method based on the extrusion of a polymer through a nozzle movable in X-Y-Z onto a base plate. The resolution of the printer is defined by the dimensions of the nozzle and the precision of its movement control. A schematic representation of FDM printer is presented in **Figure 36**.

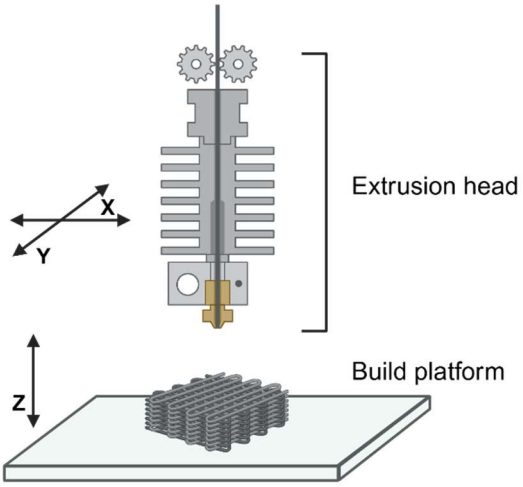

Figure 36. *Schematic representation of FDM printer. Created in https://BioRender.com*

The choice of polymeric material should meet two main criteria: relatively low melting temperature and appropriately high glass transition temperature (P. Zhang et al., 2020). The typical extrusion temperature range is 100-140 °C (Chia and Wu, 2015). Polymer can be mixed with BGs and extruded to obtain a filament used in FDM. This approach offers some advantages over paste-based approach as it is a solvent-free method, allowing the material to be printed with a pore size gradient (Distler et al., 2020). However, the extrusion temperatures are too high to include cells or bioactive molecules (Liu Tsang and Bhatia, 2004). PCL is widely used in scaffold production, particularly through FDM, due to its low melting point (59–64°C), good drug permeability, biocompatibility, solubility, excellent compatibility in blends, and ability to maintain its mechanical and physical properties long enough for tissue growth (Hajiali et al., 2018).

Wang et al. (Wang et al., 2022) produced PCL/58S scaffolds with varying percentages of BG content (0, 5, 10, 20 wt%). 58S is a silicate BG produced via sol-gel processing, designed to eliminate Na_2O from its composition (Li et al., 1991). *In vitro* and *in vivo* studies demonstrated that the scaffold with the highest BG content exhibited the most profound bone repair effect, exhibiting a maximum compressive strength of 43.52 ± 2.01 MPa and a minimum tensile strength of 4.63 ± 0.25 MPa. Despite these favourable outcomes, the best contact angle achieved was 87.99° ± 7.07°, indicating that the hydrophilicity of the scaffold was not optimal for cell adhesion.

As known, the adhesion of cells to artificial materials depends on several surface properties, including wettability, roughness, surface charge, and chemical functionalities (Ratner et al., 2004). Cells were found to adhere effectively to surfaces with moderate

wettability and water contact angles in the range of 40°-60°, as reported by Arima et al. (Arima and Iwata, 2007). Ilyas et al. (Ilyas et al., 2022) successfully addressed this issue by altering the surface of scaffolds and achieving water contact angles between 30°-65°. Such modification not only improved cell adhesion, but also conferred enhanced antibacterial properties. The study involved the creation of composite PCL scaffolds incorporating either silicate or borate BG particles (1393 and 1393-B3 glasses), coated with Sr-doped mesoporous bioactive glass nanoparticles and gelatin, and further modified with polydopamine (PDA). 13-93 is a silica-based BG that contain K_2O and MgO to expand its working range (Brink, 1997). A modified version of 13-93, known as 13-93B3, is obtained by replacing all the SiO_2 in 13-93 with B_2O_3, which leads to a higher degradation rate (Fu et al., 2010). SEM analysis showed a uniform distribution of BG particles, thanks to the hydrophobic nature of PCL. The scaffolds containing borate BG particles demonstrated equivalent or even better cell viability compared to those with silicate BG particles.

An alternative approach for altering the surface of scaffolds was found by Fathi et al. (Fathi et al., 2021) by utilizing NaOH, which effectively decreased the contact angle of the scaffolds from 76° to 61°. The study investigated several compositions of BG doped with Sr and Co or both. The aim of adding dopants was to promote both osteogenesis and angiogenesis. The most optimal mechanical properties were observed in the composition that contained both Sr and Co dopants, exhibiting a Young's modulus of over 9 MPa. Kim et al. (Kim et al., 2019) identified a limit on the BG content for PCL scaffolds produced by FDM. They discovered that a BG content exceeding 60% led to high viscosity, hindering the effectiveness of the FDM process. Through their study of different ratios of PCL to BGS-7 (for further information about this BG, please refer to [63]), they identified that a BG content of 40 wt% represented the best compromise between mechanical stability and biological compatibility.

Another widely polymer used in FDM is PLA, due to its biocompatibility, biodegradability, and suitable mechanical properties. Moreover, the degradation rate as well as the physical and mechanical properties of PLA can be adjusted by varying the molecular weight (Puppi et al., 2010; Savioli Lopes et al., 2012). In their initial attempt, Distler et al. (Distler et al., 2020) created filaments using PLA with varying amounts of 45S5 (0, 1, 2.5, 5, 10 wt%). However, the bonding between the materials was poor, which resulted in suboptimal mechanical properties even at high BG content. To improve interface adhesion, the authors suggested exploring alternative surface modifications (e.g., particle roughness,

size, and chemistry) and adjusting the bulk polymer chemistry to enhance polymer/filler interface binding. Saranti et al. (Saranti et al., 2022) did not address the bonding issue between PLA and 45S5 in their study. Instead, they fabricated PLA scaffolds with varying amounts of 45S5 and incorporated biocompatible, fluorescent carbon dots (C-dots) to enable real-time monitoring of the healing process. C-dots are biocompatible and fluorescent nanoparticles with sizes up to 10 nm, that exhibit notable photophysical and chemical properties. The C-dots used were red-emissive and preferred for biomedical applications as they operate in the near-infrared (NIR) region, reducing tissue absorption and autofluorescence (Smith et al., 2009). *In vitro* cytotoxicity tests indicated that the composites produced in their study could be safely used in vivo at low concentrations (<20 ppm).

FDM technology is capable of printing biopolymers such as sodium alginate (SA). Luo et al. (Luo et al., 2017) developed an organic-inorganic ink by blending 13-93 BG/SA with polyvinyl alcohol (PVA) in different ratios, resulting in scaffolds with improved mechanical properties when compared to pure SA scaffolds. The samples showed increased HA mineralization and released Mg^{2+} and SiO^{4-} ions. The best results were obtained for a BG/SA ratio of 2:4, with a compressive strength of 16.74 ± 1.78 MPa, a modulus of 79.49 ± 7.38 MPa, and the highest activity of primary rat bone mesenchymal stem cells (rBMSCs).

In summary, the FDM process allows the production of complex 3D structures with resolution limited by the nozzle diameter, layer height, and the viscosity of the polymer (Chia and Wu, 2015). Cells or bioactive molecules cannot be included during the printing process due to the high extrusion temperature, but they can be added after printing. FDM enables the production of parts with tuneable mechanical properties using a wide range of materials, including those with BG content up to 60 wt%.

Precision extrusion deposition

Precision extrusion deposition (PED) is a variant of FDM that allows printing directly from granules, without the need to create filaments (**Figure 37**). Extrusion is obtained by a screw, allowing an accurate control on the quantity extruded. Moreover, the XY motion system is synchronized with the extruder, obtaining a precise control on thickness and position of the fibers (Hamid et al., 2011; Shor et al., 2009; Su et al., 2021). In addition, it is possible to use a wider range of biopolymers with higher melting point, installing an assisting cooling device near the nozzle of the PED (Hamid et al., 2011).

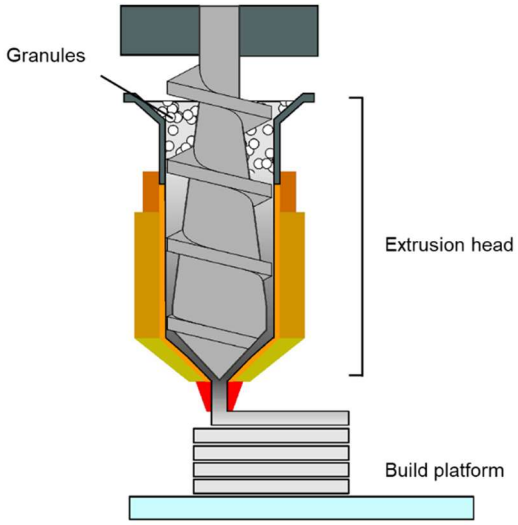

***Figure 37**. Schematic representation of PED printer. Adapted from (Gonzalez-Gutierrez et al., 2018).*

Limited research exists on PED-produced composite scaffolds. Petretta et al. (Petretta et al., 2021) produced PCL/BG composite scaffolds with varying ratios of PCL to BG (70/30 and 50/50) and found that the 50/50 ratio yielded better results, with a compressive modulus within the range required for trabecular bone (0.1-5 GPa). Furthermore, cytotoxicity tests showed no adverse effects for either ratio up to day 21. Bioactivity tests revealed that the 50/50 composition exhibited superior performance compared to the 70/30 ratio. This result may be attributed to the greater amount of BG that emerged from the polymer matrix in the 50/50 ratio, resulting in an enhanced surface roughness that promotes cell proliferation.

Similar compressive modulus was found by Daskalakis et al. (Daskalakis et al., 2022) producing PCL-based composite scaffolds with different concentrations of 45S5 (0-10-15-20 wt%). Consistent with previous studies, increasing the BG content led to improved mechanical performance, while the hydrophilic behavior was not significantly affected by the addition of BG. Interestingly, the scaffold with 10% BG exhibited the best cell activity at day 14 after cell seeding. These studies suggest that PED is a promising method for producing scaffolds containing BGs. However, the low mechanical properties of the scaffolds indicate that the technique is not yet mature enough for loading applications.

Direct ink writing

Direct Ink Writing (DIW), also known as Robocasting, is an extrusion-based layer-by-layer process (**Figure 38**) that employs highly concentrated powder suspension (slurries) composed of a mixture of ceramic powder (>40% vol), water, and additives (<3% vol) such as dispersant, binders and coagulants (Lamnini et al., 2022).

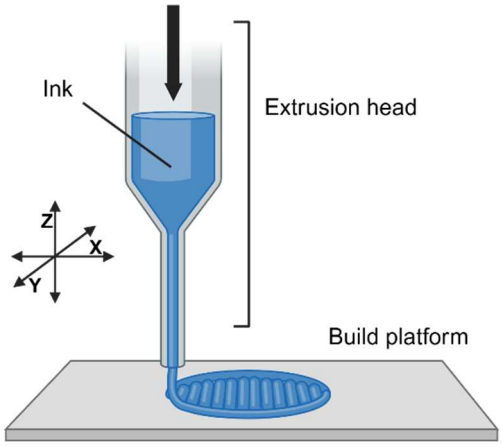

***Figure 38**. Schematic representation of DIW printer. Created in https://BioRender.com*

To be suitable as ink for robocasting manufacturing, a colloidal slurry should possess several key properties. Firstly, it should exhibit a rheology that is "yield pseudoplastic," meaning that the viscosity decreases as the applied stress increases. Secondly, it should be able to flow smoothly through a small nozzle. Finally, it should have the ability to maintain its shape after deposition (Lamnini et al., 2022). When these requirements are satisfied, DIW can be employed to fabricate intricate composite bodies that sinter into relatively strong, dense, and defect-free parts. It is important to note that the resulting product obtained through DIW is transformed into a monomaterial, no longer a composite (CESARANO III, 1999). The range of printing parameters and materials used for DIW were reviewed by Balani et al. (Balani et al., 2021).

Among all binders, Pluronic F-127 has been shown to be a universal binder for different types of BGs, regardless of their reactivity and composition (Nommeots-Nomm et al., 2018). Pluronic F-127 is an amphiphilic triblock copolymer composed of a central hydrophobic chain of poly(propylene oxide) flanked by two hydrophilic chains of poly(ethylene oxide). This composition makes Pluronic F-127 a water-soluble surfactant with rheological behavior that can be thermally reversed (Martindale and Reynolds, 1996). In the same study on Pluronic F-127, Nommeots-Nomm et al. (Nommeots-Nomm et al., 2018) evaluated the sintering outcomes of two silicate bioactive glasses with low-silica content, PSrBG and ICIE16, in comparison to the 13-93 bioactive glass. To preserve the amorphous structure of the glass, the researchers used a large particle size in their samples, but this led to limited compressive strength after sintering, ranging between 32-48 MPa. Despite these limitations, the investigated compositions displayed satisfactory sintering outcomes, with uniform

shrinkage and a porosity between 41 and 43 vol%. This finding suggests that the sintering outcomes of low-silica content BGs can be improved with larger particle sizes.

Otherwise, Ben-Arfa et al. (Ben-Arfa et al., 2019a) produced scaffolds using a high-silica sol-gel glass (HSSGG) via DIW to improve sintering and densification. However, during the thermal treatment, BG powders experienced partial crystallization, leading to limited densification and to a scaffold with 36% open microporosity. Despite this improved the responsiveness of the samples both *in vitro* and *in vivo*, it limited their compressive strength to 5 MPa. To address this issue, the authors added copper or lanthanum to the HSSGG, which had minimal effects on ink printability but significantly improved the mechanical properties of the final products. In particular, the Cu-doped glass scaffold showed a compressive strength even higher than human trabecular bone. *In vitro* tests confirmed the BGs' biocompatibility with respect to various cell lines, making them suitable for in vivo experimentation (Ben-Arfa et al., 2019b, 2019c).

The sintering of 45S5 scaffolds can be challenging due to the small sintering window (Jones, 2013). Motealleh et al. (Motealleh et al., 2017a) have extensively studied the use of DIW to produce amorphous 45S5 scaffolds. The amorphous scaffolds exhibited a faster degradation in simulated body fluid (SBF) compared to 45S5 crystallized scaffolds, resulting in a more rapid decrease in mechanical properties. Additionally, cell tests suggested that crystallized scaffolds had an improved cell viability. To enhance the compressive strength of the amorphous scaffolds, Motealleh et al. (Motealleh et al., 2017b) coated them with a HA/PCL nanocomposite coating. The study showed that the coated scaffolds had improved mechanical properties by more than 200%, but did not provide information about the biological response of the coated scaffolds.

In order to promote cell adhesion and bone regeneration a given scaffold must exhibit a hierarchical structure with pores of different sizes. To achieve this, Barberi et al. (Barberi et al., 2019) produced BG scaffolds with a porosity gradient using Pluronic F-127 as binder. However, the scaffolds obtained had defects such as voids and cracks due to air bubbles entrapped in the ink, as well as different shrinkage rates between the denser core and more porous outer shell. Despite these issues, mechanical tests showed that the compressive strength of the samples was comparable to the range of human trabecular bone. However, the values exhibited a great variability. The issue of the defects and the variability in mechanical properties of scaffolds with a porosity gradient is still a challenge that needs to be addressed.

To overcome these challenges, Touré et al. (Touré et al., 2020) developed a novel approach by combining DIW and electrospinning to fabricate composite scaffolds with multigrade porosity. They evaluated a mixture of PCL and poly(glycerol sebacate) (PGS) with varying concentrations of BGs at 0, 5, and 10 wt%. The hybrid scaffold fabrication method was effective in achieving excellent adhesion between the 3D-printed layer and the electrospun network, which improved the stiffness of the scaffolds with a 2.5-fold increase in Young's modulus. While the addition of BGs only slightly affected the mechanical response of the scaffolds (a 30% increase in elastic modulus for scaffolds with 10 wt% BGs), it significantly impacted the material degradation *in vitro* and balanced the acidic nature of PGS. This positively affected the growth of fibroblasts, with scaffolds containing 10 wt% BGs sustaining cell viability longer *in vitro*. Touré et al. recognized the potential application of these composite scaffolds in tendon and ligament replacements, given their ability to meet the mechanical requirements of native tissues with an elastic modulus in the range of 100–300 MPa.

To better understand the degradation rate of silica and borate glasses, Deliormanli et al. (Deliormanli and Rahaman, 2012) conducted a study comparing scaffolds containing 13-93 and 13-93B glass; the maximum BGs content that maintained flowability behavior of the polymeric suspension was used. X-ray diffraction (XRD) analysis indicated that no crystallization had occurred in the scaffolds. After immersing the scaffolds in SBF for 50 days, mechanical tests revealed that the borate-based scaffolds had a faster decrease in compressive strength (from 65 ± 11 MPa to 8 ± 4 MPa) compared to the silicate-based scaffolds (from 142 ± 20 MPa to 79 ± 32 MPa). This finding demonstrates the superior stability of silicate-based scaffolds in SBF, which makes them promising for the regeneration of load-bearing bones.

The influence of silicate BG structure in vivo was investigated by Tulyaganov et al. (Tulyaganov et al., 2022). The study compared granules and porous scaffolds implanted in rabbit femurs and found no statistically significant difference in new bone formation between the two approaches. However, the scaffold implants resulted in more homogenous tissue formation, underlining the value of this structure. Furthermore, Liu et al. (Liu et al., 2013) reported an intriguing result for the 13-93 scaffold implanted in rats. They found that the brittle mechanical response of the scaffolds *in vitro* changed to an elastoplastic response after implantation for longer than 2-4 weeks in vivo, thus highlighting the importance of in vivo testing for the evaluation of scaffold performance.

The DIW technique has been expanded to include natural polymers, as demonstrated by Dorj et al. (Dorj et al., 2012) in their successful production of a composite scaffold consisting of chitosan and BG. Chitosan is a semi-crystalline polysaccharide derived from chitin, which is the second most abundant biopolymer after cellulose. Due to its high positive charge, chitosan is often used as a drug carrier (Croisier and Jérôme, 2013). However, it is challenging to solidify chitosan at ambient conditions, as reported by Dorj et al (Dorj et al., 2012). To overcome this, the authors used dry ice to refrigerate the environment during printing. The addition of BG with diameters of a few hundred nanometres and a printing temperature of around -50°C resulted in a micro-porous structure. *In vitro* tests confirmed the scaffold's ability to form apatite in SBF, as well as cell adhesion and proliferation. However, further research into the scaffold's mechanical properties is necessary before considering its application.

Another promising natural polymer for producing composite scaffolds is silk fibroin (SF), obtained from silkworm cocoons, which exhibits excellent biocompatibility and mechanical properties (Yan et al., 2013). Moreover, SF can be manipulated at a temperature close to human physiological temperature, allowing for cell or biological factor loading (W. Zhang et al., 2014). Du et al. (Du et al., 2019) compared SF/BG and PCL/BG scaffolds, both with a mass ratio of 20/80, and found that the SF/BG scaffold exhibited higher mechanical properties and better biological responses *in vitro*. In addition, implantation of the scaffolds into the back of nude mice demonstrated the SF/BG scaffold's more favorable osteogenic ability in vivo. Therefore, SF has great potential as a natural polymer for producing composite scaffolds. When a sintering treatment is not required, DIW allow to print scaffold containing cells or drugs. Kolan et al. (Kolan et al., 2020) developed a method to improve the mechanical properties of hydrogel-based bioinks by modifying a DIW printer to print PLA/13-93B3 and bioink simultaneously. The resulting composite scaffold contained cells and demonstrated enhanced mechanical properties. However, live/dead evaluation revealed non-uniform cell viability, with fewer cells surviving in the bottom layer due to a hypoxic-like environment.

Wu et al. (Wu et al., 2011) produced PVA-based scaffold containing mesoporous BG and dexamethasone (DEX). DEX is a synthetic glucocorticoid that has been shown to promote osteoblast differentiation and bone tissue regeneration. Moreover, DEX has been found to reduce implant-associated inflammation. However, it should be noted that high concentrations of DEX can suppress the proliferation of osteoblasts and result in toxic side

effects (Chen et al., 2018; Franz et al., 2011; Ren et al., 2017). The study found that DEX release was highest after 2 days, with slower kinetics up to 10 days, indicating the potential of the scaffold to treat the inflammatory response following implantation. These findings are in agreement with Zhang et al.'s (J. Zhang et al., 2014) study, which reported also an enhanced osteogenic expression in Sr-doped BG/PVA scaffold compared to undoped scaffold.

In summary, DIW allows for the production of scaffolds with several BGs compositions, effectively overcoming the sintering difficulties. However, the challenge of fine-tuning microstructure and mechanical properties remains. To address the mechanical issue, one potential solution could be to coat the samples. However, it is necessary to perform in vivo validation to determine the efficacy of this solution. Further research is needed to address these challenges and fully realize the potential of DIW for scaffold production.

3.1.2. Lithography-based 3D printing

Lithography-based techniques use selective exposure to light to cure a liquid formulation via photopolymerization. The process is initiated by the excitation of a photoinitiator through the absorption of light, which then generates free radicals that start the polymerization process. The process results in the consumption of low molecular monomers, forming long polymer chains or a polymer network, leading to the solidification of the liquid formulation [86]. Lithography-based techniques are stereolithography and digital light processing.

Stereolithography

Stereolithography (SLA) employs a layer-by-layer deposition of a liquid resin that solidifies via photo-polymerization. To further enhance the mechanical properties of SLA-printed objects, a dual-curing process can be employed, e.g. combining photocuring with subsequent thermal curing (Obst et al., 2020). Additionally, the feedstock must be a liquid that rapidly solidifies upon illumination, which is a major limitation due to the limited availability of materials that meet this criterion. Creating polymer-ceramic composites requires uniform suspension of ceramic particles in the resin, which affects slurry viscosity, polymer photoreactivity, and printing resolution (Bae et al., 2017; Komissarenko et al., 2018). SLA's resolution decreases with increasing print speed (Arifin et al., 2022), with the highest resolutions for additive processing being 20 μm, although stereolithography setups based on two-photon absorption can achieve resolutions down to 100 nm (Weiß et al., 2009).

Furthermore, it is possible to incorporate bioactive molecules and cells into the printed structures (Melchels et al., 2010).

One disadvantage of using a low-resolution technique to produce composite scaffolds is that the surface of the scaffold often ends up with a polymer film that covers the BG particles during fabrication. This issue can be resolved by using SLA, as demonstrated by Elomaa et al. (Elomaa et al., 2013). In their study on PCL/S53P4 (such BG known for its antibacterial properties and commercially available as BonAlive® (Drago et al., 2013)), they showed that SLA allows for greater control over the surface of the scaffold, resulting in better exposure of the BG particles. Additionally, their study highlights the variability of mechanical properties between dry and wet scaffolds, which is a crucial consideration for in vivo applications. Understanding this variability is essential to ensure optimal performance and biocompatibility of the scaffold in vivo.

Many studies have examined how the composition of suspensions affects the final product. In one such study, Chen et al. (Chen et al., 2022) investigated the impact of the concentrations of monomers, a reactive diluent, photoinitiator/co-initiator (PI), non-reactive diluent/dispersant, and light absorber on resin rheology and cure depth to optimize the resin for porous ceramic scaffolds manufacturing. The researchers found that adding polyethylene glycol 200 (PEG-200) to the suspension improved its stability and shelf life, resulting in a more homogeneous microstructure and increased mechanical strength. However, the hardness value decreased with increasing amounts of PEG-200, as it acted as a plasticizer and lowered the Young's modulus. The team selected a 10% weight fraction of PEG-200 to avoid changes in mechanical properties. The optimized BG resin composition contained 55% BG, 10% PEG-200 as a non-reactive diluent and rheology modifier, 1% PI, and 0.015% Sudan orange G dye as a light absorber. SEM and micro computed tomography (μ-CT) results demonstrated that this composition produced dense structures without cracks. Nevertheless, this composition was evaluated only from a structural perspective, and further research is needed to assess its *in vitro* and *in vivo* effects.

Kang et al. (Kang et al., 2020) conducted a study on the optimization of the ceramic suspension of 45S5 for use in commercial 3D SLA printers. They investigated the effect of five different ratios of photocurable resin and acrylate binder and found that the highest reactivity and cure depth were obtained for a 4:6 ratio. Then, they evaluated the effect of varying the 45S5 content in the suspension (ranging from 32% to 40% volume). The maximum strength and viscosity were achieved with a 40% volume fraction of 45S5.

Importantly, no residual effects of the binder were found after sintering, suggesting that the suspension with 40% volume fraction of 45S5 can be effectively employed in scaffolds manufacture.

The relationship between structural of structural design, pore dimensions and sintering conditions on mechanical properties in 45S5-based scaffolds was evaluated by Thavornyutikarn et al. (Thavornyutikarn et al., 2017). Different microarchitecture and pore sizes were considered. To minimize shrinkage and internal stresses in the scaffold with a pore size of 550 μm, a two-stage sintering process was explored. The study found that partial pre-sintering at 550 °C, followed by re-grinding and SLA processing, and a final sintering at 950 °C led to an increase in the scaffold's mechanical strength and a shrinkage reduction. However, this process also caused a reduction in pore size and porosity that can lead to a reduced cell viability.

In summary, SLA is a 3D printing process that can work with limited polymers and can also incorporate cells or biomolecules into the feedstock. It can achieve the highest resolution for additive manufacturing processes, although it is generally slower than other methods. However, there is currently limited research on the application of SLA for producing composite scaffolds, and the lack of *in vitro* and *in vivo* testing prevents it from being recognized as a suitable method for composite scaffold production at this time.

Digital light processing

Digital Light Processing (DLP) is an advancement of SLA, which utilizes a digital micro-mirror device (DMD) to print the entire layer at once, reducing the time required to produce scaffolds (J. Zhang et al., 2020). A schematic representation of the two technologies is presented in **Figure 39**. Like SLA, photopolymerization of suspensions containing ceramic particles depends on solid content, powder size, and refractive index mismatch between ceramic powder and monomer (Badev et al., 2011; Halloran, 2016; Halloran et al., 2011). DLP resolution is determined by the projection plane set by the micro-mirror device and lens. Resolution is typically in the micron range (J. Zhang et al., 2020). According to Saha et al. (Saha et al., 2019), combining DLP and two-photon lithography (TPL) into a femtosecond projection TPL (FP-TPL) can achieve higher resolution (sub-500-nm).

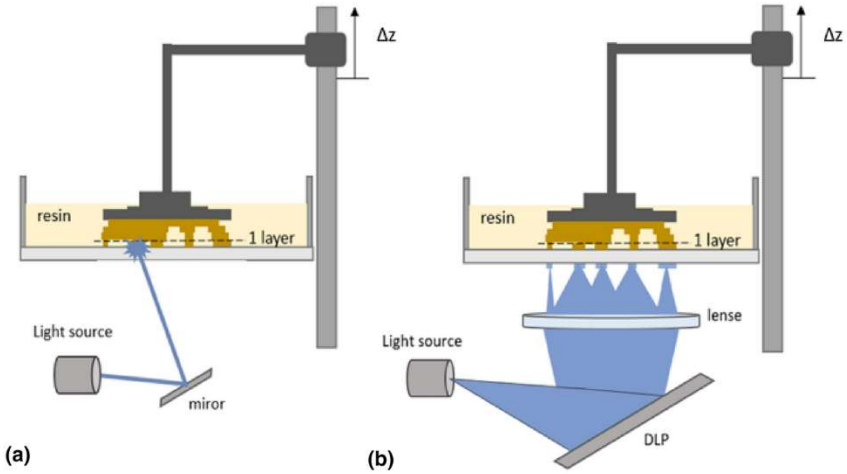

Figure 39. *Schematic representation of SLA printer (a), and DPL printer (b). Adapted from (Schittecatte et al., 2023)*

One of the main challenges in the production of scaffolds is the occurrence of "debinding failure". This issue arises when there is a non-uniform removal of the binder from the surface and core of the green body, which can be caused by high polymeric content or inadequate powder packing. This fact often results in the collapse of the printed structure, especially when the granulometry is not optimized (Wu et al., 2016). To overcome the problem, researchers have been exploring the use of binders that can contribute to the final glass composition upon firing. A possible solution is silicone. By incorporating silicone as a binder, the production of scaffolds can be improved: such material, in fact, can facilitate the debinding process and contribute to the overall strength and stability of the final product. It is important to stress that the resulting product of this approach is no longer a composite scaffold but rather a BG scaffold.

Elsayed et al. (Elsayed et al., 2020) successfully integrated DLP of glass-ceramics with a silicone reactive binder that transforms into silica upon firing. They conducted a comparison between a reference glass scaffold printed with a sacrificial binder and a "silica defective" glass variant (15 wt%) with a silicone binder (H62C). Mechanical tests and SEM images revealed that the silicone component had a binding effect, resulting in homogeneous and crack-free scaffolds with a compressive strength of 3.7±0.4 MPa. In a subsequent study, Dogrul et al. (Dogrul et al., 2021) focused on the effect of a new silicone, H44, on Biosilicate® composite scaffold produced by DLP. Biosilicate® is a BG known for its effectiveness in tissue regeneration, composed of $23.75Na_2O–23.75CaO–48.5SiO_2–4P_2O_5$ (wt%) (Crovace et al., 2016). H44 provided a way for fine-tuning the microstructures without any cytotoxic effects on stromal cell. Similarly, the use of a silane coupling agent

can improve the interaction between the methacrylate polymer matrix and the bioceramic material (Tesoro and Wu, 1991).

This approach was employed by Vyas et al. (Vyas et al., 2022); in their research, they found that there was a limit on the loading levels of glass particulate for DLP printing. They observed that beyond a certain threshold of 20 wt% of bioactive glass ceramic, the 3D printed parts resulted in uncured or dimensionally inaccurate structures. Despite demonstrating good biocompatibility, the scaffolds produced did not match the mechanical properties of cortical bone, even with a lower content of BG. Xu et al. (Xu et al., 2020) successfully reconstructed a critical-size defect in a rabbit mandible using DLP-printed composite scaffolds. The study introduced a novel BG called AP40mod, which is composed of SiO_2, P_2O_5, CaO, K_2O, Na_2O, CaF_2, and TiO_2. The scaffolds were seeded with endothelial progenitor cells (EPCs) and bone marrow mesenchymal stem cells (BMSCs), leading to excellent defect repair. However, the use of titanium for fixation necessitated a secondary surgical removal. To address this issue, the authors suggest further investigation into utilizing AP40mod or combinations of high-molecular-weight polymers (e.g., polycaprolactone) to print customized, degradable mesh and staples.

In summary, the studies demonstrate that DLP is a promising method for composite scaffolding due to its versatility and high resolution. However, further research is needed to optimize the mechanical properties that can be achieved through this technique. Moreover, additional in vivo testing is necessary to thoroughly evaluate the effects of various feedstocks on the resulting scaffolds.

3.1.3. Laser-based 3D printing

Selective laser sintering (SLS) is a process that exploits a focused laser beam to rapidly heat and fuse bed powder materials to produce solid parts (**Figure 40**). There are two primary approaches to SLS: indirect and direct. Indirect SLS involves bonding a mix of ceramic powders and a small amount of polymer binder using a low-power laser scan, resulting in a porous object that may require additional sintering in a furnace for strength. On the other hand, direct SLS employs a high-power laser beam and does not need any polymeric bonding materials, allowing it to produce parts with densities over 80% of theoretical density (Natarajan et al., 2021). Direct SLS can be further divided into three approaches: Solid state sintering (SSS), Liquid phase sintering (LPS), and Selective laser melting (SLM). SSS is a process that produces solid parts by heating material powder to a temperature just below its

melting point (Kruth et al., 2005), resulting in solid bonds between the particles. However, SSS often produces highly porous components (Agarwala et al., 1995). LPS involves heating materials near their melting temperature and using a combination of low- and high-melting-temperature materials to create a dense composite with customized properties. SLM is a laser-based additive manufacturing process that fuses material powders without the use of binding materials, creating fully dense parts with superior mechanical properties. However, SLM parts may suffer some residual stresses that can lead to distortion, cracks, and delamination (Natarajan et al., 2021).

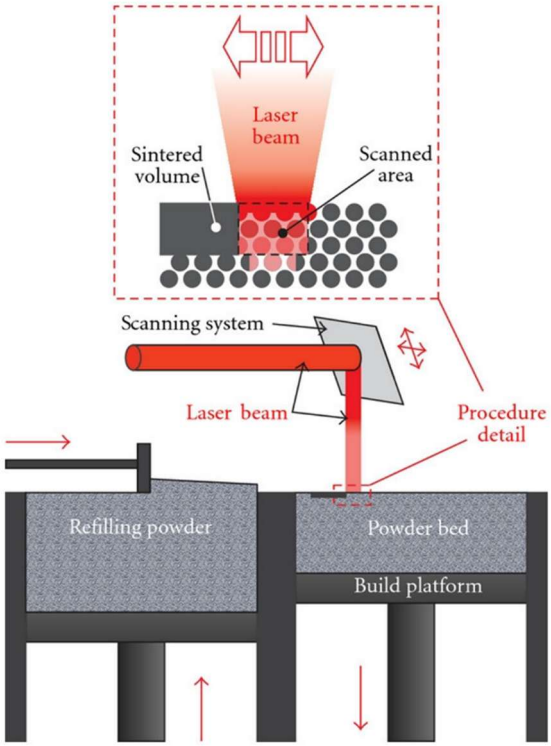

Figure 40. *Schematic representation of SLS printer. Adapted from (Tsouknidas, 2011).*

The choice between different approaches is not always clear or specified. Therefore, in this paragraph, we will refer to all approaches generically as SLS; however, when possible, we will specify accordingly.

PLA and its stereoisomers, such as PLLA and PDLLA, are widely used in SLS for TE applications. The production of PDLLA/58S scaffolds for non-load bearing applications, such as the facial skeleton, was optimized by Pereira et al. (Do Vale Pereira et al., 2014) using SLS. To achieve optimal results, the laser power was set at 5.4 W, as lower power failed to promote particles sintering while higher power led to polymer degradation. The stress-strain curves further revealed that composites with 10%wt of BG exhibited the

greatest mechanical properties, while higher BG content resulted in decreased values due to a decrease in polymer particle coalescence. To improve the biocompatibility of PLLA-based scaffolds and reduce the inflammatory response induced by their degradation, Sun et al. (Sun et al., 2020) produced PLLA/BG scaffolds doped with DEX. The researchers developed scaffolds with 10%wt of BG and varying amounts of DEX. Their research confirmed the activity of DEX post-printing, with the most effective regeneration seen in vivo for the scaffolds containing the highest concentration of DEX. Notably, the scaffolds doped with DEX exhibited a lower degradation rate compared to pure PLLA scaffolds, likely due to the hydrophobic nature of DEX which retards water penetration.

Shuai et al. (Shuai et al., 2019) investigated the use of SLS-produced mesoporous BG/PGA-PLLA scaffolds doped with varying ratios of Ag^{+} to create an effective antibacterial scaffold. The researchers utilized polydopamine to allow for the adsorption of Ag^{+} and the reduction of well-dispersed metallic nanoparticles *in situ*. Moreover, the size of the silver nanoparticles could be regulated by adjusting the concentration of Ag^{+} ions and the amount of polydopamine. Their investigation demonstrated a remarkable bacterial inhibition rate of over 99% against Escherichia coli. Additionally, mechanical, and in-vitro tests confirmed that the scaffolds possessed appropriate properties for bone replacement. However, further research is necessary to evaluate the in vivo response to the Ag content. The limitations of scaffolds, including layer separation and weak interface bonding, have been identified as barriers to effective cell migration and long-term osteochondral repair (Gotterbarm et al., 2006; Müller et al., 2006). However, multi-graded scaffolds have shown promise in overcoming these challenges (Du et al., 2017).

Karl et al. (Karl et al., 2019) conducted a study on the use of foamed spherical composite particles in SLS to produce multi-material and multi-graded scaffolds for TE. The composite particles consisted of varying amounts of BG content in a PLGA matrix, obtained using a solid-in-oil-in-water approach. However, the researchers encountered issues with larger particles that contained more than 20 wt% of BG, as these particles lost their spherical shape and broke during production. As a result, the scaffolds produced in this initial study had poor mechanical properties and were not well-suited for TE applications. To address these challenges, the researchers proposed a solution of load-bearing walls made of pure polymer, with the composite material being used as a filler phase. This solution aims for greater accuracy. To achieve this, Karl et al. proposed two technical approaches: point-by-point SLS (X. Zhang et al., 2019) or using a structure of particles, which has been patented by Aerosint

SA (Belgium) (Bedoret et al., n.d.). It should be noted that the proposed approaches by Karl et al. have not been implemented or tested yet. Further research and experimentation would be necessary to determine the effectiveness of these solutions.

Another challenge in TE is the degradation rate of scaffolds, which must be carefully controlled to match the growth rate of the tissue being generated. If the scaffold degrades too slowly, it can impede the regeneration of new tissue, while if it degrades too quickly, it can compromise the structural integrity of the scaffold and hinder the formation of functional tissue (Echeverria Molina et al., 2021). Borate BGs can create an alkaline environment during their degradation, making it possible to regulate the dissolution rate of composite scaffolds by adjusting the amount of the borate BG. Han et al. (Han et al., 2023) investigated this approach and successfully produced and implanted borate BG/PCL scaffolds to treat a critical size bone defect in the rabbit radius. Using SLS, they were able to optimize both the mechanical properties and the *in vitro* results of the scaffold, with a 20 wt% BG content chosen as the ideal composition. The scaffolds had a pore size of 650 µm, facilitating good angiogenesis and osteogenesis after 12 weeks in vivo. These promising findings suggest that this composite scaffold holds great potential as a viable option for repairing bone defects.

To summarize, laser-based techniques show great potential for enhancing interface bonding and controlling scaffold degradation rates. Additionally, the ability to print bioactive molecules using SLS makes it ideal for fabricating drug delivery scaffolds. However, further optimization is required to achieve mechanical properties suitable for load-bearing scaffolds.

*For a comprehensive list of the techniques and material combinations mentioned, please refer to **Table 7**.*

Table 8 provides a brief description of the BGs cited in this review. Additionally, **Figure 41** reports a summary of the pros and cons associated with each specific technique discussed.

Table 7. *List of techniques and material combinations for producing scaffold by AM*

Technique	Materials	Main results	Reference
Fused deposition modeling (FDM)	PCL/58S	High tuning of mechanical properties Low hydrophilicity	(Wang et al., 2022)
	PCL/13-93 PCL/13-93B3	Excellent hydrophilicity Best cell viability for 13-93B3	(Ilyas et al., 2022)
	PCL/BG-Ca PCL/BG-Sr PCL/BG-CaCo PCL/BG-SrCo	Increased hydrophilicity after surface treatment Best mechanical properties for BG-SrCo scaffold	(Fathi et al., 2021)
	PCL/BGS-7	Identified a limit on BG content	(Kim et al., 2019)
	PLA/45S5	Poor bonding between PLA and BG	(Distler et al., 2020; Saranti et al., 2022)
	SA/13-93	Best mechanical and biological properties for a SA/BG ratio of 4:2	(Luo et al., 2017)
Powder extrusion deposition (PED)	PCL/BG	Compressive modulus in trabecular bone range	(Petretta et al., 2021)
	PCL/45S5	Best cell activity with 1% BG content	(Daskalakis et al., 2022)
Direct ink writing (DIW)	Pluronic F-127/ PSrBG Pluronic F-127/ ICIE16 Pluronic F-127/ 13-93	Improved sintering of low-silica BG with larger particle size	(Nommeots-Nomm et al., 2018)
	Carboxymethyl cellulose/HSSGG	High compressive strength for Cu-doped BG	(Ben-Arfa et al., 2019a)
	Carboxymethyl cellulose /45S5	Improved mechanical properties after nanocomposite coating	(Motealleh et al., 2017a, 2017b)
	Pluronic F-127/47.5B	Failed attempt to produce a porosity gradient	(Barberi et al., 2019)
	PCL-PGS/BG	Elastic modulus in ligament range	(Touré et al., 2020)
	Ethyl cellulose/13-93 Ethyl cellulose/13-93B3	Superior stability of silicate glass in SBF	(Deliormanli and Rahaman, 2012)

	Pluronic F-127/47.5B	More homogeneous tissue formation of scaffold compared to granules	(Tulyaganov et al., 2022)
	Pluronic F-127/ 13-93	From brittle to elasto-plastic response after implantation in vivo	(Liu et al., 2013)
	Chitosan/BG	Positive *in vitro* results	(Dorj et al., 2012)
	PCL/BG Silk fibroin/BG	Best results for SF/BG scaffold	(Du et al., 2019)
	PLA/13-93B3	Death of cells in the bottom layer	(Kolan et al., 2020)
	PVA/BG	Reduced inflammatory response for DEX-doped scaffold	(Wu et al., 2011; J. Zhang et al., 2014)
Stereolithography (SLA)	PCL/S53P4	Optimized exposure of BG particles on surface	(Elomaa et al., 2013)
	Acrylic resin/BG	Improved stability, mechanical properties, and architecture with PEG-200	(Chen et al., 2022)
	Acrylic resin/45S5	Optimized BG suspension	(Kang et al., 2020)
	Acrylic resin/45S5	Increased mechanical properties with partial pre-sintering	(Thavornyutikarn et al., 2017)
Digital light processing (DLP)	Silicone/WB	Successful production of silica defective BG scaffold	(Elsayed et al., 2020)
	Silicone/Biosilicate	Fine-tuned microstructure	(Dogrul et al., 2021)
	Acrylic resin/BG	Identified a limit on BG content	(Vyas et al., 2022)
	Acrylic resin/AP40mod	Successful reconstruction in vivo	(Xu et al., 2020)
Selective laser sintering (SLS)	PDLLA/58S	Optimized the production of scaffold for non-load bearing application	(Do Vale Pereira et al., 2014)
	PLLA/BG	Improved regeneration for high content of DEX	(Sun et al., 2020)
	PGA-PLLA/mesoporous BG	Antibacterial scaffold with good mechanical properties	(Shuai et al., 2019)
	PLGA/45S5	Produced multi-graded scaffold with poor mechanical properties	(Karl et al., 2019)
	PCL/Borate BG	Optimized the process for borate BG	(Han et al., 2023)

Table 8. *List of bioactive glass and their main characteristics.*

Bioactive glass	Characteristics	Reference
45S5	Silicate Best biological properties	(Hench et al., 1971; Jones, 2013)
S53P4	Silicate Antibacterical properties	(Drago et al., 2013)
13-93	Silicate Large working range	(Brink, 1997)
13-93B3	Borate High degradation rate	(Fu et al., 2010)
58S	Silicate Alkali free Sol-gel	(Li et al., 1991)
ICIE16	Mixed alkali silicate glass	(Elgayar et al., 2005)
HSSGG	High silica content Sol-gel	(Ben-Arfa et al., 2019a)
47.5B	Silicate Large working range	(Barberi et al., 2019; Tulyaganov et al., 2022)
WB	Borosilicate	(Elsayed et al., 2019)
Biosilicate	Silicate Fair machinability	(Crovace et al., 2016)
AP40mod	Silicate TiO2 containing	(Xu et al., 2020)
BGMS10	MgO, SrO containing Ultra-high crystallization temperature	(Bellucci and Cannillo, 2018)

Fused deposition modeling (FDM)	Tuneable mechanical properties Tuneable hydrophilicity Versatility	Resolution limited by nozzle and viscosity Inadeguate for cell/bioactive molecules
Powder extrusion deposition (PED)	Granules feedstock Versatility	Low mechanical properties
Direct ink writing (DIW)	Bioprinting Overcome sintering issue	Challenging optimization of microstructure and mechanical properties
Stereolithography (SLA)	High resolution Bioprinting	Slow speed Limited research available for in vivo application.
Digital light procesing (DLP)	High resolution Versatility	Challenging optimization of mechanical properties
Selective laser sintering (SLS)	Enhanced interface control Tuneable degraation rate Drug delivery	Low mechanical properties

Figure 41. *Pros and cons of AM technique for scaffold production*

3.1.4. Conclusions

In conclusion, the field of TE has made significant progress since its inception. The discovery of BGs and their ability to stimulate the formation of new tissue has opened up a range of possibilities, particularly when combined with polymers to create composites with superior mechanical and biological properties. AM has shown great potential for scaffold fabrication, enabling the creation of structures with intricate designs and tailored properties for specific tissues. Nonetheless, there are still challenges that need to be addressed, such as optimizing scaffold design and fabrication processes and evaluating their long-term safety and efficacy in clinical settings.

However, the integration of machine learning and artificial intelligence offers promising solutions to these challenges. Machine learning algorithms can analyse vast datasets and unveil intricate patterns, providing valuable insights into the complex interactions between scaffold materials, cell behaviour, and tissue regeneration. This integration holds tremendous potential for advancing tissue engineering and optimizing scaffold production. By leveraging machine learning, researchers can expedite the design process, predict scaffold properties, and accelerate the screening of various design possibilities, thus reducing time and costs associated with trial-and-error experiments. Additionally, machine learning can aid in the evaluation of scaffold performance, safety, and personalized treatment recommendations. In summary, the combination of TE, BGs, AM, and machine learning represents a powerful synergy that can revolutionize regenerative medicine. Further research and development are

necessary to overcome existing challenges and fully harness the potential of these technologies. By doing so, we can pave the way for innovative approaches that drive tissue engineering to new frontiers, ultimately benefiting patients and transforming healthcare practices.

3.2. Mechanical, Computational, and Biological Evaluation of 3D-Printed PLA-Bioglass Scaffolds for Bone Tissue Regeneration

(This section is currently under review as: Martelli, A.; Bellucci, D.; Nobili, A.; Tian, L.; Nawaz, Q.; Boccaccini, A.; Cannillo, V. Mechanical, Computational, and Biological Evaluation of 3D-Printed PLA-Bioglass Scaffolds for Bone Tissue Regeneration.)

N.B. The introductory section is an updated and revised version of the article submitted. The changes concern the introduction only, aimed at avoiding repetition and ensuring consistency with the preceding chapters.

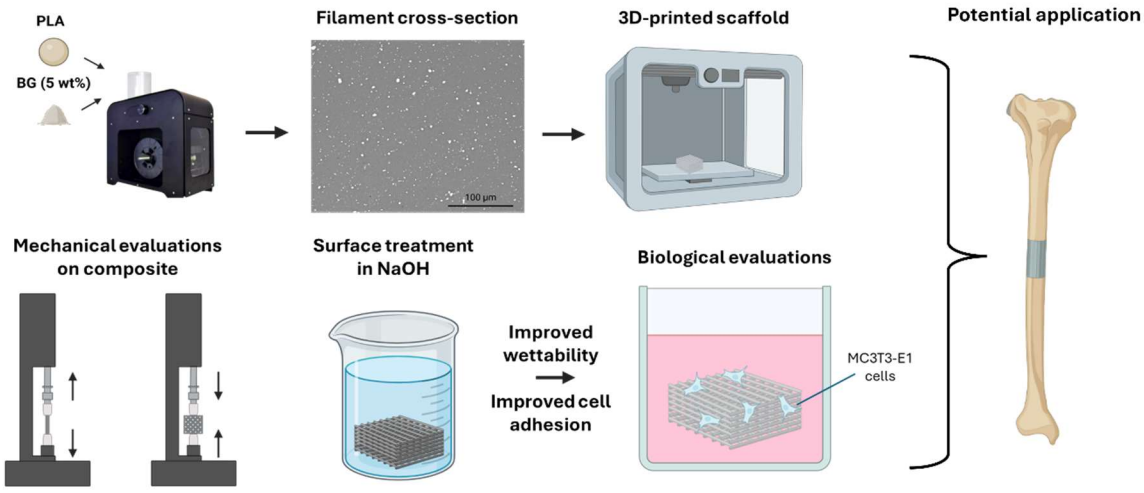

Figure 42. *Graphical abstract*

3.2.1. Introduction

Additive manufacturing (AM) ranks among the most promising approaches to produce scaffolds, thanks to the high reliability of the samples obtained and the greater design freedom it offers (Martelli et al., 2023). Within AM, fused deposition modelling (FDM) has emerged as a fabrication technique for scaffold production. FDM enables solvent-free, high-throughput printing of complex, patient-specific architectures (Alksne et al., 2020; Distler et al., 2020). Several polymers can be used in FDM printing, and some of them are approved for *in vivo* use. Among them, polylactic acid (PLA) is a biocompatible, biodegradable medical-grade thermoplastic polymer widely adopted in bone tissue engineering. Additionally, its relatively high elastic modulus and low elongation at break make PLA a good choice for bone substitution (Alksne et al., 2020; Scaffaro et al., 2016). However, the use of PLA exhibits some drawbacks. It has a relatively hydrophobic nature, resulting in water contact angle in the range between 75° and 85°, which may result in poor cell affinity,

slow degradation in aqueous media, and, in some cases, inflammatory responses from periprosthetic tissue (Alam et al., 2024; Baran and Yildirim Erbil, 2019; Burg et al., 1999; Distler et al., 2020; Fuse et al., 2024; Ratner, 1995; Schneider et al., 2020; Shi et al., 2023). In fact, cell adhesion and proliferation are influenced by the physical properties of the implanted material, such as surface wettability and bulk mechanical properties; by surface morphological characteristics, such as roughness and microporosity; and by chemical properties, including surface energy, surface charge, and surface-bound molecules (Cai et al., 2020).

To enhance PLA surface cell affinity, various treatments can be applied either to the bulk material – before or during polymerization, for example through blending or physical/chemical modification – or to the surface, such as by coating, photo-grafting, or chemical modification (Baran and Yildirim Erbil, 2019; Rasal et al., 2010), with the latter approaches directly modifying the final sample. An effective and simple way to modify PLA's surface wettability and roughness is through alkaline hydrolysis of the surface (Schneider et al., 2020; Shi et al., 2023). Unlike other techniques, alkaline hydrolysis is a green, low-cost, and scalable process. This method involves the use of a strong alkali solution, such as NaOH or KOH, to degrade the PLA surfaces. This approach introduces hydrophilic functional groups (–COOH and –OH) on the PLA surface by cleaving the ester bonds of the aliphatic polyester (Fuse et al., 2024; Wang et al., 2005). Moreover, these functional groups can improve the attachment and proliferation of osteoblast-like cells (Chang and Wang, 2011; Metwally and Stachewicz, 2019; Schnabelrauch et al., 2014).

To further tailor its mechano-biological response, PLA can be combined with a ceramic phase (Alam et al., 2024; Bernardo et al., 2022; Ding et al., 2022; Distler et al., 2020; Martel-Estrada et al., 2017). Among bioceramics, BGs have attracted particular attention because their composition and amorphous nature enable them to readily interact with biological tissue, thereby promoting osteogenesis (Hench et al., 1971; Hench and Jones, 2015). Notable examples include 45S5 Bioglass® (Hench et al., 1971), the first BG discovered, and S53P4 Bonalive® (Hanna Arstila et al., 2008), both commercially available and widely used in orthopaedic and dental applications. Furthermore, the physical and biological properties of BGs can be tuned by incorporating specific ions into their composition (Hoppe et al., 2011; Pantulap et al., 2022; Rabiee et al., 2015).

The combination of BG and PLA may help preventing inflammatory reactions while promoting a more favourable cellular environment by buffering the acidic degradation

products of PLA with the basic degradation of BG (Sultan et al., 2022). However, achieving a uniform dispersion of BG within the PLA matrix and obtaining a composite scaffold with BG exposed on the surface remains challenging when using a solvent-free approach (Distler et al., 2020). Alkaline hydrolysis, acting on the surface, may facilitate the exposure of BG particles.

This work aims to investigate the combined use of PLA+BG composite scaffolds produced by FDM and alkaline hydrolysis to improve cell adhesion and proliferation. Specifically, four different BG compositions are considered, namely 45S5, S53P4, alongside two novel BG materials, that are derived from these commercial formulations, which are named 45S5_MS and S53P4_MS. These novel BGs have been previously studied in detail and have shown good *in vitro* cell viability (Bellucci et al., 2024). Such composite materials are analysed in terms of physical and mechanical properties, while scaffold specimens are characterized both biologically and mechanically.

3.2.1. Materials and methods

PLA+BG composite filament: production

Composite filaments were manufactured mixing PLA, serving as the bulk matrix material, and BG powders (5 wt%), serving as filler. PLA was purchased in granules form (PLA, 3Devo, Netherlands). BGs were produced using a well-established melt-quenching method (Bellucci et al., 2024). The composite was manufactured as follows: all reagents (Carlo Erba Reagenti, Rodano-Milano, Italy) were accurately weighed and mixed for 2 h in a laboratory rotary mixer. The mixture was melted in a platinum crucible following this thermal treatment: heating from room temperature to 1100 °C at 10 °C/min; holding at 1100 °C for 1.5 hours for decarbonation; then heating to 1450 °C at 10 °C/min and maintaining at 1450 °C for 1 hour to obtain a homogeneous melt. The molten glass was then quenched in water to achieve rapid cooling, resulting in the formation of a frit. The frit was dried at 110 °C for 12 hours. Each frit was grinded in a porcelain jar (PM100, Retsch, Germany) and particle size was evaluated by laser scattering analysis (Zetasizer Nano ZS90 - Malvern). Glass compositions are detailed in **Table 9**.

Table 9. *Bioactive glass compositions in mol%.*

	Na_2O	CaO	MgO	SrO	P_2O_5	SO_2
45S5	24.4	26.9			2.6	46.1
S53P4	53.8	22.7			1.7	53.8
45S5_MS	46.1	9.4	5	10	2.6	46.1
S53P4_MS	53.8	7.7	5	10	1.7	53.8

In order to obtain a filament with constant diameter and homogeneously dispersed BG particles, a solvent-free method was used (Distler et al., 2020). To prevent BG powder agglomeration, the BGs were sieved through a 63 μm mesh and treated with an anti-static ionizer (STABLO-AP, Shimadzu Cooperation, Japan) before mixing with PLA. Then, PLA – BG (5 wt%) mixtures were rotationally mixed at 60 rpm for 30 min. Additionally, to reduce the moisture content, the mixed raw materials were thermally treated at 60 °C for 24 hours prior to extrusion. The resulting composite mixture was introduced into the hopper of a desktop filament extruder (Filament Maker ONE, 3Devo, Netherlands). To prevent heat-related material agglomeration, the material was fed in small portions, typically ranging from 10 to 20 grams, thereby reducing the time it spent in the hopper. This helped maintain consistent material quality. During the extrusion process, the extrusion screw was consistently covered with layers of PLA+BG to ensure a steady intake of material. Cooling fans on the extruder were activated as soon as the filament reached a diameter of 1 mm. Once a stable target diameter was achieved, the filament was wound onto a spool. Filaments diameters were then measured with a digital calliper, yielding a diameter of 1.75 ± 0.15 mm, considered suitable for the final scaffold printing. Between each filament production cycle, the extruder was purged using high molecular weight polyethylene (HMWPE, 3Devo, Netherlands) cleaning polymer to ensure that any residues from the previous run were removed.

The extruder is equipped with four heaters whose working temperature, after some optimization, was setas follows: heaters 4 to 1 were maintained at 170, 190, 185, and 170°C, respectively, with heater 4 positioned closest to the hopper and heater 1 nearest to the extrusion nozzle. The screw speed was set at 3.5 rpm, while the fan speed was adjusted to 70% of the extruder's maximum fan speed. For comparison, a pure PLA filament was produced following the same protocol.

Materials characterization

Filament morphology and BG particle distribution within the filament were evaluated by scanning electron microscopy (SEM) (Quanta 2000, FEI Co., Eindhoven, The Netherlands) on the cross-section of the filaments. To measure the real volumetric fraction of BG inside the composite filaments, the acquired images of the filament cross-section were analysed with the public domain software ImageJ.

Additionally, the following formula were used to calculate the theoretical volumetric fraction, starting from the composite constituents' densities:

$$\rho_C = \frac{1}{\frac{W_m}{\rho_m} + \frac{W_f}{\rho_f}}$$

$$V_f = \frac{\rho_c}{\rho_f} \times W_f$$

where ρ represents the density, W denotes the mass fraction, and V corresponds to the volume fraction. In this context, the subscripts *c, m,* and *f* refer to the composite, matrix, and reinforcing fraction, respectively. PLA true density was measured on PLA pellets prior to extrusion by hydrostatic balance (E42S, Gibertini, Italy) with deionized water at 27 °C as the immersion medium. Conversely, the density of the BG powders was measured using a gas pycnometer (AccuPyc II 1340, Micromeritics Instrument Corp., Norcross, GA, USA). Helium with a total purity >99.999% mol was used as the dispersion medium. For the calculation of composite density, an average value for BG density was considered.

To characterize both extruded materials from a mechanical standpoint, dog-bone specimens have been FDM-printed with the geometry shown in **Figure 43**. This specific geometry was selected to ensure a smooth transition from the gripping area to the testing area and therefore induce failure in the mid-section. The geometry was designed using computer aided design (CAD) software (Solidworks, Dassault Systèmes, USA) and sliced using a computer-aided manufacturing (CAM) software (Intamsuite Neo, Intamsys Technology, Ostfildern, Germany).

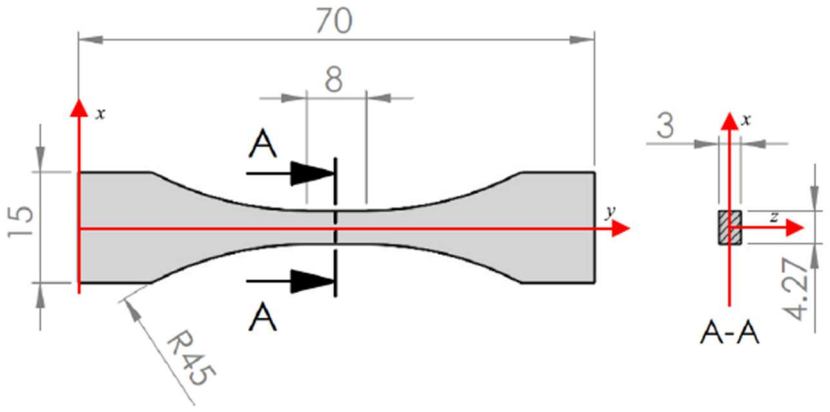

Figure 43. *Dog-bone specimens for mechanical characterization in traction*

Five dog-bone specimens, both of PLA and PLA+BG, were printed by FDM printer (Funmat Pro 310 Neo, Intamsys Technology, Ostfildern, Germany) equipped with a 400 µm diameter nozzle. To assess the presence of porosity within the dog-bone sample, the apparent density was measured using a hydrostatic balance with deionized water at 27 °C as the immersion medium. Then, the porosity was evaluated with the following formula:

$$Porosity = 1 - \frac{\rho_{app}}{\rho_{true}}$$

The hydrophilicity of PLA and PLA+BG samples was assessed using an Optical Contact Angle (OCA) system (Dataphysics, Filderstadt, Germany) with 2× magnification optics using 2 µl water droplets. Images and data were acquired via SCA20 software (Dataphysics, Filderstadt, Germany). To modify hydrophilic behaviour, a property closely linked to biological response, samples were treated with 1 M NaOH for 30, 60, 90, and 120 minutes. Changes were evaluated by OCA, with ten measurements for sample.

Mechanical properties were tested under displacement control at 0.25 mm/min using a universal testing machine (UTM) (ProLine Z50, ZwickRoell, Ulm, Germany) equipped with a 10 kN load cell and wedge grips. Since the gauge length is 8 mm, traction occurs at 0.52 mstrain/s. A digital image correlation system (DIC) monitored the test using a digital camera (U3-31N0CP-M-GL, IDS, Obersulm, Germany) operating at 1 fps equipped with a LED light source (Fiber Lite Mi-LED A2, Dolan-Jenner Industries, USA): the test setup is shown in **Supplementary 3**. DIC frames were synchronized with the UTM displacement data, allowing each frame to be matched to a specific crosshead displacement and corresponding load cell force.

Poisson's ratio was evaluated through the definition:

$$\nu = -\frac{\varepsilon_x}{\varepsilon_y}$$

where ε_x and ε_y are the transverse and longitudinal strain, respectively. Poisson's ratio was determined experimentally for each specimen at each DIC frame (corresponding to a specific time) within a reasonable time interval near, but not including, the origin – thus ensuring that linear deformations could still be assumed while excluding the initial setup adjustment phase (Volpini et al., 2022).

Young's modulus (E) was calculated from the stress-strain curve obtained by DIC integration, which is far more representative of the real specimen response and gets away with the short flat (i.e. constant stress) stage that appears in the UTM stress-strain curve as a result of the gripping system adjustment. Stress is obtained from load data assuming a specimen cross section area of 12.81 mm^2. From the Young's modulus and Poisson's ratio, the shear modulus (G) and the linear bulk modulus (K) could be calculated according to the following equations, valid for isotropic materials:

$$G = \frac{E}{2(1-\nu)}$$

$$K = \frac{E}{3(1-2\nu)}$$

From the stress-strain curve, it is possible to deduce the non-linear moduli, in particular the neo-Hookean modulus. To this aim, a finite elements (FE) analysis was carried out (Volpini et al., 2022). For a neo-Hookean material, the stored elastic energy is given by:

$$W = C_{10}(I_1 - 3) + D_1(J-1)^2$$

where I_1 is the first invariant (the trace) of the Cauchy-Green deformation tensor C, and J its determinant. For consistency with linear elasticity, it is required that:

$$C_{10} = G/2, \qquad D_1 = 2/K$$

Thus, the model is fully defined from the linear moduli.

Scaffold production and characterization

The scaffold was designed with CAD software and printed by FDM. To allow an effective cell infiltration, the scaffold had interconnected open porosity with a pore size of 600 µm, resulting in a surface area to volume ratio (SA:V) of 5.65 mm^{-1} (Bose et al., 2012; Khoshgoftar and Ansari, 2024).

Scaffolds mechanical properties were evaluated under compression using displacement control at 0.25 mm/min, equal to 0.42 mstrain/s, with a UTM equipped with a 10 kN load cell and compression plates. DIC system was also employed during the test.

Before biological evaluation, scaffolds were treated for one hour in 1 M NaOH, as suggested by the contact angle results, to enhance cell attachment.

In vitro cytocompatibility of treated scaffolds was evaluated using a WST-8 cell viability assay. MC3T3-E1 pre-osteoblasts (passage 9, Sigma-Aldrich) were used as the model cell line. Prior to cell seeding, scaffolds were sterilized under UV light for 1 h. Cells were cultured in α-MEM (Gibco), supplemented with 10% fetal bovine serum (FBS; Sigma-Aldrich), 1% penicillin–streptomycin, and 1% glutamine. A total of 1×10^5 cells were seeded directly onto each scaffold and incubated under physiological conditions (37 °C, 5% CO_2) for 1 and 7 days. Cell viability was quantified through the WST-8 assay according to the manufacturer's instructions. After each time point, cells were stained with Calcein-AM and DAPI (Life Technologies), followed by fluorescence microscopy imaging (Axio Scope A.1, Carl Zeiss) to observe cell attachment and morphology. All experiments were performed with $n \geq 3$ samples and reported as mean ± standard deviation. Statistical differences between groups were assessed through one-way ANOVA test.

3.2.3. Results and discussion

Materials characterization

The densities of bioactive glass powder were as follows: 45S5, 2.687 g/cm^3; S53P4, 2.621 g/cm^3; 45S5_MS, 3.015 g/cm^3; S53P4_MS, 2.897 g/cm^3. These results are consistent with those obtained for similar BG compositions (Chen et al., 2006; Martelli et al., 2024; Massera and Hupa, 2014). An average BG powder density of 2.805 g/cm^3 was considered, resulting in a composite density of 1.288 g/cm^3. Based on these values, the theoretical volumetric fraction of BG was calculated to be 2.3%. In contrast, the volumetric fraction measured by image analysis of the filament-cross section was 1.72 ± 0.37%, corresponding to a relative error of 25.1%. This discrepancy between the theoretical and measured values may be attributed to the tendency of BG powder to form agglomerates, as previously reported and linked to residual surfaces charges (Ajita et al., 2015; Valenzuela et al., 2012), or to its adhesion to the extruder screw and barrel.

Density measurements on the dog-bone specimens revealed a discrepancy between the theoretical bulk material density and the actual specimen density. Specifically, the printed

PLA and PLA+BG specimen density appeared 2.4% and 6.5% lower than the corresponding theoretical value, respectively. This reduction in density can be attributed to the presence of internal pores introduced during the FDM printing process. In **Table 10** the density and porosity values measured on dog-bone samples are summarized.

Table 10. *Density and porosity values measured on dog-bone samples.*

Sample	True density	Apparent density	Porosity
PLA	1.2524 g/cm^3	1.2226 g/cm^3	2.4%
PLA+BG	1.2880 g/cm^3	1.1958 g/cm^3	6.5%

Contact angle analysis, reported in **Figure 44**, highlighted a slight beneficial effect of BG addition in PLA matrix in terms of hydrophilicity, consistent with the findings of Bernardo et al. (Bernardo et al., 2025). This effect may result from surface modifications of the material and the formation of strongly polar areas due to the presence of BG particles on the surface (Bernardo et al., 2025; Mousa et al., 2018). Moreover, results showed an effective reduction of contact angle for PLA when the alkaline treatment is applied. This is in agreement with literature and can be related with the presence of carboxyl and hydroxyl groups on the surface of the sample, known to improve the wettability (Fuse et al., 2024; Jaidev and Chatterjee, 2019; Schneider et al., 2020). Interestingly, NaOH treatment on PLA+BG samples showed little to none effects up to 120 minutes. This behaviour may be explained by the presence of BG particles already exposed on the surface of untreated samples and by the progressive exposure of additional BG particles only after longer etching times, consistent with the non-linear relationship between etching and time (Schneider et al., 2020). Based on these findings, a 1 h treatment was deemed sufficient and selected to improve scaffold wettability.

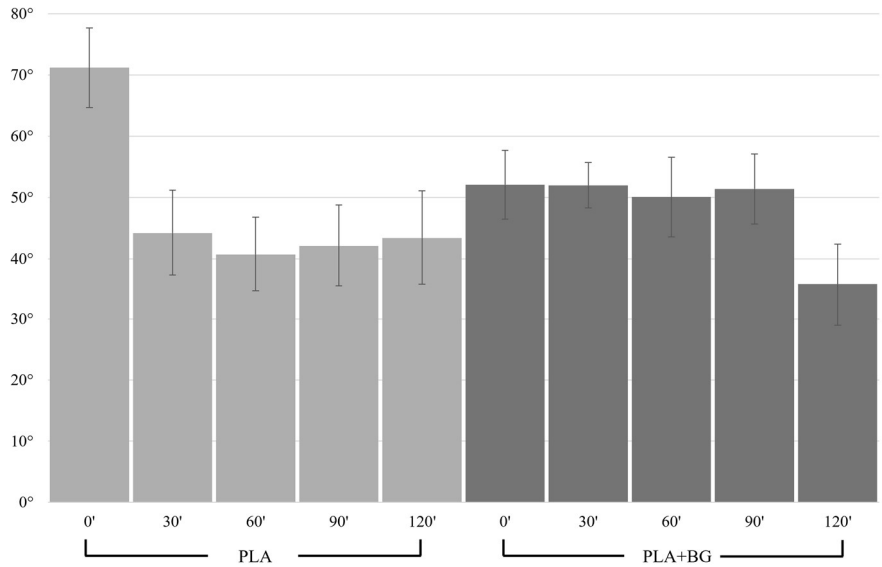

Figure 44. *Contact angle measurements of PLA (light grey) and PLA+BG (dark grey) samples treated in NaOH 1M for 0, 30, 60, 90, 120 minutes.*

The results of Poisson's ratio evaluation at each DIC frame are reported in **Figure 45**, alongside the regression line. As expected, the measured Poisson's ratio is almost time independent, as data points fluctuate only slightly and cluster around a stable mean, resulting in an almost flat regression line. Interestingly, Poisson's ratio is 53% higher for PLA+BG specimens compared to PLA specimens, increasing from 0.17 to 0.26. This is not surprising, considering the filling effect of the BG particles, which shifts the mechanical response towards the incompressibility limit, $\nu = 0.5$.

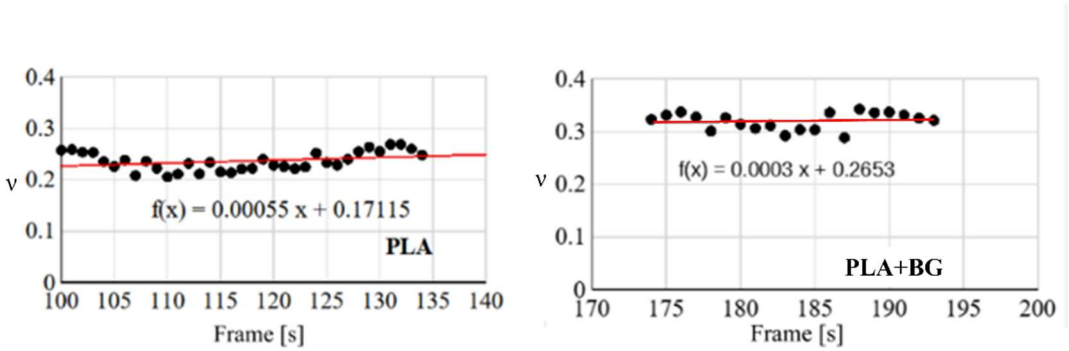

Figure 45. *Poisson ratio for a typical PLA (left) and PLA+BG (right) specimen at different times (frames) and regression line which shows that the result is almost independent of time, at least for moderate strain*

Table 11 reports the mean and the coefficient of variation (*CoV*) of the Poisson's ratio and the Young's modulus for PLA and PLA+BG samples, together with the corresponding shear and bulk moduli. Results are on the high end of the range that appears in literature, which generally reports slightly lower values for the Young's modulus compared to those

obtained here (Grasso et al., 2018; Marșavina et al., 2022; Raj et al., 2018; Wang et al., 2019). This discrepancy highlights the variability in mechanical properties introduced by the 3D printing process, mainly due to printing orientation or pore formation (Marșavina et al., 2022; Wang et al., 2019). Accordingly, it is of paramount importance to experimentally assess material constants rather than relying solely on literature data.

Table 11. *Poisson's ratio, ν, Young modulus, E, shear modulus, G, and bulk modulus, K, for PLA and PLA+BG specimens and their statistical significance.*

Sample	ν	CoV (%)	E (MPa)	CoV (%)	G	K
PLA	0.232	5.03	3934	8.27	1596	2446
PLA+BG	0.322	5.97	4591	7.40	1736	4299

Strength curves in terms of crosshead travel are plotted in **Supplementary 4** for the PLA and PLA+BG groups, each accounting for 5 specimens. The DIC analysis reveals that the crosshead travel is in-line with the imposed displacement rate, with the extension of the wedge grips taking place at the beginning of the test and accounting for the flat part of the strength curve in **Supplementary 4**. Through DIC, the crosshead displacement can be directly related to the effective strain in the specimen (specifically in the mid-section), from which the nominal stress–strain curve can be deduced. This provides a more realistic representation of the material behaviour. **Figure 46** compares the stress-strain curve for a typical PLA specimen and a PLA+BG specimen. In this representation, the plateau observed in the strength curve disappears, and the Young's modulus can be readily obtained by taking the secant modulus of this curve and dividing by the specimen cross-section (A = 12.81 mm^2).

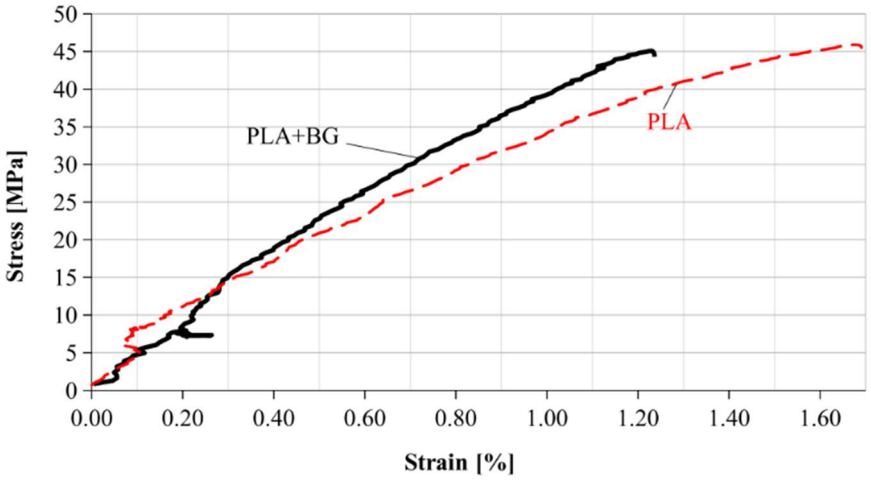

Figure 46. *Stress-strain curve for PLA (red, dashed) and PLA+BG (black, solid) typical specimens. It is seen that the curves are similar and that the plateau, that is present in Suppl. 2 and reflects the action of the grips on the specimens, disappears because grip action does not affect the gauge material*

The ultimate failure strain for PLA was experimentally measured at approximately 2.34%, although this value is highly dependent on position, the presence of defects, and the proximity to failure. Similarly, PLA+BG exhibited an ultimate failure strain of 2.30%. It is important to note that this is a pointwise assessment and does not correspond to the strain obtained by averaging over the gauge length, which is used on the abscissa in **Supplementary 4**. **Figure 47** shows the strain field just prior to failure, indicating that both PLA and PLA+BG fail at nearly the same location near the mid-section, well outside the gripping area.

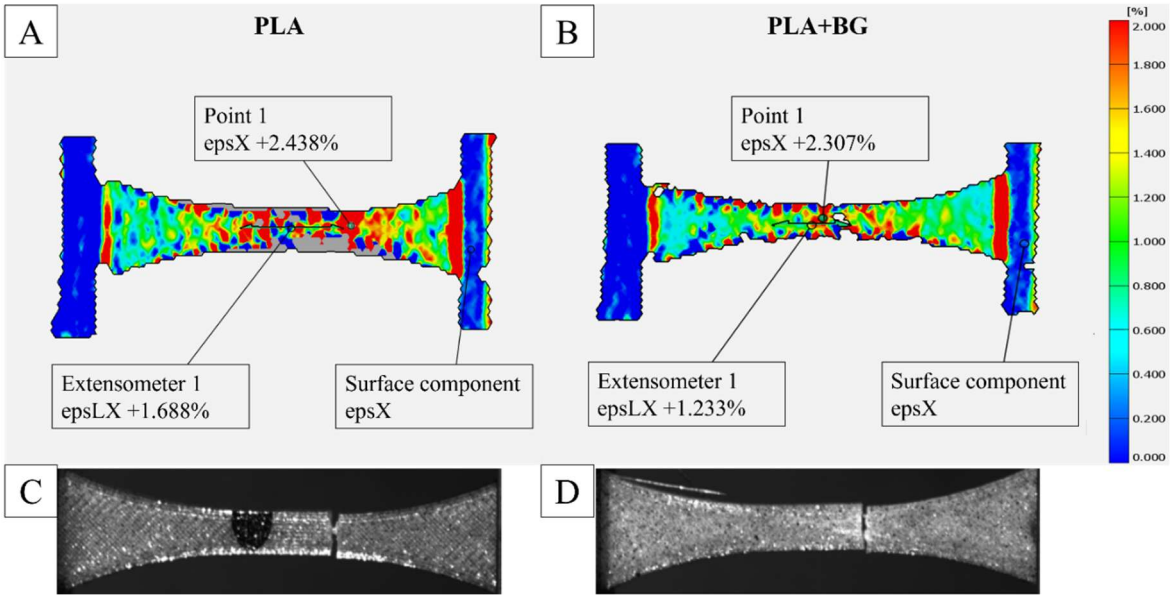

Figure 47. *Strain field for a typical specimen of A) PLA and B) PLA+BG on the verge of failure. Failure in C) PLA and in D) PLA+BG occurs in almost the same location near mid-section.*

Table 12 summarizes the corresponding values derived from the strength curves and reveals that, as expected, ultimate values generally underestimate the point-wise values obtained by DIC. Nevertheless, the greater brittleness of PLA+BG compared to PLA is confirmed, while the UTS remains nearly identical for both groups. This increased brittleness prevents the PLA+BG specimens from reaching the same ultimate force as PLA. Notably, the UTS values are consistent with those reported in the literature (Grasso et al., 2018; Marșavina et al., 2022; Raj et al., 2018; Tanveer et al., 2019).

Table 12. *Ultimate Tensile Elongation (UTE) and Stress (UTS) for PLA and PLA+BG together with mean, standard deviation and coefficient of variation (CoV).*

Sample	UTE (%)	CoV (%)	Force (N)	CoV (%)	UTS (MPa)	CoV (%)
PLA	1.72 ± 0.20	11.62	565 ± 17	3.08	44.83 ± 1.37	3.05
PLA+BG	1.41 ± 0.11	7.79	575 ± 3.82	0.66	44.89 ± 0.30	0.66

According to the FE model, as shown in **Figure 48**, the stress-strain response becomes a line that well represents the behaviour for small strain values but fails to capture the downturn observed in the experimental curve. Upon reaching the ultimate force of 600 N, the model correctly predicts a UTS of 43 MPa but underestimates the longitudinal displacement, predicting 0.48 mm instead of the expected 0.9 mm. Adopting the Mooney–Rivlin material does not provide much improvement.

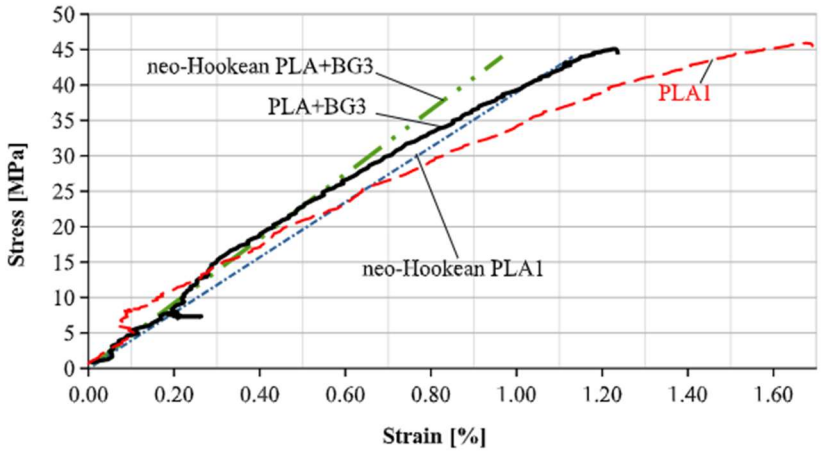

Figure 48. *Stress-strain curve for PLA1 (red, dashed) and PLA+BG3 (black, solid) specimens and FE curve obtained with the neo-Hookean material model.*

Scaffold characterization

Scaffold compression tests showed different failure mode for PLA and PLA+BG scaffolds. **Figure 49 (a-d)** illustrates the progression to failure of PLA scaffolds, which fail by cell buckling along the weakest planes, leading to catastrophic instability. The overall process occurs in several steps, requiring sufficient damage accumulation to produce a pair of sliding planes. In contrast, PLA+BG scaffolds fail suddenly through catastrophic material failure, as shown in **Figure 49 (e-g)**: the material reaches the critical strain simultaneously over a large volume, causing the specimen to fracture and resulting in immediate loss of integrity. Overall, the results confirm that PLA+BG is considerably more brittle and weaker than PLA.

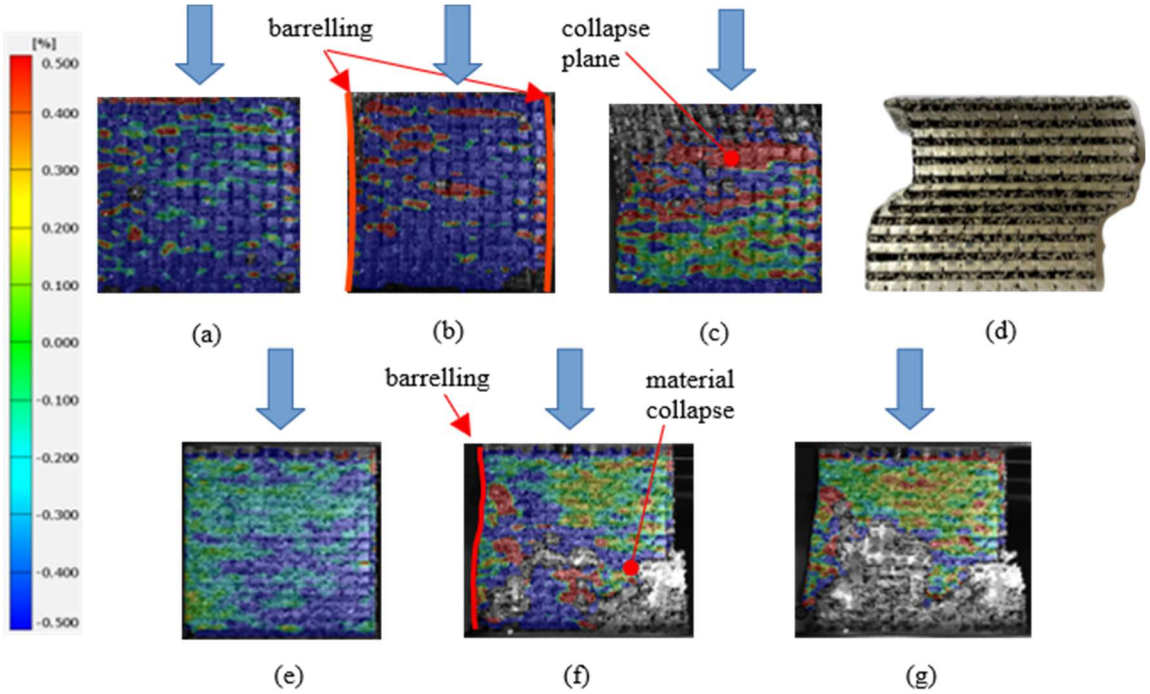

Figure 49. *Scaffold progression to failure in compression. PLA scaffold (a) initial stage, almost homogeneous strain distribution, (b) specimen barrelling and strain localization, (c) strain concentration and consequent loss of stability, (d) collapsed shape. PLA+BG scaffold (e) initial stage, homogeneous strain distribution, (f-g) material catastrophic failure in the lower bulk of the scaffold and general collapse.*

Table 13 reports the ultimate failure force (F_u), stress (σ_u) and strain (ε_u) for PLA and PLA+BG samples. The brittle response of the composite system compared to PLA is evident. PLA scaffolds fail consistently at a mean force over six times greater than that required to collapse PLA+BG scaffolds. Similarly, PLA fails at a strain level 2.5 times higher than that of PLA+BG, with yet comparable data scattering. The latter, however, is significantly higher than in the case of force, that is usually the case for strain. These findings are aligned with the literature (Distler et al., 2020; Marianna et al., 2016): a similar trend in strength with the addition of BG was observed by Distler et al. (Distler et al., 2020), who reported lower compressive strength at higher BG content. These results suggest that, at this BG content, the particles did not reinforce the PLA matrix but instead acted as stress-concentration points.

Table 13*. Failure compressive force, stress, strain for PLA and PLA+BG scaffold.*

Sample	F_u (N)	σ_u (MPa)	CoV (%)	ε_u (%)	CoV (%)
PLA	5169 ± 386	12.92 ± 0.97	7.47	10.21 ± 2.73	26.76
PLA+BG	699 ± 70	1.75 ± 0.18	9.98	3.60 ± 0.38	10.51

The cytocompatibility of the PLA and PLA–bioactive glass composite scaffolds (45S5, S53P4, 45S5_MS, and S53P4_MS) was evaluated through WST-8 assay and fluorescence microscopy. **Figure 50** shows the cell viability, expressed as percentage, of MC3T3-E1 cells

on the scaffolds after 1 and 7 days of incubation in cell culture medium. As shown in the viability graph, all scaffold types supported cell survival at both time points, confirming that neither the PLA matrix nor the incorporated BG particles induced cytotoxic effects (Bernardo et al., 2022; Distler et al., 2020; Wang et al., 2021). After 1 day, cell viability levels were comparable across all groups, suggesting that the surface-treated scaffolds provided sufficiently favourable initial adhesion conditions regardless of glass type. However, after 7 days, cell viability slightly decreased but remained within an acceptable range (>70 %); nevertheless, the release of toxic by-products cannot be excluded. Among the BG-containing scaffolds, those incorporating S53P4 displayed slightly higher metabolic activity relative to 45S5-based composites, which is consistent with the known ion-release behaviour of S53P4 and its ability to create a moderately alkaline microenvironment beneficial for osteoblastic activity (Björkenheim et al., 2021). This trend agrees with the material characteristics described in the paper, where surface-exposed BG particles and NaOH-induced hydrolysis improved hydrophilicity and introduced –COOH/–OH groups that enhance cell affinity of PLA-based scaffolds.

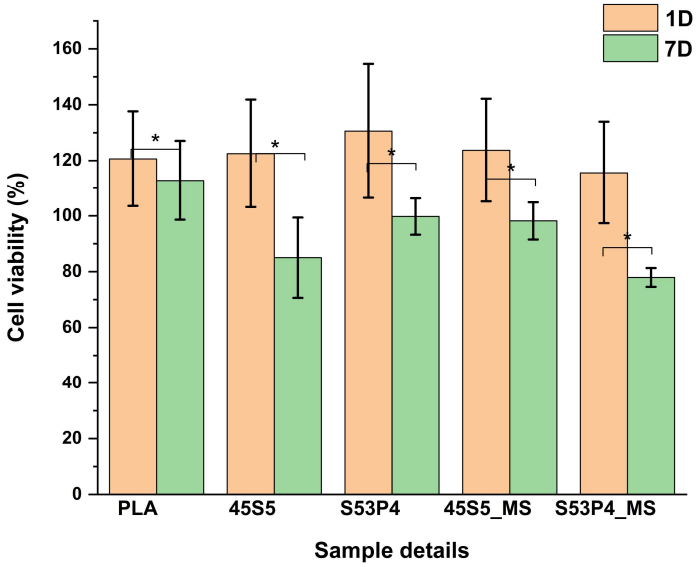

Figure 50. *WST-8 cell viability at 1 and 7 days for scaffolds treated for 1 h in 1 M NaOH.*

Fluorescence microscopy further supported the WST-8 results. Calcein-AM staining showed abundant viable cells adhering and spreading on all scaffold types, while DAPI revealed well-distributed nuclei across the filament surfaces and within the pore architecture (**Figure 51**). Cells displayed elongated morphologies, suggesting active cytoskeletal organization and stable attachment, particularly on BG-containing scaffolds where the rougher, partially etched surfaces and exposed glass particles provide micro-scale anchoring

sites. The modified-glass scaffolds (45S5_MS and S53P4_MS) exhibited especially dense and well-spread cell populations, which aligns with previous observations that Mg- and Sr-containing BGs promote osteoblastic proliferation through controlled ionic dissolution and enhanced surface reactivity (Isaac et al., 2011; Moghanian et al., 2018; Schmitz et al., 2020). Overall, the results confirm that surface-treated PLA and PLA+BG scaffolds are non-cytotoxic and promote early cell adhesion and proliferation, with S53P4- and S53P4_MS-containing scaffolds showing the most favourable biological response. These findings highlight the synergistic effect of alkaline surface modification and bioactive glass incorporation in improving the biological performance of FDM-printed PLA scaffolds intended for bone tissue engineering applications.

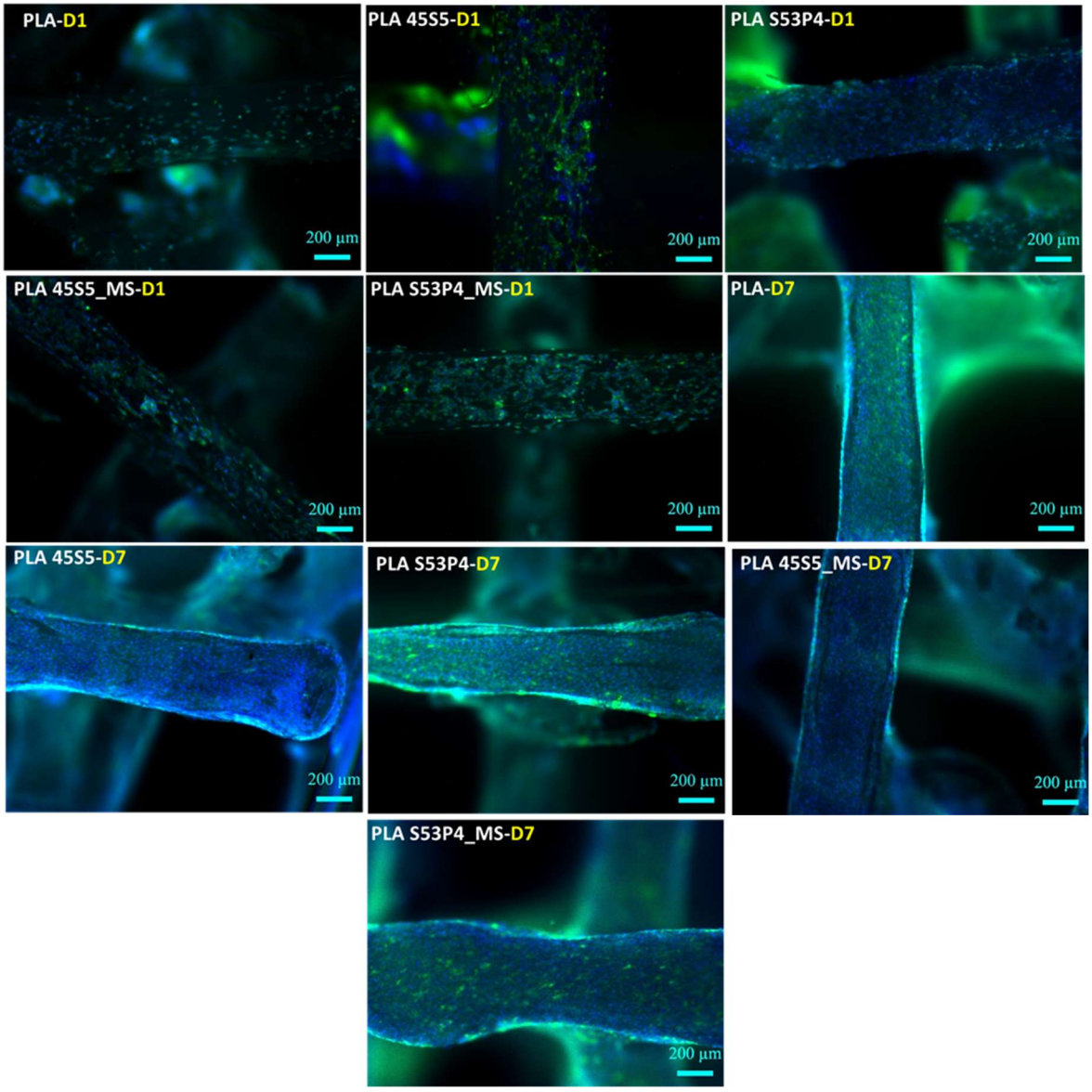

Figure 51. *Fluorescence images of cells attached on scaffold surfaces after 1 and 7 days. Nuclei are shown in blue, and cytoskeletal or cellular structures in green.*

3.2.4. Conclusions

In this work, the effect of incorporating BG particles into a PLA matrix for scaffold production was investigated. Mechanical properties of PLA and PLA+BG specimens were investigated both in tension of dog-bone specimens as well as in scaffold compression, exploiting a DIC system for accurate strain analysis. Tensile properties were little affected by BG embedment, although they suggest that BG particles act as nucleation sites for crack initiation and propagation. Compared with the literature, the obtained results appear generally higher – for example, in terms of stiffness – even for plain PLA. This may be due to the specific thermal history experienced by the material during FDM, as well as to the use of the DIC system, which, in combination with the UTM, provides a more accurate way of measuring mechanical properties than that usually adopted which solely relies on the crosshead travel for strain computation.

In contrast, scaffold compressive properties of PLA+BG and PLA are markedly different: the presence of BG significantly affects the ultimate strength, ultimate strain, and the failure progression. PLA exhibits an ultimate strength six times higher than PLA+BG, with an ultimate strain 2.5 times greater, resulting in far superior ductility. Furthermore, collapse in PLA+BG scaffolds occurs catastrophically when the material reaches its failure strain, causing the scaffold to fragment into smaller pieces. This behaviour may increase the exposed surface area and potentially facilitate degradation, resorption and interaction with surrounding tissue; however, its biological advantage depends on the specific application (e.g., it may be less suitable for load-bearing applications). By contrast, PLA scaffolds fail via stability loss, preserving their overall integrity.

Overall, the biological evaluation confirmed that all surface-treated PLA and PLA–BG scaffolds were cytocompatible, supporting cell adhesion and proliferation without signs of cytotoxicity. Notably, the S53P4- and S53P4_MS-containing scaffolds elicited the most favourable cellular response, indicating their strong potential to enhance osteogenic performance in bone tissue engineering applications. In particular, potential applications may include non-load-bearing or moderately loaded environments such as craniofacial or dental bone regeneration, where enhanced bioactivity and controlled resorption are desirable.

Future research may focus on enhancing interfacial bonding between PLA and BG, optimizing BG particle size and dispersion to reduce stress concentration, and tailoring scaffold design to balance bioactivity and mechanical stability.

3.2.5. Supplementary

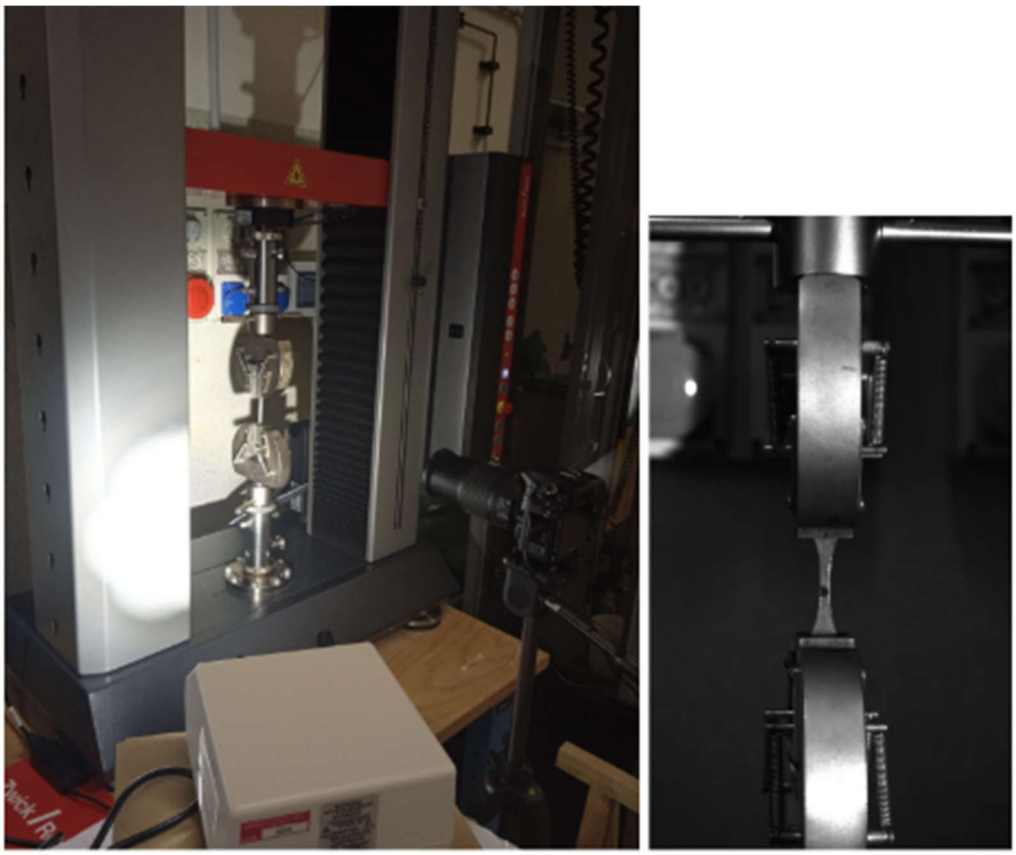

Supplementary 3. *Tensile test setup: UTM machine with wedge grips, DIC camera and light source (left), specimen area (right)*

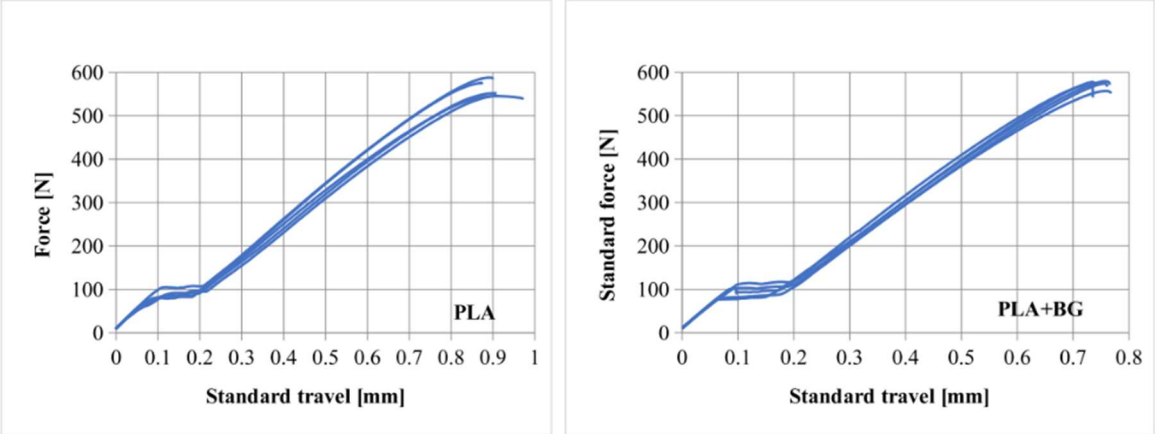

Supplementary 4*. Strength curves in terms of crosshead displacement (standard travel in mm) for PLA (left) and PLA+BG (right) specimens. Five repetitions are presented in each group which are well consistent. The plateau in the plots is a result of the compression that the grips produce on the specimen ends, that induces elongation at an almost constant force.*

4. Natural Polymers from Biomass

4.1. Valorization of metabolite-enriched carbohydrates from Theobroma biomass via ultrasound-assisted alkaline extraction

(This section has been published in: Núñez-Ramírez J.M., Martelli A., Halliday T., Thomas B., Wills C., Cannillo V., Bellucci D., Carranza C., García-Rincón P.A., Gentile P., Girón-Hernández J. Valorization of metabolite-enriched carbohydrates from Theobroma biomass via ultrasound-assisted alkaline extraction. Carbohydrate Polymers. 2025, 368 (Part 1). *https://doi.org/10.1016/j.carbpol.2025.124070*. Reproduced in accordance with the publisher's copyright policy.)

The candidate performed the experimental work, in particular polymer extraction, bioactive compound evaluation, and rheological testing, and contributed to data analysis and manuscript preparation.

4.1.1. Introduction

The *Theobroma* genus, part of the *Malvaceae* family, includes plants native to tropical America, valued for their bioactive compounds like alkaloids, flavonoids and fats (Benlloch-Tinoco et al., 2024). *Theobroma cacao* is the most recognized species due to its role in chocolate production, but other species, such as *Theobroma. grandiflorum* (cupuaçu) and *Theobroma. bicolor* (macambo), have gained attention for their high-quality fats and unique flavor profiles (Febrianto and Zhu, 2022). Despite these valuable properties, these fruits present a challenge: the considerable waste generated during post-harvest processing. Up to 70% of *T. cacao* fruit is discarded (Girón-Hernández et al., 2024a), resulting in a substantial biomass that could be harnessed for its bioactive compounds. In particular, this biomass, including its seeds, pod husks, pulp, and leaves, contains a rich diversity of biocompounds and biopolymers that have significant ecological, nutritional, and industrial value (Jean-Marie et al., 2022). Among these, polyphenols are particularly prominent, contributing to the antioxidant properties of the biomass.

Flavonoids such as catechins, epicatechins, and procyanidins are abundant in *Theobroma* seeds and pod husks, offering health benefits and enhancing food stability. Phenolic acids, including gallic and caffeic acids, are also present, contributing to bioactivity and potential therapeutic properties of *Theobroma* biomass (Mar et al., 2024). Another significant class of compounds, methylxanthines, primarily theobromine and caffeine, exhibit stimulatory effects and plant defense roles, with the highest concentrations in seeds but can also be detected in other parts of the plant (Kieck et al., 2016). Furthermore, the biopolymers in the *Theobroma* genus include polysaccharides such as cellulose, hemicelluloses and pectins,

essential for plant integrity. These polysaccharides are particularly prominent in the pod husks and play an important role in applications such as biodegradable packaging and bioenergy production (Mar et al., 2024). Revalorizing biomass for biopolymer extraction holds significant importance due to its potential to create sustainable materials, reduce agricultural waste, and support bioeconomy initiatives. The comprehensive biochemical composition of *Theobroma* biomass highlights its value across various sectors, including food, cosmetics and pharmaceuticals. This diversity underscores the importance of exploring the full potential of the genus as a source of bioactive compounds and renewable materials.

To address this, researchers have explored various methods to valorize *Theobroma* residual biomass, primarily using acidic solutions (Barrios-Rodríguez et al., 2022); however, these approaches are often limited by extraction yields below 10% (Jarrín-Chacón et al., 2023; Vriesmann et al., 2012). Recently, enzymatic and alkaline extractions aided by ultrasound have been explored (Girón-Hernández et al., 2024a). Moreover, alkalization is aligned with existing methods used in the cocoa processing industry to reduce the acidity of the beans and modify flavor, color, and solubility by adding alkalis like NaOH, KOH, K_2CO_3 or $NaHCO_3$ to cocoa powder or mass; this process also impacts the material's elastic modulus, a measure of its stiffness, which is crucial for understanding how a material behaves under different forces (Puchol-Miquel et al., 2021). In addition, studies on cocoa paste alkalinization have investigated how different alkaline solutions affect the content of metabolites in the final product. Indeed, phenols in cocoa exist in free or non-extractable forms (bound to other molecules or cellular structures), and these can be released during alkalization with NaOH. One study reported that clovamide was the only polyphenol present at higher concentrations in cocoa compared to commercial varieties following treatment with a NaOH solution and subsequent extrusion (Valverde et al., 2020). Therefore, alkaline extraction effectively breaks down plant matrices by hydrolyzing ester bonds in protopectin, facilitating soluble pectin release. This method is particularly advantageous for extracting gel-forming polysaccharides associated with pectin components, making them suitable in industry (Yang et al., 2024).

Building on these findings, our study aimed to apply the principles of cocoa paste alkalinization, combined with the use of ultrasound, to valorize the residual biomass from the three most cultivated *Theobroma* species in the Amazon region. In this work, we hypothesized that variations in structure and composition among the *Theobroma* species may influence both the yield and nature of polysaccharide and non-polysaccharide components

obtained through alkaline-assisted methods. Indeed, the pod husks of these *Theobroma* species differ markedly in the structure of the epicarp, mesocarp, and endocarp. *T. cacao* features a thick, highly lignified epicarp that provides strong protection but limits extractability. In contrast, *T. grandiflorum* has a thinner, less lignified epicarp with a looser structure that enhances solvent penetration, while *T. bicolor* shows intermediate characteristics. The mesocarp of *T. cacao* is moderately dense and rich in pectic polysaccharides; *T. grandiflorum* presents a softer, more hydrated mesocarp with higher pectin solubility, and *T. bicolor* exhibits a more fibrous yet less compact mesocarp, with a balanced polysaccharide composition. Lastly, the endocarp in *T. cacao* is thin and mucilaginous, contributing little to extractables, whereas *T. grandiflorum* has a more developed, pectin-rich endocarp, *and T. bicolor* displays a less mucilaginous and more variable endocarp structure (Benlloch-Tinoco et al., 2024; Marasca et al., 2022; Oñate-Gutiérrez et al., 2023). Furthermore, regarding the biochemical composition, *T. cacao* husks are characterized by high levels of flavanols, particularly epicatechin and isoquercitrin, which contribute to their strong antioxidant potential. In contrast, *T. grandiflorum* husks exhibit a broader spectrum of flavonol compounds, including quercetin derivatives, reflecting a more diverse phenolic profile. Meanwhile, *T. bicolor* husks present a distinct composition marked by notable concentrations of myricetin and the presence of unique minor compounds such as scopoletin, highlighting species-specific differences in secondary metabolite profiles (Tauchen et al., 2016).

Additionally, we aimed to assess whether KOH could serve as an effective alternative to NaOH for alkaline extraction, potentially offering distinct advantages in terms of biopolymer composition and functionality. The two alkalis may interact differently with plant material, possibly due to the differing properties of their associated cations (K^+ vs Na^+), which may affect the solubility and swelling behavior of the plant matrix, as well as interact ionically in distinct ways with the polysaccharides embedded within the matrix (Gai et al., 2022; Safirzadeh et al., 2017). Notably, KOH has also been reported to offer economic benefits; according to Zhang et al. (Zhang et al., 2018), it generates less than 10% of the wastewater produced by NaOH, significantly reducing treatment costs in plant processing operations.

In this work, we proposed ultrasound (US)-assisted extraction to intensify the process, based on our previous study (Girón-Hernández et al., 2023) which showed that US reduced the extraction temperature for pectic polysaccharides from apple pomace, achieving high yields while preserving bioactivity. Literature also highlights several benefits of US

including: (1) improved mixing, (2) faster energy and mass transfer, (3) lower thermal and concentration gradients, and (4) increased yield and throughput (Hu et al., 2022; D. Liu et al., 2024).

4.1.2. Materials and methods

Materials

Dichloromethane (≥99.9%), hydrochloric acid (ACS reagent, 37%), 96% ethanol, methanol (HPLC grade, ≥99.8%), 3,5-dinitrosalicylic acid (DNS) reagent, Folin-Ciocalteu reagent, Biuret reagent (protein detection level 150-1,000 µg/mL), potassium hydroxide (ACS reagent, ≥85%), sodium carbonate (ACS reagent, 99.5%), gallic acid, Trolox, quercetin (HPLC reagent ≥95%), sugar standards (≥97%), including galacturonic acid (GalA), glucuronic acid (GlcA), galactose (Gal), glucose (Glc), mannose (Man), xylose (Xyl), rhamnose (Rha), and arabinose (Ara), along with other chemicals such as acetonitrile, ammonium bicarbonate, ammonium hydroxide, formic acid and 3-(trimethylsilyl)-2,2,3,3-tetradeuteropropionic acid (TMSP-d4) were purchased from Merck, UK. Sodium hydroxide, deuterium oxide, 99.8% (D_2O) and trifluoroacetic acid (TFA) were purchased from Fisher Scientific, UK. 1-Phenyl-3-methyl-5-pyrazolone (PMP) was supplied by Apollo Scientific, UK. Distilled water (dH_2O) water and MS-grade water were obtained from a Milli-Q® system (IQ 7005, Merck, UK).

Sample preparation

Fruits from three species were collected at the physiological ripeness stage (indicating full maturity through natural development on the plant, ~5-6 months) from the University of Amazonia's farm in Colombia. They were washed, dried, and opened to separate seeds, funicle, and pods. Pods were chopped, sun-dried to constant weight, or oven-dried (40 °C, UF30, Memmert, Germany). The dried material was ground to ~200 µm using a MultiDrive Basic (IKA, Germany) and, then, stored in a desiccator.

Setup of the Design of Experiments (DoE) and extraction of biopolymers from pod husk powder

The optimization of the biopolymers extraction was conducted using Response Surface Methodology (RSM) with a Box-Behnken design. The factors studied were extraction time (Et, min), temperature (T, °C), and powder-to-solvent ratio (P, g/mL), systematically varied across 15 runs (**Supplementary 5**), where factor levels ranged from 11.11-22.22 mg/mL for the powder-to-solvent ratio, 30-80 °C for temperature, and 20-60 min for time. This design

enabled the evaluation of linear and quadratic effects, as well as factor interactions. Replicates at the central condition (Et: 40 min, T: 55 °C, P: 0.016665 g/mL) to assess model reproducibility. For the extraction, the process followed the methodology reported by Gentile's group (Girón-Hernández et al., 2024a), based on the combinations of the studied factors (Et, T, P). Pod husk powder was dissolved in a Duran glass flask with 45 mL of 0.05 M alkaline solution (NaOH or KOH) and heated to the target temperature in an ultrasonic bath (VWR, UK) at 45 kHz for the specified time. Phase separation of the coarse and diluted polymeric material was achieved by centrifugation at 3900 rpm for 30 min using a Sorvall ST1 Plus centrifuge (Thermo Fisher, UK). The supernatant was mixed with 96% ethanol (1:1 vol/vol) and stored at 4 °C for 24 h to precipitate the polymers. After refrigeration, the mixture was centrifuged at 2000 rpm for 30 min to recover the polymer as a pellet. The polymer was then dialyzed in dH_2O using cellulose membrane tubing (molecular weight cut-off 12-14 kDa Merck, UK) for 48 h, with the water changed three times daily. Finally, it was dried on non-stick baking paper in a MIR-154 incubator (Panasonic, Japan) at 37 °C until constant weight and stored.

Analysis of the moisture and ash content

Moisture content.

Moisture content was determined by drying the sample at 105 ± 2 °C to a constant weight and expressed as g/100 g, calculated as the ratio of water weight (wet weight minus dry weight) to wet weight.

Ash content.

Ash content was measured by ashing samples in a muffle furnace ELF (Carbolite Gero Ltd, UK) at 550 ± 10 °C for 2 h and expressed as g/100 g, calculated as the ratio of ash weight to sample weight.

Color measurement

Color measurements were taken at five random points on both the lightest and darkest areas of the extracted materials using a DigiEye system (DigiPix, VeriVide, UK). A white standard plate was used for calibration and background. Results were expressed in CIE Lab color space (10° observer, D65 illuminant), with L* (lightness), a* (green-red), b* (blue-yellow), and automatically calculated chroma intensity (C*) and hue angle (h*).

Bioactive profile and antioxidant capacity

Total phenolics (TP) determination

TP was assessed using a modified Folin-Ciocalteu method (Macías-Garbett et al., 2022). A 50 µL sample (1 mg/mL) was mixed with 430 µL dH_2O and 20 µL Folin-Ciocalteu reagent. After adding 50 µL Na_2CO_3 (20 g/100 mL) and incubating in darkness for 10 min, the mixture was diluted with 450 µL dH_2O. A 200 µL aliquot was transferred to a 96-well plate, and absorbance was measured at 680 nm (FLUOstar UV-Vis, BMG Labtech, Germany). A gallic acid equivalents (GAEq) calibration curve (0.05-1 mg/mL, R^2 = 0.997) was used, expressing results as mg GAE/g sample.

Total flavonoids (TF) determination

TF was quantified using the A319717-Plant Flavonoids Assay (Antibodies, UK). Samples (1 mg/mL) in 60% ethanol were mixed with 15 µL nitrite solution (5 min), then 15 µL chromogen (5 min), followed by 120 µL NaOH and 90 µL 60% ethanol (15 min). Absorbance at 502 nm was measured in a 96-well plate. A quercetin equivalents (QEq) calibration curve (0.0156-1 mg/mL, R^2 = 0.999) was used, with results as mg QEq/g sample.

Total oligomeric proanthocyanidins (TPA) determination

TPA was assessed using the A319718-Plant Oligomeric Proanthocyanidins Assay Kit (Antibodies, UK). Samples (1 mg/mL) in extraction buffer were mixed (40 µL sample + 160 µL reagent) in a 96-well plate and incubated at 30 °C for 30 min. Absorbance at 500 nm was measured. A catechin equivalents (CEq) standard curve (0.039-5 mg/mL, R^2 = 0.996) was used, with results as mg CEq/g sample.

Oxygen radical absorbance capacity (ORAC) determination

ORAC was measured using the ab233473-ORAC Assay Kit (Abcam, USA). Samples (0.02 mg/mL) in 1× assay diluent were mixed with 150 µL Fluorescein solution, incubated at 37 °C for 30 min, and fluorescence (Ex/Em = 480/520 nm) recorded. After adding 25 µL Free Radical Initiator (80 mg/mL), fluorescence was recorded every min for 1 h. A Trolox equivalents (TEq) standard curve (0-50 µM, R^2 = 0.991) was used, with results in M TEq/g sample.

Ferric reducing antioxidant power (FRAP)

FRAP was assessed using the Ferric Antioxidant Status Detection Kit (Thermo Fisher Scientific, UK). Samples (1 mg/mL, 1:10 dilution) were mixed with 75 µL FRAP reagent in a 96-well plate and incubated for 30 min. Absorbance at 560 nm was measured. An ascorbic

acid standard curve (0.05-1000 µM, R^2 = 0.999) was used, with results in mmol Fe^{2+}/g sample.

All measurements were performed in triplicate, at a minimum, following the manufacturer's specifications.

Analysis of metabolites by Mass Spectrometry (MS)

Pod powders (10 mg) were extracted in 1 mL analytical methanol, sonicated (15 min, ice-water bath), and centrifuged (15,000 rpm, 15 min, 4 °C). Supernatants were vacuum-dried (45 °C, 2 h), resuspended in 100 µL 95/5 LC/MS-grade water/acetonitrile, sonicated, and filtered (0.22 µm Costar Spin X, 10,000 rpm, 5 min). Filtrates were transferred to autosampler vials with 200 µL micro-inserts. Extraction blanks and pooled QCs were included for MS/MS exclusion/inclusion lists and stability assessment.

Chromatographic separation used a Waters HSS T3 column (2.1 mm × 150 mm, 1.7 µm, 35 °C, 250 µL min^{-1}). A binary buffer system (0.1% ammonium hydroxide) followed a gradient of Buffer A (95/5 LC/MS-grade water/acetonitrile) and Buffer B (5/95): T0-1.5 min, 95% A; T1.5-11.5 min, 5% A; T15-20 min, 95% A. Injection-to-injection time: 21.5 min. Data acquisition followed a data-dependent (Thermo AcquireX) approach. MS1: 30,000 resolution (100-1000 m/z, Quad RF 30, AGC 95%, max injection 50 ms). MS2: stepped HCD (10, 35, 60), 1.0 m/z isolation. Metrics: vaporizer temp 275 °C, ion transfer tube 300 °C, gas flow (sheath: 35, aux: 7, sweep: 0). Data were converted to .abf files and aligned using Riken MSDial 4.9. MS2 matches (≥70% similarity, 10-ppm tolerance) were verified with an authentic library. QC metrics (RSD ≤1.3%, threshold ≤15% in both modes) ensured stable MS/MS signals (RSD ≤25%) with metadata: formula, S/N ratio, retention time, m/z, adduct, MS/MS match score, and InChIKey.

Structural sugars determination

Structural sugar determination involved hydrolysis, derivatization, and quantification, based on adaptations of existing methods (Slimestad et al., 2019). One milligram of extracted material was placed in a glass vial with 1000 µL dH_2O and 500 µL TFA (4 M). The sealed vial was heated at 120 °C with stirring for 90 min and then cooled. To remove residual TFA, 200 µL of methanol was added, and the mixture was evaporated at 80 °C. The resulting residue was re-dissolved in 1 mL dH_2O. For monosaccharide derivatization, 200 µL hydrolyzed solution was mixed with 80 µL 0.3 M NaOH and 80 µL PMP in methanol, The mixture was incubated at 80 °C for 60 min, cooled, neutralized with 80 µL 0.3 M HCl, and

diluted to 1 mL. Excess PMP was removed by extraction with CH_2Cl_2 (3 × 1 mL), followed by vortexing at 30,000 rpm for 30 sec. All samples and sugar standards were derivatized, filtered (0.45 μm), and transferred to chromatographic vials. Sugar quantification was performed using UV detection (250 nm) on an ACQUITY Premier UHPLC with a single quadrupole MS. Separation was achieved on a C18 column (50 × 2.1 mm, 1.7 μm) at 25 °C, using ammonium bicarbonate/ammonium hydroxide (pH 9.2) and acetonitrile. Mass spectrometry was used to confirm the identity of peaks (ESI-MS, positive mode, 400-1000 m/z, 200 ms scan). Characteristic pseudomolecular ions included: 481 m/z (pentoses), 495 m/z (deoxy-hexoses), 511 m/z (hexoses), 525 m/z (uronic acids). Data were processed using MassLynx software (v4.2). The rhamnogalacturonan-I (RG-I) domain content was estimated using the formula RG-I (%) ≈ 2Rha (mol%) + Ara (mol%) + Gal (mol%), while the homogalacturonan (HG) as GalA(mol%) − Rha (mol%) (Wu et al., 2023).

Molecular weight determination

Molecular weight was determined by size-exclusion chromatography (Agilent, UK) using a Jasco PU-4180 pump, Kontron 480 column oven, and Shodex RI-101 detector. The system included a 1× PL Aquagel-OH MIXED-H (8 μm, 50 × 7.5 mm) guard column and 2× PL Aquagel-OH MIXED-H (8 μm, 300 × 7.5 mm) columns. Samples (10 g/L) were dissolved in 0.2 M NaNO3+ 0.01 M NaH2PO4 (pH 7), filtered (0.45 μm), and manually injected (20 μL, full-loop mode). The oven was set to 50 °C, pump pressure at 1.7 MPa. Molecular weights were calculated using Clarity GPC extension Software (v2.3) against a 10-point Agilent Pullulan calibration (Mw 340-700,000 Da).

FTIR-ATR characterization and esterification degree determination

FTIR spectra and esterification degree (DE) were analyzed using FTIR-ATR (Frontier PerkinElmer Inc., UK). Samples were placed on the ATR accessory, recording signals (4000-550 cm^{-1}, 32 scans, 2 cm^{-1} resolution). For DE, 10 mg of dry material was re-suspended in 5 mL dH_2O (pH ~5.5), dried, and analyzed. DE was calculated via Spectrum IR software (v10) following a published protocol (Dranca et al., 2020) using peak areas at 1780-1720 cm^{-1} (COOH) and 1640-1600 cm^{-1} (COO^-) as:

$$DE\ (\%) = \frac{Area\ of\ COOH}{Area\ of\ COOH + Area\ of\ COO^-}\ x\ 100 \quad (1)$$

^{1}H NMR measurement

The extracted material was analyzed using NMR spectroscopy. Saturated samples were prepared in 0.7 mL of D_2O, with TMSP-d4 added at 0.0 ppm as an internal reference. The

^{1}H NMR spectra were acquired at 80 °C using an Advance III HD 700 MHz spectrometer equipped with a Prodigy TCI probe (Bruker, UK). Each spectrum consisted of 128 scans and 32 K data points (transformed to 128 K). Baseline corrections were applied prior to integration. Data were processed by applying baseline corrections prior to integration, through Mnova software (v15.1). The degree of esterification has been calculated following the protocol reported by Grasdalen et al. (Grasdalen et al., 1988a) that is related to the intensities (I) of the line patterns A and B by the formula:

$$DE\ (\%) = \frac{I_A - I_B}{I_A + I_B}\ x\ 100 \quad (2)$$

where B refers to the signals from H-5 of charged units, and A corresponds to the signals from H-1 and H-5 of esterified units.

Thermal analysis

The thermal performance of the extracted materials was analyzed using a Thermogravimetric Analyzer (TGA 1 STARe System, Mettler-Toledo, Switzerland). Each test sample (~6 mg) was heated at a rate of 10 °C/min from room temperature (25 °C) to 800 °C in a nitrogen gas environment with a flow rate of 10 mL/min. Furthermore, the thermal properties were evaluated by Differential Scanning Calorimetry (DSC) using the DSC 1 STARe System analyzer (Mettler-Toledo, Switzerland). Approximately five mg samples of each extracted materials were sealed in aluminum pans. The samples were heated from 30 °C to 450 °C at a rate of 10 °C/min. All tests were conducted under a nitrogen atmosphere with a flow rate of 10 mL/min. Results were normalized to the sample weight to allow for comparative analysis using the STARe Software (v18.0).

Rheology test

Sample solutions (2% w/w) were solubilized in dH_2O under stirring (25 °C, 16 h) and rested overnight at 4 °C before rheological tests. Measurements were conducted using an MCR302 stress-controlled rheometer (AntonPaar GmbH, Austria) with 25 mm parallel plates. A water trap prevented dehydration, and temperature was controlled via a Peltier system. Viscosity was measured at shear rates from 0.1 to 100 1/s (1% strain), while frequency sweep tests used angular frequencies (100-0.1 rad/s, 1% strain). Tests were performed in triplicate (Girón-Hernández et al., 2023) and analyzed using the manufacturer's RheoCompass software (v1.3).

Multivariant analysis

In the statistical processing, dimensionality reduction was performed, and a multivariate Principal Component Analysis (PCA) was applied to the evaluated variables: molecular weight, thermal properties at different temperatures (DSCT1, DSCT2), phenolics, flavonoids, proanthocyanidins, FRAP, ORAC, galacturonic acid content (GalA), and degree of esterification (DE). The analyzed samples included CC-NaOH and CC-KOH (derived from T. cacao), GF-NaOH and GF-KOH (T. grandiflorum), BC-NaOH and BC-KOH (T. bicolor), and COM-P (commercial pectin used as control). A 10-variable × 7-sample data matrix was created for this purpose. The analysis was conducted using R software (R Core Team, 2025).

4.1.3. Results

Analysis of Theobroma species pod husk

The harvested fruits of the three *Theobroma* species had fresh weights of ~1 kg or more (up to ~1.5 kg), with *T. bicolor* being the heaviest, followed by *T. grandiflorum* and *T. cacao*. Upon separating the fruit components, *T. cacao* showed a residual husk mass ratio 1.5 folder more than both *T. bicolor* and *T. grandiflorum*. **Table 14** shows the average fresh weights of each fruit and its component after seed removal. The husks of *T. bicolor* were the hardest, while both *T. grandiflorum* and *T. cacao* had softer husks.

Table 14. *Fresh weight distribution of fruit components of T. cacao (CC), T. grandiflorum (GF) and T. bicolor (BC).*

Species	Fresh fruit (g)	Seeds (g)	Funiculus (g)	Pod husk (g)	Total fruit (g)	Pod/Fruit ratio
CC	103.3 ± 12.6	151.7 ± 7.6	30.0 ± 5.0	661.7 ± 22.5	946.7 ± 22.5	0.70 ± 0.01
GF	385.0 ± 55.0	236.7 ± 34.0	98.3 ± 15.3	653.3 ± 119.3	1373.3 ± 200.4	0.47 ± 0.04
BC	396.7 ± 107.5	290.0 ± 105.0	56.67 ± 2.9	740.0 ± 160.0	1483.3 ± 370.0	0.50 ± 0.02

Moisture and ash content analyses of fresh and dry pods revealed significant variations among the species, with implications for industrial processing (**Supplementary 6**). The high moisture content observed in fresh *T. cacao* pods (84.61 ± 0.86%) suggests a greater capacity for water retention, consistent with prior studies of its hydration potential (Djali et al., 2021; Dos Anjos Lopes et al., 2023). While this trait may help maintain freshness, it also increases drying time and energy consumption, posing challenges for industrial scalability. In contrast, the lower moisture contents of *T. grandiflorum* and *T. bicolor* (72.13 ± 1.14% and 75.12 ±

2.47%, respectively), are aligned with literature highlighting their lower water retention, making them more cost-efficient for drying processes (Benlloch-Tinoco et al., 2024). Regarding ash content, fresh *T. cacao* pods had the highest mineral concentration (4.36 ± 0.12%), making them promising for biofertilizer production, as reported in studies emphasizing the value of mineral-rich byproducts in soil amendment (van Vliet and Giller, 2017). Conversely, the low ash content in fresh *T. grandiflorum* pods (0.66 ± 0.09%) makes them better suited for pectin extraction, where minimal mineral interference is desired. This observation is supported by existing research (Kazemi et al., 2021), which suggests that low ash content aids in producing high-purity pectin in accordance with FAO standards for food additive specifications (Joint FAO/WHO Expert Committee on Food Additives, 2006). Notably, this trend is reversed in dry pods, with *T. grandiflorum* exhibiting the highest ash content (9.43 ± 0.21%).

Differences in fresh and dry weights, along with drying yields, underscore the variability in biomass utilization across species. *T. cacao* pods, with a fresh weight of 596.67 ± 116.23 g and a dry yield of 27.07 ± 1.44%, reflect their high initial moisture and lower drying efficiency, in line with previous findings. In contrast, *T. grandiflorum* pods demonstrated greater efficiency with a similar fresh weight of 606.67 ± 85.05 g but a substantially higher dry yield (54.37 ± 3.97%), highlighting their suitability for sustainable biomass processing. *T. bicolor* showed the highest fresh weight (765.33 ± 165.91 g) and an intermediate dry yield (48.69 ± 2.08%) (**Supplementary 7**), representing a balance profile between water content and biomass retention, making it versatile for diverse applications.

Biopolymer extraction from Theobroma species using NaOH and KOH

After characterizing the different waste biomass (exocarp) from the *Theobroma* genus, biopolymer extraction was performed using NaOH and KOH as solvents, with temperature (T), extraction time (Et), and pods powder/solvent ratio (P) as factors. Results revealed marked differences in extraction performance between NaOH and KOH, likely due to variations in the solubility of pectic-related compounds, material composition, or distinct chemical interactions with the alkaline solutions. Significant factors or their interactions (crossing the red dashed line) were identified using a Pareto chart (**Figure 52 A**), with non-influencing factors retained only if they interacted with key factors. This underscores the complex dependency on factor interactions for the extraction.

Response surface methodology provided insights into process efficacy, model reliability, and predictive performance (**Figure 52 B**). Overall, among the factors considered in the DoE

for NaOH extractions across all species, temperature consistently emerged as a key variable, highlighting its role in the biopolymers solubilization. The pods powder/solvent ratio also ranked highly, particularly in *T. cacao* and *T. grandiflorum*, highlighting its importance in optimizing yield. Conversely, KOH exhibited poor performance, with no factors identified as significant in several cases, indicating weaker chemical interactions and limited extraction efficiency. For T. *cacao* with NaOH, powder/solvent ratio significantly influenced yield, both as an independent factor (P, P·P) and through its interaction with temperature (T·P).

The model showed excellent reliability with all metrics >90%, and the predicted yield (40.7%) closely aligned with the observed yield (38.0%), with an extraction error of 7.2%. KOH extraction, however, revealed no significant factors, with limited model reliability, though predicted and observed yields were similar (23.7% vs. 23.0%). *T. grandiflorum* produced the lowest yields for both treatments. With NaOH, temperature was the dominant factor, followed by its interaction with the pods powder/solvent ratio (T·P), extraction time (Et), and the ratio itself (P). The model achieved high accuracy, all metrics >95%, with predicted (8.7%) and observed yields (8.0%) showing an 8.5% error. KOH extractions had a simplified model, with T remaining dominant, followed by P and Et·T. While moderate reliability, presenting metrics in the range of (65% to 85%), a 122% extraction error indicated a large discrepancy between predicted (11.1%) and observed yields (5%). For *T. bicolor* with NaOH, T was the most influential factor, alongside interactions (T·P, T·T). The model showed high accuracy with all coefficients >91%, with predicted (14.9%) and observed yields (14.7%) closely matching and a minimal error (1.5%). With KOH, results mirrored those of *T. cacao*, although the factors were not significant, they were retained to ensure statistical completeness.

A

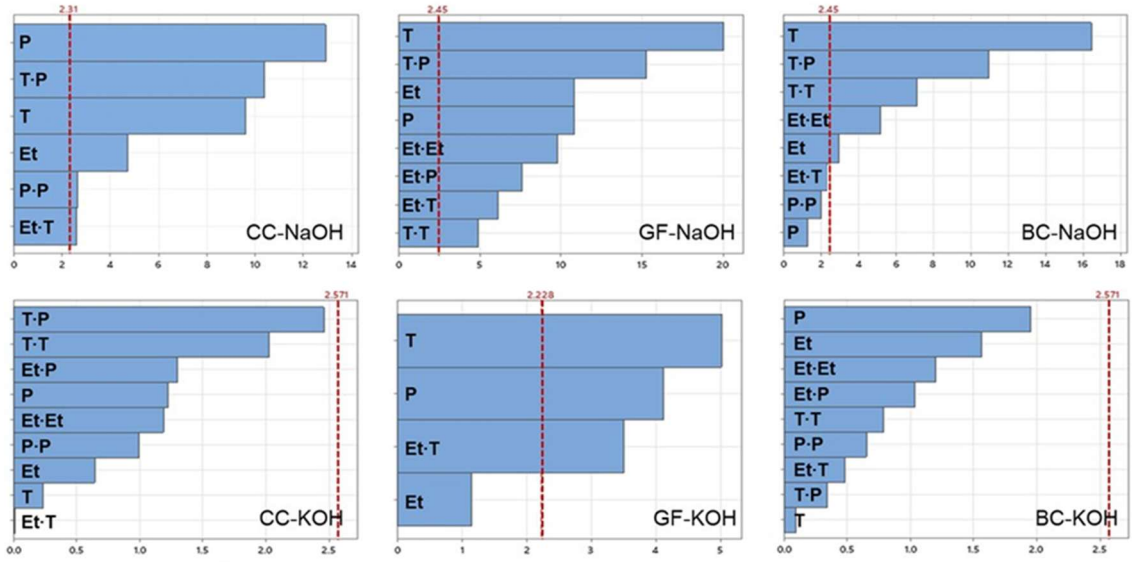

B

Sample	Regression equations for biopolymers yield extraction in uncoded units	R^2 (%)	R^2 Adj (%)	R^2 Pred (%)	Pred. Value (%)	Obs. Value (%)	Error (%)
CC-NaOH	= 63.7 + 0.3 Et - 0.8 T - 1668 P - 53934 P·P - 0.003 Et·T + 45 T·P	98.1	96.6	91.2	40.7	38.0	7.2
CC-KOH	= 53 + 0.13 Et + 0.5 T - 4694 P - 0.005 Et·Et - 0.006 T·T + 57927 P·P + 0.00005 Et·T + 20.3 Et·P + 30.6 T·P	76.7	34.6	0.0	23.7	23.0	3.0
GF-NaOH	= -5.2 + 0.2 Et + 0.1 T + 486 P - 0.002 Et·Et + 0.0005 T·T + 0.001 Et·T - 4.5 Et·P - 7.2 T·P	99.5	98.7	95.1	8.7	8.0	8.5
GF-KOH	= 8.8 - 0.1 Et - 0.04 T - 153.1 P + 0.002 Et·T	84.8	78.7	65.7	11.1	5.0	122
BC-NaOH	= 7.2 + 0.2 Et - 0.04 T + 261 P - 0.002 Et·Et + 0.002 T·T + 9317 P·P - 0.0006 Et·T - 10.8 T·P	98.8	97.2	91.1	14.9	14.7	1.5
BC-KOH	= 5.5 - 0.3 Et + 0.2 T + 540 P + 0.002 Et·Et - 0.001 T·T - 15933 P·P - 0.001 Et·T + 6.7 Et·P - 1.8 T·P	67.5	9.0	0.0	11.1	10.6	4.6

Figure 52. *Pareto charts of standardized effects (x-axis) of factors (y-axis) -temperature (T), extraction time (Et), pods powder/solvent ratio (P), and interactions- on the extraction yield (%). Bars crossing the red dashed line indicate significance (α=0.05)* ***(A)****. Fitted model equations and metrics: coefficient of determination (R^2), adjusted coefficient of determination (R^2 Adj.), predictive coefficient of determination (R^2 Pred.), the predicted extraction yield (Pred. Value), observed extraction yield (Obs. Value), and the experimental percentage error (Error), calculated as the absolute difference between the predicted and observed values, divided by the observed value (%)* ***(B)****.*

The findings confirm that temperature significantly influences pectin solubilization in *Theobroma* species, aligning with literature emphasizing its role in enhancing reaction kinetics and breaking down protopectin complexes. Elevated temperatures hydrolyze mainly ether and ester bonds, releasing soluble pectic polysaccharides (Qian et al., 2021). Optimal extraction temperatures (70-90 °C) balance yield with functional property preservation, such as methoxylation and esterification (Girón-Hernández et al., 2023). However, regardless of the solvent applied during extraction, excessive heat may affect the functional properties of extracting biopolymers, lowering molecular weight and gel-forming ability, as reported in the literature for pectic polysaccharides, which become less suitable for applications

requiring specific viscoelastic properties (Said et al., 2023). In NaOH extractions, temperature enhances solvent penetration, disrupting cell matrices and releasing bound pectin (Sandarani, 2017). Studies on sunflower heads and sugar beet pulp confirm temperature accelerates pectin solubilization while maintaining high yields and purity (Muñoz-Almagro et al., 2023; Peighambardoust et al., 2021).

Although both NaOH and KOH are strong bases, Na^+ and K^+ exhibit different ion–polymer interactions due to differences in ionic radius and hydration behavior, which can affect solvent penetration and disruption of plant cell wall structures. Higher extraction yields with NaOH may result from its more effective breaking down of plant cell walls and solubilization of protopectin (Abang Zaidel et al., 2017). In contrast, KOH may induce milder structural disruption, preserving functional properties and producing cleaner extracts, altough with slightly lower yields (Iglesias and Lozano, 2004). NaOH's aggressive action also extracts impurities, requiring further purification, whereas KOH retains more structural integrity, minimizing contamination (Iglesias and Lozano, 2004).

Moisture and ash content measurement

For the moisture content of the extracted materials (

Supplementary 8), *T. cacao* exhibited the lowest value in both treatments (NaOH: 4.17 ± 0.53%, KOH: 3.03 ± 0.61%), indicating lower water retention capacity compared to the other species. In contrast, *T. bicolor* showed the highest values (NaOH: 7.11 ± 1.14%, KOH: 5.42 ± 0.66%), suggesting higher water retention, which could influence extraction processes and final product properties. *T. grandiflorum* exhibited intermediate values (NaOH: 5.75 ± 1.45%, KOH: 4.93 ± 1.35%), indicating similar behavior to *T. bicolor*, even with lower water retention capacity.

Regarding ash results, *T. cacao* showed the highest ash content with KOH treatment (3.77 ± 0.60%), indicating a higher mineral concentration. *T. grandiflorum* exhibited the lowest ash values across both treatments (NaOH: 3.01 ± 0.31%, KOH: 2.58 ± 0.30%), making it more suitable for applications requiring low mineral content, such as the food industry, where ash levels must be controlled. *T. bicolor* had intermediate ash values, higher than *T. grandiflorum* but lower than *T. cacao*, with 3.47 ± 0.16% in NaOH and 3.07 ± 0.13% in KOH, indicating a moderate mineral concentration.

Color measurements

NaOH extraction produces darker samples than KOH, with *T. cacao* and *T. bicolor* showing reddish hues and *T. grandiflorum* a yellowish hue. **Figure 53 A** illustrates the color variations of the extracted materials by source and method. Notably, cocoa husk extraction with NaOH shifts the hue angle from 333.89° (blue) to 38.40° (red-orange) (**Figure 53 B**), as consequence of the different content of phenolic compounds (see below).

A

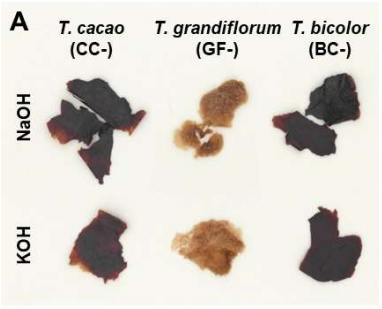

B

Sample	Area	L*	a*	b*	C*	hº
CC-NaOH	L	27.53±0.22	0.84±0.09	-0.41±0.15	0.95±0.09	333.89±8.99
	D	42.13±2.14	13.12±2.47	11.11±2.38	20.95±9.17	38.40±8.65
CC-KOH	L	29.12±0.92	7.06±2.91	0.08±0.60	7.10±2.96	350.99±8.95
	D	51.26±3.47	16.01±4.78	17.27±6.04	23.10±6.14	46.99±6.78
GF-NaOH	L	44.53±3.52	16.00±1.89	24.55±2.15	29.33±2.49	56.93±2.76
	D	63.29±6.04	15.13±4.10	33.89±5.07	37.19±5.95	66.12±4.11
GF-KOH	L	52.89±2.76	20.54±1.15	36.50±1.27	41.88±1.66	60.91±0.53
	D	78.30±1.68	7.81±0.80	29.40±0.89	30.42±1.05	75.15±1.05
BC-NaOH	L	22.25±3.11	1.13±0.30	-0.16±0.05	1.15±0.31	348.28±6.89
	D	38.93±3.06	15.84±3.44	8.91±4.18	21.05±6.18	38.34±2.49
BC-KOH	L	28.92±3.97	6.18±2.70	1.00±2.03	5.07±3.20	16.74±9.42
	D	61.36±5.53	12.45±3.11	7.41±1.91	17.20±8.48	61.68±6.55

Figure 53. *(**A**) Images of the materials extracted from T. cacao, T. bicolor, and T. grandiflorum using NaOH and KOH. (**B**) Average values and standard deviations of color coordinates, chroma, and hue measured on both the lightest and darkest areas of the extracted materials.*

Bioactive profile and antioxidant capacity

Figure 54 A summarizes assay results, while **Figure 54 B** compares normalized bioactive profiles and antioxidant capacity. NaOH extraction increased phenolics, flavonoids, and proanthocyanidins in *T. cacao* and *T. bicolor* pod husks. *T. grandiflorum* showed stable bioactive content, though proanthocyanidins were higher with KOH (1580 ± 250 mg CEq/g). *T. bicolor* (NaOH) had the highest bioactive profile: 460 ± 9 mg GAEq/g phenolics, 328 ± 5 mg QEq/g flavonoids, and 2090 ± 880 mg CEq/g proanthocyanidins.

These results contrast with prior findings on *T. bicolor* seed husks (Baldera Ocampo et al., 2021; Vázquez-Ovando et al., 2015), likely due to differences in sample treatment. Vázquez-Ovando et al. analyzed defatted pod husks, while Ocampo et al. used hot-water infusion extracts. extracted material is notable, as its pulp has higher reported values. This may reflect the pod husk's structural role, which may not require high secondary metabolite content for fruit protection (Jean-Marie et al., 2022; Mar et al., 2024; Sanchez-Ballesta et al., 2022).

A

	Bioactive profile			Antioxidant capacity	
Sample	**Phenolics[1]**	**Flavonoids[2]**	**Proathocyanidins[3]**	**FRAP[4]**	**ORAC[5]**
CC-NaOH	360±7	195±53	2450±406	127.82±6.44	3.26±0.1
CC-KOH	172±19	156±11	1630±365	56.28±4.65	3.03±0.1
GF-NaOH	170±18	57±6	1160±128	32.56±3.78	2.59±0.1
GF-KOH	152±4	65±12	1580±250	31.92±0.77	2.52±0.1
BC-NaOH	460±9	328±5	2090±880	232.69±1.09	2.18±0.1
BC-KOH	320±20	270±20	1570±117	157.31±4.90	1.75±0.1
COM-P	90±6	37±3	1040±158	27.44±0.89	2.93±0.0

Values are expressed as equivalents (Eq) on a dry basis: [1]mg GAEq/g, [2]mg QEq/g, [3]mg CEq/g, [4]mmol Fe^{2+}/g, [5]M Trolox Eq/g

B

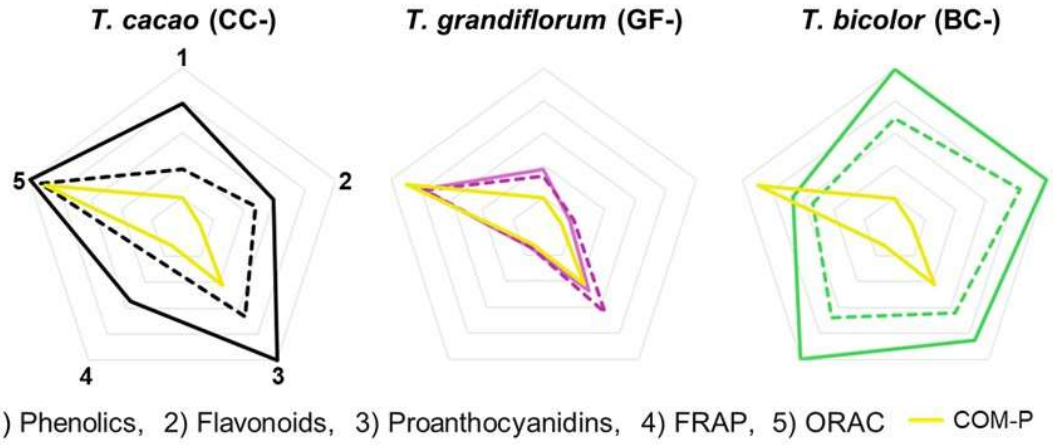

Figure 54. *Bioactive profile and antioxidant capacity of the extracted polysaccharides (**A**). Comparative representation of normalized data, illustrating differences between sample sources and extraction methods with NaOH in solid line and KOH in dashed line (**B**). Commercial citrus pectin (COM-P) is included as a reference.*

The *Theobroma* samples exhibited higher bioactive content than commercial citrus pectin (90 ± 6 mg GAEq/g phenolics, 37 ± 3 mg QEq/g flavonoids, 1040 ± 158 mg CEq/g proanthocyanidins). However, proanthocyanidins assays have limitations, as non-specific reactions with dihydrochalcones, anthocyanins, flavan-3-ols, and ascorbic acid can lead to overestimation (Waterman and Mole, 1994). Factors such as solvent acidity, proanthocyanidins concentration, and temperature fluctuations further impact accuracy (Sun et al., 1998; Waterman and Mole, 1994). Regarding the antioxidant activity, NaOH extractions yielded higher FRAP values than KOH, particularly in cocoa (127.8 ± 6.4 vs. 56.3 ± 4.7 mmol Fe^{2+}/g) and *T. bicolor* (232.7 ± 1.1 vs. 157.3 ± 4.9 mmol Fe^{2+}/g). Commercial pectin (27.4 ± 0.9 mmol Fe^{2+}/g) exhibited lower reducing power than most extracts, except for *T. grandiflorum*, highlighting NaOH's superior extraction efficacy. ORAC values showed smaller differences, with NaOH slightly outperforming KOH in cocoa (3.3 ± 0.1 vs. 3.0 ± 0.1 M Trolox/g) and *T. bicolor* (2.2 ± 0.1 vs. 1.8 ± 0.1 M Trolox/g). For *T. grandiflorum*, differences were negligible. Commercial pectin (2.9 ± 0.01 M Trolox/g)

exhibited comparable or higher ORAC values, suggesting its antioxidant profile favors radical scavenging over reducing power.

Comparisons of these values should consider limited literature on *Theobroma* pectic materials and variations in extraction analysis methods (Benlloch-Tinoco et al., 2024). Also, proanthocyanidin content may be influenced by sample color (Mannino et al., 2021), while the Folin-Ciocalteu assay may overestimate phenolics due to contributions from non-phenolic reducing agents (Munteanu and Apetrei, 2021).

These findings indicate that alkaline extraction (0.05M), particularly NaOH, is advantageous for preserving phenolics better than acidic or microwave-assisted methods (Mellinas et al., 2020), likely due to reduced heat-related degradation (~70 °C vs. ~100 °C in microwave extractions).

Metabolomic profiling of extracted material

The analysis revealed that both solvents enabled the extraction of comparable metabolite pools. However, all extractions performed using NaOH resulted in the detection of >200 metabolites, whereas in KOH-based extractions, this threshold was surpassed only in the case of *T. grandiflorum* (**Supplementary 9**). Metabolites were classified into ten main functional groups, along with an additional "others" category (**Figure 55**). Fatty acids emerged as the dominant class, ranging from 48% in CC-KOH up to 81% in GF-NaOH extracted materials, in agreement with their key role as major constituents of plant cell membranes (Reszczyńska and Hanaka, 2020). Carboxylic acids represented the second most abundant group (up to 19.4% in the CC-KOH extract). Indeed, intermediate compounds such as citric, succinic, and maleic acids were detected. These compounds likely reflect residual metabolic activity or degradation products (**Supplementary 9**). Interestingly, amino acids were also prominently identified, with KOH extractions favoring a higher recovery of this group (17.5% for CC-KOH). Notably, tyrosine, tryptophan and phenylalanine were recovered in significant quantities (**Table S5**), consistent with their well-established role as precursors in polyphenol biosynthesis. Tyrosine serves as a central precursor in antioxidant biosynthesis pathways (Marchiosi et al., 2020).

Furthermore, direct detection of phenolic compounds in the extracted materials was noteworthy (relative abundance from 2.7 to 6.2%), considering their bioactive potential and their reported contribution to cytocompatibility in our previous studies (Girón-Hernández et al., 2024b). These phenolic constituents may also enhance the crosslinking efficiency of

polysaccharide-based formulations (Pan et al., 2024). Among them, p-coumaric acid was prominently detected, aligning with its role in the phenylpropanoid biosynthetic pathway responsible for polyphenol production. Alkaloids were also identified (from 0.12 to 0.99%), as expected for the studied genus, with trigonelline, theobromine, and caffeine being the most representative. These compounds are well known for their stimulant properties, particularly in *Theobroma* species (Jazayeri et al., 2021). Finally, a similar relative abundance (up to ~0.5%) of vitamins, nucleic acids and hormones was detected because of the transformation processes induced by the extraction treatment. Notably, within the other compounds category, traces of serotonin were observed, potentially originating from the metabolic transformation of tryptophan present in the extracted material (Walther et al., 2003).

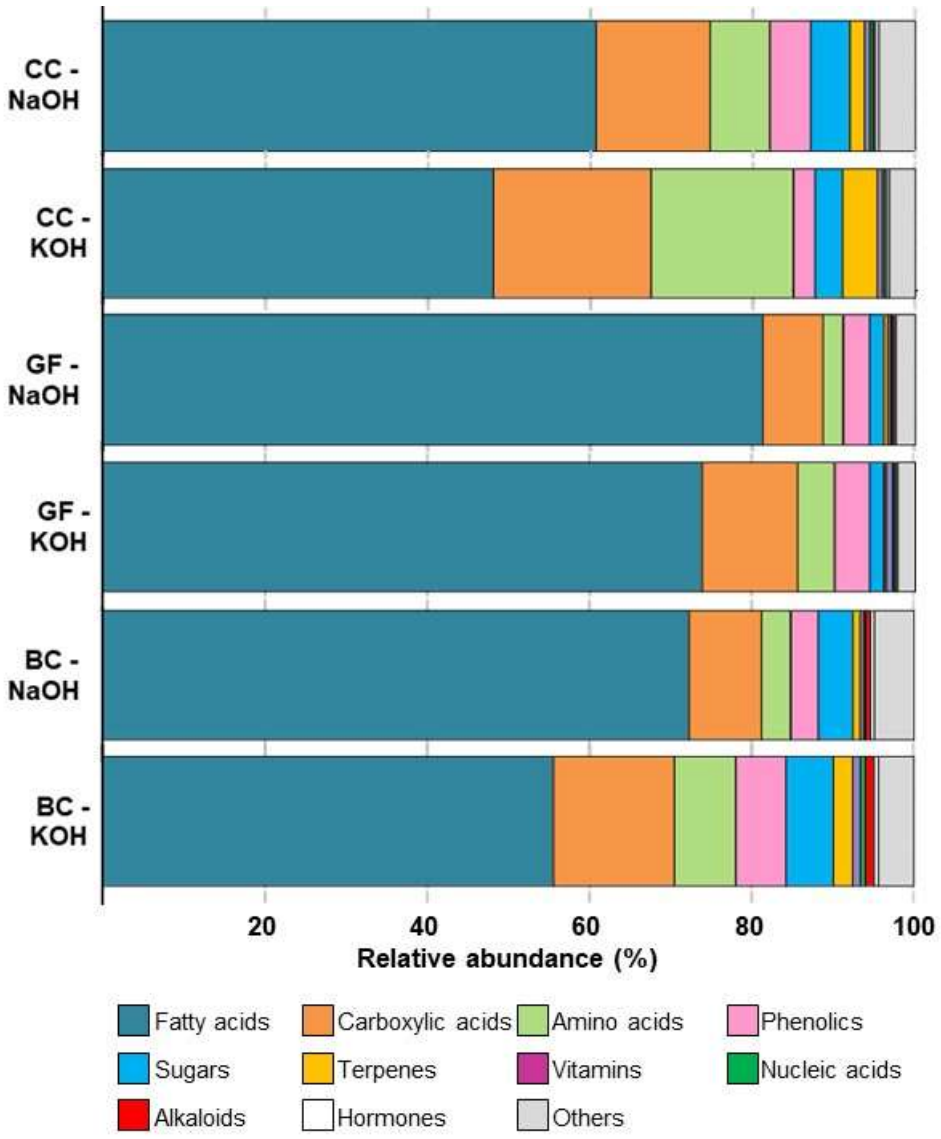

Figure 55. *Relative abundance (%) of metabolite classes identified in samples treated with NaOH and KOH from three different Theobroma matrices based on metabolomic analysis.*

Structural sugars, monosaccharides composition

The sugar composition of pectic materials from *Theobroma* species varied based on extraction method (NaOH vs. KOH) (**Figure 56 A**). KOH extraction preserved more rhamnose, a key component of rhamnogalacturonan-I (Davis et al., 1990). In *T. cacao*, rhamnose increased from 10.9% (NaOH) to 18% (KOH), while galactose decreased from 17.1% to 9.8%, that may be related to the presence of different pools of extracted polysaccharides. In *T. grandiflorum*, KOH yielded higher galacturonic acid (40% vs. 29.9% with NaOH) and lower galactose (9.6% vs. 17.1%), while *T. bicolor* showed a similar trend, with higher galacturonic acid (37.6% vs. 34.1%) but lower glucose and rhamnose.

The calculated proportions of the RG-I and HG domains are reported in **Figure 56 B**. As reported in the literature, Rha content plays a key role in defining the primary structure of pectic polysaccharides. The RG-I domain backbone is composed of repeating GalA and Rha units; therefore, a higher Rha content reflects a longer RG-I chain. The side chains, primarily consisting of neutral sugars such as Gal and Ara, are interwoven and attached to the backbone, forming the RG-I domain (Vincken et al., 2003). Notably, the materials BC-NaOH and CC- both NaOH and KOH treatment had significantly higher Rha content, corresponding to the highest RG-I domain proportions, compared with materials extracted from *T. grandiflorum*. This structural feature can be associated with an increased presence of bioactive compounds, such as flavonoids (**Figure 54 A**).

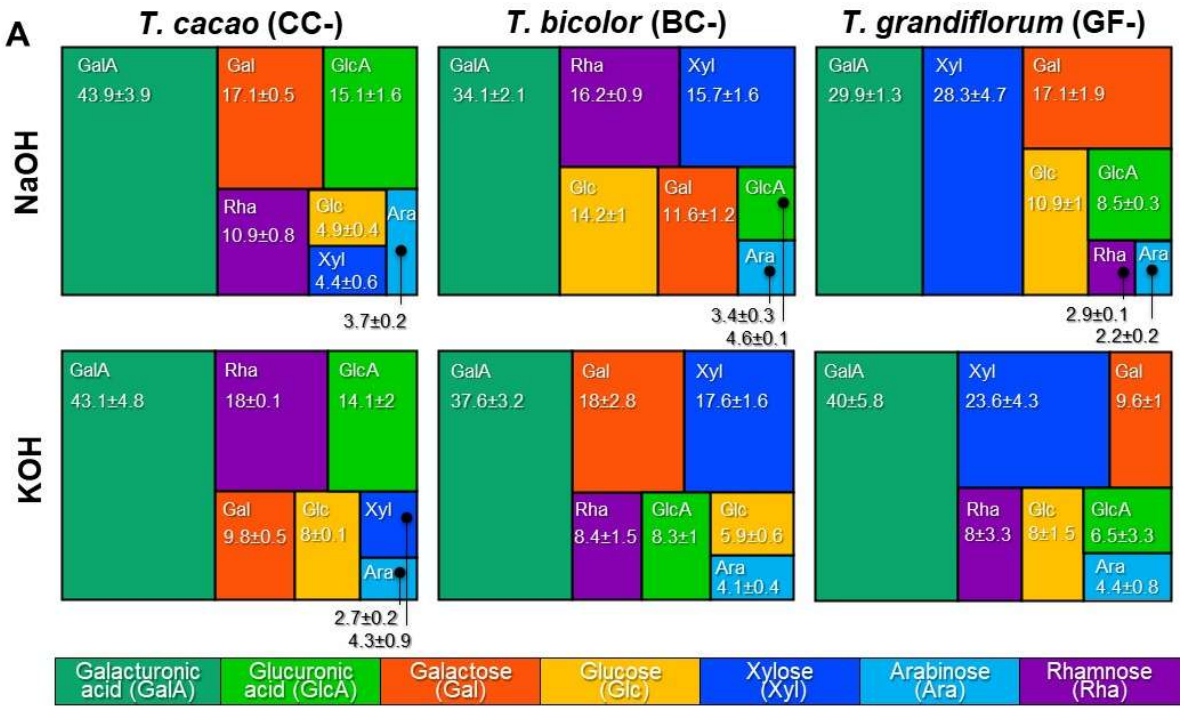

B

	CC-NaOH	CC-KOH	BC-NaOH	BC-KOH	GF-NaOH	GF-KOH
HG (%)	33.0±4.0	25.1±4.8	17.9±2.3	29.2±3.5	27.0±1.3	32.0±6.7
RG-I (%)	42.6±1.3	48.5±0.7	47.4±2.2	39.0±3.5	25.1±1.9	30.0±4.7

Figure 56. *(**A**) Structural sugar composition (%) of the polysaccharides extracted from the different Theobroma genus biomasses using NaOH and KOH alkaline treatments, analyzed by UHPLC. (**B**) Table reporting the corresponding calculated values (%) for the homogalacturonan (HG) and rhamnogalacturonan I (RG-I) domains. The homogalacturonan (HG) domain content was estimated as GalA(mol%) − Rha (mol%) while the rhamnogalacturonan-I (RG-I) using the formula RG-I (%) ≈ 2Rha (mol%) + Ara (mol%) + Gal (mol%).*

Furthermore, HG is a linear polymer made up of α-1,4-linked D-galacturonic acid units, which can carry varying degrees of methoxycarbonyl substitutions. In our work, CC-NaOH showed the highest proportions of the HG domain (~33%) similar to results reported by Wu et al. (Wu et al., 2023) that have extracted pectic polysaccharides from citrus segment membranes.

Species-specific differences in sugar composition were notable. *T. grandiflorum* exhibited particularly high xylose content (28.3% with NaOH and 23.6% with KOH), indicating a greater presence of xylan, xyloglucan or xylogalacturonan structures compared to *T. cacao* and *T. bicolor*. These polysaccharides, along with cellulose and lignin, contribute to the strength and resilience of fruit pods, providing mechanical protection and aiding the plant's defense against herbivores, damage, and pathogens (Munzert and Engelsdorf, 2024). These

structural features are crucial for seeds or pods that must withstand harsh environmental conditions before germination.

Molecular weight measurement

Figure 57 A illustrates the molecular weight (Mw) profiles of the different fragments of the samples extracted from the *Theobroma* species pod husks. Regardless of the fruit type and both alkaline conditions, all extracted pectic polysaccharides exhibited a bimodal Mw distribution. Notably, in all the samples, the first fragment to appear in the SEC elution profile (Peak 1) exhibited the highest Mw, where the highest Mw (783 kDa) was observed in the material extracted from *T. cacoa* after using NaOH as extraction solvent, while the lowest Mw (92.5 kDa) was found in the *T. grandiflorum* extract obtained with KOH. Regarding the remaining fragments (Peak 2 and Peak 3), the estimated Mw ranged between ~9 and ~37 kDa.

*Furthermore, the molecular weight distribution of the extracted pectic polysaccharides is presented in **Figure 57 B**, highlighting distinct differences in their Mw profiles. The calculated values are available in the supplementary material (*

Supplementary 10). As control, the commercial citrus pectin exhibited a predominantly high-Mw population (513 kDa), accounting for ~91.5% of the total signal.

In contrast, the biopolymers extracted from *Theobroma* species demonstrated more complex Mw distribution, with up to 3 distinct populations. Such multimodal patterns have been consistently reported in the literature across various plant sources (Benito-Román et al., 2024; Li et al., 2019). Among the three species, *T. bicolor* yielded the lowest Mw values, followed by *T. grandiflorum* and *T. cacao*. Notably, KOH extraction resulted in a higher proportion of low-MW fractions in *T. bicolor* (20.5 kDa, ~78.8% relative area) and *T. grandiflorum* (92.5 kDa, ~61.6% relative area). Conversely, *T. cacao* showed a predominance of high-Mw materials under both extraction methods: 1069.5 kDa (~85.9% area) and 1567.1 kDa (~76.8% area) for KOH-extracted samples. However, the high polydispersity index (PDI > 1.7) in these samples suggests a broad distribution of molecular sizes. The commercial citrus pectin, despite having a single dominant peak, showed an even higher PDI (>2.2), indicating an even more heterogeneous mixture of molecular weights.

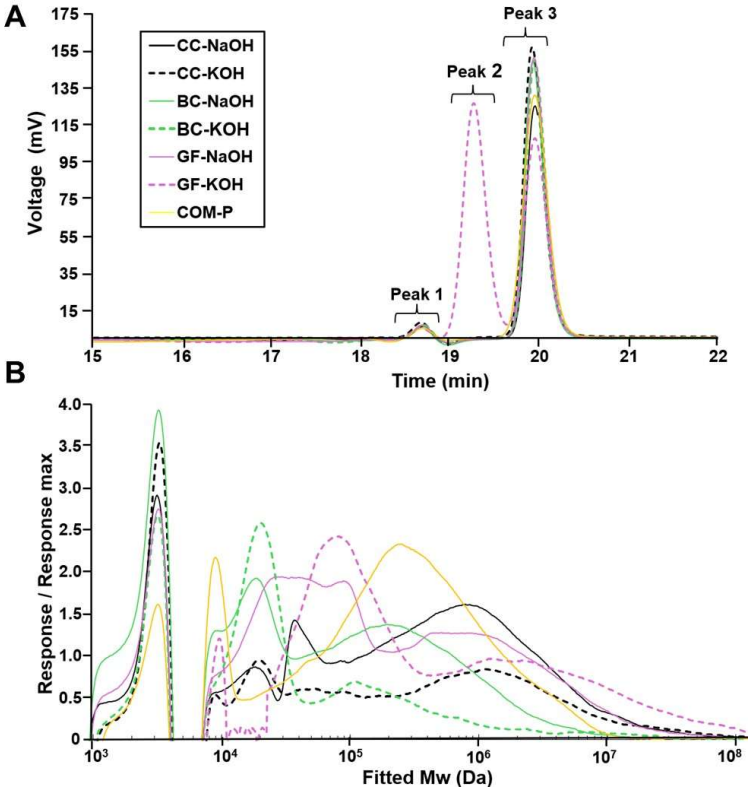

Figure 57. *Chromatographic SEC profiles of extracted pectic polysaccharides and COM-P (A) and the associated Mw distribution (B).*

^{1}H NMR measurement

To elucidate the structural features of the materials extracted from *Theobroma* species, ^{1}H NMR spectroscopic analysis was performed at 80 °C. This temperature was selected to reduce sample viscosity and improve resolution, thereby enabling more accurate chemical shift assignment, particularly for anomeric proton environments. The anomeric region (5.5-4.3 ppm) of the spectra exhibited well-defined resonances that are characteristic of typical glycosidic linkages present in pectic and hemicellulosic polysaccharides. Notably, the signal at 5.28 ppm, corresponding to the α-(1→4)-linked oligomers of galacturonic acid (Hachem et al., 2016) was clearly identified in all extracted samples (**Figure 58**). In contrast, the resonance at 4.55 ppm, attributed to β-(1→4)-linked oligomers of galacturonic acid, was detected only in the BC-NaOH sample.

The signal at 5.27 ppm, attributed to the anomeric proton of rhamnose residues involved in both 1,2- and 1,2,4-linkages (indicative of branched rhamnogalacturonan regions), was most prominent in the GF-NaOH, CC-KOH, and BC-KOH extracts. A closely related signal at 5.25 ppm was observed in the CC-NaOH and BC-NaOH samples, likely representing the same structural motif. The slight shift in chemical shift may reflect differences in the local conformational environment of the rhamnose residues, such as variations in hydrogen

bonding, ionic interactions or chain flexibility and hydration (Shi et al., 2017). The signal at 5.17 ppm, characteristic of internal α-(1→5)-linked arabinofuranosyl (Araf) residues in a linear arabinan or branched α-Araf substituted at O-3 or O-2, was exclusively observed in the BC-NaOH and BC-KOH spectra, indicating a unique structural feature in the polysaccharides extracted from *T. bicolor*; while an intense peak in the range of 5.10-5.12 ppm was detected across all extracts and was assigned to terminal α-(1→ 5) arabinofuranosyl residues (non-reducing end α-L-arabinofuranosyl) (Konishi et al., 2006). Furthermore, in CC-NaOH and CC-KOH samples, a distinct signal at 5.06 ppm was assigned to α-(1→4)-linked galactopyranosyl (GalpA) uronic acid. This was accompanied by minor resonances at 5.04 and 5.01 ppm, which were less apparent in the other samples and may reflect local variation in glycosidic environments or branching patterns (Colquhoun et al., 1990).

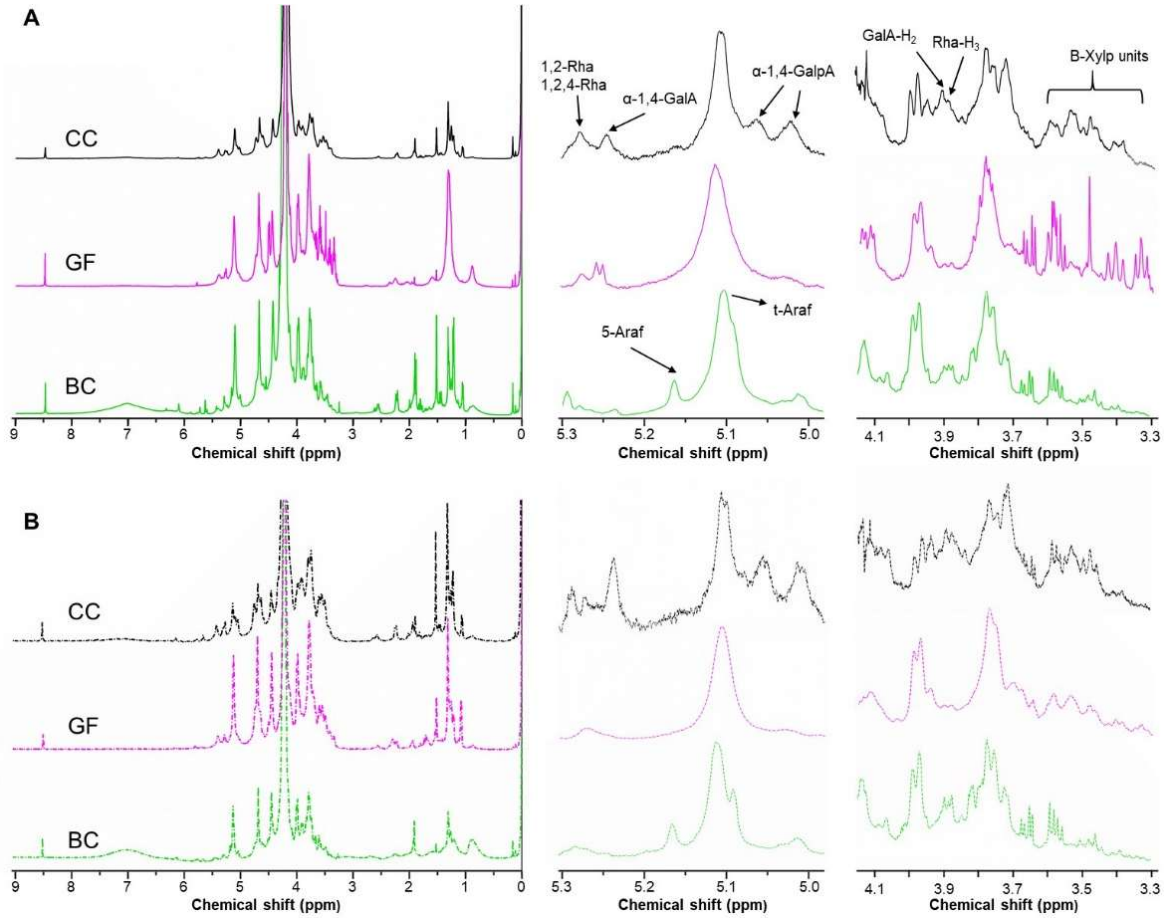

Figure 58. *^{1}H NMR spectra (700 MHz) of the extracted materials, showing the full spectra (left of each panel) and expanded regions corresponding to the chemical shifts δ 5.3-5.0 ppm (middle) and δ 4.1-3.3 ppm (right). Panel (**A**) shows the NaOH-extracted materials, while panel (**B**) corresponds to the KOH-extracted materials.*

Additional signals corresponding to ring protons of α-galacturonic acid residues were consistently observed across all extracts. The H-5 resonance appeared at 4.67 ppm, H-4 at 4.43 ppm, and H-2 at ~3.90 ppm (Hotchkiss et al., 2023). The H-3 signal was found near 4.11 ppm but partially overlapped with the residual D_2O peak and adjacent resonances from rhamnose units. The H-3 proton of α-rhamnose was assigned to a signal at 3.87 ppm. The H-6 methyl protons of rhamnose appeared as doublets centered at 1.23 and 1.30 ppm in all samples, except for GF-NaOH, where a single peak was observed at ~1.30 ppm. Interestingly, the ratio of substituted (1,2,4-Rha) to unsubstituted (1,2-Rha) rhamnose ranged from 5.5:1 for CC-NaOH to 1.1:1 for BC-NaOH, based on the integration of the H6,6′ signals at 1.22 and 1.29 ppm, respectively.

These resonances are attributed to rhamnose residues linked via (1→2) glycosidic bonds to galacturonic acid, as well as (2→1)-linked rhamnose units bearing O-4-substituted galacturonic acid branches, structural features consistent with rhamnogalacturonan-I (RG-I) domains (Huamani-Palomino et al., 2023). Additionally, two distinct signals between 2.0 and 2.2 ppm were assigned to acetyl groups attached at the 2-O and 3-O positions of GalA residues (Bédouet et al., 2003). Peaks in the 3.3-3.6 ppm range were attributed to the H-2, H-3, H-4 and H-5 protons of β-xylopyranose (β-Xylp) units, with higher intensities observed in the materials extracted from *T. grandiflorum* and *T. bicolor* (Patova et al., 2021). The H-1 of β-1.4-xylopyranosyl units typically appears between 4.4-4.5 ppm; however, its proximity to the H-4 signal of galacturonic acid may result in spectral overlap. Finally, a resonance at 8.5 ppm was detected in all the extracts. This signal is indicative of aromatic protons from phenolic compounds (Kontogianni et al., 2013). The presence of this signal suggests the co-extraction or retention of aromatic phenolics, potentially from cell wall-bound polyphenols, during the alkaline extraction process.

The degree of esterification (DE) of the extracted materials was determined via ^{1}H NMR using the method developed by H. Grasdalen et al. (Grasdalen et al., 1988b), resulting in a DE ranging from of 38.09% calculated for CC-NaOH to 22.65% for GF-KOH (**Supplementary 11**) where the extractions in NaOH revealed higher DE.

FTIR-ATR characterization and esterification degree determination

Figure 59 shows the FTIR-ATR spectra of extracted materials and commercial pectin, revealing similar peaks across all samples. A broad band at 3313 cm^{-1} corresponds to hydroxyl group stretching, while the 2925 cm^{-1} band, prominent in commercial pectin, represents C–H bending vibrations (CH, CH_2, CH_3). Other signals in this range result from

O–H stretching due to hydrogen bonding in carboxyl groups (Ghoshal and Negi, 2020). The broad O–H absorption highlights intermolecular hydrogen bonds, affecting galacturonic acid's hydroxyl groups (Gnanasambandam and Proctor, 2000). As a result, O–CH_3 activity is masked by hydroxyl groups, making it unreliable as an indicator of methoxylation (Ghoshal and Negi, 2020), masking O–CH_3 activity as a methoxylation indicator.

The esterified carboxyl group (COOR) appears at 1725 cm^{-1}, supporting the presence of pectic polysaccharides in the extracted materials. The 1800-1500 cm^{-1} spectral region was crucial for determining DE via FTIR, with 1725 cm^{-1} (C=O stretching) and 1610 cm^{-1} (COO^- asymmetrical stretching) indicating carboxylic ester and acid groups (Manrique & Lajolo, 2002).Using Chatjigakis' method (Chatjigakis et al., 1998), DE ranged from 25.6% (GF-KOH) to 38.8% (CC-NaOH), aligning with ^1H NMR results (**Supplementary 11**).

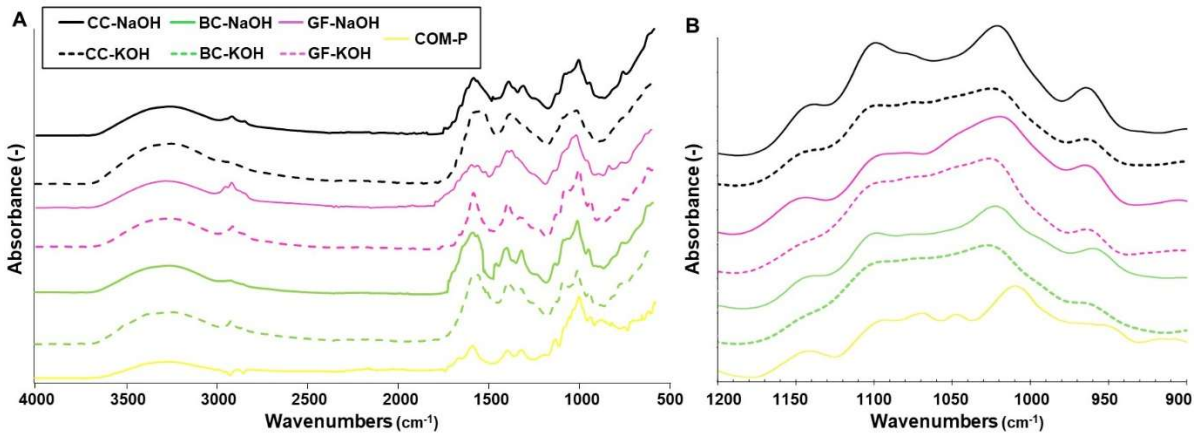

***Figure 59**. FTIR-ATR spectra of the biopolymers extracted from the Theobroma genus recorded in the mid-infrared range (4000-550 cm^{-1}) (**A**) and in the 1200-800 cm^{-1} region for the identification of monosaccharides with different structures and compositions (**B**). COM-P refers to the commercial pectin.*

Below 1430 cm^{-1}, characteristic pectin bands at 1313, 1230, and 1145 cm^{-1} correspond to methyl groups, C–H bending, and C–O–C stretching in the pyranose ring that is part of the structure of the sugars that make up pectin (Pereira et al., 2016) and hemicellulose polysaccharides (Peng and Wu, 2010).

Furthermore, FTIR-ATR analysis revealed that each extracted material exhibits a distinct absorption maximum within the 1200-900 cm^{-1} range (**Figure 59 B**). This spectral region is primarily influenced by ring vibrations, along with contributions from C–OH stretching and C–O–C glycosidic bond vibrations. Notably, bands at ~1070 and ~1043 cm^{-1} can be attributed to rhamnogalacturonan, consistent with previous reports (Kacuráková et al., 2000). However, a band at 1072 cm^{-1} was also characteristic of β-galactan, that is associated to pectic polysaccharide. Also, a slight peak observed at 1066-1064 cm^{-1} can be assigned to

the β-(1→4)-mannan, a typical component of hemicellulosic polysaccharides (Kacuráková et al., 2000). Commercial pectin differs in band shape due to industrial extraction and raw material variation, as pectin's structural properties depend on feedstock and isolation methods (Chan and Choo, 2013).

Differential Scanning Calorimetry (DSC) and Thermo-Gravimetric Analysis (TGA)

DSC measurements were conducted for each extracted sample and compared with the analysis of a commercial pectin (**Figure 60 A**). The thermograms of all samples revealed similar behavior, highlighting the presence of exothermic and endothermic peaks (**Supplementary 12**). The broad endothermic peaks, observed in the range from 146.2 °C for GF-KOH to 169.6 °C for BC-NaOH, indicated weight loss due to the vaporization of water. Similarly, Siqueira et al. (Siqueira et al., 2022) identified an endothermic peak at 132 °C in films produced of pectin extracted from *C. brasiliense* mesocarp. Interestingly, the materials extracted using NaOH presented higher endothermic peaks, resulting more comparable to the commercial counterpart. Exothermic peaks were observed in the range from 237.1 °C for CC-KOH to 267.0 °C for BC-NaOH, reflecting decomposition caused by pectic polysaccharides chain degradation. Nisar et al. reported exothermic decomposition temperatures ranging from 231.53 °C to 234.88 °C for citrus pectin films containing clove essential oil (Nisar et al., 2018). Similarly, Cervera et al. (Cervera et al., 2004) and Chaudhari and Singhal (Chaudhari and Singhal, 2015) observed peaks between 200 °C and 300 °C, associating them with characteristic polymeric decomposition.

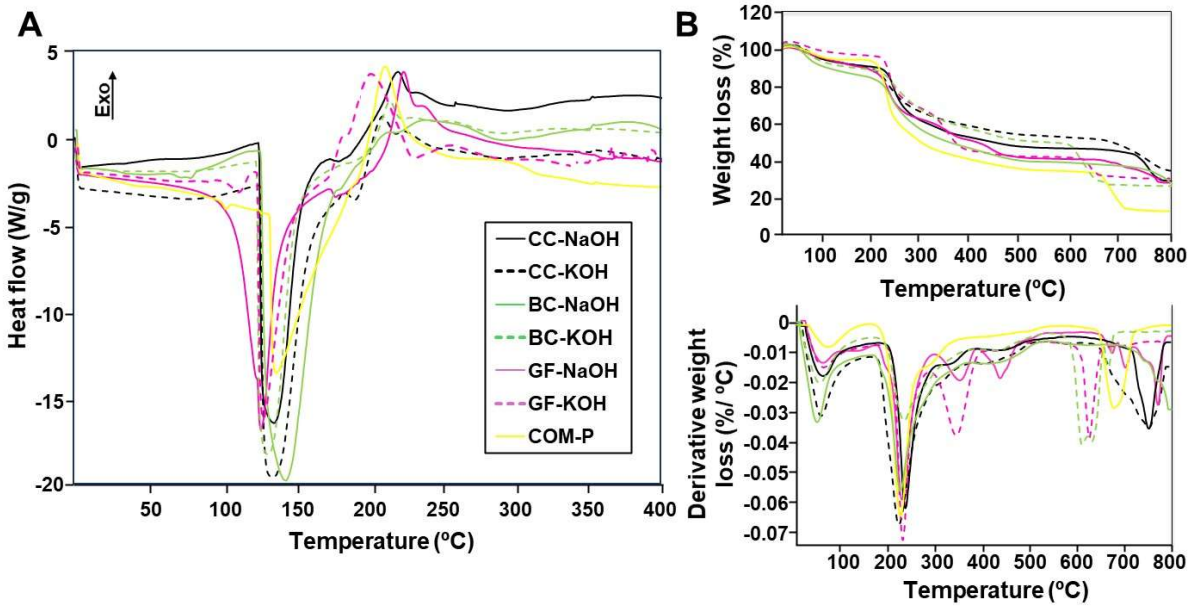

***Figure 60**. Thermal characterization of the extracted materials and the commercial pectin: (**A**) DSC thermograms and (**B**) TGA (top) and DTG curves (bottom).*

Figure 60 B presents on the top the TGA thermographs, illustrating the weight loss trend as a function of temperature, while on the bottom it displays the DTG thermographs, highlighting the maximum thermal degradation temperature (T_{max}) for the extracted polysaccharides and commercial pectin. The TGA traces display similar mass loss patterns demonstrating comparable resistance to thermal degradation that occurred in four distinct stages. The first stage took place from room temperature up to 115 °C, with a T_{max} ranging from 70 °C for GF-KOH and to 74.2 °C for CC-NaOH (**Supplementary 13**) and ~6% weight loss.

The first stage corresponds to the loss of free water weakly bound to the polymer, facilitated by pectin's hydrophilic nature, aligning with Nešić et al. (Nešić et al., 2017). The second stage (185-260 °C), visible in all the extracted materials, showed a T_{max} from 235.0 °C (CC-KOH) to 243.4 °C (CC-NaOH) with a 30% weight loss, that can be attributed to the decomposition of pectic polysaccharides (Wang et al., 2016). Additionally, a third stage (285-400 °C), more pronounced in the materials extracted from *T. grandiflorum* (both extraction methods) and *T. cacao* (using NaOH), exhibited degradation peaks around 350 °C and 420 °C, with weight loss ranging from 40% (*T. cacao*) to 58% (*T. grandiflorum*). These peaks can be attributed to the decomposition of the hemicellulosic polysaccharides (Werner et al., 2014).

Beyond 500 °C, mass loss slowed as remaining char degraded, confirmed by exothermic heat flow traces. Notably, *T. grandiflorum* materials degraded at lower temperatures (640-675 °C) than *T. cacao* (750-755 °C). All extracted materials exhibited thermal behavior like commercial pectin but with higher residual char at 800 °C (~40% vs. ~18%), likely due to residual hemicelluloses and celluloses.

Rheological analysis

Rheological analysis showed distinct behaviors between *Theobroma*-derived materials and commercial pectin (COM-P, Merck). **Figure 61 A** illustrates viscosity as a function of shear rate, where all solutions exhibited shear-thinning behavior, typical of pectin solutions due to polymer chain alignment under shear stress (Chan et al., 2017).

CC-NaOH and CC-KOH displayed the highest viscosity, suggesting *T. cacao* materials form a highly structured, viscous network, likely due to high molecular weight and strong intermolecular interactions. COM-P had the lowest viscosity, highlighting the superior rheological performance of NaOH-extracted samples.

Frequency sweep tests at 25 °C showed GEL behavior (G’ > G’’) for all solutions, including COM-P (**Figure 61 B**). At higher frequencies (>50 rad/s), BC-KOH exhibited SOL behavior (G’ < G’’), indicating a transition in mechanical properties. The extraction process significantly influenced solution behavior, possibly because of the higher content of bioactive compounds, with NaOH-extracted *T. cacao* and *T. bicolor* materials achieving higher viscosity. These findings suggest that *T. cacao*-derived materials are most suitable for applications requiring high viscosity and strong gel structures, *T. bicolor* materials are ideal for moderate viscosity needs, and *T. grandiflorum* materials are better suited for applications requiring more fluid-like properties. The choice of biomass and extraction method can be tailored to optimize materials functionality for specific industrial uses.

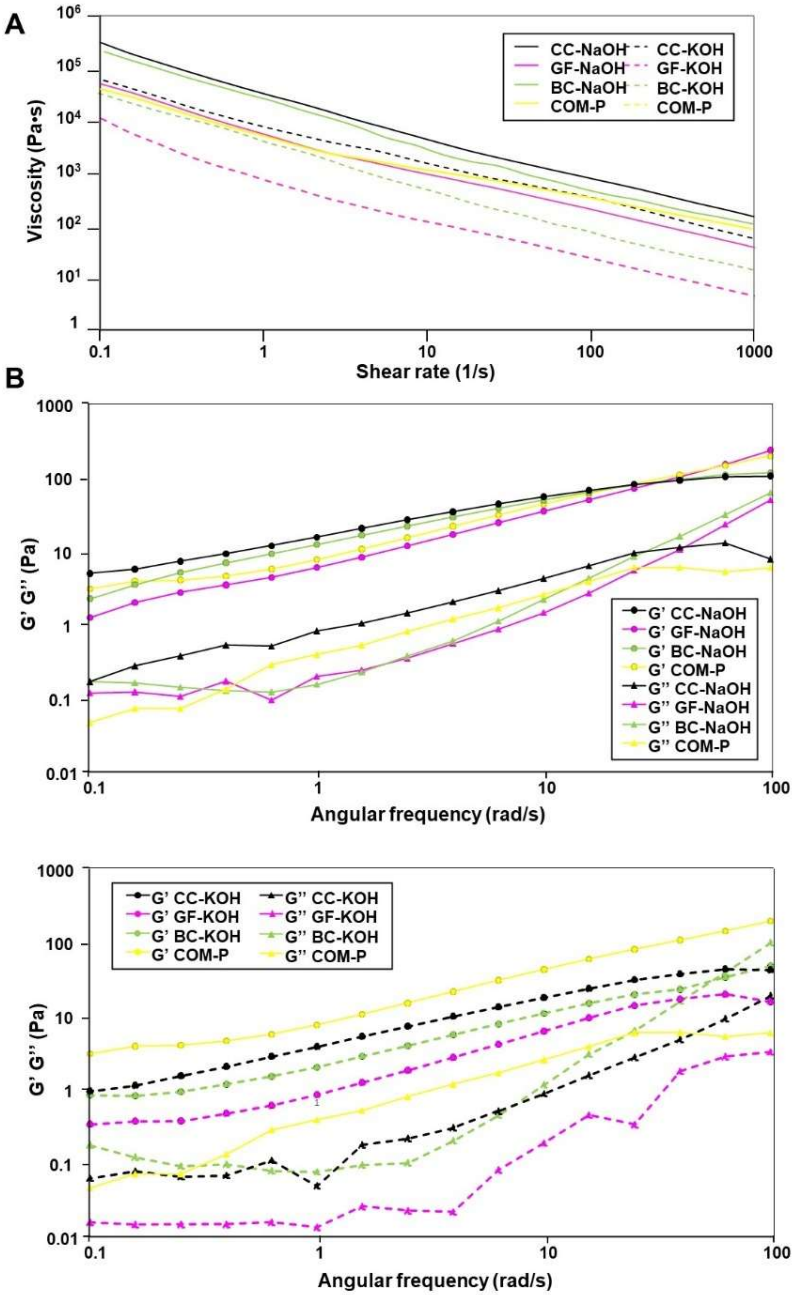

Figure 61. *(A) Flow-curves and (B) rheological properties obtained from frequency sweep tests of the solutions prepared from the extracted materials. Citrus pectin from Merck (COM-P) has been used as control.*

Multivariant analysis

Principal Component Analysis (PCA) of samples showed that PC1 and PC2 accounted for 76.4% of the variance (**Figure 62**). PC1 was driven by GalA content, molecular weight (Mw), and degree of esterification (DE), while PC2 reflected antioxidant activities (ORAC, FRAP) and thermal properties (DSC). The scores plot revealed distinct clustering, with higher DE and Mw samples separating from lower values, emphasizing their impact on samples behavior. The loadings analysis confirmed GalA, Mw, and DE strongly correlated with PC1, defining structural properties, while PC2 was linked to antioxidant activity and

thermal stability, suggesting extraction influences these attributes. Mw and DE showed a positive correlation, while variations in ORAC and FRAP indicated structural modifications affecting radical scavenging properties.

Higher DSC values corresponded to altered thermal stability due to molecular interactions from chemical modifications. The correlation between Mw, DE, and GalA supports their role in solubility and gelation, consistent with studies emphasizing esterification and molecular weight in the extracted materials functionality.

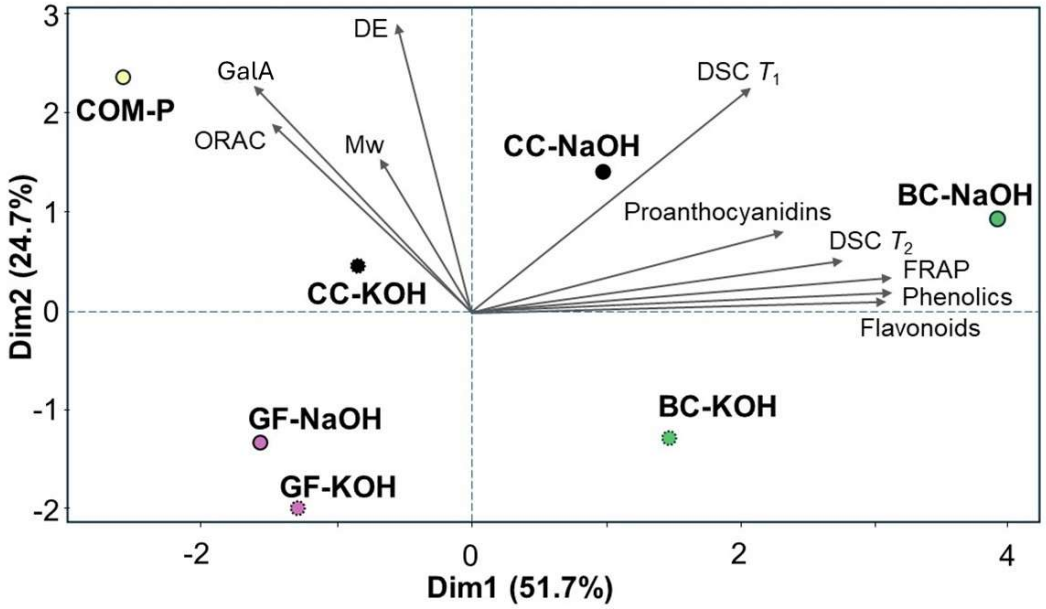

Figure 62. *Principal Component Analysis (PCA) biplot illustrating the distribution of pectin samples and the contribution of the evaluated variables.*

4.1.4. Conclusion

This study examined polysaccharides extraction from *T. cacao* (CC), *T. grandiflorum* (GF), and *T. bicolor* (BC) using NaOH and KOH, revealing significant differences in yield, bioactivity, and functionality. *T. bicolor* (NaOH) exhibited the highest bioactive content, antioxidant activity, and diverse metabolomic profile, including amino acids, phenolics and alkaloids, enhancing its therapeutic potential. *T. cacao* (NaOH) had the highest molecular weight (~783 kDa) and viscosity, ideal for gel-forming applications requiring structural stability, and *T. cacao* (KOH) had the highest galacturonic acid content (43%). NaOH extraction generally yielded higher bioactive compounds (e.g. phenolics) content and structural integrity, while KOH preserved homogalacturonan integrity, offering distinct functional advantages. The extraction yields varied by species and solvent, with *T. cacao* (NaOH) showing the highest recovery, whereas *T. grandiflorum* had the lowest.

Compared to commercial citrus pectin, *T. bicolor* and *T. cacao* materials exhibited superior bioactive profiles, molecular weights, and gel-forming properties. Their antioxidant properties exceeded commercial pectin, making them suitable for nutraceutical and pharmaceutical applications. Enhanced viscosity, gel strength, and superior thermal stability in *T. cacao* and *T. bicolor* suggest their feasibility in industrial applications requiring heat resistance. These findings highlight *Theobroma* polysaccharides as functional material, offering tailored physicochemical and bioactive properties for specific applications.

This study has some limitations, including the lower extraction efficiency observed with KOH and the high variability in biomass composition among *Theobroma* species, which may affect process reproducibility. Moreover, the need for further purification and standardization constrains immediate scalability. For translation towards clinical or industrial use, future research should focus on optimizing downstream processing to improve purity and standardize composition, conducting scale-up studies to ensure reproducibility across biomass batches, and evaluating bioactivity in application-specific models. In particular, the antioxidant, prebiotic, and anti-inflammatory properties of the extracts warrant investigation for their potential use as functional ingredients or supplements in functional foods, or as gel-forming scaffolds in tissue engineering applications.

4.1.5. Supplementary

Supplementary 5. *Values of explanatory variables: powder-to-solvent ratio (X_1), temperature (X_2), extraction time (X_3).*

Run	X_1, powder-to-solvent ratio (g/mL)	X_2, Temperature (°C)	X_3, Extraction time (min)
1	0.0222	55	20
2	0.0167	55	40
3	0.0111	55	20
4	0.0111	30	40
5	0.0167	30	60
6	0.0167	30	20
7	0.0111	55	60
8	0.0167	55	40
9	0.0222	30	40
10	0.0222	80	40
11	0.0167	80	60
12	0.0167	55	40
13	0.0222	55	60
14	0.0111	80	40
15	0.0167	80	20

Supplementary 6. *Moisture and ash composition in fresh and dry shells of T. cacao (CC), T. grandiflorum (GF) and T. bicolor (BC).*

Species	Fresh shell moisture (%)	Fresh shell ash (%)	Dry shell moisture (%)	Dry shell ash (%)
CC	84.61 ± 0.86	4.36 ± 0.12	8.03 ± 0.39	3.31 ± 0.33
GF	72.13 ± 1.14	0.66 ± 0.09	8.84 ± 0.08	9.43 ± 0.21
BC	75.12 ± 2.47	1.60 ± 0.07	9.19 ± 0.67	4.99 ± 0.1

Supplementary 7. *Fresh and dry weight and yield percentage of fruit shells T. cacao (CC), T. grandiflorum (GF) and T. bicolor (BC).*

Species	Initial fresh weight (g)	Dry weight (g)	Yield (%)
CC	596.67 ± 116.23	57.67 ± 13.47	27.07 ± 1.44
GF	606.67 ± 85.05	328.33 ± 36.17	54.37 ± 3.97
BC	765.33 ± 165.91	126.50 ± 41.64	48.69 ± 2.08

Supplementary 8. *Moisture and ash composition in fresh and dry shells of T. cacao (CC), T. grandiflorum (GF) and T. bicolor (BC). The values are expressed in g/ 100g.*

Species	Biopolymer moisture (NaOH)	Biopolymer moisture (KOH)	Biopolymer ash (NaOH)	Biopolymer ash (KOH)
CC	4.17 ± 0.53	3.03 ± 0.61	3.46 ± 0.43	3.77 ± 0.60
GF	5.75 ± 1.45	4.93 ± 1.35	3.01 ± 0.31	2.58 ± 0.30
BC	7.11 ± 1.14	5.42 ± 0.66	3.47 ± 0.16	3.07 ± 0.13

Supplementary 9. *List of the metabolites found in the extracted materials along with their relative abundance (Worksheet Supplementary material Metabolite list provided at: https://doi.org/10.1016/j.carbpol.2025.124070)*

Supplementary 10. *Estimation of Mp, Mn and Mw (kDa), PDI and the relative area (%) of the peaks detected from the biopolymers extracted from T. cacao (CC), T. grandiflorum (GF) and T. bicolor (BC) in NaOH and KOH alkaline conditions respectively. Commercial pectin (COM-P) has been used as control.*

	Mp (kDa)	**Mn (kDa)**	**Mw (kDa)**	**PDI**	**Area (%)**
T. cacao NaOH (CC-NaOH)					
Peak 1	785.7	410.0	1069.5	2.608	85.9
Peak 2	36.9	38.6	39.3	1.018	9.4
Peak 3	17.8	18.2	18.7	1.030	4.7
T. cacao KOH (CC-KOH)					
Peak 1	1145.9	890.8	1567.1	1.759	76.8
Peak 2	19.5	19.0	19.7	1.038	23.2
T. bicolor NaOH (BC-NaOH)					
Peak 1	191.3	177.8	331.7	1.866	71.9
Peak 2	18.8	16.2	17.9	1.105	28.1
T. bicolor KOH (BC-KOH)					
Peak 1	108.9	131.1	161.3	1.230	21.2
Peak 2	20.1	18.7	20.5	1.099	78.8
T. grandiflorum NaOH (GF-NaOH)					
Peak 1	511.0	878.6	1562.6	1.779	71.9
Peak 2	29.3	43.2	57.6	1.334	28.1
T. grandiflorum KOH (GF-KOH)					
Peak 1	91.35	1022.2	1293.8	1.266	32.6
Peak 2	14.0	91.1	92.5	1.016	61.6
Peak 3	9.6	9.5	9.5	1.014	5.8
Commercial pectin (COM-P)					
Peak 1	254.6	226.4	512.8	2.265	91.5
Peak 2	8.8	8.8	8.9	1.010	8.5

Supplementary 11. *Degree of esterification (DE) of the extracted biopolymers was determined via* ^{1} *H-NMR and FTIR-ATR*

	DE (%)	
Sample	^{1} NMR	FTIR-ATR
CC-NaOH	38.09	38.8
CC-KOH	35.97	33.1
GF-NaOH	27.18	29.2
GF-KOH	22.65	25.6
BC-NaOH	36.90	38.1
BC-KOH	32.16	33.3

Supplementary 12. *Endothermic peak (T1) and exothermic peak (T2) detected in the DSC thermograms of all the extracted biopolymers and commercial pectin.*

Sample	T_1	T_2
CC-NaOH	161.6	247.8
CC-KOH	159.7	237.1
GF-NaOH	147.0	242.5
GF-KOH	146.2	238.5
BC-NaOH	169.6	267.0
BC-KOH	158.1	243.1
COM-P	160.9	237.3

Supplementary 13. *Temperature of the degradation peaks detected by DGA analysis.*

	Degradation temperature (ºC)				
Sample	Peak 1	Peak 2	Peak 3	Peak 4	Peak 5
CC-NaOH	74.2	243.3	321.6	438.3	755.0
CC-KOH	71.6	235.0	n.d.	419.6	756.6
GF-NaOH	70.8	239.1	356.6	439.2	675.8, 771.7
GF-KOH	70.0	235.8	354.1	417.5	640.8
BC-NaOH	72.6	235.4	n.d.	421.6	n.d.
BC-KOH	7	246.6	n.d.	439.2	611.6, 632.5
COM-P	81.6	233.3	n.d.	n.d.	679.2

5. Future Perspectives: Artificial Intelligence in Biomaterials

5.1. The role of artificial intelligence in biomaterials science: a review

*(This section has been published in: Martelli, A.; Bellucci, D.; Cannillo, V. The Role of Artificial Intelligence in Biomaterials Science: A Review. Polymers **2025**, 17, 2668. https://doi.org/10.3390/polym17192668. Reproduced in accordance with the publisher's copyright policy.)*

N.B. The introductory section is an updated and revised version of the article published. The changes concern the introduction only, aimed at avoiding repetition and ensuring consistency with the preceding chapters.

5.1.1. Introduction

Artificial intelligence (AI) can be defined as the ability of machines to mimic human cognition, making decisions, and processing complex reasoning through advanced algorithms (Kerner et al., 2021). AI is increasingly utilized across various aspects of daily life, such as virtual assistants on smartphones. Moreover, its use is revolutionizing scientific fields as well. Examples of AI applications in medicine include the identification of carcinogenic human metabolites, the detection of skin cancer, and the diagnosis of conditions like Parkinson's disease (Mittal et al., 2022; Smak Gregoor et al., 2023; Yang et al., 2022). Similarly, AI has the potential to significantly advance research in biomaterials science.

Currently, biomaterials research heavily relies on a "trial-and-error" approach, which often leads to significant waste of resources, including manpower, time, materials, and finances (Sha et al., 2020). A potential solution to this problem is the use of AI for pattern recognition and property prediction, with a consequent reduction in extensive experimentation.

Although several reviews have discussed the application of AI in biomaterials, they typically focus on a single material class or provide only a broad overview of AI techniques (Gokcekuyu et al., 2024; Sarvestani et al., 2024; Suwardi et al., 2022; Xie, 2023). To fill this gap, the aim of this review article is to highlight the key results achieved through the application of AI models in biomaterials science. The first part will explain how AI models work and address the main challenges in their use. Subsequently, the major results achieved in biomaterials research will be presented, categorized by material class.

5.1.2. Methodology

Purpose: This review aims to highlight recent advances, identify current challenges, and outline future perspectives for the integration of AI in biomaterials science. Given its exploratory and integrative objectives, it adopts a narrative review format rather than a systematic review.

Scope: The review is limited to peer-reviewed publications in English reporting AI or machine learning applications in materials science, with particular emphasis on biomedical uses. Non-peer-reviewed sources were excluded. Literature was retrieved from major databases (e.g., Scopus, Google Scholar, and PubMed) using keyword combinations such as *Artificial Intelligence*, *Machine Learning*, *Biomaterial*, and *Polymer*.

Function: The review organizes and critically synthesizes the retrieved studies by material class (polymers, ceramics, metals, composites) and AI function (property prediction, process optimization, material design, or biological response prediction), enabling balanced comparisons across different systems and algorithms.

Intent: The intention is to provide researchers and clinicians—including those not specialized in AI—with an integrated overview that identifies knowledge gaps, highlights promising approaches, and offers guidance for future experimental and regulatory developments.

5.1.3. Artificial Intelligence: from data science to machine learning

AI can be defined as a system capable of mimicking human cognition by making decisions and processing complex reasoning through advanced algorithms, with little to no human intervention (Kerner et al., 2021; Russell and Norivg, 2021). To achieve this, AI relies heavily on data science, which is one of its key components. Data science involves extracting knowledge from large datasets, both structured and unstructured. This data-driven approach enables AI to make predictions about future outcomes, with accuracy depending on the size and quality of the dataset. Initially, AI was based on hard-coded rules linked by logical inference, such as “if the premises are true, then the conclusion is...”. As a result, early AI systems were limited by the human ability to express all the knowledge required to perform complex tasks (Janiesch et al., 2021).

Machine learning (ML), with its approach based on data science, overcomes these limitations. ML improves its accuracy through an iterative process, learning from training

data and discovering new patterns not explicitly programmed in each cycle (Kerner et al., 2021). A major advantage of the ML approach is its ability to address both forward and inverse problem designs. In simpler terms, this means that ML can be used for predictive tasks, such as forecasting the properties of a given material structure. Additionally, it can be applied to inverse tasks, such as identifying which materials exhibit specific properties based on predefined requirements.

ML is broadly categorized into four types: supervised, unsupervised, semi-supervised, and reinforcement learning.

Supervised learning relies on labelled data and user-defined output targets, enabling the machine to learn from these labelled examples. The goal is to learn a mapping function from input to output. For instance, labelled data might consist of thousands of images of materials, each annotated with information about the material type. The resulting model will be able to distinguish one material from another.

In contrast, unsupervised learning works on unlabelled data. In this case, the goal is to discover hidden patterns or clusters in the data without explicit guidance on what to look for (Alloghani et al., 2020). For example, given a dataset of mechanical properties associated with unknown materials, this approach enables ML to identify patterns and potentially cluster the materials into conventional categories such as metals, ceramics, polymers, and composites.

Semi-supervised learning combines aspects of both supervised and unsupervised learning by leveraging both labelled and unlabelled data. The aim is to improve prediction accuracy beyond what can be achieved using only labelled data (Sarker, 2021).

Reinforcement learning, on the other hand, is an approach based on feedback from the environment, in which algorithms tackle sequential decision-making problems in dynamic and often uncertain settings (Sutton and Barto, 1998).

The objective of any reinforcement learning algorithm is to learn the rules that connect its actions with the environment, thereby achieving rewards for favourable outcomes. This means that algorithms select their actions based solely on their current observations, and by the end of the learning process, they are able to choose actions that yield optimal outcomes and higher rewards (Littman, 2023; Sequeira and Gervasio, 2020). In other words, reinforcement learning follows a computational trial-and-error strategy. A practical example

of this approach is an optimization process in which the model maximizes desired material properties while minimizing costs or waste.

Within supervised and unsupervised learning, various models exist, each tailored to specific tasks.

Classification algorithms group input data into specific categories based on their features and are typically used with labelled data to predict class labels. Regression models, on the other hand, predict numerical values from input features, requiring labelled data to learn the mapping between inputs and desired numerical outputs (Aized Amin Soofi and Arshad Awan, 2017). Unlike classifiers, which produce discrete outputs, regression models can predict continuous values (Sidey-Gibbons and Sidey-Gibbons, 2019). Both classification and regression models are commonly used for prediction tasks within supervised learning. Association learning aims to discover meaningful relationships between variables in unlabelled datasets, identifying associations and correlations that occur more frequently than would be expected by chance (Sarker, 2021). Clustering, often used with unlabelled datasets, groups similar entities based on quantitative similarity measures (Sarker, 2021). Association learning and clustering are commonly used for recognizing underlying structures and patterns in data within an unsupervised learning approach (Kerner et al., 2021).

These models use various methods—such as decision trees, random forests, and linear regression—that differ in prediction accuracy, training speed, and the number of variables they can handle. Therefore, selecting the appropriate algorithm is essential and should be based on the specific problem being addressed.

A further evolution and subcategory of ML is deep learning (DL), which can tackle more complex tasks through a specialized approach (Janiesch et al., 2021). One significant advantage of DL is its ability to extract higher-level features from raw input data, a process that could be time-consuming, fragile, and not easily scalable with traditional ML methods. However, it is important to note that employing a reliable DL model typically necessitates a larger number of samples compared to other ML models (Choudhary et al., 2022).

DL relies on multi-layer artificial neural networks (ANNs), also known as deep neural networks. These networks are inspired by the biological nervous system and consist of interconnected elements called neurons. Neurons are arranged in layers, and each layer analyses different aspects of the input data through previously presented algorithms. For example, the first layer might detect the colour of an image, the next one might identify

shapes, and subsequent layers gradually build up to recognize the entire object. In this way, the input signal propagates through each layer, allowing the model to train and refine its predictions (Abdolrasol et al., 2021; Bishop, 2006).

For a schematic representation of the relationships among AI, ML, and DL, please refer to **Figure 63**. To provide an accessible overview of the AI approach, we will present a simplified version of the algorithm in **Figure 64**. For a more comprehensive understanding of the process, please refer to the cited reviews (Karande et al., 2022; Song et al., 2020). For practical, hands-on guidance on developing AI, readers can refer to the work of Meyer et al. (Meyer et al., 2023).

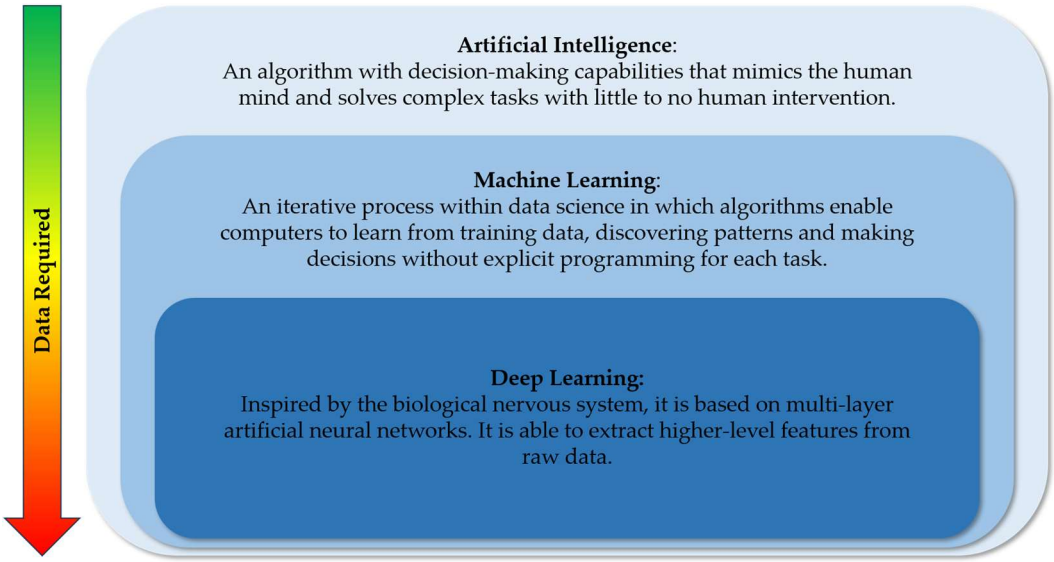

***Figure 63**. Representation of the relationships among AI, ML, and DL, with increasing data requirements.*

The process begins by identifying a specific goal, typically related to material or process design, or knowledge discovery. This is followed by data collection, which may involve conducting experiments or simulations and extracting information from reference materials. It is essential to emphasize that data quality is paramount, necessitating a data-cleaning step. Once the data is prepared, it needs to be formatted for the AI algorithm, often involving the conversion of non-numerical information into a machine-readable format. Data collection and translation are particularly critical in material science and will thus be the focus of the following sections.

The next critical step involves selecting an appropriate model based on the specific problem at hand. This choice depends on various factors, such as task type (e.g., property prediction, inverse design), the size and type of data (e.g., numerical, graphical), and the requirements for interpretability. Once the model is chosen, it needs to be trained, which

involves the optimization of its parameters for best performance. Prototyping at this stage is crucial, as it allows for assessing the reasonableness of the results. Common challenges include model overfitting and underfitting. Overfitting occurs when a model captures unnecessary details from the training dataset, which can degrade its performance. To mitigate this, techniques such as resampling (e.g., dropout) or regularization (e.g., Lasso or Ridge regression) can be applied, or a portion of the training data can be set aside for validation. Underfitting, on the other hand, happens when the model fails to capture underlying patterns due to insufficient data, resulting in poor performance. In such cases, the primary solution is to increase the amount of training data.

To determine which model or dataset best meets the study's objectives, different models can be compared using evaluation metrics such as R^2 or the F1 score (Vamathevan et al., 2019). R^2 and F1 are performance metrics representing, respectively, the proportion of variance in the dependent variable explained by the independent variables, and the harmonic mean of precision and recall. Once a model has been successfully trained and validated through prototyping, it is ready for its intended application, contributing to the achievement of the initial goal. By systematically following these steps, AI methods can be effectively applied to address the specific problem at hand.

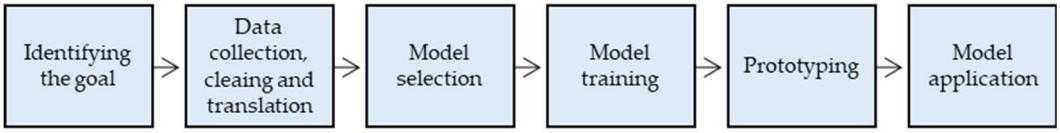

Figure 64. *The AI approach, step by step.*

It is evident that building a traditional algorithm differs significantly from creating an AI algorithm. Traditional algorithms are rule-based procedures designed to solve specific computational problems, which limits their versatility without human intervention. In contrast, AI algorithms learn from data without explicit inputs, thus expanding their versatility and ability to discern patterns as they are free from a priori assumptions. This suggests that traditional algorithms rely heavily on human input, while AI algorithms are heavily reliant on data, which must be both numerous and high-quality. Furthermore, traditional algorithms are fully programmed and can be considered “white box”, unlike AI algorithms, which are regarded as “black box”, leading to a lack of interpretability in the decision-making process. Finally, AI algorithms require a higher level of hardware compared to traditional algorithms (Lai, 2019; O’Mahony et al., 2020; Rajula et al., 2020; Taye, 2023). The pros and cons of both methods are summarized in **Table 15**.

Table 15. *Pros and cons of traditional and AI algorithms.*

Traditional algorithms		Artificial Intelligence algorithms	
Pros	Cons	Pros	Cons
Transparent process	Limited versatility	Free from assumption	Lack of interpretability of the process
High efficiency for well-defined problems	Human-dependency	High adaptability and scalability	Data-dependency
Low computational requirements			High computational requirements

Data collection

As previously mentioned, AI operates using a data-driven approach. A key challenge in crafting robust AI algorithms lies in the availability and comparability of data (Cencer et al., 2022). For well-known properties (e.g., thermal characteristics) it is possible to refer to handbooks or online databases (**Table 16**) to increase the size of datasets. However, experimental datasets frequently encounter constraints and lack comparability, primarily due to variations in experimental procedures or data analysis methods. Indeed, although numerous handbooks and databases exist for different materials, they often suffer from fragmented data and provide only a limited range of properties.

This poses a significant challenge when attempting to predict poorly labelled or sparsely measured properties, such as in vivo degradation in biomaterials, due to the limited size of available datasets (McDonald et al., 2023). Furthermore, the lack of a clearly defined and measurable standard for concepts like biocompatibility further limits the effectiveness of data mining techniques, as highlighted by Mateu-Sanz et al. (Mateu-Sanz et al., 2024).

Table 16. *Examples of online databases for material properties*

Database	Material	Reference
PI1M	Polymer	(Ma and Luo, 2020)
PolyInfo	Polymer	(Otsuka et al., 2011)
Khazana	Polymer	(R. Ramprasad Group, n.d.)
Polymers: a Property Database	Polymer	(CHEMnetBASE Products, 2022)
Polymer Property Predictor and Database	Polymer	(Center for Hierarchical Material Design, n.d.)
Block Copolymer Phase Behavior Database	Polymer	(Rebello et al., n.d.)
CAMPUS	Polymer	("CAMPUS," n.d.)
Electron Affinity and Ionization Potential Data	Polymer	(Aldeghi and Coley, 2022)
Silkome	Spider silk	(Arakawa et al., 2022)
SciGlass	Ceramic	(iScienceSearch, n.d.)
Interglad	Ceramic	(International Glass Database System, n.d.)
The Materials Project	Miscellanea	(Jain et al., 2013)
Ansys Granta	Miscellanea	(ANSYS Inc., n.d.)
MatWeb	Miscellanea	("MatWeb. Material property data," n.d.)
Atomly	Miscellanea	(Miao and Sheng, n.d.)

Small datasets can lead to problems such as model underfitting or overfitting, and several examples of this can be found in the following paragraphs (Brauer et al., 2007; Chen et al., 2025; Douest et al., 2024; Ege and Boccaccini, 2024; Kuenneth et al., 2021a). In such cases, two main strategies can be employed to address the issue: increasing the dataset size during data collection, or selecting AI models able to perform well with limited amounts of data. Examples of such models include support vector machines (SVM), Gaussian process regression (GPR), deep neural networks (DNN) or generative models like generative adversarial networks (GAN), variational autoencoders (VAE) (Xu et al., 2023; Z. Yu et al., 2021).

One effective strategy to address the challenge of limited data is to leverage *simulated datasets* derived from well-understood properties, as exemplified by John et al. in their research on optoelectronic properties (St John et al., 2019). This approach shows great potential, particularly for generating labelled datasets for properties that are rarely characterized due to their inherent complexity or limited application. However, it is important to recognize that error propagation represents a significant drawback of this

method. Therefore, careful consideration and thorough evaluation are essential to ensure the accuracy and reliability of the predicted properties, thereby safeguarding their fidelity.

As an alternative, experimental data can also be leveraged. However, as mentioned earlier, the trial-and-error approach consumes significant time and resources. To mitigate this, high throughput or automated experiments can be employed to acquire more data in a shorter timeframe, optimizing the efficiency of the data generation process (J. N. Kumar et al., 2019; Reis et al., 2021). Strategies for high-throughput experimentation to create polymer libraries were comprehensively outlined by Oliver et al. (Oliver et al., 2019). In general, high-throughput approaches hold promise for properties that can be measured using small quantities of material, such as cytotoxicity (McDonald et al., 2023).

A third approach to data acquisition lies between simulated data and experimental data. Through transfer learning, a model pre-trained on a large simulated dataset can be fine-tuned using a smaller experimental dataset. This hybrid approach effectively addresses concerns related to error propagation while concurrently minimizing the quantity of required experimental data (Yamada et al., 2019). However, it is important to note that the number of experiments needed is still greater than what is typically obtained during a research endeavour (McDonald et al., 2023). This highlights the ongoing challenge of balancing data efficiency and accuracy in the modeling process. For additional insights into transfer learning, Zhuang et al. provide detailed information and summarizes over 40 representative transfer learning approaches (Zhuang et al., 2021). **Figure 65** illustrates the data collection methods.

Figure 65. *Data collection methods*

Despite significant efforts in creating numerous databases, the need for comprehensive data sharing within the scientific community remains crucial. This involves ensuring data homogenization and enrichment with relevant chemical and physical properties. Implementing benchmarks or standardized testing approaches emerges as a viable strategy for achieving comparable data standards.

Data translation

The properties of materials are intricately dependent on their atomic structures, making the computational representation of chemical structures a challenging task. To ensure the effectiveness of AI methods, the machine-readable representations of a material's structure must meet specific criteria (Damewood et al., 2023): a) the similarity or dissimilarity between two data points should accurately reflect the similarity or dissimilarity between the underlying structures they represent, b) the representation should be broadly applicable across the full domain of materials of interest, c) it should be computationally more efficient than directly calculating the target property. Several methodologies have been developed to address this challenge.

Atomistic geometries can be described using local, global, and topological descriptors (Damewood et al., 2023). Local descriptors characterize the chemical structure by detailing the immediate surroundings of each atom, representing the entire structure as a composition of these localized features (Behler and Parrinello, 2007). These representations can be generated through a Voronoi tessellation of a chemical structure. In a Voronoi tessellation,

space is divided into cells, each containing a single atom and encompassing the region closer to that atom than to any other. These descriptors enable the development of AI models with high predictive accuracy, while also allowing for the separate examination of distinct fragments. This feature is particularly useful when optimizing materials compositions in materials design (Isayev et al., 2017). For example, local descriptors can define chemical bonds and their lengths, which can then be used to predict the bond dissociation energy of a compound (Y. Liu et al., 2024).

Global descriptors consider both atom types and their positions, simultaneously defining geometric and physical properties. These descriptors, inspired by the nuclear repulsion term in the molecular Hamiltonian and free energy, represent molecules as Coulomb matrices (Rupp et al., 2012). Unlike local descriptors, which focus on specific parts of a material, global descriptors represent the entire material, allowing for faster evaluation of properties. However, their main limitation is the inability to evaluate local interactions, such as surface or interfacial interactions between materials (Halldin Stenlid and Abild-Pedersen, 2024).

Topological descriptors are widely used to characterize structures within complex, high-dimensional datasets. When applied to the spatial arrangements of atoms in amorphous or crystalline structures, topological methods reveal inherent geometric features that provide valuable insights for downstream predictions, including phase changes, reactivity, and separations. Among these descriptors, the persistent homology method excels in identifying significant structural features that are both machine-readable and physically interpretable (Carlsson, 2020). However, this approach is computationally expensive, requiring a careful balance between the advantages of capturing complex structural information and the computational cost of generating these features (Damewood et al., 2023). Using these descriptors, Jiang et al. (Jiang et al., 2021) developed a model for predicting the properties of crystalline materials. Trained on a dataset of over 30,000 compounds, the model revealed a limitation of topological descriptors: lower prediction accuracy was observed for compounds containing less common elements.

Graph-based representations allow to represent chemical structures from structural data. This method converts a set of atoms, characterized by atomic nodes and edges that define their relative positions, into a graph. Examples of such representations include Crystal Graph Convolution Neural Networks (CGCNN) (Xie and Grossman, 2018), MatErials Graph Networks (MEGNet) (Chen et al., 2019), and the Simplified Molecular Input Line System (SMILES) (Weininger, 1988).

CGCNN has demonstrated strong predictive performance for material properties such as shear modulus, as well as atomic-scale properties like formation energy (Xie and Grossman, 2018). However, the model does not account for global state descriptors, such as temperature, that are crucial for predicting state-dependent properties like free energy. To overcome this limitation, the MEGNet model (Chen et al., 2019) was developed, incorporating such inputs and extending the model's application from crystals to molecules.

Similarly, SMILES was developed to describe molecular structures of polymers as graphs (Weininger, 1988). However, a major limitation of SMILES lies in its inability to represent the stochastic nature of polymers. The introduction of BigSMILES aimed to address this issue, applying the SMILES syntax to repeated units and including additional bonding descriptors to accurately represent complex polymer structures (Lin et al., 2019).

Despite their advantages, graph-based representations still face challenges—in particular, their dependence on known atomic positions and their limited ability to predict molecular distortions (Damewood et al., 2023). Accurately capturing the dynamic behaviour of molecules often requires computationally expensive simulations to model structural distortions and their impact on material properties.

Stoichiometry-based representations rely on well-established atomic information, such as atomic radii, which are readily available from databases (Ward et al., 2016). This approach makes AI methodologies more accessible to non-experts, especially compared to methods that require detailed structural data. However, it produces only a single prediction for each stoichiometry, even when multiple synthesizable structures may exist (Damewood et al., 2023). In summary, stoichiometry-based representations offer a practical solution for non-experts, particularly when atomic-level structural information is unavailable or when conducting a broad exploration of various chemical compositions.

For a more comprehensive overview of data descriptors for materials, we recommend referring to the cited review (Damewood et al., 2023; Stuart et al., 2023) or exploring the DScribe database (Himanen et al., 2020), which provides common descriptors for materials along with tutorials for their use.

Model selection

Selecting the appropriate AI model for a specific task can be challenging due to the wide range of models available. Because of the intrinsic complexity of different problems and the unique characteristics of each AI approach, certain models are better suited to specific

scenarios. In biomaterials science, the main AI applications can be broadly categorized into property prediction and material design, with the latter representing an inverse design problem.

Property prediction is likely the most extensively explored task, as it is generally less complex than inverse design and can produce reliable results even with relatively small datasets (McDonald et al., 2023). Supervised regression models are commonly used to predict well-characterized properties, such as thermal behaviour, while graph-based models are particularly well-suited for graph-structured data formats (e.g., SMILES notation) (Reiser et al., 2022). Additionally, when large datasets are available, deep learning models can be effectively employed to predict material properties (Liang et al., 2025).

In contrast, material design tasks often rely on deep learning approaches, which are typically data-hungry and require large, high-quality datasets (Choudhary et al., 2022). In particular, generative models, which approximate probability distributions, represent a promising approach for material discovery, although they may generate unstable or chemically infeasible compounds (Dan et al., 2020; Menon and Ranganathan, 2022; Zeni et al., 2023). To address such limitations, emerging strategies such as physics-informed neural networks (PINNs) offer a compelling alternative. By embedding physical laws directly into the training process, PINNs help reduce data requirements and enhance model generalizability (Khatamsaz et al., 2023; Raissi et al., 2019).

Table 17 summarizes the categories of models commonly used for property prediction and material design, along with a brief description of their data requirements and limitations of the models. It is important to note that the size and format of the dataset should guide researchers in selecting the appropriate AI model.

Table 17. *Brief description of models commonly used in material science. Random forest (RF), support vector machine (SVM), Gaussian process regression (GPR), crystal graph convolution neural networks (CGCNN), materials graph networks (MEGNet), artificial neural networks (ANN), convolutional neural network (CNN), generative adversarial networks (GAN), variational autoencoders (VAE).*

Model	Requirements	Advantages	Limitations	Ref.
Classical ML (RF, SVM, GPR, etc.)	Effective on small to medium-sized datasets (ranging from tens to thousands of samples) when using structured, curated features.	Easier interpretation. Fast training on structured data.	Requires manual feature engineering. Limited generalization and sensitive to data redundancy.	(Gokcekuyu et al., 2024; Li et al., 2023)
Graph Neural Networks (CGCNN, MEGNet, etc.)	Require large graph-based datasets.	Can capture complex relational/structural information.	Computationally demanding. Sensitive to training quality. Poor performance on limited data.	(Reiser et al., 2022)
Deep learning (ANN, CNN, etc.)	Requires large, high-dimensional datasets (e.g., images, spectra). Benefits from pretraining.	Can learn complex, non-linear relationships. Flexible input types.	Requires tuning and high compute resources. Black box. Overfitting on small data.	(Choudhary et al., 2022)
Generative models (GAN, VAE, etc.)	Requires large datasets (often > 104 samples). Typically uses composition matrices or structural encodings derived from large databases.	Can generate novel materials and expand datasets.	Generated structures may violate chemical or stability constraints. Difficult to train.	(Dan et al., 2020; Menon and Ranganathan, 2022; Pyzer-Knapp et al., 2025; Zeni et al., 2023)

5.1.4. Machine learning for biomaterials

Biomaterials, as previously defined, encompass a broad category of materials and implants engineered to interact with biological systems for medical purposes. These materials, which can be either natural or synthetic, are used across various medical fields, including diagnostic devices, dental and orthopaedic implants, drug delivery systems, and regenerative medicine. Their design aims to fulfil specific functions when in contact with

biological fluids, living tissues, and organs. To achieve this, biomaterials must exhibit essential properties, such as biocompatibility, hemocompatibility (the ability to interface with blood without eliciting adverse reactions), bioactivity (the capacity to form stable chemical bonds with living tissues), as well as adequate mechanical strength and tailored degradation characteristics suited to their intended in vivo application.

To effectively design biomaterials, it is crucial to establish well-defined physical, chemical, or biological properties as input parameters, providing the basis for predicting the corresponding output properties. A clear example of this is the identification of the optimal material for bone scaffolding, as studied by Javaid et al. (Javaid et al., 2023). First, the mechanical properties of natural cortical and cancellous bone were considered in selecting the synthetic biomaterials. These properties were then used to develop an AI model. The results of their study revealed that brushite and titanium alloy emerged as the most suitable materials for mimicking cancellous and cortical bones, respectively. Conversely, polycaprolactone (PCL) and chitosan were identified as the least suitable materials for replicating cancellous and cortical bones, respectively. Furthermore, AI methodologies can be harnessed to predict the mechanical properties of devices manufactured with various patterns, as demonstrated by Agarwal et al. in their investigation of polylactic acid (PLA)-based bone screws produced via AM technique (Agarwal et al., 2022).

Ceramics and Bioactive glasses

Ceramics find extensive application in the field of medicine owing to their remarkable biocompatibility and superior mechanical properties, particularly in wear applications. Among these ceramics, zirconia stands out for its widespread use in dentistry, thanks in part to its colour, which closely matches that of natural teeth. Therefore, in aesthetic dentistry, achieving a perfect colour match between ceramic restorations and surrounding teeth is highly challenging, due to the variable clinical situation. To address this challenge, Yang et al. (J. Yang et al., 2023) successfully developed a regression model based on three categories of input: material types, background colours and thicknesses. As a consequence, a large dataset of 720 samples was obtained, which was subsequently partitioned into training and validation sets at an 8:2 ratio. The model's primary outputs—colour difference and lightness difference—were carefully chosen to gauge its efficacy. The resulting model demonstrated impressive predictive capabilities. However, it is important to note, as acknowledged by the authors, that its utility lies in serving as a time-saving guidance tool rather than a substitute

for the expertise of dental professionals. Ultimately, the application of knowledge and clinical expertise by professionals remains primary in making the final determination.

In orthopaedics, hydroxyapatite (HA) is among the most commonly used ceramics, given its status as one of the main components of natural bone (Shi et al., 2021). Trying to design HA scaffolds with mechanical, physical, and microarchitectural properties resembling those of bone, Ibrahimi et al. (Ibrahimi et al., 2024) explored scaffold architectures based on Triply Periodic Minimal Surfaces topology. Initially, they employed an ML model to generate a set of scaffolds with the desired architecture. Then, the mechanical, physical, and morphometric properties of the generated scaffolds were assessed using the finite element method (FEM). The acquired properties served as a dataset for another ML model, which predicted the optimal topology parameters to achieve specific properties. Simulation tests on the optimized scaffold demonstrated properties comparable to trabecular bone. However, it is worth noting that the feasibility of this structure with current technologies remains unverified. Additionally, the model did not consider the possible presence of defects resulting from the manufacturing process. Further studies on these aspects are necessary to ascertain the reliability of the model.

Bioceramics can also exhibit bioactive and bioresorbable behaviours within a biological system. Furthermore, incorporating doping agents into ceramic compositions can enhance or introduce certain therapeutic properties. Common examples of such behaviours include HA, β-tricalcium phosphate (β-TCP), and bioactive glass (BG). These materials are often utilized as fillers, for example, in bone injuries, to aid in the healing process. To explore the relationship between chemical compositions and physical behaviours in HA nanopowders, Yu et al. (J. Yu et al., 2021) developed two AI models, an ANN and a genetic programming model, using their own experimental dataset. The robustness of these predictive models was subsequently validated using a genetic programming approach. The results showed good accuracy of the models in predicting the crystallite size, micro-strain, and grain boundary volume fraction of HA nanopowders based on chemical compositions, with an $R^2 > 0.8$ for each variable.

Evaluating the correlations between chemical compositions and physical properties is fundamental also for BG development. However, measuring these properties can pose challenges due to the various techniques involved in characterization. In response to this challenge, Cassar et al. (Cassar et al., 2021) devised a model by gathering data from the SciGlass database (iScienceSearch, n.d.), aiming to predict parameters such as glass

transition temperature, liquidus temperature, Young's modulus, thermal expansion coefficient, refractive index, and Abbe number. Specifically, they compared three different AI algorithms. The results showcased high predictive accuracy across all models, attributed to the high amount of data utilized. Nonetheless, it is worth noting that these predictions exhibit higher errors for glasses containing chemical elements with limited representation in the training dataset.

Understanding ceramic bioactivity and the resulting bone formation from a biomaterial graft is non-trivial, typically necessitating expensive and time-consuming in vivo tests. To address this challenge, numerous studies are focusing on predicting bone formation following graft procedures. Wu et al. (Wu et al., 2021) have developed an ANN model that correlates the outcomes of an animal study involving scaffold treatment for a major segmental defect in sheep tibia. Both bone regeneration outcomes and simulated data were utilized as training data for this model. Remarkably, the model successfully predicts bone remodelling at 12 months following the application of a Sr–Hardystonite–Gahnite scaffold in a large segmental defect of a sheep tibia.

With a similar objective, Motojima et al. (Motojima et al., 2023) built a ML model capable of predicting bone formation rates, material properties, crystalline phases, and functional groups based on test settings. This model was also designed to aid in the formulation of experimental conditions for novel bioceramics. Remarkably, the model successfully facilitated the design of new biomaterials with enhanced bone regeneration capabilities. However, it is important to note that no experiments were conducted to validate the model initially. Subsequent to this limitation, a follow-up study by the same research group addressed this gap by validating the predicted bone regeneration rate through experimental tests conducted on porcine tibiae (Horikawa et al., 2024). In particular, they constructed two ML models – one mapping fabrication conditions to scaffold properties, and another predicting in vivo bone-forming ability from those properties. An inverse design analysis proposed fabrication recipes for target bone formation; the actual bone formation in 12-week porcine implant tests fell within the predicted error range.

Similarly, Lin et al. (Lin et al., 2024) conducted a study to assess the accuracy of ML models in predicting the osteoinductivity of biomaterials, using a literature-derived database spanning three decades. To address challenges related to limited or incomplete data, a data enhancement strategy was employed. The resulting model was then used to guide the experimental design of a biphasic calcium phosphate scaffold, which was tested in an *in vivo*

study on beagles. The study demonstrated that the extreme gradient boosting algorithm (XGBoost) outperformed other models in predictive accuracy and enabled the design of a scaffold that exhibited enhanced osteogenesis compared to the average outcomes reported in the literature. These studies demonstrate how AI predictions of bio-ceramic performance (e.g., osteogenesis) can be confirmed by animal studies, effectively bridging the gap between computational design and biological reality.

The resorbability of BG is attributed to their solubility in aqueous environments, a characteristic closely linked to the chemical composition of the specific BG. Numerous studies have explored the variations in BG compositions to optimize their degradation behaviour. Among these efforts, Brauer et al. (Brauer et al., 2007) attempted to address this challenge using an ANN model. Their study focused on the dissolution of phosphate-based BG in deionized water, aiming to model the solubility behaviour of these glasses. While the study highlights the potential of this innovative approach, the limited number of experiments conducted may have constrained the accuracy of the model.

This limitation was overcome by Han et al. (Han et al., 2020), who developed a model based on a comprehensive dataset comprising over 1300 experimental observations. Their model was specifically trained to predict the dissolution behaviour of four distinct types of BG: sodium borosilicate, sodium aluminoborate, sodium aluminoborosilicate, and sodium boro-phosphosilicate. Each dataset entry included ten inputs (such as glass composition, initial solvent pH, temperature, system surface area-to-volume ratio, and time) and one output (expressing the degree of glass dissolution as normalized mass loss of critical ions). The results showed the model's exceptional predictive capabilities. However, as noted by the authors, a broader and more diverse database is necessary to enable the model to engage in optimization processes, such as predicting the requisite BG composition to achieve a desired dissolution rate.

Thanks to their dissolution in biological environments, BG can exploit their therapeutic effects. By manipulating their chemical composition, it is possible to give various desirable traits, including antibacterial activity. Various elements, such as Ag and Cu, have been explored for their antibacterial potential (Anand et al., 2022; Pajares-Chamorro et al., 2021). However, achieving optimal chemical compositions can be time-consuming due to the multitude of variables involved. In an effort to simplify this research, Echezarreta and Landin (Echezarreta-López and Landin, 2013) developed an algorithm capable of predicting the antibacterial effects of BGs. Following an extensive literature review to identify critical

variables influencing antibacterial effects, they employed neuro-fuzzy logic to reduce the complexity, focusing on key variables: SiO_2 concentration (*w/w*%), CaO concentration (*w/w*%), BG concentrations (mg/mL), bacterial species, and the pH recorded post-bacterial cultivation with BG. Fuzzy systems, like the one employed in this study, are well-suited for tackling problems with unclear or ambiguous variable relationships. By utilizing a rule-based approach, fuzzy systems can integrate expert knowledge and effectively handle uncertainty (Sedigh et al., 2023). Their findings revealed that antibacterial activity primarily depends on the release of alkaline ions into the solution, resulting in a rise in pH levels. Notably, differences in BG antibacterial efficacy across different bacterial species are primarily attributable to the composition of BG, particularly its calcium ion content.

Due to their aforementioned properties, BGs can be used in orthopaedics for bone tissue restoration. Specifically, AM is frequently employed to create porous structures, typically referred to as scaffolds, which aim to mimic the architecture of natural bone tissue (Martelli et al., 2023). However, optimizing scaffolds poses challenges due to the complexity of bone structure. In addressing this issue, AI techniques are applicable for optimizing the design of AM bone scaffolds, offering a promising avenue for enhancing scaffold performance and functionality. In a pioneering effort, Wu et al. (Wu et al., 2024) implemented a mechano-biological optimization strategy for 3D printed bioactive glass-ceramic scaffolds with cost-effective evaluation methods. The study demonstrated the design of scaffolds tailored for critical size segmental bone defects in sheep tibiae, employing a lithography-based ceramic manufacturing technique to fabricate the optimized scaffolds. Three distinct structures were chosen as candidate unit cell structures for optimization. In this investigation, the Young's modulus associated with each unit cell was treated as input, while the locally varying micro-strain component linked with each unit cell served as the output. The results demonstrated that the optimized functionally graded scaffolds outperformed conventional empirical designs, resulting in enhanced bone formation.

Polymers

Polymers are extensively used in tissue engineering thanks to their adaptability, optimal biocompatibility, and good mechanical properties. Currently, synthetic polymers serve as the preferred choice due to their higher mechanical properties and reduced allergic response compared to natural polymers (Kalirajan et al., 2021). In both cases, mechanical, chemical, and biological properties can be adjusted by combining different monomers or modifying their ratios. The resulting polymer, known as a copolymer, exhibits a combination of

properties derived from its constituent monomers (Semenov and Nyrkova, 2012). However, predicting copolymer properties can be challenging due to the numerous variables. Good results have been obtained with an AI model that used a weighted average of two or more homopolymer fingerprints to generate a copolymer fingerprint, and predict the glass transition temperature (T_g), melting temperature (T_m), and degradation temperature (T_d) of copolymers with an R^2 value of 0.94 (Kuenneth et al., 2021b). These characteristic temperatures are fundamental to characterizing a polymer, since they are indicators of structural properties, processability and thermal stability. Additionally, the same group compared the accuracy of single-task and multi-task models in predicting 36 polymer properties. Results revealed that single-task model are more sensitive to data sparsity and missing data, with normalized root mean squared error (*RMSE*) up to 1. On the other hand, the multi-task approach addressed the challenge of limited data availability by identifying inter-property correlations and required less training time compared to many single-task models (Kuenneth et al., 2021a).

Dataset size is a common issue in AI approaches. An alternative for addressing this challenge in polymer science is the use of simulated data based on a large dataset of molecular building blocks. Utilizing this solution along with a variational autoencoder (VAE) model, Batra et al. (Batra et al., 2020) designed novel polymers with high thermal and electrical requirements. Moreover, the study highlighted the versatility of this approach for predicting numerous properties. Similarly, polymers can be designed using a genetic algorithm (GA), a model based on the natural selection process. This method visualizes a polymer as a sequence of interconnected building blocks that define its properties and can be rearranged to achieve different characteristics. Although this approach requires fewer tuning parameters compared to other generative models, it is highly influenced by the dataset, the mutation rate, and the available building blocks (Kim et al., 2021).

AI models exhibit a notable capability to accurately predict the mechanical properties of materials. This attribute becomes particularly advantageous in scenarios where mechanical assessments pose challenges, such as with hydrogels. Hydrogels represent a category of polymers extensively utilized in diverse areas of tissue engineering, notably in the regeneration of soft tissues like skin and muscle. These materials are defined by their structure as networks of water-soluble polymers, which can be crosslinked either physically or chemically to form a gel. However, one of the primary drawbacks associated with hydrogels is their inherently low mechanical properties, particularly when compared to other

biomaterials (J. Yu et al., 2021). To predict the mechanical properties of hydrogels, a model was developed to examine the effects of alginate dialdehyde (ADA) content, cross-linker content, pore size, and BG content on the stiffness of ADA-gelatine hydrogels using the extreme gradient boosting ML algorithm. The model showed high predictive accuracy and appeared to fit the data well. However, the absolute errors between the predicted and observed values remained relatively high. This discrepancy may be attributed to the small dataset, based on literature data, which likely led to overfitting, as noted by the authors (Ege and Boccaccini, 2024).

An analogous study focused on Polyvinyl alcohol (PVA)/Gelatine porous hydrogels (Khalvandi et al., 2023). Leveraging over 30.000 data points obtained from mechanical tests, the model employed input parameters including the concentrations of PVA, Gelatine, and cross-linker, alongside the duration of the tests. The resultant stress and strain values in a uniaxial compressive test constituted the model's output. Demonstrating high accuracy across all three regimes—linear elastic, plateau, and densification—the predictive model proved to be highly accurate. Similarly, Das et al. (Das et al., 2023) developed a model to predict the porosity of alginate gel scaffolds. The model was trained with over 100 samples with known porosities and considered viscosity, contact angle, and surface tension as inputs. Subsequently, the model was employed to forecast the optimal parameters for achieving maximum porosity, which were then utilized to fabricate an alginate gel scaffold, resulting in an apparent porosity closely aligned with the predicted values. Notably, the model demonstrated considerable potential, particularly due to its incorporation of the contact angle, a parameter greatly influenced by surfactant content, as an input.

Cytotoxicity—defined as the property of being toxic to cells—is a pivotal parameter in assessing the safety of materials for biological applications. Nevertheless, conducting cytotoxicity tests requires significant time and expertise. Thus, the ability to predict the cytotoxic behaviour of materials holds considerable promise. In response to this challenge, Xu et al. (Xu et al., 2022) developed a decision tree algorithm to forecast the cytotoxicity of micro- and nano-plastics with an accuracy of 95%. Their dataset was compiled through a comprehensive literature review on the subject. Their findings revealed that key factors influencing cell viability include the plastic source, zeta potential, exposure concentration, and the biological model representing various cell types. This suggests that cytotoxicity manifests as an intrinsic property of micro- and nano-plastics within specific cell lines under

defined experimental conditions. Notably, the study did not identify a discernible relationship between particle size and toxic effects.

Another important biological parameter is cell adhesion and proliferation. Through the use of a computational model Hao et al. (Hao et al., 2023) optimized a mixture of polyethylene glycol (PEG) and arginine-glutamic acid-aspartic acid-valine peptide to obtain high endothelial cell selectivity against smooth muscle cells. The dataset was derived from numerous experiments, and the resulting model (ResNet50V2) achieved an accuracy of over 95%. Additionally, the optimal composition was used as a surface coating formula for implantable cardiovascular devices made of nickel-titanium, demonstrating successful endothelialisation of the surface.

An inflammatory response is a typical phenomenon that follows the implantation of grafts or medical devices, as our bodies recognize foreign materials and attempt to reject them. The general strategy to maximize engraftment rates is to minimize the host immune response through anti-inflammatory therapies (Crupi et al., 2015). A contribution to minimizing the inflammatory process can be made by using polymers with anti-inflammatory properties. To predict the immunomodulatory potential of polymers, two models—K-nearest neighbours and Naïve Bayes—were compared by Akkache et al. (Akkache et al., 2024). The models used cellular assays of 50 polymers on murine macrophages as training data for immunomodulatory behaviour. The secretion of nitric oxide and tumour necrosis factor alpha by macrophages was considered as input markers for the inflammatory process. The best accuracy was achieved by the K-nearest neighbours model; however, the limited data and the oversimplified system considered reduce the model to an initial decision-making step rather than an efficient classifier.

In another study, Gong et al. (Gong et al., 2022) applied AI models to a dataset of poly(beta-amino ester) (PBAE) gene-delivery polymers. The models predicted which polymer compositions would yield high *in vitro* transfection efficiency. Synthesized candidate polymers were tested in macrophage and liver cell cultures, and predicted transfection levels correlated strongly with experimental values (Spearman's $\rho \approx 0.57–0.66$). Notably, model explainability analysis identified tuneable parameters, like hydrophobicity and carbon atom count, that significantly influence gene delivery performance. These insights offer valuable guidance for the rational design of next-generation polymeric gene delivery systems.

Polymers can also exhibit antimicrobial properties, as demonstrated in numerous studies (Olmos and González-benito, 2021). In order to easily identify peptides with high antimicrobial properties, Huang et al. (Huang et al., 2023) developed a model that mines billions of peptide sequences for peptides composed of 6–9 amino acids with potential antimicrobial properties. The identified peptides showed excellent results against a wide range of multi-drug-resistant pathogens. Further confirmation of the model's reliability was obtained through in vivo tests in mice with bacterial pneumonia, which showed effects comparable to penicillin.

The high moldability of polymers makes them suitable for numerous manufacturing techniques. Among these, electrospinning is a common technique in tissue engineering to produce fibrous scaffolds for wound healing (Zulkifli et al., 2023). The influence of process parameters on mechanical properties can be evaluated using AI models. This approach was successfully applied to predict the tensile strength and suture retention of PCL using an ANN. Notably, the model exhibited a negligible difference between experimental and predicted data, with deviations of less than 2.8% for suture retention and under 0.4% for tensile strength (Reddy et al., 2021). Alternatively, evaluating the effects of electrospinning parameters on the orientation, angle and diameter of the resulting fibres can represent a method for process optimization. In particular, a convolutional neural network has demonstrated higher predictability compared to other regression models when faced with a limited amount of data. Notably, to mitigate model overfitting caused by the small data size, the authors employed oversampling, hyperparameter optimization, and k-fold cross-validation during models' development and evaluation (López-Flores et al., 2024).

Similarly, in a comparative study on the process optimization of fused deposition modelling using a dataset derived from the literature, XGBoost emerged as the best predictor, achieving an R^2 above 0.94 (Ege et al., 2023). Further refinement of the model can be obtained by the use of Shapley Additive exPlanation (SHAP), as demonstrated by another study, which achieved an R^2 of 0.976. However, the hierarchical importance of the printing parameters differed between the models with and without the use of SHAP, highlighting how the choice of analysis technique influences the output (Nasiri et al., 2024).

Optimization has also been a focus in bioprinting, as demonstrated by Mohammadrezaei et al. (Mohammadrezaei et al., 2024). In this study, the authors collected both experimental data and bibliographic data, resulting in a dataset of 591 data points. The chosen model was a regression neural network, built to predict cell viability for gelatine- and alginate-based

bioinks, and to identify the most critical parameters. However, the model achieved an R^2 of 0.71, highlighting the need for additional data to refine it. One possible way to increase the experimental data for process optimization could be to use a design of experiments (DoE) approach (J. Zhang et al., 2019).

It is worth emphasizing that the methods discussed earlier represent just a fraction of the diverse techniques available in polymer science. This is particularly evident when considering that the methods employed in drug discovery can also be effectively applied in polymer science, given the shared use of small molecules in their synthesis (Yan and Li, 2023). For an in-depth exploration of machine learning methods applied in polymer science, we recommend consulting the comprehensive reviews provided (McDonald et al., 2023; Meyer et al., 2023; Yan and Li, 2023).

Metals

Metals find extensive use in applications requiring robust mechanical properties, particularly in orthopaedics and dentistry. Titanium and its alloys (Ti alloys) are among the most widely used materials in biomedical applications. Ti alloys offer numerous advantages, including high specific strength, exceptional corrosion resistance in biological environments, and favourable biocompatibility. Additionally, they provide a balance between low elastic modulus and high strength, making them particularly desirable. This characteristic is crucial, as a material with an elastic modulus comparable to that of bone can significantly reduce the risks of stress shielding and potential implant failure (Li et al., 2022). However, despite these benefits, the discrepancy between the elastic modulus of Ti alloys (approximately 50–120 GPa) and that of cortical bone (approximately 30 GPa) still does not fully prevent stress shielding (Guo et al., 2015). Among these alloys, Ti-6Al-4V remains the most widely used due to its relatively low modulus compared to other alloys. Nevertheless, it faces a significant challenge regarding the release of vanadium and aluminium, which are implicated in various diseases such as Alzheimer's (Domingo, 2002). Consequently, extensive research efforts are focused on identifying alternative alloy compositions with reduced biological risks and elastic moduli more closely matched to bone.

To obtain a titanium alloy with an elastic modulus comparable to that of bone, Wu et al. (Wu et al., 2020) developed an algorithm to predict compositions meeting this criterion. Their approach was based on the premise that a Ti alloy's low elastic modulus could be achieved by stabilizing the β phase, which correlates with the martensitic transformation start temperature (*Ms*). By using the alloying elements' content (in *wt*%) as input and elastic

modulus and *Ms* as outputs, they identified the Ti-12Nb-12Zr-12Sn alloy as having the desired properties. Subsequent testing confirmed its high tensile strength, satisfactory ductility, and biocompatibility. The same topic was recently explored using 254 quenched *β*-Ti alloy compositions from the literature, comparing different AI models. The findings highlighted the need for complex prediction models to understand the relationship between alloy compositions and elastic modulus. As a result, the XGBoost model exhibited the highest accuracy, with an R^2 of 0.962 (Kanapaakala and Subramani, 2024).

Similarly, Jha et al. (Jha and Dulikravich, 2021) investigated the same alloying elements, Nb, Zr and Sn, to produce a fully stabilized *β* phase Ti alloy. They employed a hybrid approach, combining Calculation of Phase Diagram (CALPHAD) techniques with AI models to predict the concentrations of metastable phases for novel compositions and the optimal temperature for maximizing the stability of the *β* phase. Their study generated predictions for five compositions expected to satisfy their criteria for *β* phase stability. Furthermore, a subsequent numerical study (Raj and Datta, 2023) confirmed the efficacy of Nb, Zr, and Sn as key alloying elements to decrease the elastic modulus while maintaining adequate yield strength in Ti alloys. Additionally, the study suggested a beneficial effect of Mo and V. Three different models (multiple linear regression, fuzzy inference systems, and ANN) were compared to elucidate the roles of alloying elements and processing parameters in determining these two mechanical properties. The models were trained on literature data and considered both composition and thermal treatment as input variables. The results showed the superior performance of ANN compared to the other models, with R^2 above 0.88. However, it is important to note that no experimental validation was performed to confirm these predictions.

Sultana et al. (Sultana et al., 2014) conducted a multi-objective study to address mechanical and biological challenges, aiming to identify an alloy with a low elastic modulus, high yield strength, improved biocompatibility, and cost-effectiveness. As expected, their findings suggested the utilization of *β*-Ti alloys, well-known for their low modulus. Specifically, the optimal solutions recommended a high content of Nb, moderate amounts of Ta, Mo, Cr and Zr, and minimal to no presence of Al and V. Pursuing a similar objective, Banu and Rani (Noori Banu and Devaki Rani, 2018) used ANN models to predict tensile strength, yield strength and modulus based on alloy composition, thermomechanical processing and microstructure. Their investigation focused on Ti-xNb-yTa alloy, optimizing *x* and *y* (*wt*%) and examining the role of minor alloying agents. The simulations illustrated

increased tensile strength and yield strength with higher Ta and Nb contents. Additionally, the modulus was observed to decrease with elevated levels of Ta and Nb, while the presence of Al was associated with an increased in modulus. Furthermore, adding Zr to Ti-Nb and Ti-Nb-Ta alloys further reduced the modulus, enhancing biocompatibility.

AI has been applied to predict biological responses to metal implants. In particular, the macrophage immune response when in contact with the titanium surface was studied by Chen et al. (Chen et al., 2025), comparing different AI models. The models—RF, XGBoost, SVM and multilayer perceptron (MLP)—were trained on literature data and considered both surface properties (e.g., roughness) and material–cell interaction (e.g., cell seeding density) as input features, with pro- and anti-inflammatory cytokine levels as target outputs. Notably, RF, XGBoost and MLP showed an $R^2 > 0.7$; however, only the MLP model was selected for *in vitro* verification due to its lower mean absolute percentage error. Results showed that, despite some discrepancies between predicted and experimental values, the overall trends were consistent, demonstrating the potential of the model. The authors attributed these discrepancies to four main factors: the limited training dataset, which excluded potentially relevant features such as elemental composition; variability and possible errors in the experimental data; range constraints during data input that failed to capture reported variability; and heterogeneous distribution of the literature-derived data.

Similarly, the osteogenic response to modified titanium surfaces was studied using a DL approach. The model leveraged early-stage osteoblast morphology to predict alkaline phosphatase activity, a key marker of osteogenesis. It demonstrated excellent predictive performance, which was further validated by *in vitro* experiments (Li et al., 2025).

Another class of metals is represented by bulk metallic glasses (BMGs). These materials have gained significant attention in recent decades due to their unique amorphous atomic structures. BMGs typically exhibit high strength, lower Young's modulus, improved wear resistance, good fatigue endurance, and excellent corrosion resistance (Li and Zheng, 2016). To identify new BMG compositions, Douest et al. (Douest et al., 2024) developed two predictive AI models for the Ti-Zr-Cu-Pd system. Data were collected from a literature review, resulting in a dataset of 643 BMGs. The first model was trained on the atomic percentages of the constituent elements, while the second model utilized material and chemical properties associated with each alloy. In both cases, the output variables considered were the maximum rod diameter (D_{max}) at which a fully amorphous structure is preserved and the supercooled liquid region (ΔT_x). The obtained compositions were then classified to

maximize D_{max} and ΔT_x while minimizing the Cu content. Only the most promising candidate was produced to verify the accuracy of the models, revealing discrepancies between predicted and experimental outputs. The limited predictability of the models may be attributed to the small and relatively homogeneous dataset, as well as the restricted number of experimental trials conducted on the predicted compositions.

Composites

A composite material is created by combining two materials with distinct physical and chemical properties, where the primary phase is referred to as the matrix, and the secondary phase is known as the filler. In biomaterial applications, composites take advantage of the combined advantageous properties of multiple materials simultaneously, making them highly versatile and valuable in various medical fields.

In orthopaedics, ultra-high molecular weight polyethylene (UHMWPE) is a widely used polymer known for its excellent mechanical and tribological properties. To further enhance these properties, Vinoth et al. (Vinoth et al., 2021) incorporated carbon fibers into UHMWPE and utilized a multi-objective approach to optimize the composite composition. Their study considered both nano and micro carbon fibres as reinforcement, with a total of 16 input parameters, including the weight percentage and particle size of the nano/micro particles. The developed ANN models were used to minimize the output factors of the coefficient of friction and specific wear rate, while simultaneously maximizing the elastic modulus, hardness, and ultimate tensile strength. Notably, the study highlighted the differences between single-objective and multi-objective optimization approaches, emphasizing the importance of considering multiple factors simultaneously when optimizing composite materials.

As we mentioned in the previous paragraphs, hydrogels are a class of polymers known for their low mechanical properties (J. Yu et al., 2021). One viable strategy for enhancing their mechanical properties is to create composites in which hydrogels serve as the matrix. Conventional approaches for determining the mechanical properties of these composites typically involve experiments or FEM. However, both approaches have drawbacks, such as being time-consuming and computationally expensive. Combining FEM and AI can address these issues, as shown in different studies (Gholami et al., 2023; Shokrollahi et al., 2022). In fact, Gholami et al. (Gholami et al., 2023) demonstrated the high accuracy of this approach by comparing two deep neural network models, ResNet and AlexNet. Their study considered a dataset of 9000 generated microstructural images with different particle shapes, along with

their Young's modulus and Poisson's ratio computed by FEM analysis. The models exhibited high accuracy in predicting the mechanical properties of collagen hydrogel reinforced with BG particles. Notably, the AlexNet model demonstrated the highest accuracy, with an R^2 >0.92 for all particle shapes. Similarly, the combination of FEM analysis and deep neural networks has proven highly effective in extracting the elastic properties of the constituent phases in composites. This approach is particularly promising for evaluating the mechanical properties of cells within real tissues, as *in vitro* analyses on isolated (non-embedded) cells often yield results that differ significantly from those of embedded cells, and are typically challenging and unreliable (Ye et al., 2022). Moreover, the same research group has demonstrated that this method is also feasible for predicting the surface elastic properties of materials from feature images that describe the mechanical and geometric characteristics of surface microstructures, further highlighting the versatility of the approach (Ye et al., 2021).

Alternatively, the combination of AI and response surface methodology (RSM) has also proven efficient, as shown in a study on composite hydrogels containing heparinized ZnO nanoparticles (Joorabloo et al., 2019). In this study, different models were compared to predict the degree of swelling and the water vapor transmission rate as the composition of the composite hydrogel varied. After determining the best model, the results were used to graphically optimize the composition using RSM. The optimal composition was then produced and characterized, revealing small discrepancies between the actual and predicted properties.

A contrasting approach was taken in the study by Shera et al. (Shera et al., 2018), which compared the accuracy of ANN and RSM in predicting the effects of composition, porosity, and swelling on the drug release of chloramphenicol in a silk fibroin–xanthan gum composite scaffold. The experimental tests demonstrated the higher accuracy of ANN compared to RSM, highlighting the success of ANN in predicting non-linear relationships. A similar trend was observed in a study by Boztepe et al. (Boztepe et al., 2020), which investigated drug release behaviour from highly swellable, pH- and temperature-responsive hydrogels synthesized via interpenetrating polymer network techniques using free radical polymerization in the presence of microgels and a pore-forming agent. ANN, SVM, and support vector regression (SVR) models were compared for predicting doxorubicin release under varying pH and temperature conditions. Using a dataset of 540 experimental observations for model training and validation, the results again demonstrated the superior accuracy of ANN in capturing complex, non-linear relationships.

The use of AI models can be extended also to nanocomposites. Zhu et al. (Zhu et al., 2021) demonstrated the power of combining high-throughput phase-field simulations with ML to design Ti-Nb nanocomposite alloys with exceptional mechanical properties, including ultralow Young's modulus, linear super elasticity, and nearly zero hysteresis. Using an ANN for multi-objective optimization, the study identified ideal microstructural configurations based on Nb concentration, nanofiller volume fraction, and other parameters. This approach led to the discovery of a nanocomposite with properties suitable for orthopaedic implants, addressing key challenges like stress shielding and hysteresis-related inefficiencies in shape memory alloys. However, a key limitation of the study lies in the absence of experimental synthesis and mechanical testing of the proposed alloy, which is necessary to confirm the reliability of the computational predictions. A similar effort in nanocomposite optimization is seen in the work of Wang et al. (Wang et al., 2024), where ANNs were used to predict various physical and mechanical properties of PVA-based scaffolds, including pore size, porosity, compressive strength, elastic modulus, and water absorption. These predictions were made based on the weight percentages of nano-hydroxyapatite and magnetic nanoparticles incorporated into the PVA matrix. Both studies reported a R^2 greater than 0.96, highlighting the high predictive accuracy of ANN models and reinforcing the potential of ML-driven approaches in optimizing biomechanical compatibility in nanocomposites.

Composite materials can also be used as bioinks for scaffold production. An early attempt to predict the printability of biomaterial ink formulations for AM scaffold production involved comparing decision trees, random forests, and DL models (Chen et al., 2023). The models were trained on experimental data from 210 formulations derived from 16 distinct biomaterials. The results indicated that the random forests model had the best accuracy; however, the DL model exhibited a higher recall, meaning it was less likely to miss printable formulations. Notably, all models displayed signs of overfitting.

Similarly, Hashemi et al. optimized a chitosan-agarose-gelatine ink (Hashemi et al., 2024). The printing parameters were refined using Bayesian optimization based on previous work (Ruberu et al., 2021), and a transfer learning approach was applied to include ink composition among the input variables. This strategy proved to be beneficial, as it identified the optimal parameters in fewer trials compared to those typically required by experienced users. Analogous studies for the optimization of bioinks can be found in the works of Lee et al. (Lee et al., 2020) and in the review article of Ramesh et al. (Ramesh et al., 2024).

5.1.5. Challenges and future perspectives

The role of AI in biomaterials science presents numerous challenges and opportunities. Computational models enable the prediction of many properties—both biological and non-biological—that would otherwise require significant resources to evaluate. However, achieving reliable and accurate predictions, particularly for properties that are less commonly evaluated (e.g., bioactivity, cytotoxicity, etc.), requires large volumes of high-quality, standardized data for model training and validation. In fact, the primary cause of low prediction accuracy is often the use of small, sparse, or heterogeneous datasets. An ideal solution would be the standardization of property evaluations and comprehensive data sharing, in agreement with the principles of FAIR (Findable, Accessible, Interoperable, Reusable) (Mozafari, 2025). Nonetheless, a practical approach to address this issue could involve data mining from the literature or artificially increasing dataset size through data augmentation techniques (Bonatti et al., 2024). For instance, PINNs embed known physical laws (e.g., diffusion or reaction kinetics) into the learning process, enabling accurate predictions even with limited data. Generative models like GANs or diffusion models can augment datasets by synthesizing realistic new examples. Recent work like MatterGen uses a diffusion-based model to produce novel, stable materials given target properties (Zeni et al., 2023). Such models can, in effect, simulate a vast space of biomaterial designs to supplement experimental data. However, it is crucial to ensure that the dataset used is as clean as possible through data preprocessing, normalization, and outlier detection to avoid redundant or noisy data, which could negatively impact model performance.

Additionally, the use of different AI models may lead to different results, and the black-box nature of these models limits our understanding of the principles behind the prediction process. This highlights the need for experimental validation or for more transparent techniques, such as the Shapley Additive Explanation, as suggested by FDA guidelines for AI-based medical products (Food and Drug Administration, 2025). Moreover, the properties of biomaterials are often strongly linked to the analytical methods and processing conditions, which complicates the adaptation of data to different contexts. A potential solution to this challenge would be to use models that integrate traditional computational methods, such as finite element analysis, or domain knowledge, such as physical or chemical laws, to enhance the interpretability and reliability of the models.

A concrete proposal for integrating AI with regulatory standards and experimental validation could combine these approaches. First, data acquisition and preprocessing should

be transparent and well-documented to ensure reproducibility. Second, models should meet clear performance metrics, such as high R^2, low *RMSE*, and the use of explainable AI techniques (e.g., Shapley Additive Explanation) to enhance interpretability. Third, validation should follow a multi-stage protocol (*in silico*, *in vitro*, and *in vivo*), and, when feasible, include interlaboratory testing to assess robustness. In addition, the use of benchmark datasets would facilitate comparison across studies, and a standardized datasheet or reporting template could help users quickly evaluate model quality and compliance.

5.1.6. Conclusions

AI and its derivatives are currently a hot topic, as highlighted by the increasing number of studies that use this approach. Indeed, AI models represent powerful tools that can potentially improve the quality of research, reduce time and resource waste, and find alternative patterns that are difficult for human knowledge to identify. Nonetheless, the findings presented in this study suggest that this technology is still immature, often leaving room for reasonable doubt regarding the predicted results. Consequently, it is imperative to recognize AI as an exceptional complementary resource rather than a replacement for traditional research and studies. Therefore, critical supervision of the obtained results is always highly recommended to ensure the accuracy and validity of AI-assisted findings. Embedding FAIR data practices and adhering to emerging AI guidance will help translate biomaterial AI/ML models into safe, effective clinical technologies.

6. Conclusions and future challenges

This Thesis investigated the development of next-generation biomaterials for regenerative medicine, focusing on improving the thermal processability, mechanical performance, and biological functionality of bioactive glasses and polymer-based scaffolds, while also exploring natural polymers and data-driven strategies for materials design.

The first part addressed a long-standing limitation of bioactive glasses: their propensity to crystallize during thermal processing. Incorporating Mg^{2+}, Sr^{2+}, and K^{+} into established formulations effectively widened the sintering window, stabilized the amorphous phase, and improved densification. The doped glasses exhibited enhanced mechanical behaviour, controlled dissolution, and sustained bioactivity, as well as reduced pH excursions during SBF testing. Their cytocompatibility with human dermal fibroblasts suggests potential applications beyond hard tissue regeneration. The development of the S53P4_MSK composition further demonstrated that high sinterability at low temperature can be achieved without crystallization, while retaining strong bioactivity and favourable mechanical properties. This establishes S53P4_MSK as a promising candidate for thermally processed scaffolds and coatings.

The investigation of polymer–BG composites showed that introducing BG particles into PLA has limited impact on tensile behaviour but markedly influences compressive properties and failure modes. The resulting brittle, fragmenting response can be leveraged for controlled degradation while preserving cytocompatibility. The strongest biological outcomes were observed in composites containing S53P4 and S53P4_MS, indicating that targeted compositional tuning represents and effective strategy for application-specific scaffold engineering.

The exploration of natural polymers extracted from *Theobroma* species expanded the material palette beyond inorganic systems. These polysaccharides exhibited high molecular weight, notable antioxidant activity, and favourable rheological behaviour, in some cases clearly outperforming commercial pectin. Their characteristics make them promising as bioactive components, hydrogel matrices, or antioxidant additives. However, variability in extraction and the need for more standardized and rigorous purification protocols remain key challenges for large-scale implementation.

The final section examined how artificial intelligence can support biomaterials development. While AI provides clear advantages for property prediction, design

optimisation, and the identification of novel formulations, its performance is currently constrained by limited, heterogeneous, and non-standardized datasets. This thesis outlined practical strategies to mitigate these limitations, including improved data curation, data augmentation, physics-informed modelling, and explainable AI approaches aligned with evolving regulatory expectations. These methods can reduce experimental workload and accelerate the discovery of high-performance biomaterials, as long as computational predictions are validated through rigorous multi-stage testing.

Overall, this Thesis shows that the integration of chemical modification, composite engineering, natural polymer research, and AI-assisted analysis offers a realistic route toward biomaterials that are more predictable, manufacturable, and biologically effective. Future work should prioritise the validation of the most promising glass compositions and composites in complex biological models, refinement of extraction and standardisation methods for natural polymers, and the incorporation of AI-based tools into routine materials development workflows. By addressing both fabrication constraints and the increasing role of data-driven design, these findings contribute practical pathways for advancing regenerative medicine and the engineering of functional, clinically relevant scaffolds.

7. List of publications

1. Onofri E., Cristiani E., Martelli A., Gentile P., Giron-Hernandez J., Pontrelli G. A general multi-stratum model for a nanofunctionalized releasing capsule: An experiment-driven computational study. Mathematical Biosciences and Engineering. 2026, Vol. 23. https://doi.org/10.3934/mbe.2026001
2. Martelli A., Mohamed Y., Gallego-Ferrer G., Gentile P., Giron-Hernandez J. Revolutionizing gut health: advances in encapsulation strategies for probiotics and bioactive molecules. Biotechnology Advances. 2025, 83. https://doi.org/10.1016/j.biotechadv.2025.108630
3. Martelli A., Bellucci D., Cannillo V. The role of Artificial Intelligence in Biomaterials Science: a Review. Polymers. 2025, 17(19), 2668. https://doi.org/10.3390/polym17192668
4. Nunez-Ramirez J.M., Martelli A., Halliday T., Thomas B., Wills C., Cannillo V., Bellucci D., Carranza C., Garcia-Rincon P.A., Gentile P. Giron-Hernandez J. Valorization of metabolite-enriched carbohydrates from Theobroma biomass via ultrasound-assisted alkaline extraction. Carbohydrate Polymers. 2025, 368 (Part 1). https://doi.org/10.1016/j.carbpol.2025.124070
5. Martelli A., Bellucci D., Cannillo V. An Enhanced Bioactive Glass Composition with Improved Thermal Stability and Sinterability. Materials. 2024, 17(24), 6175. https://doi.org/10.3390/ma17246175
6. Bellucci D., Mazzilli A., Martelli A., Mecca F.G., Bonacorsi S., Lofaro F.D., Boraldi F., Quaglino D., Cannillo V. Enrichment of strontium and magnesium improves the physical, mechanical and biological properties of bioactive glasses undergoing thermal treatments: New cues for biomedical applications. Ceramics International. 2024, 50 (Part A). https://doi.org/10.1016/j.ceramint.2024.10.135
7. Rogati G., Caravaggi P., Martelli A., Fognani R., Leardini A., Baleani M. Validation of a Simple Device for the Evaluation of Ankle Plantar- and Dorsi- Flexor Forces Consistent with Standard Clinical Evaluations, Applied Sciences 2024, 14, 2461. https://doi.org/10.3390/app14062461
8. Martelli A., Bellucci D., Cannillo V. Additive Manufacturing of Polymer/Bioactive Glass Scaffolds for Regenerative Medicine: A Review, Polymers 2023, 15, 2473. https://doi.org/10.3390/polym15112473

9. Martelli, A.; Erani, P.; Pazzagli, N.; Cannillo, V.; Baleani, M. Surface Analysis of Ti-Alloy Micro-Grooved 12/14 Tapers Assembled to Non-Sleeved and Sleeved Ceramic Heads: A Comparative Study of Retrieved Hip Prostheses. Materials 2023, 16, 1067. https://doi.org/10.3390/ma16031067

8. References

Aalto-Setälä, L., Uppstu, P., Sinitsyna, P., Lindfors, N.C., Hupa, L., 2021. Dissolution of amorphous s53p4 glass scaffolds in dynamic in vitro conditions. Materials 14, 1–14. https://doi.org/10.3390/ma14174834

Abang Zaidel, D.N., Hamidon, N.H., Mat Zahir, N., 2017. Extraction and characterization of pectin from sweet potato (Ipomoea batatas) peels using alkaline extraction method, in: Acta Horticulturae. https://doi.org/10.17660/ActaHortic.2017.1152.29

Abdolrasol, M.G.M., Suhail Hussain, S.M., Ustun, T.S., Sarker, M.R., Hannan, M.A., Mohamed, R., Ali, J.A., Mekhilef, S., Milad, A., 2021. Artificial neural networks based optimization techniques: A review. Electronics (Switzerland). https://doi.org/10.3390/electronics10212689

Agarwal, R., Singh, J., Gupta, V., 2022. Predicting the compressive strength of additively manufactured PLA-based orthopedic bone screws: A machine learning framework. Polym. Compos. 43. https://doi.org/10.1002/pc.26881

Agarwala, M., Bourell, D., Beaman, J., Marcus, H., Barlow, J., 1995. Direct selective laser sintering of metals. Rapid Prototyp. J. 1. https://doi.org/10.1108/13552549510078113

Aized Amin Soofi, Arshad Awan, 2017. Classification Techniques in Machine Learning: Applications and Issues. Journal of Basic & Applied Sciences 13. https://doi.org/10.6000/1927-5129.2017.13.76

Ajita, J., Saravanan, S., Selvamurugan, N., 2015. Effect of size of bioactive glass nanoparticles on mesenchymal stem cell proliferation for dental and orthopedic applications. Materials Science and Engineering: C 53, 142–149. https://doi.org/10.1016/J.MSEC.2015.04.041

Akkache, A., Clavier, L., Mezhenskyi, O., Andriienkova, K., Soubrié, T., Lavalle, P., Vrana, N.E., Gribova, V., 2024. Machine Learning-Based Prediction of Immunomodulatory Properties of Polymers: Toward a Faster and Easier Development of Anti-Inflammatory Biomaterials. Adv. Nanobiomed Res. 4. https://doi.org/10.1002/anbr.202300085

Akunna, C., Cerruti, M., 2024. Structural connectivity and bioactivity in sol–gel silicate glass design. Acta Biomater. 188, 374–392. https://doi.org/10.1016/J.ACTBIO.2024.08.030

Alam, M., Manivannan, E., Rizwan, M., Gopan, G., Mani, M., Kannan, S., 2024. 3D printed polylactide-based zirconia-toughened alumina composites: fabrication, mechanical, and in vitro evaluation. Int. J. Appl. Ceram. Technol. 21. https://doi.org/10.1111/ijac.14559

Aldeghi, M., Coley, C.W., 2022. A graph representation of molecular ensembles for polymer property prediction. Chem. Sci. 13. https://doi.org/10.1039/d2sc02839e

Alksne, M., Kalvaityte, M., Simoliunas, E., Rinkunaite, I., Gendviliene, I., Locs, J., Rutkunas, V., Bukelskiene, V., 2020. In vitro comparison of 3D printed polylactic acid/hydroxyapatite and polylactic acid/bioglass composite scaffolds: Insights into materials for bone regeneration. J. Mech. Behav. Biomed. Mater. 104, 103641. https://doi.org/10.1016/J.JMBBM.2020.103641

Allan, I., Newman, H., Wilson, M., 2001. Antibacterial activity of particulate Bioglass® against supra- and subgingival bacteria. Biomaterials 22. https://doi.org/10.1016/S0142-9612(00)00330-6

Alloghani, M., Al-Jumeily, D., Mustafina, J., Hussain, A., Aljaaf, A.J., 2020. A Systematic Review on Supervised and Unsupervised Machine Learning Algorithms for Data Science. https://doi.org/10.1007/978-3-030-22475-2_1

Amberg, R., Elad, A., Rothamel, D., Fienitz, T., Szakacs, G., Heilmann, S., Witte, F., 2018. Design of a migration assay for human gingival fibroblasts on biodegradable magnesium surfaces. Acta Biomater. 79, 158–167. https://doi.org/10.1016/J.ACTBIO.2018.08.034

Amini, Z., Lari, R., 2021. A systematic review of decellularized allograft and xenograft–derived scaffolds in bone tissue regeneration. Tissue Cell. https://doi.org/10.1016/j.tice.2021.101494

Anand, A., Sengupta, S., Kaňková, H., Švančárková, A., Beltrán, A.M., Galusek, D., Boccaccini, A.R., Galusková, D., 2022. Influence of Copper-Strontium Co-Doping on Bioactivity, Cytotoxicity and Antibacterial Activity of Mesoporous Bioactive Glass. Gels 8. https://doi.org/10.3390/gels8110743

Anesi, A., Ferretti, M., Salvatori, R., Bellucci, D., Cavani, F., Di Bartolomeo, M., Palumbo, C., Cannillo, V., 2023. In-vivo evaluations of bone regenerative potential of two novel bioactive glasses. J. Biomed. Mater. Res. A 111. https://doi.org/10.1002/jbm.a.37526

ANSYS Inc., n.d. Ansys GRANTA EduPack software [WWW Document]. URL www.ansys.com/materials (accessed 2.12.24).

Antonakos, A., Liarokapis, E., Leventouri, T., 2007. Micro-Raman and FTIR studies of synthetic and natural apatites. Biomaterials 28, 3043–3054. https://doi.org/10.1016/J.BIOMATERIALS.2007.02.028

Arakawa, K., Kono, N., Malay, A.D., Tateishi, A., Ifuku, N., Masunaga, H., Sato, R., Tsuchiya, K., Ohtoshi, R., Pedrazzoli, D., Shinohara, A., Ito, Y., Nakamura, H., Tanikawa, A., Suzuki, Y., Ichikawa, T., Fujita, S., Fujiwara, M., Tomita, M., Blamires, S.J., Chuah, J.A., Craig, H., Foong, C.P., Greco, G., Guan, J., Holland, C., Kaplan, D.L., Sudesh, K., Mandal, B.B., Norma-Rashid, Y., Oktaviani, N.A., Preda, R.C., Pugno, N.M., Rajkhowa, R., Wang, X., Yazawa, K., Zheng, Z., Numata, K., 2022. 1000 spider silkomes: Linking sequences to silk physical properties. Sci. Adv. 8. https://doi.org/10.1126/sciadv.abo6043

Arcos Navarrete, D., Vallet-Regí, M., n.d. Bioactive glasses : properties, composition and recent applications.

Arifin, N., Sudin, I., Ngadiman, N.H.A., Ishak, M.S.A., 2022. A Comprehensive Review of Biopolymer Fabrication in Additive Manufacturing Processing for 3D-Tissue-Engineering Scaffolds. Polymers (Basel). 14, 1–22. https://doi.org/10.3390/polym14102119

Arima, Y., Iwata, H., 2007. Effect of wettability and surface functional groups on protein adsorption and cell adhesion using well-defined mixed self-assembled monolayers. Biomaterials 28. https://doi.org/10.1016/j.biomaterials.2007.03.013

Arinzeh, T.L., Tran, T., Mcalary, J., Daculsi, G., 2005. A comparative study of biphasic calcium phosphate ceramics for human mesenchymal stem-cell-induced bone formation. Biomaterials 26, 3631–3638. https://doi.org/10.1016/J.BIOMATERIALS.2004.09.035

Arstila, H., Hupa, L., Karlsson, K.H., Hupa, M., 2008. Influence of heat treatment on crystallization of bioactive glasses. J. Non. Cryst. Solids 354. https://doi.org/10.1016/j.jnoncrysol.2007.06.092

Arstila, Hanna, Tukiainen, M., Taipale, S., Kellomäki, M., Hupa, L., 2008. Liquidus temperatures of bioactive glasses, in: Advanced Materials Research. Trans Tech Publications, pp. 287–292. https://doi.org/10.4028/www.scientific.net/amr.39-40.287

Arstila, H., Vedel, E., Hupa, L., Hupa, M., 2007. Factors affecting crystallization of bioactive glasses. J. Eur. Ceram. Soc. 27. https://doi.org/10.1016/j.jeurceramsoc.2006.04.017

Asghari, F., Samiei, M., Adibkia, K., Akbarzadeh, A., Davaran, S., 2017. Biodegradable and biocompatible polymers for tissue engineering application: a review. Artif. Cells Nanomed. Biotechnol. 45, 185–192. https://doi.org/10.3109/21691401.2016.1146731

Awonusi, A., Morris, M.D., Tecklenburg, M.M.J., 2007. Carbonate assignment and calibration in the Raman spectrum of apatite. Calcif. Tissue Int. 81, 46–52. https://doi.org/10.1007/S00223-007-9034-0/FIGURES/5

Azimzadeh, A., Meyer, C., Ravanat, C., Cazenave, J.P., Wolf, P., 1996. Xenograft rejection: Molecular mechanisms and therapeutic prospects. Hematol. Cell Ther. https://doi.org/10.1007/s00282-996-0331-2

Badev, A., Abouliatim, Y., Chartier, T., Lecamp, L., Lebaudy, P., Chaput, C., Delage, C., 2011. Photopolymerization kinetics of a polyether acrylate in the presence of ceramic fillers used in stereolithography. J. Photochem. Photobiol. A Chem. 222. https://doi.org/10.1016/j.jphotochem.2011.05.010

Bae, C.J., Ramachandran, A., Chung, K., Park, S., 2017. Ceramic stereolithography: Additive manufacturing for 3D complex ceramic structures. Journal of the Korean Ceramic Society 54. https://doi.org/10.4191/kcers.2017.54.6.12

Bahati, D., Bricha, M., El Mabrouk, K., 2023. Synthesis, characterization, and in vitro apatite formation of strontium-doped sol-gel-derived bioactive glass nanoparticles for bone regeneration applications. Ceram. Int. 49. https://doi.org/10.1016/j.ceramint.2023.04.128

Baino, F., Fiume, E., Barberi, J., Kargozar, S., Marchi, J., Massera, J., Verné, E., 2019. Processing methods for making porous bioactive glass-based scaffolds—A state-of-the-art review. Int. J. Appl. Ceram. Technol. 16. https://doi.org/10.1111/ijac.13195

Baino, F., Hamzehlou, S., Kargozar, S., 2018. Bioactive Glasses: Where Are We and Where Are We Going? J. Funct. Biomater. 9, 25. https://doi.org/10.3390/JFB9010025

Baino, F., Novajra, G., Vitale-Brovarone, C., 2015. Bioceramics and scaffolds: A winning combination for tissue engineering. Front. Bioeng. Biotechnol. https://doi.org/10.3389/fbioe.2015.00202

Baino, F., Verne, E., 2017. Glass-based coatings on biomedical implants: A state-of-the-art review. Biomedical Glasses. https://doi.org/10.1515/bglass-2017-0001

Bakry, A.S., Takahashi, H., Otsuki, M., Tagami, J., 2014. Evaluation of new treatment for incipient enamel demineralization using 45S5 bioglass. Dent. Mater. 30, 314–320. https://doi.org/10.1016/J.DENTAL.2013.12.002

Bakry, A.S., Tamura, Y., Otsuki, M., Kasugai, S., Ohya, K., Tagami, J., 2011. Cytotoxicity of 45S5 bioglass paste used for dentine hypersensitivity treatment. J. Dent. 39, 599–603. https://doi.org/10.1016/J.JDENT.2011.06.003

Balani, S.B., Ghaffar, S.H., Chougan, M., Pei, E., Şahin, E., 2021. Processes and materials used for direct writing technologies: A review. Results in Engineering 11. https://doi.org/10.1016/j.rineng.2021.100257

Baldera Ocampo, J.F., Granda Santos, M.S., Chavez Quintana, S.G., 2021. Capacidad antioxidante y polifenoles totales de infusión de cascarilla de cacao (Theobroma cacao) y macambo (Theobroma bicolor). Revista de Investigación de Agroproducción Sustentable 5. https://doi.org/10.25127/aps.20213.814

Baran, E.H., Yildirim Erbil, H., 2019. Surface Modification of 3D Printed PLA Objects by Fused Deposition Modeling: A Review. Colloids and Interfaces 2019, Vol. 3, Page 43 3, 43. https://doi.org/10.3390/COLLOIDS3020043

Barberi, J., Baino, F., Fiume, E., Orlygsson, G., Nommeots-Nomm, A., Massera, J., Verné, E., 2019. Robocasting of SiO2-based bioactive glass scaffolds with porosity gradient for bone regeneration and potential load-bearing applications. Materials 12. https://doi.org/10.3390/ma12172691

Barrios-Rodríguez, Y.F., Salas-Calderón, K.T., Orozco-Blanco, D.A., Gentile, P., Girón-Hernández, J., 2022. Cocoa Pod Husk: A High-Pectin Source with Applications in the Food and Biomedical Fields. ChemBioEng Reviews. https://doi.org/10.1002/cben.202100061

Batra, R., Dai, H., Huan, T.D., Chen, L., Kim, C., Gutekunst, W.R., Song, L., Ramprasad, R., 2020. Polymers for Extreme Conditions Designed Using Syntax-Directed

Variational Autoencoders. Chemistry of Materials 32. https://doi.org/10.1021/acs.chemmater.0c03332

Bedoret, A., Hick, M., Eckes, K., n.d. Device and method for creating a particle structure. BE1024613B1.

Bédouet, L., Courtois, B., Courtois, J., 2003. Rapid quantification of O-acetyl and O-methyl residues in pectin extracts. Carbohydr. Res. 338. https://doi.org/10.1016/S0008-6215(02)00500-1

Behler, J., Parrinello, M., 2007. Generalized neural-network representation of high-dimensional potential-energy surfaces. Phys. Rev. Lett. 98. https://doi.org/10.1103/PhysRevLett.98.146401

Bellucci, D., Bolelli, G., Cannillo, V., Cattini, A., Sola, A., 2011. In situ Raman spectroscopy investigation of bioactive glass reactivity: Simulated body fluid solution vs TRIS-buffered solution. Mater. Charact. 62. https://doi.org/10.1016/j.matchar.2011.07.008

Bellucci, D., Cannillo, V., 2018. A novel bioactive glass containing strontium and magnesium with ultra-high crystallization temperature. Mater. Lett. 213, 67–70. https://doi.org/10.1016/J.MATLET.2017.11.020

Bellucci, Devis, Cannillo, V., Sola, A., 2011. Calcium and potassium addition to facilitate the sintering of bioactive glasses. Mater. Lett. 65. https://doi.org/10.1016/j.matlet.2011.03.060

Bellucci, D., Mazzilli, A., Martelli, A., Mecca, F.G., Bonacorsi, S., Lofaro, F.D., Boraldi, F., Quaglino, D., Cannillo, V., 2024. Enrichment of strontium and magnesium improves the physical, mechanical and biological properties of bioactive glasses undergoing thermal treatments: New cues for biomedical applications. Ceram. Int. https://doi.org/10.1016/j.ceramint.2024.10.135

Bellucci, D., Sola, A., Cannillo, V., 2012. Low temperature sintering of innovative bioactive glasses. Journal of the American Ceramic Society 95, 1313–1319. https://doi.org/10.1111/J.1551-2916.2012.05100.X

Bellucci, D., Sola, A., Salvatori, R., Anesi, A., Chiarini, L., Cannillo, V., 2017a. Role of magnesium oxide and strontium oxide as modifiers in silicate-based bioactive glasses: Effects on thermal behaviour, mechanical properties and in-vitro bioactivity. Materials Science and Engineering: C 72, 566–575. https://doi.org/10.1016/J.MSEC.2016.11.110

Bellucci, D., Sola, A., Salvatori, R., Anesi, A., Chiarini, L., Cannillo, V., 2017b. Role of magnesium oxide and strontium oxide as modifiers in silicate-based bioactive glasses: Effects on thermal behaviour, mechanical properties and in-vitro bioactivity. Materials Science and Engineering C 72. https://doi.org/10.1016/j.msec.2016.11.110

Bellucci, D., Veronesi, E., Dominici, M., Cannillo, V., 2020. A new bioactive glass with extremely high crystallization temperature and outstanding biological performance. Materials Science and Engineering C 110. https://doi.org/10.1016/j.msec.2020.110699

Ben-Arfa, B.A.E., Neto, A.S., Palamá, I.E., Miranda Salvado, I.M., Pullar, R.C., Ferreira, J.M.F., 2019a. Robocasting of ceramic glass scaffolds: Sol–gel glass, new horizons. J. Eur. Ceram. Soc. 39, 1625–1634. https://doi.org/10.1016/j.jeurceramsoc.2018.11.019

Ben-Arfa, B.A.E., Neto, S., Miranda Salvado, I.M., Pullar, R.C., Ferreira, J.M.F., 2019b. Robocasting of Cu2+ & La3+ doped sol–gel glass scaffolds with greatly enhanced mechanical properties: Compressive strength up to 14 MPa. Acta Biomater. 87. https://doi.org/10.1016/j.actbio.2019.01.048

Ben-Arfa, B.A.E., Palamá, I.E., Miranda Salvado, I.M., Ferreira, J.M.F., Pullar, R.C., 2019c. Cytotoxicity and bioactivity assessments for Cu2+ and La3+ doped high-silica sol-gel derived bioglasses: The complex interplay between additive ions revealed. J. Biomed. Mater. Res. A 107. https://doi.org/10.1002/jbm.a.36772

Benito-Román, Melgosa, R., Illera, A.E., Sanz, M.T., Beltrán, S., 2024. Kinetics of extraction and degradation of pectin derived compounds from onion skin wastes in subcritical water. Food Hydrocoll. 153, 109957. https://doi.org/10.1016/J.FOODHYD.2024.109957

Benlloch-Tinoco, M., Nuñez Ramírez, J.M., García, P., Gentile, P., Girón-Hernández, J., 2024. Theobroma genus: Exploring the therapeutic potential of T. grandiflorum and T. bicolor in biomedicine. Food Biosci. 61, 104755. https://doi.org/10.1016/J.FBIO.2024.104755

Berbecaru, C., Alexandru, H. V., Stan, G.E., Marcov, D.A., Pasuk, I., Ianculescu, A., 2010. First stages of bioactivity of glass-ceramics thin films prepared by magnetron sputtering technique. Materials Science and Engineering: B 169. https://doi.org/10.1016/j.mseb.2010.01.007

Bernardo, M.P., da Silva, B.C.R., Hamouda, A.E.I., de Toledo, M.A.S., Schalla, C., Rütten, S., Goetzke, R., Mattoso, L.H.C., Zenke, M., Sechi, A., 2022. PLA/Hydroxyapatite scaffolds exhibit in vitro immunological inertness and promote robust osteogenic differentiation of human mesenchymal stem cells without osteogenic stimuli. Sci. Rep. 12. https://doi.org/10.1038/s41598-022-05207-w

Bernardo, M.P., Ferreira, F. V., Oliveira, L.F., Mattoso, L.H.C., Lopes, J.H., 2025. Revolutionizing bone regeneration: 3D printing of PLA/MFBG composites with advanced healing properties. Mater. Today Chem. 43, 102447. https://doi.org/10.1016/J.MTCHEM.2024.102447

Betz, R.R., 2002. Limitations of autograft and allograft: New synthetic solutions. Orthopedics 25. https://doi.org/10.3928/0147-7447-20020502-04

Bishop, C.M., 2006. Pattern Recognition and Machine Learning. Springer New York, NY. https://doi.org/https://doi.org/10.1007/978-0-387-45528-0

Björkenheim, R., Jämsen, E., Eriksson, E., Uppstu, P., Aalto-Setälä, L., Hupa, L., Eklund, K.K., Ainola, M., Lindfors, N.C., Pajarinen, J., 2021. Sintered S53P4 bioactive glass scaffolds have anti-inflammatory properties and stimulate osteogenesis in vitro. Eur. Cell. Mater. 41, 15–30. https://doi.org/10.22203/ECM.V041A02

Boccaccini, A.R., Blaker, J.J., 2005. Bioactive composite materials for tissue engineering scaffolds. Expert Rev. Med. Devices. https://doi.org/10.1586/17434440.2.3.303

Boccaccini, A.R., Chen, Q., Lefebvre, L., Gremillard, L., Chevalier, J., 2007. Sintering, crystallisation and biodegradation behaviour of Bioglass®-derived glass-ceramics. Faraday Discuss. 136. https://doi.org/10.1039/b616539g

Boccaccini, A.R., Ma, P.X., Liverani, L., 2021. Tissue Engineering Using Ceramics and Polymers, Third Edition, Tissue Engineering Using Ceramics and Polymers, Third Edition. https://doi.org/10.1016/C2019-0-01031-X

Bonatti, A.F., Vozzi, G., De Maria, C., 2024. Enhancing quality control in bioprinting through machine learning. Biofabrication. https://doi.org/10.1088/1758-5090/ad2189

Boraldi, F., Bartolomeo, A., Di Bari, C., Cocconi, A., Quaglino, D., 2015. Donor's age and replicative senescence favour the in-vitro mineralization potential of human fibroblasts. Exp. Gerontol. 72, 218–226. https://doi.org/10.1016/J.EXGER.2015.10.009

Boraldi, F., Lofaro, F.D., Bonacorsi, S., Mazzilli, A., Garcia-Fernandez, M., Quaglino, D., 2024. The Role of Fibroblasts in Skin Homeostasis and Repair. Biomedicines 2024, Vol. 12, Page 1586 12, 1586. https://doi.org/10.3390/BIOMEDICINES12071586

Borandeh, S., van Bochove, B., Teotia, A., Seppälä, J., 2021. Polymeric drug delivery systems by additive manufacturing. Adv. Drug Deliv. Rev. 173, 349–373. https://doi.org/10.1016/J.ADDR.2021.03.022

Bose, S., Roy, M., Bandyopadhyay, A., 2012. Recent advances in bone tissue engineering scaffolds. Trends Biotechnol. 30, 546. https://doi.org/10.1016/J.TIBTECH.2012.07.005

Boztepe, C., Künkül, A., Yüceer, M., 2020. Application of artificial intelligence in modeling of the doxorubicin release behavior of pH and temperature responsive poly(NIPAAm-co-AAc)-PEG IPN hydrogel. J. Drug Deliv. Sci. Technol. 57, 101603. https://doi.org/10.1016/J.JDDST.2020.101603

Brandao-Burch, A., Utting, J.C., Orriss, I.R., Arnett, T.R., 2005. Acidosis inhibits bone formation by osteoblasts in vitro by preventing mineralization. Calcif. Tissue Int. 77, 167–174. https://doi.org/10.1007/S00223-004-0285-8

Brauer, D.S., Rüssel, C., Kraft, J., 2007. Solubility of glasses in the system P2O5-CaO-MgO-Na2O-TiO2: Experimental and modeling using artificial neural networks. J. Non. Cryst. Solids 353. https://doi.org/10.1016/j.jnoncrysol.2006.12.005

Bretcanu, O., Chatzistavrou, X., Paraskevopoulos, K., Conradt, R., Thompson, I., Boccaccini, A.R., 2009. Sintering and crystallisation of 45S5 Bioglass® powder. J. Eur. Ceram. Soc. 29. https://doi.org/10.1016/j.jeurceramsoc.2009.06.035

Bretcanu, O., Chen, Q., Misra, S.K., Boccaccini, A.R., Roy, I., Verne, E., Brovarone, C.V., 2007. Biodegradable polymer coated 45S5 Bioglass-derived glass-ceramic scaffolds for bone tissue engineering. Glass Technology: European Journal of Glass Science and Technology Part A 48.

Brink, M., 1997. The influence of alkali and alkaline earths on the working range for bioactive glasses. J. Biomed. Mater. Res. 36. https://doi.org/10.1002/(SICI)1097-4636(199707)36:1<109::AID-JBM13>3.0.CO;2-D

Brink, M., Turunen, T., Happonen, R.P., Yli-Urpo, A., 1997. Compositional dependence of bioactivity of glasses in the system Na2O- K2O-MgO-Cao-B2O3-P2O5-SiO2. J.

Biomed. Mater. Res. 37. https://doi.org/10.1002/(SICI)1097-4636(199710)37:1<114::AID-JBM14>3.0.CO;2-G

Brückner, R., Tylkowski, M., Hupa, L., Brauer, D.S., 2016. Controlling the ion release from mixed alkali bioactive glasses by varying modifier ionic radii and molar volume. J. Mater. Chem. B 4, 3121–3134. https://doi.org/10.1039/C5TB02426A

Burg, K.J.L., Holder, W.D., Culberson, C.R., Beiler, R.J., Greene, K.G., Loebsack, A.B., Roland, W.D., Mooney, D.J., Halberstadt, C.R., 1999. Parameters affecting cellular adhesion to polylactide films. J. Biomater. Sci. Polym. Ed. 10. https://doi.org/10.1163/156856299X00108

Cacciotti, I., 2017. Bivalent cationic ions doped bioactive glasses: the influence of magnesium, zinc, strontium and copper on the physical and biological properties. J. Mater. Sci. 52. https://doi.org/10.1007/s10853-017-1010-0

Cai, S., Wu, C., Yang, W., Liang, W., Yu, H., Liu, L., 2020. Recent advance in surface modification for regulating cell adhesion and behaviors. Nanotechnol. Rev. 9. https://doi.org/10.1515/ntrev-2020-0076

CAMPUS [WWW Document], n.d. URL https://www.campusplastics.com/campus/

Cannillo, V., Esposito, L., Rambaldi, E., Sola, A., Tucci, A., 2009. Effect of porosity on the elastic properties of porcelainized stoneware tiles by a multi-layered model. Ceram. Int. 35. https://doi.org/10.1016/j.ceramint.2007.10.015

Cannillo, V., Leonelli, C., Boccaccini, A.R., 2002. Numerical models for thermal residual stresses in Al2O3 platelets/borosilicate glass matrix composites. Materials Science and Engineering: A 323, 246–250. https://doi.org/10.1016/S0921-5093(01)01345-4

Cannillo, V., Montorsi, M., Siligardi, C., Sola, A., de Portu, G., Micele, L., Pezzotti, G., 2006. Microscale computational simulation and experimental measurement of thermal residual stresses in glass–alumina functionally graded materials. J. Eur. Ceram. Soc. 26, 1411–1419. https://doi.org/10.1016/J.JEURCERAMSOC.2005.02.012

Cannillo, V., Sola, A., 2009. Potassium-based composition for a bioactive glass. Ceram. Int. 35. https://doi.org/10.1016/j.ceramint.2009.06.011

Carlsson, G., 2020. Topological methods for data modelling. Nature Reviews Physics. https://doi.org/10.1038/s42254-020-00249-3

Carvalho, M.S., Cabral, J.M.S., da Silva, C.L., Vashishth, D., 2021. Bone Matrix Non-Collagenous Proteins in Tissue Engineering: Creating New Bone by Mimicking the Extracellular Matrix. Polymers 2021, Vol. 13, Page 1095 13, 1095. https://doi.org/10.3390/POLYM13071095

Cassar, D.R., Mastelini, S.M., Botari, T., Alcobaça, E., de Carvalho, A.C.P.L.F., Zanotto, E.D., 2021. Predicting and interpreting oxide glass properties by machine learning using large datasets. Ceram. Int. 47. https://doi.org/10.1016/j.ceramint.2021.05.105

Cencer, M.M., Moore, J.S., Assary, R.S., 2022. Machine learning for polymeric materials: an introduction. Polym. Int. https://doi.org/10.1002/pi.6345

Center for Hierarchical Material Design, n.d. Polymer Property Predictor and Database [WWW Document]. URL https://pppdb.uchicago.edu/ (accessed 1.26.24).

Cerruti, M., Greenspan, D., Powers, K., 2005. Effect of pH and ionic strength on the reactivity of Bioglass® 45S5. Biomaterials 26, 1665–1674. https://doi.org/10.1016/J.BIOMATERIALS.2004.07.009

Cervera, M.F., Heinämäki, J., Krogars, K., Jörgensen, A.C., Karjalainen, M., Colarte, A.I., Yliruusi, J., 2004. Solid-state and mechanical properties of aqueous chitosan-amylose starch films plasticized with polyols. AAPS PharmSciTech 5. https://doi.org/10.1007/bf02830583

CESARANO III, J., 1999. Robocasting of Ceramics and Composites Using Fine Particle Suspensions. University of North Texas Libraries.

Chan, B.P., Leong, K.W., 2008. Scaffolding in tissue engineering: General approaches and tissue-specific considerations, in: European Spine Journal. https://doi.org/10.1007/s00586-008-0745-3

Chan, S.Y., Choo, W.S., 2013. Effect of extraction conditions on the yield and chemical properties of pectin from cocoa husks. Food Chem. 141. https://doi.org/10.1016/j.foodchem.2013.06.097

Chan, S.Y., Choo, W.S., Young, D.J., Loh, X.J., 2017. Pectin as a rheology modifier: Origin, structure, commercial production and rheology. Carbohydr. Polym. https://doi.org/10.1016/j.carbpol.2016.12.033

Chang, H.-I., Wang, Y., 2011. Cell Responses to Surface and Architecture of Tissue Engineering Scaffolds, in: Regenerative Medicine and Tissue Engineering - Cells and Biomaterials. https://doi.org/10.5772/21983

Chatjigakis, A.K., Pappas, C., Proxenia, N., Kalantzi, O., Rodis, P., Polissiou, M., 1998. FT-IR spectroscopic determination of the degree of esterification of cell wall pectins from stored peaches and correlation to textural changes. Carbohydr. Polym. 37. https://doi.org/10.1016/S0144-8617(98)00057-5

Chaudhari, S.A., Singhal, R.S., 2015. Cutin from watermelon peels: A novel inducer for cutinase production and its physicochemical characterization. Int. J. Biol. Macromol. 79. https://doi.org/10.1016/j.ijbiomac.2015.05.006

CHEMnetBASE Products, 2022. Polymers: A Property Database [WWW Document]. URL https://poly.chemnetbase.com/polymers/PolymerSearch.xhtml?dswid=2933 (accessed 1.26.24).

Chen, C., Xie, Z., Yang, S., Wu, H., Bi, Z., Zhang, Q., Xiao, Y., 2025. Machine Learning Approach to Investigating Macrophage Polarization on Various Titanium Surface Characteristics. BME Front. 6. https://doi.org/10.34133/BMEF.0100

Chen, C., Ye, W., Zuo, Y., Zheng, C., Ong, S.P., 2019. Graph Networks as a Universal Machine Learning Framework for Molecules and Crystals. Chemistry of Materials 31. https://doi.org/10.1021/acs.chemmater.9b01294

Chen, H., Liu, Y., Balabani, S., Hirayama, R., Huang, J., 2023. Machine Learning in Predicting Printable Biomaterial Formulations for Direct Ink Writing. Research. https://doi.org/10.34133/research.0197

Chen, Q., Schmidt, F., Görke, O., Asif, A., Weinhold, J., Aghaei, E., Ur Rehman, I., Gurlo, A., Shah, A.T., 2022. Ceramic Stereolithography of Bioactive Glasses: Influence of Resin Composition on Curing Behavior and Green Body Properties. Biomedicines 10. https://doi.org/10.3390/biomedicines10020395

Chen, Q.Z., Thompson, I.D., Boccaccini, A.R., 2006. 45S5 Bioglass®-derived glass-ceramic scaffolds for bone tissue engineering. Biomaterials 27. https://doi.org/10.1016/j.biomaterials.2005.11.025

Chen, Y., Kawazoe, N., Chen, G., 2018. Preparation of dexamethasone-loaded biphasic calcium phosphate nanoparticles/collagen porous composite scaffolds for bone tissue engineering. Acta Biomater. 67. https://doi.org/10.1016/j.actbio.2017.12.004

Chia, H.N., Wu, B.M., 2015. Recent advances in 3D printing of biomaterials. J. Biol. Eng. 9. https://doi.org/10.1186/s13036-015-0001-4

Choudhary, K., DeCost, B., Chen, C., Jain, A., Tavazza, F., Cohn, R., Park, C.W., Choudhary, A., Agrawal, A., Billinge, S.J.L., Holm, E., Ong, S.P., Wolverton, C., 2022. Recent advances and applications of deep learning methods in materials science. npj Computational Materials 2022 8:1 8, 1–26. https://doi.org/10.1038/s41524-022-00734-6

Ciapetti, G., Cenni, E., Pratelli, L., Pizzoferrato, A., 1993. In vitro evaluation of cell/biomaterial interaction by MTT assay. Biomaterials 14, 359–364. https://doi.org/10.1016/0142-9612(93)90055-7

Ciraldo, F.E., Boccardi, E., Melli, V., Westhauser, F., Boccaccini, A.R., 2018. Tackling bioactive glass excessive in vitro bioreactivity: Preconditioning approaches for cell culture tests. Acta Biomater. https://doi.org/10.1016/j.actbio.2018.05.019

Clupper, D.C., Hench, L.L., 2003. Crystallization kinetics of tape cast bioactive glass 45S5. J. Non. Cryst. Solids 318. https://doi.org/10.1016/S0022-3093(02)01857-4

Colquhoun, I.J., de Ruiter, G.A., Schols, H.A., Voragen, A.G.J., 1990. Identification by n.m.r. spectroscopy of oligosaccharides obtained by treatment of the hairy regions of apple pectin with rhamnogalacturonase. Carbohydr. Res. 206, 131–144. https://doi.org/10.1016/0008-6215(90)84012-J

Croisier, F., Jérôme, C., 2013. Chitosan-based biomaterials for tissue engineering. Eur. Polym. J. https://doi.org/10.1016/j.eurpolymj.2012.12.009

Crovace, M.C., Souza, M.T., Chinaglia, C.R., Peitl, O., Zanotto, E.D., 2016. Biosilicate® - A multipurpose, highly bioactive glass-ceramic. in vitro, in vivo and clinical trials. J. Non. Cryst. Solids 432. https://doi.org/10.1016/j.jnoncrysol.2015.03.022

Crupi, A., Costa, A., Tarnok, A., Melzer, S., Teodori, L., 2015. Inflammation in tissue engineering: The Janus between engraftment and rejection. Eur. J. Immunol. 45. https://doi.org/10.1002/eji.201545818

Damewood, J., Karaguesian, J., Lunger, J.R., Tan, A.R., Xie, M., Peng, J., Gómez-Bombarelli, R., 2023. Representations of Materials for Machine Learning. Annu. Rev. Mater. Res. https://doi.org/10.1146/annurev-matsci-080921-085947

Dan, Y., Zhao, Y., Li, X., Li, S., Hu, M., Hu, J., 2020. Generative adversarial networks (GAN) based efficient sampling of chemical composition space for inverse design of inorganic materials. NPJ Comput. Mater. 6, 1–7. https://doi.org/10.1038/s41524-020-00352-0

Darvell, B.W., Smith, A.J., 2022. Inert to bioactive – A multidimensional spectrum. Dental Materials 38, 2–6. https://doi.org/10.1016/J.DENTAL.2021.11.002

Das, R., Karthika, S., Bhasarkar, J., Bal, D.K., 2023. GA-coupled ANN model for predicting porosity in alginate gel scaffolds. J. Mech. Behav. Biomed. Mater. 148. https://doi.org/10.1016/j.jmbbm.2023.106204

Dash, P.A., Mohanty, S., Nayak, S.K., 2023. A review on bioactive glass, its modifications and applications in healthcare sectors. J. Non. Cryst. Solids 614, 122404. https://doi.org/10.1016/J.JNONCRYSOL.2023.122404

Daskalakis, E., Huang, B., Vyas, C., Acar, A.A., Fallah, A., Cooper, G., Weightman, A., Koc, B., Blunn, G., Bartolo, P., 2022. Novel 3D Bioglass Scaffolds for Bone Tissue Regeneration. Polymers (Basel). 14. https://doi.org/10.3390/polym14030445

Dave, K., Gomes, V.G., 2019. Interactions at scaffold interfaces: Effect of surface chemistry, structural attributes and bioaffinity. Materials Science and Engineering: C 105, 110078. https://doi.org/10.1016/J.MSEC.2019.110078

Davis, E.A., Derouet, C., Herve Du Penhoat, C., Morvan, C., 1990. Isolation and an N.M.R. study of pectins from flax (linum usitatissimum L.). Carbohydr. Res. 197, 205–215. https://doi.org/10.1016/0008-6215(90)84143-I

Davoudinejad, A., 2021. Vat photopolymerization methods in additive manufacturing. Addit. Manuf. 159–181. https://doi.org/10.1016/B978-0-12-818411-0.00007-0

Day, R.M., Boccaccini, A.R., Shurey, S., Roether, J.A., Forbes, A., Hench, L.L., Gabe, S.M., 2004. Assessment of polyglycolic acid mesh and bioactive glass for soft-tissue engineering scaffolds. Biomaterials 25, 5857–5866. https://doi.org/10.1016/j.biomaterials.2004.01.043

de Araujo Bastos Santana, L., Oliveira Junior, P.H., Damia, C., dos Santos Tavares, D., dos Santos, E.A., 2021. Bioactivity in SBF versus trace element effects: The isolated role of Mg2+ and Zn2+ in osteoblast behavior. Mater. Sci. Eng. C Mater. Biol. Appl. 118. https://doi.org/10.1016/J.MSEC.2020.111320

Deliormanli, A.M., Rahaman, M.N., 2012. Direct-write assembly of silicate and borate bioactive glass scaffolds for bone repair. J. Eur. Ceram. Soc. 32. https://doi.org/10.1016/j.jeurceramsoc.2012.05.005

Detsch, R., Alles, S., Hum, J., Westenberger, P., Sieker, F., Heusinger, D., Kasper, C., Boccaccini, A.R., 2015. Osteogenic differentiation of umbilical cord and adipose derived stem cells onto highly porous 45S5 Bioglass®-based scaffolds. J. Biomed. Mater. Res. A 103, 1029–1037. https://doi.org/10.1002/JBM.A.35238

Diba, M., Tapia, F., Boccaccini, A.R., Strobel, L.A., 2012. Magnesium-Containing Bioactive Glasses for Biomedical Applications. Int. J. Appl. Glass Sci. 3. https://doi.org/10.1111/j.2041-1294.2012.00095.x

Ding, Y., Liu, X., Zhang, J., Lv, Z., Meng, X., Yuan, Z., Long, T., Wang, Y., 2022. 3D printing polylactic acid polymer-bioactive glass loaded with bone cement for bone defect in weight-bearing area. Front. Bioeng. Biotechnol. 10. https://doi.org/10.3389/fbioe.2022.947521

Distler, T., Fournier, N., Grünewald, A., Polley, C., Seitz, H., Detsch, R., Boccaccini, A.R., 2020. Polymer-Bioactive Glass Composite Filaments for 3D Scaffold Manufacturing by Fused Deposition Modeling: Fabrication and Characterization. Front. Bioeng. Biotechnol. 8, 1–17. https://doi.org/10.3389/fbioe.2020.00552

Djali, M., Kayaputri, I.L., Kurniati, D., Sukarminah, E., Mudjenan, I.M.H., Utama, G.L., 2021. Degradation of Lignocelluloses Cocoa Shell (Theobroma cacao L.) by Various Types of Mould Treatments. J. Food Qual. 2021. https://doi.org/10.1155/2021/6127029

Do Vale Pereira, R., Salmoria, G.V., De Moura, M.O.C., Aragones, Á., Fredel, M.C., 2014. Scaffolds of PDLLA/Bioglass 58S produced via selective laser sintering. Materials Research 17. https://doi.org/10.1590/S1516-14392014005000075

Dogrul, F., Ożóg, P., Michálek, M., Elsayed, H., Galusek, D., Liverani, L., Boccaccini, A.R., Bernardo, E., 2021. Polymer-derived biosilicate®-like glass-ceramics: Engineering of

formulations and additive manufacturing of three-dimensional scaffolds. Materials 14. https://doi.org/10.3390/ma14185170

Domingo, J.L., 2002. Vanadium and Tungsten Derivatives as Antidiabetic Agents. Biol. Trace Elem. Res. 88. https://doi.org/10.1385/bter:88:2:097

Dorj, B., Park, J.H., Kim, H.W., 2012. Robocasting chitosan/nanobioactive glass dual-pore structured scaffolds for bone engineering. Mater. Lett. 73. https://doi.org/10.1016/j.matlet.2011.12.107

Dos Anjos Lopes, S.M., Martins, M.V., de Souza, V.B., Tulini, F.L., 2023. Evaluation of the Nutritional Composition of Cocoa Bean Shell Waste (Theobroma cacao) and Application in the Production of a Phenolic-rich Iced Tea. Journal of Culinary Science and Technology 21. https://doi.org/10.1080/15428052.2021.2016531

Douest, Y., Forrest, R.M., Ter-Ovanessian, B., Courtois, N., Tancret, F., Greer, A.L., Chevalier, J., Fabrègue, D., 2024. Machine learning-guided exploration and experimental assessment of unreported compositions in the quaternary Ti-Zr-Cu-Pd biocompatible metallic glass system. Acta Biomater. 175. https://doi.org/10.1016/j.actbio.2023.12.028

Drago, L., Romanò, D., De Vecchi, E., Vassena, C., Logoluso, N., Mattina, R., Romanò, C.L., 2013. Bioactive glass bag-S53P4 for the adjunctive treatment of chronic osteomyelitis of the long bones: An in vitro and prospective clinical study. BMC Infect. Dis. 13. https://doi.org/10.1186/1471-2334-13-584

Dranca, F., Vargas, M., Oroian, M., 2020. Physicochemical properties of pectin from Malus domestica 'Fălticeni' apple pomace as affected by non-conventional extraction techniques. Food Hydrocoll. 100, 105383. https://doi.org/10.1016/J.FOODHYD.2019.105383

Du, X., Wei, D., Huang, L., Zhu, M., Zhang, Y., Zhu, Y., 2019. 3D printing of mesoporous bioactive glass/silk fibroin composite scaffolds for bone tissue engineering. Materials Science and Engineering C 103. https://doi.org/10.1016/j.msec.2019.05.016

Du, Y., Liu, H., Yang, Q., Wang, S., Wang, J., Ma, J., Noh, I., Mikos, A.G., Zhang, S., 2017. Selective laser sintering scaffold with hierarchical architecture and gradient composition for osteochondral repair in rabbits. Biomaterials 137. https://doi.org/10.1016/j.biomaterials.2017.05.021

Dukle, A., Murugan, D., Nathanael, A.J., Rangasamy, L., Oh, T.H., 2022. Can 3D-Printed Bioactive Glasses Be the Future of Bone Tissue Engineering? Polymers (Basel). 14, 1–20. https://doi.org/10.3390/polym14081627

Dyson, R.W., 1987. Polymer structures and general properties. Specialty Polymers 3–19. https://doi.org/10.1007/978-1-4615-7894-9_2

Ebrahimi, M., Manafi, S., Sharifianjazi, F., 2023. The effect of Ag2O and MgO dopants on the bioactivity, biocompatibility, and antibacterial properties of 58S bioactive glass synthesized by the sol-gel method. J. Non. Cryst. Solids 606. https://doi.org/10.1016/j.jnoncrysol.2023.122189

Echeverria Molina, M.I., Malollari, K.G., Komvopoulos, K., 2021. Design Challenges in Polymeric Scaffolds for Tissue Engineering. Front. Bioeng. Biotechnol. https://doi.org/10.3389/fbioe.2021.617141

Echezarreta-López, M.M., Landin, M., 2013. Using machine learning for improving knowledge on antibacterial effect of bioactive glass. Int. J. Pharm. 453. https://doi.org/10.1016/j.ijpharm.2013.06.036

Ege, D., Boccaccini, A.R., 2024. Investigating the Effect of Processing and Material Parameters of Alginate Dialdehyde-Gelatin (ADA-GEL)-Based Hydrogels on Stiffness by XGB Machine Learning Model. Bioengineering 11. https://doi.org/10.3390/bioengineering11050415

Ege, D., Sertturk, S., Acarkan, B., Ademoglu, A., 2023. Machine learning models to predict the relationship between printing parameters and tensile strength of 3D Poly (lactic acid) scaffolds for tissue engineering applications. Biomed. Phys. Eng. Express 9. https://doi.org/10.1088/2057-1976/acf581

Ekladious, I., Colson, Y.L., Grinstaff, M.W., 2019. Polymer–drug conjugate therapeutics: advances, insights and prospects. Nat. Rev. Drug Discov. 18, 273–294. https://doi.org/10.1038/S41573-018-0005-0;SUBJMETA

El Damrawi, G., Ramadan, R.M., El Baiomy, M., 2021. Effect of SrO on the Structure of Apatite and Wollastonite Phases of Na2O-CaO-SiO2-P2O5 Glass System. New Journal of Glass and Ceramics 11, 45–56. https://doi.org/10.4236/njgc.2021.112003

Elgayar, I., Aliev, A.E., Boccaccini, A.R., Hill, R.G., 2005. Structural analysis of bioactive glasses. J. Non. Cryst. Solids 351. https://doi.org/10.1016/j.jnoncrysol.2004.07.067

El-Ghannam, A., Ducheyne, P., Shapiro, I.M., 1997. Formation of surface reaction products on bioactive glass and their effects on the expression of the osteoblastic phenotype and the deposition of mineralized extracellular matrix. Biomaterials 18, 295–303. https://doi.org/10.1016/S0142-9612(96)00059-2

El-Ghannam, A., Hamazawy, E., Yehia, A., 2001. Effect of thermal treatment on bioactive glass microstructure, corrosion behavior ζ potential, and protein adsorption. J. Biomed. Mater. Res. 55. https://doi.org/10.1002/1097-4636(20010605)55:3<387::AID-JBM1027>3.0.CO;2-V

Elomaa, L., Kokkari, A., Närhi, T., Seppälä, J. V., 2013. Porous 3D modeled scaffolds of bioactive glass and photocrosslinkable poly(ε-caprolactone) by stereolithography. Compos. Sci. Technol. 74. https://doi.org/10.1016/j.compscitech.2012.10.014

El-Rashidy, A.A., Roether, J.A., Harhaus, L., Kneser, U., Boccaccini, A.R., 2017. Regenerating bone with bioactive glass scaffolds: A review of in vivo studies in bone defect models. Acta Biomater. https://doi.org/10.1016/j.actbio.2017.08.030

Elsayed, H., Picicco, M., Dasan, A., Kraxner, J., Galusek, D., Bernardo, E., 2020. Glass powders and reactive silicone binder: Application to digital light processing of bioactive glass-ceramic scaffolds. Ceram. Int. 46. https://doi.org/10.1016/j.ceramint.2020.06.323

Elsayed, H., Picicco, M., Dasan, A., Kraxner, J., Galusek, D., Bernardo, E., 2019. Glass powders and reactive silicone binder: Interactions and application to additive manufacturing of bioactive glass-ceramic scaffolds. Ceram. Int. 45. https://doi.org/10.1016/j.ceramint.2019.04.070

Elsayed, H., Romero, A.R., Ferroni, L., Gardin, C., Zavan, B., Bernardo, E., 2017. Bioactive glass-ceramic scaffolds from novel “inorganic gel casting” and sinter-crystallization. Materials 10. https://doi.org/10.3390/ma10020171

Fabert, M., Ojha, N., Erasmus, E., Hannula, M., Hokka, M., Hyttinen, J., Rocherullé, J., Sigalas, I., Massera, J., 2017. Crystallization and sintering of borosilicate bioactive glasses for application in tissue engineering. J. Mater. Chem. B 5. https://doi.org/10.1039/c7tb00106a

Farag, M.M., 2023. Recent trends on biomaterials for tissue regeneration applications: review. J. Mater. Sci. 58, 527–558. https://doi.org/10.1007/S10853-022-08102-X/FIGURES/22

Fathi, A., Kermani, F., Behnamghader, A., Banijamali, S., Mozafari, M., Baino, F., Kargozar, S., 2021. Three-dimensionally printed polycaprolactone/multicomponent bioactive glass scaffolds for potential application in bone tissue engineering. Biomedical Glasses 6. https://doi.org/10.1515/bglass-2020-0006

Febrianto, N.A., Zhu, F., 2022. Comparison of bioactive components and flavor volatiles of diverse cocoa genotypes of Theobroma grandiflorum, Theobroma bicolor, Theobroma subincanum and Theobroma cacao. Food Research International 161. https://doi.org/10.1016/j.foodres.2022.111764

Feoktistova, M., Geserick, P., Leverkus, M., 2016. Crystal Violet Assay for Determining Viability of Cultured Cells. Cold Spring Harb. Protoc. 2016, 343–346. https://doi.org/10.1101/PDB.PROT087379

Ferreira, J.M.F., 2017. The key Features expected from a Perfect Bioactive Glass –How Far we still are from an Ideal Composition? Biomed. J. Sci. Tech. Res. 1. https://doi.org/10.26717/bjstr.2017.01.000335

Filho, O.P., Latorre, G.P., Hench, L.L., 1996. Effect of crystallization on apatite-layer formation of bioactive glass 45S5. J. Biomed. Mater. Res. 30. https://doi.org/10.1002/(SICI)1097-4636(199604)30:4<509::AID-JBM9>3.0.CO;2-T

Fiume, E., Ciavattini, S., Verné, E., Baino, F., 2021. Foam replica method in the manufacturing of bioactive glass scaffolds: Out-of-date technology or still underexploited potential? Materials. https://doi.org/10.3390/ma14112795

Flores-Rojas, G.G., Gómez-Lazaro, B., López-Saucedo, F., Vera-Graziano, R., Bucio, E., Mendizábal, E., 2023. Electrospun Scaffolds for Tissue Engineering: A Review. Macromol 2023, Vol. 3, Pages 524-553 3, 524–553. https://doi.org/10.3390/MACROMOL3030031

Food and Drug Administration, 2025. Artificial Intelligence-Enabled Device Software Functions: Lifecycle Management and Marketing Submission Recommendations [WWW Document]. URL https://www.fda.gov/regulatory-information/search-fda-

guidance-documents/artificial-intelligence-enabled-device-software-functions-lifecycle-management-and-marketing (accessed 5.10.25).

Franz, S., Rammelt, S., Scharnweber, D., Simon, J.C., 2011. Immune responses to implants - A review of the implications for the design of immunomodulatory biomaterials. Biomaterials. https://doi.org/10.1016/j.biomaterials.2011.05.078

Fredholm, Y.C., Karpukhina, N., Law, R. V., Hill, R.G., 2010. Strontium containing bioactive glasses: Glass structure and physical properties, in: Journal of Non-Crystalline Solids. https://doi.org/10.1016/j.jnoncrysol.2010.06.078

Fu, Q., Rahaman, M.N., Fu, H., Liu, X., 2010. Silicate, borosilicate, and borate bioactive glass scaffolds with controllable degradation rate for bone tissue engineering applications. I. Preparation and in vitro degradation. J. Biomed. Mater. Res. A 95. https://doi.org/10.1002/jbm.a.32824

Fu, Q., Saiz, E., Rahaman, M.N., Tomsia, A.P., 2011. Bioactive glass scaffolds for bone tissue engineering: State of the art and future perspectives. Materials Science and Engineering C. https://doi.org/10.1016/j.msec.2011.04.022

Fujikura, K., Karpukhina, N., Kasuga, T., Brauer, D.S., Hill, R.G., Law, R. V., 2012. Influence of strontium substitution on structure and crystallisation of Bioglass® 45S5. J. Mater. Chem. 22, 7395–7402. https://doi.org/10.1039/C2JM14674F

Fuse, M., Kuwada-Kusunose, T., Ogura, A., 2024. Effect of Alkaline Treatment on the Bioactivity of Poly(lactic acid) (PLA) Films in Vitro. International Journal of Oral-Medical Sciences 23, 18–25. https://doi.org/10.5466/ijoms.23.18

Gaharwar, A.K., Singh, I., Khademhosseini, A., 2020. Engineered biomaterials for in situ tissue regeneration. Nat. Rev. Mater. https://doi.org/10.1038/s41578-020-0209-x

Gai, L., Ren, E.F., Tian, W., Niu, D., Sun, W., Hang, F., Li, K., 2022. Ultrasonic-Assisted Dual-Alkali Pretreatment and Enzymatic Hydrolysis of Sugarcane Bagasse Followed by Candida tropicalis Fermentation to Produce Xylitol. Front. Nutr. 9, 913106. https://doi.org/10.3389/FNUT.2022.913106/BIBTEX

Gao, Yongsheng, Peng, Kevin, Mitragotri, Samir, Gao, Y, Peng, K, Mitragotri, S, 2021. Covalently Crosslinked Hydrogels via Step-Growth Reactions: Crosslinking Chemistries, Polymers, and Clinical Impact. Advanced Materials 33, 2006362. https://doi.org/10.1002/ADMA.202006362

Gavinho, S.R., Pádua, A.S., Holz, L.I.V., Sá-Nogueira, I., Silva, J.C., Borges, J.P., Valente, M.A., Graça, M.P.F., 2023. Bioactive Glasses Containing Strontium or Magnesium Ions to Enhance the Biological Response in Bone Regeneration. Nanomaterials 13. https://doi.org/10.3390/nano13192717

Gholami, K., Ege, F., Barzegar, R., 2023. Prediction of Composite Mechanical Properties: Integration of Deep Neural Network Methods and Finite Element Analysis. Journal of Composites Science 7. https://doi.org/10.3390/jcs7020054

Ghoshal, G., Negi, P., 2020. Isolation of pectin from kinnow peels and its characterization. Food and Bioproducts Processing 124. https://doi.org/10.1016/j.fbp.2020.09.008

Giannoudis, P. V., Dinopoulos, H., Tsiridis, E., 2005. Bone substitutes: an update. Injury. https://doi.org/10.1016/j.injury.2005.07.029

Girón-Hernández, J., Pazmino, M., Barrios-Rodríguez, Y.F., Turo, C.T., Wills, C., Cucinotta, F., Benlloch-Tinoco, M., Gentile, P., 2023. Exploring the effect of utilising organic acid solutions in ultrasound-assisted extraction of pectin from apple pomace, and its potential for biomedical purposes. Heliyon 9, e17736. https://doi.org/10.1016/J.HELIYON.2023.E17736

Girón-Hernández, J., Rodríguez, Y.B., Corbezzolo, N., Blanco, D.O., Gutiérrez, C.C., Cheung, W., Gentile, P., 2024a. Exploiting residual cocoa biomass to extract advanced materials as building blocks for manufacturing nanoparticles aimed at alleviating formation-induced oxidative stress on human dermal fibroblasts. Nanoscale Adv. 6, 3809–3824. https://doi.org/10.1039/d4na00248b

Girón-Hernández, J., Tombe, A., Chemban Koyilot, M., Salas-Calderón, K.T., Charlton, A., Wills, C., Gentile, P., 2024b. From cocoa waste to sustainable bioink: valorising pectin for circular economy-driven tissue engineering. Eur. Polym. J. 210, 112967. https://doi.org/10.1016/J.EURPOLYMJ.2024.112967

Gnanasambandam, R., Proctor, A., 2000. Determination of pectin degree of esterification by diffuse reflectance Fourier transform infrared spectroscopy. Food Chem. 68. https://doi.org/10.1016/S0308-8146(99)00191-0

Gokcekuyu, Y., Ekinci, F., Guzel, M.S., Acici, K., Aydin, S., Asuroglu, T., 2024. Artificial Intelligence in Biomaterials: A Comprehensive Review. Applied Sciences 2024, Vol. 14, Page 6590 14, 6590. https://doi.org/10.3390/APP14156590

Gong, D., Ben-Akiva, E., Singh, A., Yamagata, H., Est-Witte, S., Shade, J.K., Trayanova, N.A., Green, J.J., 2022. Machine learning guided structure function predictions enable in silico nanoparticle screening for polymeric gene delivery. Acta Biomater. 154, 349–358. https://doi.org/10.1016/J.ACTBIO.2022.09.072

González, P., Serra, J., Liste, S., Chiussi, S., León, B., Pérez-Amor, M., 2003. Raman spectroscopic study of bioactive silica based glasses. J. Non. Cryst. Solids 320. https://doi.org/10.1016/S0022-3093(03)00013-9

Gonzalez-Gutierrez, J., Cano, S., Schuschnigg, S., Kukla, C., Sapkota, J., Holzer, C., 2018. Additive Manufacturing of Metallic and Ceramic Components by the Material Extrusion of Highly-Filled Polymers: A Review and Future Perspectives. Materials 2018, Vol. 11, Page 840 11, 840. https://doi.org/10.3390/MA11050840

Gotterbarm, T., Richter, W., Jung, M., Berardi Vilei, S., Mainil-Varlet, P., Yamashita, T., Breusch, S.J., 2006. An in vivo study of a growth-factor enhanced, cell free, two-layered collagen-tricalcium phosphate in deep osteochondral defects. Biomaterials 27. https://doi.org/10.1016/j.biomaterials.2006.01.041

Grasdalen, H., Einar Bakøy, O., Larsen, B., 1988a. Determination of the degree of esterification and the distribution of methylated and free carboxyl groups in pectins by 1H-n.m.r. spectroscopy. Carbohydr. Res. 184, 183–191. https://doi.org/10.1016/0008-6215(88)80016-8

Grasdalen, H., Einar Bakøy, O., Larsen, B., 1988b. Determination of the degree of esterification and the distribution of methylated and free carboxyl groups in pectins by 1H-n.m.r. spectroscopy. Carbohydr. Res. 184. https://doi.org/10.1016/0008-6215(88)80016-8

Grasso, M., Azzouz, L., Ruiz-Hincapie, P., Zarrelli, M., Ren, G., 2018. Effect of temperature on the mechanical properties of 3D-printed PLA tensile specimens. Rapid Prototyp. J. 24, 1337–1346. https://doi.org/10.1108/RPJ-04-2017-0055

Guo, S., Meng, Q., Zhao, X., Wei, Q., Xu, H., 2015. Design and fabrication of a metastable β-type titanium alloy with ultralow elastic modulus and high strength. Sci. Rep. 5. https://doi.org/10.1038/srep14688

Hachem, K., Benabdesslem, Y., Ghomari, S., Hasnaoui, O., Kaid-Harche, M., 2016. Partial structural characterization of pectin cell wall from Argania spinosa leaves. Heliyon 2, e00076. https://doi.org/10.1016/J.HELIYON.2016.E00076

Haines, N.M., Lack, W.D., Seymour, R.B., Bosse, M.J., 2016. Defining the Lower Limit of a "critical Bone Defect" in Open Diaphyseal Tibial Fractures. J. Orthop. Trauma 30. https://doi.org/10.1097/BOT.0000000000000531

Hajiali, F., Tajbakhsh, S., Shojaei, A., 2018. Fabrication and Properties of Polycaprolactone Composites Containing Calcium Phosphate-Based Ceramics and Bioactive Glasses in Bone Tissue Engineering: A Review. Polymer Reviews. https://doi.org/10.1080/15583724.2017.1332640

Hall, C., 1981. Polymers: Molecular Structure. Polymer Materials 1–31. https://doi.org/10.1007/978-1-349-10187-0_1

Halldin Stenlid, J., Abild-Pedersen, F., 2024. Revealing Local and Directional Aspects of Catalytic Active Sites by the Nuclear and Surface Electrostatic Potential. Journal of Physical Chemistry C 128. https://doi.org/10.1021/acs.jpcc.3c08512

Halloran, J.W., 2016. Ceramic Stereolithography: Additive Manufacturing for Ceramics by Photopolymerization. Annu. Rev. Mater. Res. https://doi.org/10.1146/annurev-matsci-070115-031841

Halloran, J.W., Tomeckova, V., Gentry, S., Das, S., Cilino, P., Yuan, D., Guo, R., Rudraraju, A., Shao, P., Wu, T., Alabi, T.R., Baker, W., Legdzina, D., Wolski, D., Zimbeck, W.R., Long, D., 2011. Photopolymerization of powder suspensions for shaping ceramics. J. Eur. Ceram. Soc. 31. https://doi.org/10.1016/j.jeurceramsoc.2010.12.003

Hamid, Q., Snyder, J., Wang, C., Timmer, M., Hammer, J., Guceri, S., Sun, W., 2011. Fabrication of three-dimensional scaffolds using precision extrusion deposition with an assisted cooling device. Biofabrication 3. https://doi.org/10.1088/1758-5082/3/3/034109

Han, J., Wu, J., Xiang, X., Lingxia, X., Chen, R., Li, L., Ma, K., Sun, Q., Yang, R., Huang, T., Tong, L., Zhu, L., Wang, H., Wen, C., Zhao, Y., Wang, J., 2023. Biodegradable BBG/PCL composite scaffolds fabricated by selective laser sintering for directed regeneration of critical-sized bone defects. Mater. Des. 225. https://doi.org/https://doi.org/10.1016/j.matdes.2022.111543

Han, T., Stone-Weiss, N., Huang, J., Goel, A., Kumar, A., 2020. Machine learning as a tool to design glasses with controlled dissolution for healthcare applications. Acta Biomater. 107. https://doi.org/10.1016/j.actbio.2020.02.037

Handel, M., Hammer, T.R., Nooeaid, P., Boccaccini, A.R., Hoefer, D., 2013. 45S5-Bioglass®-Based 3D-Scaffolds Seeded with Human Adipose Tissue-Derived Stem Cells Induce In Vivo Vascularization in the CAM Angiogenesis Assay. https://home.liebertpub.com/tea 19, 2703–2712. https://doi.org/10.1089/TEN.TEA.2012.0707

Hao, H., Xue, Y., Wu, Y., Wang, C., Chen, Y., Wang, X., Zhang, P., Ji, J., 2023. A paradigm for high-throughput screening of cell-selective surfaces coupling orthogonal gradients and machine learning-based cell recognition. Bioact. Mater. 28. https://doi.org/10.1016/j.bioactmat.2023.04.022

Hashemi, A., Ezati, M., Zumberg, I., Vicar, T., Chmelikova, L., Cmiel, V., Provaznik, V., 2024. Characterization and optimization of a biomaterial ink aided by machine learning-assisted parameter suggestion. Mater. Today Commun. 40. https://doi.org/10.1016/j.mtcomm.2024.109777

Henao, J., Poblano-Salas, C., Monsalve, M., Corona-Castuera, J., Barceinas-Sanchez, O., 2019. Bio-active glass coatings manufactured by thermal spray: A status report. Journal of Materials Research and Technology. https://doi.org/10.1016/j.jmrt.2019.07.011

Hench, L.L., 1998. Bioceramics. Journal of the American Ceramic Society 81, 1705–1728. https://doi.org/https://doi.org/10.1111/j.1151-2916.1998.tb02540.x

Hench, L.L., 1991. Bioceramics: From Concept to Clinic. Journal of the American Ceramic Society 74, 1487–1510. https://doi.org/10.1111/J.1151-2916.1991.TB07132.X

Hench, L.L., Jones, J.R., 2015. Bioactive glasses: Frontiers and Challenges. Front. Bioeng. Biotechnol. https://doi.org/10.3389/fbioe.2015.00194

Hench, L.L., Paschall, H.A., 1973. Direct chemical bond of bioactive glass-ceramic materials to bone and muscle. J. Biomed. Mater. Res. 7, 25–42. https://doi.org/10.1002/JBM.820070304

Hench, L.L., Splinter, R.J., Allen, W.C., Greenlee, T.K., 1971. Bonding mechanisms at the interface of ceramic prosthetic materials. J. Biomed. Mater. Res. 5. https://doi.org/10.1002/jbm.820050611

Hench, L.L., Thompson, I., 2010. Twenty-first century challenges for biomaterials. J. R. Soc. Interface. https://doi.org/10.1098/rsif.2010.0151.focus

Hill, R.G., Brauer, D.S., 2011. Predicting the bioactivity of glasses using the network connectivity or split network models. J. Non. Cryst. Solids 357, 3884–3887. https://doi.org/10.1016/J.JNONCRYSOL.2011.07.025

Himanen, L., Jäger, M.O.J., Morooka, E. V., Federici Canova, F., Ranawat, Y.S., Gao, D.Z., Rinke, P., Foster, A.S., 2020. DScribe: Library of descriptors for machine learning in materials science. Comput. Phys. Commun. 247. https://doi.org/10.1016/j.cpc.2019.106949

Hollister, S.J., 2005. Porous scaffold design for tissue engineering. Nat. Mater. 4, 518–524. https://doi.org/10.1038/NMAT1421;KWRD

Hoppe, A., Güldal, N.S., Boccaccini, A.R., 2011. A review of the biological response to ionic dissolution products from bioactive glasses and glass-ceramics. Biomaterials. https://doi.org/10.1016/j.biomaterials.2011.01.004

Horikawa, S., Suzuki, K., Motojima, K., Nakano, K., Nagaya, M., Nagashima, H., Kaneko, H., Aizawa, M., 2024. Material Design of Porous Hydroxyapatite Ceramics via Inverse Analysis of an Estimation Model for Bone-Forming Ability Based on Machine Learning and Experimental Validation of Biological Hard Tissue Responses. Materials 17. https://doi.org/10.3390/ma17030571

Hotchkiss, A.T., Chau, H.K., Strahan, G.D., Nuñez, A., Harron, A., Simon, S., White, A.K., Yadav, M.P., Yeom, H.W., 2023. Carrot rhamnogalacturonan I structure and composition changed during 2017 in California. Food Hydrocoll. 137, 108411. https://doi.org/10.1016/J.FOODHYD.2022.108411

Hou, Y., Wang, X., Wang, Y., Chen, X., Wei, B., Zhang, J., Zhu, L., Kou, H., Li, W., Wang, H., 2023. Electrospun Nanofibrous Conduit Filled with a Collagen-Based Matrix (ColM) for Nerve Regeneration. Molecules 28, 7675. https://doi.org/10.3390/MOLECULES28227675/S1

Hu, W., Cheng, H., Wu, D., Chen, J., Ye, X., Chen, S., 2022. Enhanced extraction assisted by pressure and ultrasound for targeting RG-I enriched pectin from citrus peel wastes: A mechanistic study. Food Hydrocoll. 133, 107778. https://doi.org/10.1016/J.FOODHYD.2022.107778

Huamani-Palomino, R.G., Pedro Ramos, M., Oliveira, G., Kock, F.V.C., Venâncio, T., Córdova, B.M., 2023. Structural elucidation of pectin extracted from cocoa pod husk (Theobroma Cacao L.): Evaluation of the degree of esterification using FT-IR and 1H NMR. Biomass Convers. Biorefin. 15, 2047–2061. https://doi.org/10.1007/S13399-023-04082-3/METRICS

Huang, J., Xu, Yanchao, Xue, Y., Huang, Y., Li, X., Chen, X., Xu, Yao, Zhang, D., Zhang, P., Zhao, J., Ji, J., 2023. Identification of potent antimicrobial peptides via a machine-learning pipeline that mines the entire space of peptide sequences. Nat. Biomed. Eng. 7. https://doi.org/10.1038/s41551-022-00991-2

Huang, W., Day, D.E., Kittiratanapiboon, K., Rahaman, M.N., 2006. Kinetics and mechanisms of the conversion of silicate (45S5), borate, and borosilicate glasses to hydroxyapatite in dilute phosphate solutions. J. Mater. Sci. Mater. Med. 17. https://doi.org/10.1007/s10856-006-9220-z

Hupa, L., Fagerlund, S., Massera, J., Björkvik, L., 2016. Dissolution behavior of the bioactive glass S53P4 when sodium is replaced by potassium, and calcium with magnesium or strontium. J. Non. Cryst. Solids 432. https://doi.org/10.1016/j.jnoncrysol.2015.03.026

Ibrahimi, S., D'Andrea, L., Gastaldi, D., Rivolta, M.W., Vena, P., 2024. Machine Learning approaches for the design of biomechanically compatible bone tissue engineering scaffolds. Comput. Methods Appl. Mech. Eng. 423. https://doi.org/10.1016/j.cma.2024.116842

Iglesias, M.T., Lozano, J.E., 2004. Extraction and characterization of sunflower pectin. J. Food Eng. 62. https://doi.org/10.1016/S0260-8774(03)00234-6

Ilyas, K., Akhtar, M.A., Ammar, E. Ben, Boccaccini, A.R., 2022. Surface Modification of 3D-Printed PCL / BG Composite Scaffolds via Mussel-Inspired Polydopamine and Effective Antibacterial Coatings for Biomedical Applications. https://doi.org/https://doi.org/10.3390/ma15238289

International Glass Database System, n.d. Interglad Ver. 8 [WWW Document]. URL https://www.newglass.jp/interglad_n/gaiyo/info_e.html (accessed 2.13.24).

International Standard Organization, n.d. ISO 10993-12:2021 - Biological evaluation of medical devices — Part 12: Sample preparation and reference materials.

Isaac, J., Nohra, J., Lao, J., Jallot, E., Nedelec, J.M., Berdal, A., Sautier, J.M., 2011. Effects of strontium-doped bioactive glass on the differentiation of cultured osteogenic cells. Eur. Cell. Mater. 21, 130–143. https://doi.org/10.22203/ECM.V021A11,

Isayev, O., Oses, C., Toher, C., Gossett, E., Curtarolo, S., Tropsha, A., 2017. Universal fragment descriptors for predicting properties of inorganic crystals. Nat. Commun. https://doi.org/10.1038/ncomms15679

iScienceSearch, n.d. SciGlass [WWW Document]. URL https://www.akoscheminformatics.de/sciglass/sciglass.htm (accessed 2.13.24).

Jadbabaei, S., Kolahdoozan, M., Naeimi, F., Ebadi-Dehaghani, H., 2021. Preparation and characterization of sodium alginate–PVA polymeric scaffolds by electrospinning method for skin tissue engineering applications. RSC Adv. 11, 30674–30688. https://doi.org/10.1039/D1RA04176B

Jaidev, L.R., Chatterjee, K., 2019. Surface functionalization of 3D printed polymer scaffolds to augment stem cell response. Mater. Des. 161, 44–54. https://doi.org/10.1016/J.MATDES.2018.11.018

Jain, A., Ong, S.P., Hautier, G., Chen, W., Richards, W.D., Dacek, S., Cholia, S., Gunter, D., Skinner, D., Ceder, G., Persson, K.A., 2013. Commentary: The materials project: A materials genome approach to accelerating materials innovation. APL Mater. https://doi.org/10.1063/1.4812323

Janiesch, C., Zschech, P., Heinrich, K., 2021. Machine learning and deep learning. Electronic Markets 31. https://doi.org/10.1007/s12525-021-00475-2

Jarrín-Chacón, J.P., Núñez-Pérez, J., Espín-Valladares, R. del C., Manosalvas-Quiroz, L.A., Rodríguez-Cabrera, H.M., Pais-Chanfrau, J.M., 2023. Pectin Extraction from Residues of the Cocoa Fruit (Theobroma cacao L.) by Different Organic Acids: A Comparative Study. Foods 2023, Vol. 12, Page 590 12, 590. https://doi.org/10.3390/FOODS12030590

Javaid, S., Gorji, H.T., Soulami, K.B., Kaabouch, N., 2023. Identification and ranking biomaterials for bone scaffolds using machine learning and PROMETHEE. Research on Biomedical Engineering 39. https://doi.org/10.1007/s42600-022-00257-5

Jazayeri, S.M., Oviedo-Bayas, B., Guerrero-Chuez, R., Torres-Navarrete, Y., Villamar-Torres, R.O., 2021. Environmental factors enhance production of plant secondary

metabolites toward more tolerance and human health: Cocoa and coffee two model species. Innovations in Biotechnology for a Sustainable Future 155–183. https://doi.org/10.1007/978-3-030-80108-3_9/TABLES/2

Jean-Marie, E., Jiang, W., Bereau, D., Robinson, J.C., 2022. Theobroma cacao and Theobroma grandiflorum: Botany, Composition and Pharmacological Activities of Pods and Seeds. Foods. https://doi.org/10.3390/foods11243966

Jha, P., Singh, K., 2016. Effect of MgO on bioactivity, hardness, structural and optical properties of SiO 2-K 2 O-CaO-MgO glasses. Ceram. Int. 42, 436–444. https://doi.org/10.1016/j.ceramint.2015.08.128

Jha, R., Dulikravich, G.S., 2021. Discovery of new Ti-based alloys aimed at avoiding/minimizing formation of α" and ω-phase using calphad and artificial intelligence. Metals (Basel). 11. https://doi.org/10.3390/met11010015

Jiang, Y., Chen, D., Chen, X., Li, T., Wei, G.W., Pan, F., 2021. Topological representations of crystalline compounds for the machine-learning prediction of materials properties. NPJ Comput. Mater. 7. https://doi.org/10.1038/s41524-021-00493-w

Joint FAO/WHO Expert Committee on Food Additives, 2006. Combined compendium of food additive specifications.

Jones, J.R., 2015. Reprint of: Review of bioactive glass: From Hench to hybrids. Acta Biomater. https://doi.org/10.1016/j.actbio.2015.07.019

Jones, J.R., 2013. Review of bioactive glass: From Hench to hybrids. Acta Biomater. 9, 4457–4486. https://doi.org/10.1016/j.actbio.2012.08.023

Jones, J.R., Clare, A.G., 2012. Bio-Glasses: An Introduction. Bio-Glasses: An Introduction. https://doi.org/10.1002/9781118346457

Joorabloo, A., Khorasani, M.T., Adeli, H., Mansoori-Moghadam, Z., Moghaddam, A., 2019. Fabrication of heparinized nano ZnO/poly(vinylalcohol)/carboxymethyl cellulose bionanocomposite hydrogels using artificial neural network for wound dressing application. Journal of Industrial and Engineering Chemistry 70. https://doi.org/10.1016/j.jiec.2018.10.022

Joseph, B., George, A., Gopi, S., Kalarikkal, N., Thomas, S., 2017. Polymer sutures for simultaneous wound healing and drug delivery – A review. Int. J. Pharm. https://doi.org/10.1016/j.ijpharm.2017.03.041

Joshi, S.R., Pendyala, G.S., Shah, P., Mopagar, V.P., Padmawar, N., Padubidri, M., 2020. Scaffolds--The Ground for Regeneration: A Narrative Review. J. Int. Soc. Prev. Community Dent. 10.

Kačarević, Ž.P., Rider, P.M., Alkildani, S., Retnasingh, S., Smeets, R., Jung, O., Ivanišević, Z., Barbeck, M., 2018. An introduction to 3D bioprinting: Possibilities, challenges and future aspects. Materials. https://doi.org/10.3390/ma11112199

Kacuráková, M., Capek, P., Sasinková, V., Wellner, N., Ebringerová, A., 2000. FT-IR study of plant cell wall model compounds: pectic polysaccharides and hemicelluloses. Carbohydr. Polym. 43, 195–203. https://doi.org/10.1016/S0144-8617(00)00151-X

Kalirajan, C., Dukle, A., Nathanael, A.J., Oh, T.H., Manivasagam, G., 2021. A Critical Review on Polymeric Biomaterials for Biomedical Applications. Polymers 2021, Vol. 13, Page 3015 13, 3015. https://doi.org/10.3390/POLYM13173015

Kanapaakala, G., Subramani, V., 2024. Predictive modeling for design of low elastic modulus and biocompatible β-Ti alloys: A comprehensive machine learning-data driven approach with XGBoost as the key predictor. Proc. Inst. Mech. Eng. C J. Mech. Eng. Sci. https://doi.org/10.1177/09544062241253712

Kang, J.H., Jang, K.J., Sakthiabirami, K., Oh, G.J., Jang, J.G., Park, C., Lim, H.P., Yun, K.D., Park, S.W., 2020. Mechanical properties and optical evaluation of scaffolds produced from 45S5 bioactive glass suspensions via stereolithography. Ceram. Int. 46. https://doi.org/10.1016/j.ceramint.2019.09.242

Kanzaki, N., Onuma, K., Treboux, G., Tsutsumi, S., Ito, A., 2000. Inhibitory Effect of Magnesium and Zinc on Crystallization Kinetics of Hydroxyapatite. Journal of Physical Chemistry B 104, 4189–4194. https://doi.org/10.1021/JP9939726

Karande, P., Gallagher, B., Han, T.Y.J., 2022. A Strategic Approach to Machine Learning for Material Science: How to Tackle Real-World Challenges and Avoid Pitfalls. Chemistry of Materials 34. https://doi.org/10.1021/acs.chemmater.2c01333

Karati, D., 2023. A concise review on bio-responsive polymers in targeted drug delivery system. Polymer Bulletin 80, 7023–7045. https://doi.org/10.1007/S00289-022-04424-7/FIGURES/6

Kargozar, S., Montazerian, M., Fiume, E., Baino, F., 2019. Multiple and promising applications of strontium (Sr)-containing bioactive glasses in bone tissue engineering. Front. Bioeng. Biotechnol. 7, 453733. https://doi.org/10.3389/FBIOE.2019.00161

Karl, D., Jastram, B., Kamm, P.H., Schwandt, H., Gurlo, A., Schmidt, F., 2019. Evaluating porous polylactide-co-glycolide/bioactive glass composite microsphere powders for laser sintering of scaffolds. Powder Technol. 354. https://doi.org/10.1016/j.powtec.2019.06.010

Kaur, G., Pandey, O.P., Singh, K., Homa, D., Scott, B., Pickrell, G., 2014. A review of bioactive glasses: Their structure, properties, fabrication and apatite formation. J. Biomed. Mater. Res. A. https://doi.org/10.1002/jbm.a.34690

Kazemi, M., Amiri Samani, S., Ezzati, S., Khodaiyan, F., Hosseini, S.S., Jafari, M., 2021. High-quality pectin from cantaloupe waste: eco-friendly extraction process, optimization, characterization and bioactivity measurements. J. Sci. Food Agric. 101. https://doi.org/10.1002/jsfa.11327

Kerner, J., Dogan, A., von Recum, H., 2021. Machine learning and big data provide crucial insight for future biomaterials discovery and research. Acta Biomater. https://doi.org/10.1016/j.actbio.2021.05.053

Khalvandi, A., Tayebi, L., Kamarian, S., Saber-Samandari, S., Song, J. il, 2023. Data-driven supervised machine learning to predict the compressive response of porous PVA/Gelatin hydrogels and in-vitro assessments: Employing design of experiments. Int. J. Biol. Macromol. 253. https://doi.org/10.1016/j.ijbiomac.2023.126906

Khanna, C., Sah, M.K., Flora, B., 2021. Composite Biomaterials in Tissue Engineering: Retrospective and Prospects, in: Biomaterials in Tissue Engineering and Regenerative Medicine: From Basic Concepts to State of the Art Approaches. https://doi.org/10.1007/978-981-16-0002-9_5

Khatamsaz, D., Neuberger, R., Roy, A.M., Zadeh, S.H., Otis, R., Arróyave, R., 2023. A physics informed bayesian optimization approach for material design: application to NiTi shape memory alloys. NPJ Comput. Mater. 9, 1–11. https://doi.org/10.1038/S41524-023-01173-7

Khoshgoftar, M.J., Ansari, H., 2024. Design and Analysis of Unit Cell Geometry to Improve Mechanical Properties and Surface-to-Volume Ratio of Used Scaffold in Treating

Damaged Bone Tissue. Adv. Eng. Mater. 26, 2301600. https://doi.org/10.1002/ADEM.202301600

Kieck, J.S., Zug, K.L.M., Huamaní Yupanqui, H.A., Gómez Aliaga, R., Cierjacks, A., 2016. Plant diversity effects on crop yield, pathogen incidence, and secondary metabolism on cacao farms in Peruvian Amazonia. Agric. Ecosyst. Environ. 222. https://doi.org/10.1016/j.agee.2016.02.006

Kim, C., Batra, R., Chen, L., Tran, H., Ramprasad, R., 2021. Polymer design using genetic algorithm and machine learning. Comput. Mater. Sci. 186. https://doi.org/10.1016/j.commatsci.2020.110067

Kim, J.I., Hwang, T.I., Aguilar, L.E., Park, C.H., Kim, C.S., 2016. A Controlled Design of Aligned and Random Nanofibers for 3D Bi-functionalized Nerve Conduits Fabricated via a Novel Electrospinning Set-up. Sci. Rep. 6, 1–12. https://doi.org/10.1038/SREP23761;TECHMETA

Kim, Y.B., Lim, J.Y., Yang, G.H., Seo, J.H., Ryu, H.S., Kim, G.H., 2019. 3D-printed PCL/bioglass (BGS-7) composite scaffolds with high toughness and cell-responses for bone tissue regeneration. Journal of Industrial and Engineering Chemistry 79. https://doi.org/10.1016/j.jiec.2019.06.027

Klojdová, I., Milota, T., Smetanová, J., Stathopoulos, C., 2023. Encapsulation: A Strategy to Deliver Therapeutics and Bioactive Compounds? Pharmaceuticals 16, 362. https://doi.org/10.3390/PH16030362

Kokubo, T., Kushitani, H., Sakka, S., Kitsugi, T., Yamamuro, T., 1990. Solutions able to reproduce in vivo surface-structure changes in bioactive glass-ceramic A-W3. J. Biomed. Mater. Res. 24, 721–734. https://doi.org/10.1002/JBM.820240607

Kokubo, T., Takadama, H., 2006. How useful is SBF in predicting in vivo bone bioactivity? Biomaterials 27. https://doi.org/10.1016/j.biomaterials.2006.01.017

Kolan, K.C.R., Semon, J.A., Bindbeutel, A.T., Day, D.E., Leu, M.C., 2020. Bioprinting with bioactive glass loaded polylactic acid composite and human adipose stem cells. Bioprinting 18. https://doi.org/10.1016/j.bprint.2020.e00075

Komissarenko, D.A., Sokolov, P.S., Evstigneeva, A.D., Shmeleva, I.A., Dosovitsky, A.E., 2018. Rheological and curing behavior of acrylate-based suspensions for the DLP 3D printing of complex zirconia parts. Materials 11. https://doi.org/10.3390/ma11122350

Konishi, T., Ono, H., Ohnishi-Kameyama, M., Kaneko, S., Ishii, T., 2006. Identification of a Mung Bean Arabinofuranosyltransferase That Transfers Arabinofuranosyl Residues onto (1, 5)-Linked α-l-Arabino-Oligosaccharides. Plant Physiol. 141, 1098–1105. https://doi.org/10.1104/PP.106.080309

Kontogianni, V.G., Charisiadis, P., Primikyri, A., Pappas, C.G., Exarchou, V., Tzakos, A.G., Gerothanassis, I.P., 2013. Hydrogen bonding probes of phenol –OH groups. Org. Biomol. Chem. 11, 1013–1025. https://doi.org/10.1039/C2OB27117F

Koons, G.L., Diba, M., Mikos, A.G., 2020. Materials design for bone-tissue engineering. Nat. Rev. Mater. https://doi.org/10.1038/s41578-020-0204-2

Kruth, J.P., Mercelis, P., Van Vaerenbergh, J., Froyen, L., Rombouts, M., 2005. Binding mechanisms in selective laser sintering and selective laser melting. Rapid Prototyp. J. https://doi.org/10.1108/13552540510573365

Kuenneth, C., Rajan, A.C., Tran, H., Chen, L., Kim, C., Ramprasad, R., 2021a. Polymer informatics with multi-task learning. Patterns 2. https://doi.org/10.1016/j.patter.2021.100238

Kuenneth, C., Schertzer, W., Ramprasad, R., 2021b. Copolymer Informatics with Multitask Deep Neural Networks. Macromolecules 54. https://doi.org/10.1021/acs.macromol.1c00728

Kumar, A., Kargozar, S., Baino, F., Han, S.S., 2019. Additive Manufacturing Methods for Producing Hydroxyapatite and Hydroxyapatite-Based Composite Scaffolds: A Review. Front. Mater. https://doi.org/10.3389/fmats.2019.00313

Kumar, J.N., Li, Q., Jun, Y., 2019. Challenges and opportunities of polymer design with machine learning and high throughput experimentation. MRS Commun. 9. https://doi.org/10.1557/mrc.2019.54

Lai, Y., 2019. A Comparison of Traditional Machine Learning and Deep Learning in Image Recognition, in: Journal of Physics: Conference Series. https://doi.org/10.1088/1742-6596/1314/1/012148

Lamnini, S., Elsayed, H., Lakhdar, Y., Baino, F., Smeacetto, F., Bernardo, E., 2022. Robocasting of advanced ceramics: ink optimization and protocol to predict the printing parameters - A review. Heliyon 8, e10651. https://doi.org/10.1016/j.heliyon.2022.e10651

Lara, C., Pascual, M.J., Durán, A., 2004. Glass-forming ability, sinterability and thermal properties in the systems RO-BaO-SiO2 (R = Mg, Zn), in: Journal of Non-Crystalline Solids. https://doi.org/10.1016/j.jnoncrysol.2004.08.140

Lee, J., Oh, S.J., An, S.H., Kim, W.D., Kim, S.H., Kim, S.H., 2020. Machine learning-based design strategy for 3D printable bioink: Elastic modulus and yield stress determine printability. Biofabrication 12. https://doi.org/10.1088/1758-5090/ab8707

Lefebvre, L., Chevalier, J., Gremillard, L., Zenati, R., Thollet, G., Bernache-Assolant, D., Govin, A., 2007. Structural transformations of bioactive glass 45S5 with thermal treatments. Acta Mater. 55, 3305–3313. https://doi.org/10.1016/J.ACTAMAT.2007.01.029

Lefebvre, L., Gremillard, L., Chevalier, J., Zenati, R., Bernache-Assolant, D., 2008. Sintering behaviour of 45S5 bioactive glass. Acta Biomater. 4. https://doi.org/10.1016/j.actbio.2008.05.019

Leite, Á.J., Gonçalves, A.I., Rodrigues, M.T., Gomes, M.E., Mano, J.F., 2018. Strontium-Doped Bioactive Glass Nanoparticles in Osteogenic Commitment. ACS Appl. Mater. Interfaces 10. https://doi.org/10.1021/acsami.8b06154

Levy, S., Van Dalen, M., Agonafer, S., Soboyejo, W.O., 2007. Cell/surface interactions and adhesion on bioactive glass 45S5, in: Journal of Materials Science: Materials in Medicine. https://doi.org/10.1007/s10856-006-0666-9

Li, A., Li, X., Zhang, Z., Huang, Z., He, L., Yang, Y., Dong, J., Cai, S., Liu, X., Zhao, H., He, Y., 2025. Deep learning assisted prediction of osteogenic capability of orthopedic implant surfaces based on early cell morphology. Acta Biomater. 195, 559–568. https://doi.org/10.1016/J.ACTBIO.2025.01.059

Li, H.F., Zheng, Y.F., 2016. Recent advances in bulk metallic glasses for biomedical applications. Acta Biomater. https://doi.org/10.1016/j.actbio.2016.03.047

Li, Q., Fu, N., Omee, S.S., Hu, J., 2023. MD-HIT: Machine learning for materials property prediction with dataset redundancy control. npj Computational Materials 2024 10:1 10, 1–11. https://doi.org/10.1038/S41524-024-01426-Z

Li, R., Clark, A.E., Hench, L.L., 1991. An investigation of bioactive glass powders by sol-gel processing. J. Appl. Biomater. 2. https://doi.org/10.1002/jab.770020403

Li, S., Lee, W.T., Yeom, J.T., Kim, J.G., Oh, J.S., Lee, T., Liu, Y., Nam, T.H., 2022. Towards bone-like elastic modulus in Ti[sbnd]Nb[sbnd]Sn alloys with large recovery strain for biomedical applications. J. Alloys Compd. 925. https://doi.org/10.1016/j.jallcom.2022.166724

Li, W.J., Fan, Z.G., Wu, Y.Y., Jiang, Z.G., Shi, R.C., 2019. Eco-friendly extraction and physicochemical properties of pectin from jackfruit peel waste with subcritical water. J. Sci. Food Agric. 99, 5283–5292. https://doi.org/10.1002/JSFA.9729;WGROUP:STRING:PUBLICATION

Liang, Y., Wei, X., Peng, Y., Wang, X., Niu, X., 2025. A review on recent applications of machine learning in mechanical properties of composites. Polym. Compos. 46, 1939–1960. https://doi.org/10.1002/PC.29082

Lin, S., Zhuang, Y., Chen, K., Lu, J., Wang, K., Han, L., Li, M., Li, X., Zhu, X., Yang, M., Yin, G., Lin, J., Zhang, X., 2024. Osteoinductive biomaterials: Machine learning for prediction and interpretation. Acta Biomater. 187, 422–433. https://doi.org/10.1016/J.ACTBIO.2024.08.017

Lin, T.S., Coley, C.W., Mochigase, H., Beech, H.K., Wang, W., Wang, Z., Woods, E., Craig, S.L., Johnson, J.A., Kalow, J.A., Jensen, K.F., Olsen, B.D., 2019. BigSMILES: A Structurally-Based Line Notation for Describing Macromolecules. ACS Cent. Sci. 5. https://doi.org/10.1021/acscentsci.9b00476

Lindfors, N.C., 2011. Clinical Experience on Bioactive Glass S53P4 in Reconstructive Surgery in the Upper Extremity Showing Bone Remodelling, Vascularization, Cartilage Repair and Antibacterial Properties of S53P4. J. Biotechnol. Biomater. 01. https://doi.org/10.4172/2155-952X.1000111

Littman, M.L., 2023. Memoryless Policies: Theoretical Limitations and Practical Results, in: From Animals to Animats 3. https://doi.org/10.7551/mitpress/3117.003.0041

Liu, D., Xia, W., Liu, J., Wang, X., Xue, J., 2024. Ultrasound-assisted alkali extraction of RG-I enriched pectin from thinned young apples: Structural characterization and gelling properties. Food Hydrocoll. 151, 109879. https://doi.org/10.1016/J.FOODHYD.2024.109879

Liu, H., Yazici, H., Ergun, C., Webster, T.J., Bermek, H., 2008. An in vitro evaluation of the Ca/P ratio for the cytocompatibility of nano-to-micron particulate calcium phosphates for bone regeneration. Acta Biomater. 4. https://doi.org/10.1016/j.actbio.2008.02.025

Liu, J., Glasmacher, U.A., Lang, M., Trautmann, C., Voss, K.O., Neumann, R., Wagner, G.A., Miletich, R., 2008. Raman spectroscopy of apatite irradiated with swift heavy ions with and without simultaneous exertion of high pressure. Appl. Phys. A Mater. Sci. Process. 91. https://doi.org/10.1007/s00339-008-4402-9

Liu Tsang, V., Bhatia, S.N., 2004. Three-dimensional tissue fabrication. Adv. Drug Deliv. Rev. https://doi.org/10.1016/j.addr.2004.05.001

Liu, X., Rahaman, M.N., Hilmas, G.E., Bal, B.S., 2013. Mechanical properties of bioactive glass (13-93) scaffolds fabricated by robotic deposition for structural bone repair. Acta Biomater. 9. https://doi.org/10.1016/j.actbio.2013.02.026

Liu, X., Rodeheaver, D.P., White, J.C., Wright, A.M., Walker, L.M., Zhang, F., Shannon, S., 2018. A comparison of in vitro cytotoxicity assays in medical device regulatory studies. Regulatory Toxicology and Pharmacology 97, 24–32. https://doi.org/10.1016/J.YRTPH.2018.06.003

Liu, Y., Li, Y., Yang, Q., Yang, J.D., Zhang, L., Luo, S., 2024. Prediction of Bond Dissociation Energy for Organic Molecules Based on a Machine-Learning Approach. Chin. J. Chem. 1967–1974. https://doi.org/10.1002/cjoc.202400049

Liu, Y., Liu, X., Guo, H., Wang, X., Li, A., Qiu, D., Gu, Q., 2023. 3D bioprinting bioglass to construct vascularized full-thickness skin substitutes for wound healing. Mater. Today Bio 24. https://doi.org/10.1016/J.MTBIO.2023.100899

Liu, Z., Ramakrishna, S., Liu, X., 2020. Electrospinning and emerging healthcare and medicine possibilities. APL Bioeng. 4. https://doi.org/10.1063/5.0012309

Loh, Z.W., Mohd Zaid, M.H., Matori, K.A., Kechik, M.M.A., Fen, Y.W., Mayzan, M.Z.H., Liza, S., Cheong, W.M., 2023. Phase transformation and mechanical properties of new bioactive glass-ceramics derived from CaO–P2O5–Na2O–B2O3–SiO2 glass system. J. Mech. Behav. Biomed. Mater. 143. https://doi.org/10.1016/j.jmbbm.2023.105889

López-Flores, F.J., Ornelas-Guillén, J.A., Pérez-Nava, A., González-Campos, J.B., Ponce-Ortega, J.M., 2024. Data-Driven Machine Learning Approach for Modeling the

Production and Predicting the Characteristics of Aligned Electrospun Nanofibers. Ind. Eng. Chem. Res. https://doi.org/10.1021/acs.iecr.4c00075

Lotfibakhshaiesh, N., Brauer, D.S., Hill, R.G., 2010. Bioactive glass engineered coatings for Ti6Al4V alloys: Influence of strontium substitution for calcium on sintering behaviour, in: Journal of Non-Crystalline Solids. https://doi.org/10.1016/j.jnoncrysol.2010.05.017

Lu, Y., Aimetti, A.A., Langer, R., Gu, Z., 2016. Bioresponsive materials. Nat. Rev. Mater. 2, 1–17. https://doi.org/10.1038/NATREVMATS.2016.75;SUBJMETA

Luo, G., Ma, Y., Cui, X., Jiang, L., Wu, M., Hu, Y., Luo, Y., Pan, H., Ruan, C., 2017. 13-93 bioactive glass/alginate composite scaffolds 3D printed under mild conditions for bone regeneration. RSC Adv. 7. https://doi.org/10.1039/c6ra27669e

Ma, J., Chen, C.Z., Wang, D.G., Jiao, Y., Shi, J.Z., 2010. Effect of magnesia on the degradability and bioactivity of sol-gel derived SiO2-CaO-MgO-P2O5 system glasses. Colloids Surf. B Biointerfaces 81. https://doi.org/10.1016/j.colsurfb.2010.06.022

Ma, R., Luo, T., 2020. PI1M: A benchmark database for polymer informatics. J. Chem. Inf. Model. 60. https://doi.org/10.1021/acs.jcim.0c00726

Macías-Garbett, R., Sosa-Hernández, J.E., Iqbal, H.M.N., Contreras-Esquivel, J.C., Chen, W.N., Melchor-Martínez, E.M., Parra-Saldívar, R., 2022. Combined Pulsed Electric Field and Microwave-Assisted Extraction as a Green Method for the Recovery of Antioxidant Compounds with Electroactive Potential from Coffee Agro-Waste. Plants 11. https://doi.org/10.3390/plants11182362

Magallanes-Perdomo, M., De Aza, A.H., Sobrados, I., Sanz, J., Pena, P., 2012. Structure and properties of bioactive eutectic glasses based on the Ca3(PO4)2–CaSiO3–CaMg(SiO3)2 system. Acta Biomater. 8, 820–829. https://doi.org/10.1016/J.ACTBIO.2011.10.017

Maitra, J., Shukla, V.K., 2014. Cross-linking in Hydrogels - A Review. American Journal of Polymer Science 4, 25–31. https://doi.org/10.5923/J.AJPS.20140402.01

Mannino, G., Chinigò, G., Serio, G., Genova, T., Gentile, C., Munaron, L., Bertea, C.M., 2021. Proanthocyanidins and where to find them: A meta-analytic approach to investigate their chemistry, biosynthesis, distribution and effect on human health. Antioxidants. https://doi.org/10.3390/antiox10081229

Manrique, G.D., Lajolo, F.M., 2002. FT-IR spectroscopy as a tool for measuring degree of methyl esterification in pectins isolated from ripening papaya fruit. Postharvest Biol. Technol. 25. https://doi.org/10.1016/S0925-5214(01)00160-0

Mar, J.M., da Fonseca Júnior, E.Q., Corrêa, R.F., Campelo, P.H., Sanches, E.A., Bezerra, J. de A., 2024. Theobroma spp.: A review of it's chemical and innovation potential for the food industry. Food Chemistry Advances 4, 100683. https://doi.org/10.1016/J.FOCHA.2024.100683

Marasca, N., Brito, M.R., Rambo, M.C.D., Pedrazzi, C., Scapin, E., Rambo, M.K.D., 2022. Analysis of the potential of cupuaçu husks (*Theobroma grandiflorum*) as raw material for the synthesis of bioproducts and energy generation. Food Science and Technology 42, e48421. https://doi.org/10.1590/FST.48421

Marchiosi, R., dos Santos, W.D., Constantin, R.P., de Lima, R.B., Soares, A.R., Finger-Teixeira, A., Mota, T.R., de Oliveira, D.M., Foletto-Felipe, M. de P., Abrahão, J., Ferrarese-Filho, O., 2020. Biosynthesis and metabolic actions of simple phenolic acids in plants. Phytochemistry Reviews 2020 19:4 19, 865–906. https://doi.org/10.1007/S11101-020-09689-2

Marianna, C., Bruna, T., Daniel, K., Rossana Mara, T., 2016. Structural evaluation of PLA scaffolds obtained by 3D printing via fused deposition modeling (FDM) technique for applications in Tissue Engineering. Front. Bioeng. Biotechnol. 4. https://doi.org/10.3389/CONF.FBIOE.2016.01.00092

Marikani, A., Maheswaran, A., Premanathan, M., Amalraj, L., 2008. Synthesis and characterization of calcium phosphate based bioactive quaternary P2O5-CaO-Na2O-K2O glasses. J. Non. Cryst. Solids 354. https://doi.org/10.1016/j.jnoncrysol.2008.05.005

Marin, E., Boschetto, F., Pezzotti, G., 2020. Biomaterials and biocompatibility: An historical overview. J. Biomed. Mater. Res. A 108, 1617–1633. https://doi.org/10.1002/JBM.A.36930

Marșavina, L., Vălean, C., Mărghitaș, M., Linul, E., Razavi, N., Berto, F., Brighenti, R., 2022. Effect of the manufacturing parameters on the tensile and fracture properties of FDM 3D-printed PLA specimens. Eng. Fract. Mech. 274, 108766. https://doi.org/10.1016/J.ENGFRACMECH.2022.108766

Martel-Estrada, S.-A., Olivas-Armendariz, I., Rodriguez, C., Adriana Martel Estrada, S., Olivas Armendáriz, I., Torres García, A., Francisco Hernández Paz, J., Alejandra Rodríguez González, C., 2017. Evaluation of in Vitro Bioactivity of 45S5 Bioactive Glass/Poly Lactic Acid Scaffolds Produced by 3D Printing. International Journal of Composite Materials 2017.

Martelli, A., Bellucci, D., Cannillo, V., 2024. An Enhanced Bioactive Glass Composition with Improved Thermal Stability and Sinterability. Materials 2024, Vol. 17, Page 6175 17, 6175. https://doi.org/10.3390/MA17246175

Martelli, A., Bellucci, D., Cannillo, V., 2023. Additive Manufacturing of Polymer/Bioactive Glass Scaffolds for Regenerative Medicine: A Review. Polymers (Basel). https://doi.org/10.3390/polym15112473

Martelli, A., Mohamed, Y.O.A., Gallego-Ferrer, G., Gentile, P., Girón-Hernández, J., 2025. Revolutionizing gut health: advances in encapsulation strategies for probiotics and bioactive molecules. Biotechnol. Adv. 83, 108630. https://doi.org/10.1016/J.BIOTECHADV.2025.108630

Martindale, W., Reynolds, J.E., 1996. Martindale: the extra pharmacopoeia, 31st Editi. ed. Royal Pharmaceutical Society.

Mason, C., Dunnill, P., 2008. A brief definition of regenerative medicine. Regenerative Med. https://doi.org/10.2217/17460751.3.1.1

Massera, J., Fagerlund, S., Hupa, L., Hupa, M., 2012. Crystallization mechanism of the bioactive glasses, 45S5 and S53P4. Journal of the American Ceramic Society 95. https://doi.org/10.1111/j.1551-2916.2011.05012.x

Massera, J., Hupa, L., 2014. Influence of SrO substitution for CaO on the properties of bioactive glass S53P4. J. Mater. Sci. Mater. Med. 25. https://doi.org/10.1007/s10856-013-5120-1

Mateu-Sanz, M., Fuenteslópez, C. V., Uribe-Gomez, J., Haugen, H.J., Pandit, A., Ginebra, M.P., Hakimi, O., Krallinger, M., Samara, A., 2024. Redefining biomaterial biocompatibility: challenges for artificial intelligence and text mining. Trends Biotechnol. 42, 402–417. https://doi.org/10.1016/j.tibtech.2023.09.015

Matsuno, T., Omata, K., Hashimoto, Y., Tabata, Y., Satoh, T., 2010. Alveolar bone tissue engineering using composite scaffolds for drug delivery. Japanese Dental Science Review 46, 188–192. https://doi.org/10.1016/J.JDSR.2009.12.001

MatWeb. Material property data [WWW Document], n.d. URL https://www.matweb.com/index.aspx (accessed 1.26.24).

McAndrew, J., Efrimescu, C., Sheehan, E., Niall, D., 2013. Through the looking glass; Bioactive glass S53P4 (BonAlive®) in the treatment of chronic osteomyelitis. Ir. J. Med. Sci. 182, 509–511. https://doi.org/10.1007/S11845-012-0895-5/FIGURES/1

McDonald, S.M., Augustine, E.K., Lanners, Q., Rudin, C., Catherine Brinson, L., Becker, M.L., 2023. Applied machine learning as a driver for polymeric biomaterials design. Nat. Commun. 14. https://doi.org/10.1038/S41467-023-40459-8

Mecca, F.G., Bellucci, D., Cannillo, V., 2023. Effect of Thermal Treatments and Ion Substitution on Sintering and Crystallization of Bioactive Glasses: A Review. Materials 2023, Vol. 16, Page 4651 16, 4651. https://doi.org/10.3390/MA16134651

Melchels, F.P.W., Feijen, J., Grijpma, D.W., 2010. A review on stereolithography and its applications in biomedical engineering. Biomaterials. https://doi.org/10.1016/j.biomaterials.2010.04.050

Mellinas, A.C., Jiménez, A., Garrigós, M.C., 2020. Optimization of microwave-assisted extraction of cocoa bean shell waste and evaluation of its antioxidant, physicochemical and functional properties. LWT 127. https://doi.org/10.1016/j.lwt.2020.109361

Menon, D., Ranganathan, R., 2022. A Generative Approach to Materials Discovery, Design, and Optimization. ACS Omega 7, 25958–25973. https://doi.org/10.1021/acsomega.2c03264

Metwally, S., Stachewicz, U., 2019. Surface potential and charges impact on cell responses on biomaterials interfaces for medical applications. Materials Science and Engineering C. https://doi.org/10.1016/j.msec.2019.109883

Meyer, T.A., Ramirez, C., Tamasi, M.J., Gormley, A.J., 2023. A User's Guide to Machine Learning for Polymeric Biomaterials. ACS Polymers Au 3. https://doi.org/10.1021/acspolymersau.2c00037

Miao, L., Sheng, M., n.d. Atomly [WWW Document]. URL https://atomly.net/#/ (accessed 4.4.24).

Mittal, A., Mohanty, S.K., Gautam, V., Arora, S., Saproo, S., Gupta, R., Sivakumar, R., Garg, P., Aggarwal, A., Raghavachary, P., Dixit, N.K., Singh, V.P., Mehta, A., Tayal, J., Naidu, S., Sengupta, D., Ahuja, G., 2022. Artificial intelligence uncovers carcinogenic human metabolites. Nat. Chem. Biol. 18. https://doi.org/10.1038/s41589-022-01110-7

Moghanian, A., Sedghi, A., Ghorbanoghli, A., Salari, E., 2018. The effect of magnesium content on in vitro bioactivity, biological behavior and antibacterial activity of sol–gel derived 58S bioactive glass. Ceram. Int. 44, 9422–9432. https://doi.org/10.1016/J.CERAMINT.2018.02.159

Mohamad Yunos, D., Bretcanu, O., Boccaccini, A.R., 2008. Polymer-bioceramic composites for tissue engineering scaffolds, in: Journal of Materials Science. https://doi.org/10.1007/s10853-008-2552-y

Mohammadrezaei, D., Podina, L., Silva, J. De, Kohandel, M., 2024. Cell viability prediction and optimization in extrusion-based bioprinting via neural network-based Bayesian optimization models. Biofabrication 16. https://doi.org/10.1088/1758-5090/ad17cf

Montazerian, M., Shearer, A., Mauro, J.C., 2023. Perspectives on the impact of crystallization in bioactive glasses and glass-ceramics. International Journal of Ceramic Engineering and Science. https://doi.org/10.1002/ces2.10194

Montazerian, M., Zanotto, E.D., Mauro, J.C., 2020. Model-driven design of bioactive glasses: from molecular dynamics through machine learning. International Materials Reviews 65, 297–321. https://doi.org/10.1080/09506608.2019.1694779

Montoya, C., Du, Y., Gianforcaro, A.L., Orrego, S., Yang, M., Lelkes, P.I., 2021. On the road to smart biomaterials for bone research: definitions, concepts, advances, and outlook. Bone Res. 9, 1–16. https://doi.org/10.1038/S41413-020-00131-Z;SUBJMETA

Motealleh, A., Eqtesadi, S., Civantos, A., Pajares, A., Miranda, P., 2017a. Robocast 45S5 bioglass scaffolds: in vitro behavior. J. Mater. Sci. 52. https://doi.org/10.1007/s10853-017-0775-5

Motealleh, A., Eqtesadi, S., Pajares, A., Miranda, P., Salamon, D., Castkova, K., 2017b. Case study: Reinforcement of 45S5 bioglass robocast scaffolds by HA/PCL nanocomposite coatings. J. Mech. Behav. Biomed. Mater. 75. https://doi.org/10.1016/j.jmbbm.2017.07.012

Motojima, K., Shiratsuchi, R., Suzuki, K., Aizawa, M., Kaneko, H., 2023. Machine Learning Model for Predicting the Material Properties and Bone Formation Rate and Direct Inverse Analysis of the Model for New Synthesis Conditions of Bioceramics. Ind. Eng. Chem. Res. 62. https://doi.org/10.1021/acs.iecr.3c00332

Mousa, H.M., Abdal-Hay, A., Bartnikowski, M., Mohamed, I.M.A., Yasin, A.S., Ivanovski, S., Park, C.H., Kim, C.S., 2018. A Multifunctional Zinc Oxide/Poly(Lactic Acid) Nanocomposite Layer Coated on Magnesium Alloys for Controlled Degradation and Antibacterial Function. ACS Biomater. Sci. Eng. 4, 2169–2180. https://doi.org/10.1021/ACSBIOMATERIALS.8B00277

Mozafari, M., 2025. How artificial intelligence shapes the future of biomaterials? Next Materials 7, 100381. https://doi.org/10.1016/J.NXMATE.2024.100381

Müller, P.E., Schrimpf, F., Milz, S., Kircher, J., Dürr, H.R., Wegener, B., Pellengahr, C., Jansson, V., 2006. Repair of osteochondral defects in the knee by resorbable bioimplants in a rabbit model. Acta Orthop. 77. https://doi.org/10.1080/17453670610013321

Muñoz-Almagro, N., Molina-Tijeras, J.A., Montilla, A., Vezza, T., Sánchez-Milla, M., Rico-Rodríguez, F., Villamiel, M., 2023. Pectin from sunflower by-products obtained by ultrasound: Chemical characterization and in vivo evaluation of properties in inflammatory bowel disease. Int. J. Biol. Macromol. 246. https://doi.org/10.1016/j.ijbiomac.2023.125505

Munteanu, I.G., Apetrei, C., 2021. Analytical methods used in determining antioxidant activity: A review. Int. J. Mol. Sci. https://doi.org/10.3390/ijms22073380

Munzert, K.S., Engelsdorf, T., 2024. Plant cell wall structure and dynamics in plant–pathogen interactions and pathogen defence. J. Exp. Bot. erae442. https://doi.org/10.1093/jxb/erae442

Murimadugula, S., Prasad, A., Lakshmi, A.M., Kumari, S., Rao, P.V., Raju, G.N., Kumari, K., Özcan, M., Madaboosi, N., Prasad, P.S., 2024. Biomimetic Bi3+ substituted borate bioactive glasses for bone tissue engineering via enhanced biological and antimicrobial activity. Surfaces and Interfaces 51. https://doi.org/10.1016/j.surfin.2024.104697

Muschler, G.F., Nakamoto, C., Griffith, L.G., 2004. Engineering principles of clinical cell-based tissue engineering. Journal of Bone and Joint Surgery. https://doi.org/10.2106/00004623-200407000-00029

Naseri, S., Lepry, W.C., Nazhat, S.N., 2017. Bioactive glasses in wound healing: hope or hype? J. Mater. Chem. B 5, 6167–6174. https://doi.org/10.1039/C7TB01221G

Nasiri, H., Dadashi, A., Azadi, M., 2024. Machine learning for fatigue lifetime predictions in 3D-printed polylactic acid biomaterials based on interpretable extreme gradient boosting model. Mater. Today Commun. 39. https://doi.org/10.1016/j.mtcomm.2024.109054

Natarajan, J., Cheepu, M., Yang, C., 2021. Advances in Additive Manufacturing Processes, Advances in Additive Manufacturing Processes. Bentham Books. https://doi.org/10.2174/9789815036336121010101

Nešić, A., Ružić, J., Gordić, M., Ostojić, S., Micić, D., Onjia, A., 2017. Pectin-polyvinylpyrrolidone films: A sustainable approach to the development of biobased packaging materials. Compos. B Eng. 110. https://doi.org/10.1016/j.compositesb.2016.11.016

Ngo, T.D., Kashani, A., Imbalzano, G., Nguyen, K.T.Q., Hui, D., 2018. Additive manufacturing (3D printing): A review of materials, methods, applications and challenges. Compos. B Eng. https://doi.org/10.1016/j.compositesb.2018.02.012

Nisar, T., Wang, Z.C., Yang, X., Tian, Y., Iqbal, M., Guo, Y., 2018. Characterization of citrus pectin films integrated with clove bud essential oil: Physical, thermal, barrier, antioxidant and antibacterial properties. Int. J. Biol. Macromol. 106. https://doi.org/10.1016/j.ijbiomac.2017.08.068

Nommeots-Nomm, A., Lee, P.D., Jones, J.R., 2018. Direct ink writing of highly bioactive glasses. J. Eur. Ceram. Soc. 38. https://doi.org/10.1016/j.jeurceramsoc.2017.08.006

Noori Banu, P.S., Devaki Rani, S., 2018. Artificial neural network based optimization of prerequisite properties for the design of biocompatible titanium alloys. Comput. Mater. Sci. 149. https://doi.org/10.1016/j.commatsci.2018.03.039

Obst, P., Riedelbauch, J., Oehlmann, P., Rietzel, D., Launhardt, M., Schmölzer, S., Osswald, T.A., Witt, G., 2020. Investigation of the influence of exposure time on the dual-curing

reaction of RPU 70 during the DLS process and the resulting mechanical part properties. Addit. Manuf. 32. https://doi.org/10.1016/j.addma.2019.101002

O'Donnell, M.D., Candarlioglu, P.L., Miller, C.A., Gentleman, E., Stevens, M.M., 2010. Materials characterisation and cytotoxic assessment of strontium-substituted bioactive glasses for bone regeneration. J. Mater. Chem. 20, 8934–8941. https://doi.org/10.1039/C0JM01139H

O'Donnell, M.D., Hill, R.G., 2010. Influence of strontium and the importance of glass chemistry and structure when designing bioactive glasses for bone regeneration. Acta Biomater. 6, 2382–2385. https://doi.org/10.1016/J.ACTBIO.2010.01.006

Ohtsuki, C., Kushitani, H., Kokubo, T., Kotani, S., Yamamuro, T., 1991. Apatite formation on the surface of ceravital-type glass-ceramic in the body. J. Biomed. Mater. Res. 25, 1363–1370. https://doi.org/10.1002/JBM.820251105

Oliver, S., Zhao, L., Gormley, A.J., Chapman, R., Boyer, C., 2019. Living in the Fast Lane - High Throughput Controlled/Living Radical Polymerization. Macromolecules. https://doi.org/10.1021/acs.macromol.8b01864

Oliver, W.C., Pharr, G.M., 1992. An improved technique for determining hardness and elastic modulus using load and displacement sensing indentation experiments. J. Mater. Res. 7. https://doi.org/10.1557/jmr.1992.1564

Olmos, D., González-benito, J., 2021. Polymeric materials with antibacterial activity: A review. Polymers (Basel). https://doi.org/10.3390/polym13040613

O'Mahony, N., Campbell, S., Carvalho, A., Harapanahalli, S., Hernandez, G.V., Krpalkova, L., Riordan, D., Walsh, J., 2020. Deep Learning vs. Traditional Computer Vision, in: Advances in Intelligent Systems and Computing. https://doi.org/10.1007/978-3-030-17795-9_10

Oñate-Gutiérrez, J.A., Díaz-Sánchez, L.M., Urbina, D.L., Pinzón, J.R., Blanco-Tirado, C., Combariza, M.Y., 2023. Exploring the chemical composition and coloring qualities of cacao fruit epicarp extracts. RSC Adv. 13, 12712–12722. https://doi.org/10.1039/D3RA01049J

Otsuka, S., Kuwajima, I., Hosoya, J., Xu, Y., Yamazaki, M., 2011. PoLyInfo: Polymer database for polymeric materials design, in: Proceedings - 2011 International

Conference on Emerging Intelligent Data and Web Technologies, EIDWT 2011. https://doi.org/10.1109/EIDWT.2011.13

Padilla, S., Román, J., Sánchez-Salcedo, S., Vallet-Regí, M., 2006. Hydroxyapatite/SiO2-CaO-P2O5 glass materials: In vitro bioactivity and biocompatibility. Acta Biomater. 2, 331–342. https://doi.org/10.1016/J.ACTBIO.2006.01.006

Pajares-Chamorro, N., Wagley, Y., Maduka, C. V., Youngstrom, D.W., Yeger, A., Badylak, S.F., Hammer, N.D., Hankenson, K., Chatzistavrou, X., 2021. Silver-doped bioactive glass particles for in vivo bone tissue regeneration and enhanced methicillin-resistant Staphylococcus aureus (MRSA) inhibition. Materials Science and Engineering C 120. https://doi.org/10.1016/j.msec.2020.111693

Pan, J., Li, C., Liu, J., Jiao, Z., Zhang, Q., Lv, Z., Yang, W., Chen, D., Liu, H., 2024. Polysaccharide-Based Packaging Coatings and Films with Phenolic Compounds in Preservation of Fruits and Vegetables—A Review. Foods 2024, Vol. 13, Page 3896 13, 3896. https://doi.org/10.3390/FOODS13233896

Pantulap, U., Arango-Ospina, M., Boccaccini, A.R., 2022. Bioactive glasses incorporating less-common ions to improve biological and physical properties. J. Mater. Sci. Mater. Med. https://doi.org/10.1007/s10856-021-06626-3

Patova, O.A., Luanda, A., Paderin, N.M., Popov, S. V., Makangara, J.J., Kuznetsov, S.P., Kalmykova, E.N., 2021. Xylogalacturonan-enriched pectin from the fruit pulp of Adansonia digitata: Structural characterization and antidepressant-like effect. Carbohydr. Polym. 262, 117946. https://doi.org/10.1016/J.CARBPOL.2021.117946

Pedone, A., Malavasi, G., Menziani, M.C., 2009. Computational insight into the effect of CaO/MgO substitution on the structural properties of phospho-silicate bioactive glasses. Journal of Physical Chemistry C 113, 15723–15730. https://doi.org/10.1021/JP904131T

Peighambardoust, S.H., Jafarzadeh-Moghaddam, M., Pateiro, M., Lorenzo, J.M., Domínguez, R., 2021. Physicochemical, thermal and rheological properties of pectin extracted from sugar beet pulp using subcritical water extraction process. Molecules 26. https://doi.org/10.3390/molecules26051413

Penel, G., Leroy, G., Rey, C., Bres, E., 1998. MicroRaman spectral study of the PO4 and CO3 vibrational modes in synthetic and biological apatites. Calcif. Tissue Int. 63, 475–481. https://doi.org/10.1007/S002239900561

Peng, Y., Wu, S., 2010. The structural and thermal characteristics of wheat straw hemicellulose. J. Anal. Appl. Pyrolysis 88, 134–139. https://doi.org/10.1016/J.JAAP.2010.03.006

Pereira, P.H.F., Oliveira, T.Í.S., Rosa, M.F., Cavalcante, F.L., Moates, G.K., Wellner, N., Waldron, K.W., Azeredo, H.M.C., 2016. Pectin extraction from pomegranate peels with citric acid. Int. J. Biol. Macromol. 88. https://doi.org/10.1016/j.ijbiomac.2016.03.074

Pérez-Tanoira, R., Kinnari, T.J., Hyyrynen, T., Soininen, A., Pietola, L., Tiainen, V.M., Konttinen, Y.T., Aarnisalo, A.A., 2015. Effects of S53P4 bioactive glass on osteoblastic cell and biomaterial surface interaction. J. Mater. Sci. Mater. Med. 26, 1–11. https://doi.org/10.1007/S10856-015-5568-2/TABLES/2

Petretta, M., Gambardella, A., Boi, M., Berni, M., Cavallo, C., Marchiori, G., Maltarello, M.C., Bellucci, D., Fini, M., Baldini, N., Grigolo, B., Cannillo, V., 2021. Composite scaffolds for bone tissue regeneration based on pcl and mg-containing bioactive glasses. Biology (Basel). 10. https://doi.org/10.3390/biology10050398

Poh, P.S.P., Valainis, D., Bhattacharya, K., van Griensven, M., Dondl, P., 2019. Optimization of Bone Scaffold Porosity Distributions. Sci. Rep. 9, 9170. https://doi.org/10.1038/S41598-019-44872-2

Ponton, C.B., Rawlings, R.D., 1989a. Vickers indentation fracture toughness test Part 1 review of literature and formulation of standardised indentation toughness equations. Materials Science and Technology (United Kingdom) 5. https://doi.org/10.1179/mst.1989.5.9.865

Ponton, C.B., Rawlings, R.D., 1989b. Vickers indentation fracture toughness test Part 2 application and critical evaluation of standardised indentation toughness equations. Materials Science and Technology (United Kingdom) 5. https://doi.org/10.1179/mst.1989.5.10.961

Prasad, K., Bazaka, O., Chua, M., Rochford, M., Fedrick, L., Spoor, J., Symes, R., Tieppo, M., Collins, C., Cao, A., Markwell, D., Ostrikov, K., Bazaka, K., 2017. Metallic

biomaterials: Current challenges and opportunities. Materials. https://doi.org/10.3390/ma10080884

Puchol-Miquel, M., Palomares, C., Fernández-Segovia, I., Barat, J.M., Perez-Esteve, É., 2021. Effect of the type and degree of alkalization of cocoa powder on the physico-chemical and sensory properties of sponge cakes. LWT 152. https://doi.org/10.1016/j.lwt.2021.112241

Puppi, D., Chiellini, F., Piras, A.M., Chiellini, E., 2010. Polymeric materials for bone and cartilage repair. Progress in Polymer Science (Oxford). https://doi.org/10.1016/j.progpolymsci.2010.01.006

Pyzer-Knapp, E.O., Manica, M., Staar, P., Morin, L., Ruch, P., Laino, T., Smith, J.R., Curioni, A., 2025. Foundation models for materials discovery – current state and future directions. NPJ Comput. Mater. 11, 1–10. https://doi.org/10.1038/S41524-025-01538-0

Qian, J., Zhao, F., Gao, J., Qu, L.J., He, Z., Yi, S., 2021. Characterization of the structural and dynamic changes of cell wall obtained by ultrasound-water and ultrasound-alkali treatments. Ultrason. Sonochem. 77, 105672. https://doi.org/10.1016/J.ULTSONCH.2021.105672

R. Ramprasad Group, n.d. Khazana. A computational materials knowledgebase [WWW Document]. URL https://khazana.gatech.edu/ (accessed 1.26.24).

Rabe, M., Verdes, D., Seeger, S., 2011. Understanding protein adsorption phenomena at solid surfaces. Adv. Colloid Interface Sci. 162, 87–106. https://doi.org/10.1016/J.CIS.2010.12.007

Rabiee, S.M., Nazparvar, N., Azizian, M., Vashaee, D., Tayebi, L., 2015. Effect of ion substitution on properties of bioactive glasses: A review. Ceram. Int. https://doi.org/10.1016/j.ceramint.2015.02.140

Raissi, M., Perdikaris, P., Karniadakis, G.E., 2019. Physics-informed neural networks: A deep learning framework for solving forward and inverse problems involving nonlinear partial differential equations. J. Comput. Phys. 378, 686–707. https://doi.org/10.1016/J.JCP.2018.10.045

Raj, A.C.A., Datta, S., 2023. Designing Ti Alloy for Hard Tissue Implants: A Machine Learning Approach. J. Mater. Eng. Perform. 32. https://doi.org/10.1007/s11665-023-07912-7

Raj, S.A., Muthukumaran, E., Jayakrishna, K., 2018. A Case Study of 3D Printed PLA and Its Mechanical Properties. Mater. Today Proc. 5, 11219–11226. https://doi.org/10.1016/J.MATPR.2018.01.146

Rajula, H.S.R., Verlato, G., Manchia, M., Antonucci, N., Fanos, V., 2020. Comparison of conventional statistical methods with machine learning in medicine: Diagnosis, drug development, and treatment. Medicina (Lithuania) 56. https://doi.org/10.3390/medicina56090455

Ramesh, S., Deep, A., Tamayol, A., Kamaraj, A., Mahajan, C., Madihally, S., 2024. Advancing 3D bioprinting through machine learning and artificial intelligence. Bioprinting 38, e00331. https://doi.org/10.1016/j.bprint.2024.e00331

Ramp, W.K., Lenz, L.G., Kaysinger, K.K., 1994. Medium pH modulates matrix, mineral, and energy metabolism in cultured chick bones and osteoblast-like cells. Bone Miner. 24. https://doi.org/10.1016/S0169-6009(08)80131-6

Rasal, R.M., Janorkar, A. V., Hirt, D.E., 2010. Poly(lactic acid) modifications. Progress in Polymer Science (Oxford). https://doi.org/10.1016/j.progpolymsci.2009.12.003

Ratner, B., Hoffman, A., Schoen, F., Lemons, J., 2004. Biomaterials Science An Introduction to Materials in Medicine, 2nd Editio. ed.

Ratner, B.D., 1995. Surface modification of polymers: chemical, biological and surface analytical challenges. Biosens. Bioelectron. 10. https://doi.org/10.1016/0956-5663(95)99218-A

Rebello, N., Arora, A., Mochigase, H., Lin, T.-S.L., Audus, D., Olsen, B., n.d. Block Copolymer Phase Behavior Database (BCDB) [WWW Document]. URL https://github.com/olsenlabmit/BCDB (accessed 1.26.24).

Reddy, B.S., In, K.H., Panigrahi, B.B., Paturi, U.M.R., Cho, K.K., Reddy, N.S., 2021. Modeling tensile strength and suture retention of polycaprolactone electrospun nanofibrous scaffolds by artificial neural networks. Mater. Today Commun. 26. https://doi.org/10.1016/j.mtcomm.2021.102115

Reddy, N., Reddy, R., Jiang, Q., 2015. Crosslinking biopolymers for biomedical applications. Trends Biotechnol. 33, 362–369. https://doi.org/10.1016/j.tibtech.2015.03.008

Reis, M., Gusev, F., Taylor, N.G., Chung, S.H., Verber, M.D., Lee, Y.Z., Isayev, O., Leibfarth, F.A., 2021. Machine-Learning-Guided Discovery of 19F MRI Agents Enabled by Automated Copolymer Synthesis. J. Am. Chem. Soc. 143. https://doi.org/10.1021/jacs.1c08181

Reiser, P., Neubert, M., Eberhard, A., Torresi, L., Zhou, C., Shao, C., Metni, H., van Hoesel, C., Schopmans, H., Sommer, T., Friederich, P., 2022. Graph neural networks for materials science and chemistry. Communications Materials 2022 3:1 3, 1–18. https://doi.org/10.1038/s43246-022-00315-6

Ren, H., Chen, S., Jin, Y., Zhang, C., Yang, X., Ge, K., Liang, X.J., Li, Z., Zhang, J., 2017. A traceable and bone-targeted nanoassembly based on defect-related luminescent mesoporous silica for enhanced osteogenic differentiation. J. Mater. Chem. B 5. https://doi.org/10.1039/C6TB02552H

Reszczyńska, E., Hanaka, A., 2020. Lipids Composition in Plant Membranes. Cell Biochem. Biophys. 78, 401. https://doi.org/10.1007/S12013-020-00947-W

Rodrigues, C., Naasani, L.I.S., Zanatelli, C., Paim, T.C., Azevedo, J.G., de Lima, J.C., da Cruz Fernandes, M., Buchner, S., Wink, M.R., 2019. Bioglass 45S5: Structural characterization of short range order and analysis of biocompatibility with adipose-derived mesenchymal stromal cells in vitro and in vivo. Materials Science and Engineering: C 103, 109781. https://doi.org/10.1016/J.MSEC.2019.109781

Ruberu, K., Senadeera, M., Rana, S., Gupta, S., Chung, J., Yue, Z., Venkatesh, S., Wallace, G., 2021. Coupling machine learning with 3D bioprinting to fast track optimisation of extrusion printing. Appl. Mater. Today 22. https://doi.org/10.1016/j.apmt.2020.100914

Rupp, M., Tkatchenko, A., Müller, K.R., Von Lilienfeld, O.A., 2012. Fast and accurate modeling of molecular atomization energies with machine learning. Phys. Rev. Lett. 108. https://doi.org/10.1103/PhysRevLett.108.058301

Russell, S., Norivg, P., 2021. Artificial Intelligence: A Modern Approach (Global Edition). Artificial Intelligence: A Modern Approach.

Sachlos, E., Czernuszka, J.T., Gogolewski, S., Dalby, M., 2003. Making tissue engineering scaffolds work. Review on the application ofsolid freeform fabrication technology to the production of tissue engineeringscaffolds. Eur. Cell. Mater. https://doi.org/10.22203/ecm.v005a03

Safirzadeh, S., Chorom, M., Karimi, R., Ariz, A., Behravan, H.R., Fadami, M., 2017. Effects of Alkaline Pretreatments on Chemical Composition of Sugarcane Bagasse for Easy Degradation in Soil. Sugar Tech 19, 89–94. https://doi.org/10.1007/S12355-016-0435-0/FIGURES/3

Saha, S.K., Wang, D., Nguyen, V.H., Chang, Y., Oakdale, J.S., Chen, S.C., 2019. Scalable submicrometer additive manufacturing. Science (1979). 366. https://doi.org/10.1126/science.aax8760

Said, N.S., Olawuyi, I.F., Lee, W.Y., 2023. Pectin Hydrogels: Gel-Forming Behaviors, Mechanisms, and Food Applications. Gels. https://doi.org/10.3390/gels9090732

Salinas, A.J., Vallet-Regi, M., Heikkilä, J., 2018. Use of bioactive glasses as bone substitutes in orthopedics and traumatology. Bioactive Glasses: Materials, Properties and Applications, Second Edition 337–364. https://doi.org/10.1016/B978-0-08-100936-9.00014-9

Sanchez-Ballesta, M.T., Maoz, I., Figueroa, C.R., 2022. Editorial: Secondary metabolism and fruit quality. Front. Plant Sci. https://doi.org/10.3389/fpls.2022.1072193

Sandarani, M., 2017. A Review: Different Extraction Techniques of Pectin. J. Pharmacogn. Nat. Prod. 03. https://doi.org/10.4172/2472-0992.1000143

Sanders, D.W., Bhandari, M., Guyatt, G., Heels-Ansdell, D., Schemitsch, E.H., Swiontkowski, M., Tornetta, P., Walter, S., 2014. Critical-sized defect in the Tibia: Is it critical? Results from the SPRINT trial. J. Orthop. Trauma 28. https://doi.org/10.1097/BOT.0000000000000194

Santos, A.R.C., Almeida, H.A., Bártolo, P.J., 2013. Additive manufacturing techniques for scaffold-based cartilage tissue engineering: A review on various additive manufacturing technologies in generating scaffolds for cartilage tissue engineering. Virtual Phys. Prototyp. 8. https://doi.org/10.1080/17452759.2013.838825

Saranti, A., Tiron-Stathopoulos, A., Papaioannou, L., Gioti, C., Ioannou, A., Karakassides, M.A., Avgoustakis, K., Koutselas, I., Dimos, K., 2022. 3D-printed bioactive scaffolds

for bone regeneration bearing carbon dots for bioimaging purposes. Smart Mater. Med. 3, 12–19. https://doi.org/10.1016/J.SMAIM.2021.11.002

Sarker, I.H., 2021. Machine Learning: Algorithms, Real-World Applications and Research Directions. SN Comput. Sci. https://doi.org/10.1007/s42979-021-00592-x

Sarvestani, H.Y., Singh, A., Ashrafi, B., 2024. Bridging Nature and Technology: A Perspective on Role of Machine Learning in Bioinspired Ceramics. Adv. Eng. Mater. 2400792. https://doi.org/10.1002/ADEM.202400792

Savioli Lopes, M., Jardini, A.L., Maciel Filho, R., 2012. Poly (lactic acid) production for tissue engineering applications, in: Procedia Engineering. https://doi.org/10.1016/j.proeng.2012.07.534

Scaffaro, R., Lopresti, F., Botta, L., Rigogliuso, S., Ghersi, G., 2016. Integration of PCL and PLA in a monolithic porous scaffold for interface tissue engineering. J. Mech. Behav. Biomed. Mater. 63, 303–313. https://doi.org/10.1016/J.JMBBM.2016.06.021

Scalzone, A., Ferreira, A.M., Tonda-Turo, C., Ciardelli, G., Dalgarno, K., Gentile, P., 2019. The interplay between chondrocyte spheroids and mesenchymal stem cells boosts cartilage regeneration within a 3D natural-based hydrogel. Sci. Rep. 9, 1–12. https://doi.org/10.1038/S41598-019-51070-7;TECHMETA

Schittecatte, L., Geertsen, V., Bonamy, D., Nguyen, T., Guenoun, P., 2023. From resin formulation and process parameters to the final mechanical properties of 3D printed acrylate materials. MRS Commun. 13, 357–377. https://doi.org/10.1557/S43579-023-00352-3/METRICS

Schlaepfer, D.D., Hanks, S.K., Hunter, T., Geer, P. Van Der, 1994. Integrin-mediated signal transduction linked to Ras pathway by GRB2 binding to focal adhesion kinase. Nature 1994 372:6508 372, 786–791. https://doi.org/10.1038/372786a0

Schmitz, S.I., Widholz, B., Essers, C., Becker, M., Tulyaganov, D.U., Moghaddam, A., Gonzalo de Juan, I., Westhauser, F., 2020. Superior biocompatibility and comparable osteoinductive properties: Sodium-reduced fluoride-containing bioactive glass belonging to the CaO–MgO–SiO2 system as a promising alternative to 45S5 bioactive glass. Bioact. Mater. 5, 55–65. https://doi.org/10.1016/J.BIOACTMAT.2019.12.005

Schnabelrauch, M., Wyrwa, R., Rebl, H., Bergemann, C., Finke, B., Schlosser, M., Walschus, U., Lucke, S., Weltmann, K.D., Nebe, J.B., 2014. Surface-coated polylactide fiber

meshes as tissue engineering matrices with enhanced cell integration properties. Int. J. Polym. Sci. 2014. https://doi.org/10.1155/2014/439784

Schneider, M., Fritzsche, N., Puciul-Malinowska, A., Baliś, A., Mostafa, A., Bald, I., Zapotoczny, S., Taubert, A., 2020. Surface etching of 3D printed poly(lactic acid) with NaOH: A systematic approach. Polymers (Basel). 12. https://doi.org/10.3390/POLYM12081711

Sedigh, A., Ghelich, P., Quint, J., Mollocana-Lara, E.C., Samandari, M., Tamayol, A., Tomlinson, R.E., 2023. Approximating scaffold printability utilizing computational methods. Biofabrication 15. https://doi.org/10.1088/1758-5090/acbbf0

Semenov, A.N., Nyrkova, I.A., 2012. 1.02 - Statistical Description of Chain Molecules, in: Polymer Science: A Comprehensive Reference: Volume 1-10. https://doi.org/10.1016/B978-0-444-53349-4.00002-9

Sequeira, P., Gervasio, M., 2020. Interestingness elements for explainable reinforcement learning: Understanding agents' capabilities and limitations. Artif. Intell. 288. https://doi.org/10.1016/j.artint.2020.103367

Sha, W., Guo, Y., Yuan, Q., Tang, S., Zhang, X., Lu, S., Guo, X., Cao, Y.-C., Cheng, S., 2020. Artificial Intelligence to Power the Future of Materials Science and Engineering. Advanced Intelligent Systems 2. https://doi.org/10.1002/aisy.201900143

Shah, F.A., 2020. Towards refining Raman spectroscopy-based assessment of bone composition. Sci. Rep. 10. https://doi.org/10.1038/s41598-020-73559-2

Sharifianjazi, F., Moradi, M., Abouchenari, A., Pakseresht, A.H., Esmaeilkhanian, A., Shokouhimehr, M., Shahedi Asl, M., 2020. Effects of Sr and Mg dopants on biological and mechanical properties of SiO2–CaO–P2O5 bioactive glass. Ceram. Int. 46. https://doi.org/10.1016/j.ceramint.2020.06.030

Shekhawat, D., Singh, A., Bhardwaj, A., Patnaik, A., 2021. A Short Review on Polymer, Metal and Ceramic Based Implant Materials, in: IOP Conference Series: Materials Science and Engineering. https://doi.org/10.1088/1757-899X/1017/1/012038

Shelby, J.E., 2005. Introduction to Glass Science and Technology. Introduction to Glass Science and Technology. https://doi.org/10.1039/9781847551160

Shera, S.S., Sahu, S., Banik, R.M., 2018. Preparation of Drug Eluting Natural Composite Scaffold Using Response Surface Methodology and Artificial Neural Network Approach. Tissue Eng. Regen. Med. 15. https://doi.org/10.1007/s13770-017-0100-z

Shi, H., Yu, L., Shi, Y., Lu, J., Teng, H., Zhou, Y., Sun, L., 2017. Structural Characterization of a Rhamnogalacturonan I Domain from Ginseng and Its Inhibitory Effect on Galectin-3. Molecules 2017, Vol. 22, Page 1016 22, 1016. https://doi.org/10.3390/MOLECULES22061016

Shi, H., Zhou, Z., Li, W., Fan, Y., Li, Z., Wei, J., 2021. Hydroxyapatite based materials for bone tissue engineering: A brief and comprehensive introduction. Crystals (Basel). https://doi.org/10.3390/cryst11020149

Shi, J., Zhang, J., Zhang, Y., Zhang, L., Yang, Y.B., Manor, O., You, J., 2023. Crystallinity Dependence of PLLA Hydrophilic Modification during Alkali Hydrolysis. Polymers (Basel). 15, 75. https://doi.org/10.3390/POLYM15010075/S1

Shimoda, K., Tobu, Y., Hatakeyama, M., Nemoto, T., Saito, K., 2007. Structural investigation of Mg local environments in silicate glasses by ultra-high field 25Mg 3QMAS NMR spectroscopy. American Mineralogist 92, 695–698. https://doi.org/10.2138/AM.2007.2535

Shokrollahi, Y., Dong, P., Gamage, P.T., Patrawalla, N., Kishore, V., Mozafari, H., Gu, L., 2022. Finite Element-Based Machine Learning Model for Predicting the Mechanical Properties of Composite Hydrogels. Applied Sciences (Switzerland) 12. https://doi.org/10.3390/app122110835

Shor, L., Güçeri, S., Chang, R., Gordon, J., Kang, Q., Hartsock, L., An, Y., Sun, W., 2009. Precision extruding deposition (PED) fabrication of polycaprolactone (PCL) scaffolds for bone tissue engineering. Biofabrication 1. https://doi.org/10.1088/1758-5082/1/1/015003

Shuai, C., Xu, Y., Feng, P., Wang, G., Xiong, S., Peng, S., 2019. Antibacterial polymer scaffold based on mesoporous bioactive glass loaded with in situ grown silver. Chemical Engineering Journal 374. https://doi.org/10.1016/j.cej.2019.03.273

Sidey-Gibbons, J.A.M., Sidey-Gibbons, C.J., 2019. Machine learning in medicine: a practical introduction. BMC Med. Res. Methodol. 19. https://doi.org/10.1186/s12874-019-0681-4

Silver, I.A., Deas, J., Erecińska, M., 2001. Interactions of bioactive glasses with osteoblasts in vitro: effects of 45S5 Bioglass®, and 58S and 77S bioactive glasses on metabolism, intracellular ion concentrations and cell viability. Biomaterials 22, 175–185. https://doi.org/10.1016/S0142-9612(00)00173-3

Simorgh, S., Alasvand, N., Khodadadi, M., Ghobadi, F., Malekzadeh, M., Brouki, P., Kargozar, S., Baino, F., Mobasheri, A., Mozafari, M., 2023. Additive manufacturing of bioactive glass biomaterials. Methods 208, 75–91. https://doi.org/10.1016/j.ymeth.2022.10.010

Siqueira, R.A., Veras, J.M.L., de SOUSA, T.L., de FARIAS, P.M., de OLIVEIRA FILHO, J.G., Bertolo, M.R.V., Egea, M.B., Plácido, G.R., 2022. Pequi mesocarp: a new source of pectin to produce biodegradable film for application as food packaging. Food Science and Technology (Brazil) 42. https://doi.org/10.1590/fst.71421

Slimestad, R., Holm, V., Barsett, H., 2019. Sample Preparation and Analysis of Tomato Pectin Monomers. Chromatographia 82. https://doi.org/10.1007/s10337-019-03719-8

Smak Gregoor, A.M., Sangers, T.E., Bakker, L.J., Hollestein, L., Uyl – de Groot, C.A., Nijsten, T., Wakkee, M., 2023. An artificial intelligence based app for skin cancer detection evaluated in a population based setting. NPJ Digit. Med. 6. https://doi.org/10.1038/s41746-023-00831-w

Smith, A.M., Mancini, M.C., Nie, S., 2009. Bioimaging: Second window for in vivo imaging. Nat. Nanotechnol. https://doi.org/10.1038/nnano.2009.326

Song, Z., Chen, X., Meng, F., Cheng, G., Wang, C., Sun, Z., Yin, W.J., 2020. Machine learning in materials design: Algorithm and application. Chinese Physics B. https://doi.org/10.1088/1674-1056/abc0e3

St John, P.C., Phillips, C., Kemper, T.W., Wilson, A.N., Guan, Y., Crowley, M.F., Nimlos, M.R., Larsen, R.E., 2019. Message-passing neural networks for high-throughput polymer screening. Journal of Chemical Physics 150. https://doi.org/10.1063/1.5099132

Stebbins, J.F., 1998. Structure and dynamics of magnesium in silicate melts: A high-temperature 25Mg NMR study. American Mineralogist 83, 1022–1029. https://doi.org/10.2138/AM-1998-9-1010/MACHINEREADABLECITATION/RIS

Stevens, M.M., Marini, R.P., Schaefer, D., Aronson, J., Langer, R., Shastri, V.P., 2005. In vivo engineering of organs: The bone bioreactor. Proc. Natl. Acad. Sci. U. S. A. 102. https://doi.org/10.1073/pnas.0504705102

Stiller, A., Engblom, M., Vainio, E., Hupa, L., 2024. Understanding the crystallization behavior of bioactive glass S53P4 powder compacts under various heating conditions. J. Non. Cryst. Solids 644. https://doi.org/10.1016/j.jnoncrysol.2024.123178

Strömberg, G., Aalto-Setälä, L., Uppstu, P., Björkenheim, R., Pajarinen, J., Eriksson, E., Lindfors, N.C., Hupa, L., 2023. Development and Characterization of Non-coated and PLGA-Coated S53P4 and S59 Bioactive Glass Scaffolds for Treatment of Load-Bearing Defects. Biomedical Materials & Devices. https://doi.org/10.1007/s44174-023-00099-4

Stuart, S., Watchorn, J., Gu, F.X., 2023. Sizing up feature descriptors for macromolecular machine learning with polymeric biomaterials. NPJ Comput. Mater. 9. https://doi.org/10.1038/s41524-023-01040-5

Su, X., Wang, T., Guo, S., 2021. Applications of 3D printed bone tissue engineering scaffolds in the stem cell field. Regen. Ther. https://doi.org/10.1016/j.reth.2021.01.007

Suamte, L., Tirkey, A., Barman, J., Jayasekhar Babu, P., 2023. Various manufacturing methods and ideal properties of scaffolds for tissue engineering applications. Smart Materials in Manufacturing 1, 100011. https://doi.org/10.1016/J.SMMF.2022.100011

Sultan, S., Thomas, N., Varghese, M., Dalvi, Y., Joy, S., Hall, S., Mathew, A.P., 2022. The Design of 3D-Printed Polylactic Acid–Bioglass Composite Scaffold: A Potential Implant Material for Bone Tissue Engineering. Molecules 27, 7214. https://doi.org/10.3390/MOLECULES27217214/S1

Sultana, N., Sikdar, S., Chattopadhyay, P.P., Datta, S., 2014. Informatics based design of prosthetic Ti alloys. Materials Technology 29. https://doi.org/10.1179/1753555713Y.0000000103

Sun, B., Ricardo-da-Silva, J.M., Spranger, I., 1998. Critical Factors of Vanillin Assay for Catechins and Proanthocyanidins. J. Agric. Food Chem. 46. https://doi.org/10.1021/jf980366j

Sun, Z., Wu, F., Gao, H., Cui, K., Xian, M., Zhong, J., Tian, Y., Fan, S., Wu, G., 2020. A Dexamethasone-Eluting Porous Scaffold for Bone Regeneration Fabricated by

Selective Laser Sintering. ACS Appl. Bio Mater. 3. https://doi.org/10.1021/acsabm.0c01126

Sutton, R.S., Barto, A.G., 1998. Reinforcement Learning: An Introduction. IEEE Trans. Neural Netw. 9. https://doi.org/10.1109/tnn.1998.712192

Suwardi, Ady, Wang, Fuke, Xue, Kun, Han, Ming-Yong, Teo, Peili, Wang, Pei, Wang, Shijie, Liu, Ye, Ye, Enyi, Li, Zibiao, Loh, Xian Jun, Suwardi, A, Wang, F, Xue, K, Han, M.-Y, Teo, P, Wang, P, Wang, S, Liu, Y, Ye, E, Li, Z, Loh, X J, 2022. Machine Learning-Driven Biomaterials Evolution. Advanced Materials 34, 2102703. https://doi.org/10.1002/ADMA.202102703

Tainio, J.M., Salazar, D.A.A., Nommeots-Nomm, A., Roiland, C., Bureau, B., Neuville, D.R., Brauer, D.S., Massera, J., 2020. Structure and in vitro dissolution of Mg and Sr containing borosilicate bioactive glasses for bone tissue engineering. J. Non. Cryst. Solids 533. https://doi.org/10.1016/j.jnoncrysol.2020.119893

Tanveer, M.Q., Haleem, A., Suhaib, M., 2019. Effect of variable infill density on mechanical behaviour of 3-D printed PLA specimen: an experimental investigation. SN Appl. Sci. 1, 1–12. https://doi.org/10.1007/S42452-019-1744-1

Tauchen, J., Bortl, L., Huml, L., Miksatkova, P., Doskocil, I., Marsik, P., Villegas, P.P.P., Flores, Y.B., Van Damme, P., Lojka, B., Havlik, J., Lapcik, O., Kokoska, L., 2016. Phenolic composition, antioxidant and anti-proliferative activities of edible and medicinal plants from the Peruvian Amazon. Revista Brasileira de Farmacognosia 26, 728–737. https://doi.org/10.1016/J.BJP.2016.03.016

Taye, M.B., 2022. Biomedical applications of ion-doped bioactive glass: a review. Applied Nanoscience (Switzerland) 12, 3797–3812. https://doi.org/10.1007/S13204-022-02672-7/TABLES/3

Taye, M.M., 2023. Understanding of Machine Learning with Deep Learning: Architectures, Workflow, Applications and Future Directions. Computers. https://doi.org/10.3390/computers12050091

Terzopoulou, Z., Zamboulis, A., Koumentakou, I., Michailidou, G., Noordam, M.J., Bikiaris, D.N., 2022. Biocompatible Synthetic Polymers for Tissue Engineering Purposes. Biomacromolecules 23, 1841–1863. https://doi.org/10.1021/ACS.BIOMAC.2C00047

Tesoro, G., Wu, Y., 1991. Silane coupling agents: The role of the organofunctional group. J. Adhes. Sci. Technol. 5. https://doi.org/10.1163/156856191X00206

Thavornyutikarn, B., Tesavibul, P., Sitthiseripratip, K., Chatarapanich, N., Feltis, B., Wright, P.F.A., Turney, T.W., 2017. Porous 45S5 Bioglass®-based scaffolds using stereolithography: Effect of partial pre-sintering on structural and mechanical properties of scaffolds. Materials Science and Engineering: C 75, 1281–1288. https://doi.org/10.1016/J.MSEC.2017.03.001

Todaro, G.J., Green, H., 1963. Quantitative studies of the growth of mouse embryo cells in culture and their development into established lines. Journal of Cell Biology 17, 299–313. https://doi.org/10.1083/JCB.17.2.299

Todros, S., Todesco, M., Bagno, A., 2021. Biomaterials and Their Biomedical Applications: From Replacement to Regeneration. Processes 2021, Vol. 9, Page 1949 9, 1949. https://doi.org/10.3390/PR9111949

Touré, A.B.R., Mele, E., Christie, J.K., 2020. Multi-layer scaffolds of poly(Caprolactone), poly(glycerol sebacate) and bioactive glasses manufactured by combined 3d printing and electrospinning. Nanomaterials 10. https://doi.org/10.3390/nano10040626

Tsouknidas, A., 2011. Friction Induced Wear of Rapid Prototyping Generated Materials: A Review. Advances in Tribology 2011, 746270. https://doi.org/10.1155/2011/746270

Tulyaganov, D.U., Fiume, E., Akbarov, A., Ziyadullaeva, N., Murtazaev, S., Rahdar, A., Massera, J., Verné, E., Baino, F., 2022. In Vivo Evaluation of 3D-Printed Silica-Based Bioactive Glass Scaffolds for Bone Regeneration. J. Funct. Biomater. 13. https://doi.org/https://doi.org/10.3390/jfb13020074

Tylkowski, M., Brauer, D.S., 2013. Mixed alkali effects in Bioglass® 45S5. J. Non. Cryst. Solids 376. https://doi.org/10.1016/j.jnoncrysol.2013.05.039

Vaiani, L., Boccaccio, A., Uva, A.E., Palumbo, G., Piccininni, A., Guglielmi, P., Cantore, S., Santacroce, L., Charitos, I.A., Ballini, A., 2023. Ceramic Materials for Biomedical Applications: An Overview on Properties and Fabrication Processes. J. Funct. Biomater. https://doi.org/10.3390/jfb14030146

Valenzuela, F., Covarrubias, C., Martínez, C., Smith, P., Díaz-Dosque, M., Yazdani-Pedram, M., 2012. Preparation and bioactive properties of novel bone-repair bionanocomposites

based on hydroxyapatite and bioactive glass nanoparticles. J. Biomed. Mater. Res. B Appl. Biomater. 100B, 1672–1682. https://doi.org/10.1002/JBM.B.32736

Valverde, D., Behrends, B., Pérez-Esteve, Kuhnert, N., Barat, J.M., 2020. Functional changes induced by extrusion during cocoa alkalization. Food Research International 136. https://doi.org/10.1016/j.foodres.2020.109469

Vamathevan, J., Clark, D., Czodrowski, P., Dunham, I., Ferran, E., Lee, G., Li, B., Madabhushi, A., Shah, P., Spitzer, M., Zhao, S., 2019. Applications of machine learning in drug discovery and development. Nat. Rev. Drug Discov. https://doi.org/10.1038/s41573-019-0024-5

van Gestel, N.A.P., Gabriels, F., Geurts, J.A.P., Hulsen, D.J.W., Wyers, C.E., van de Bergh, J.P., Ito, K., Hofmann, S., Arts, J.J., van Rietbergen, B., 2019. The Implantation of Bioactive Glass Granules Can Contribute the Load-Bearing Capacity of Bones Weakened by Large Cortical Defects. Materials 2019, Vol. 12, Page 3481 12, 3481. https://doi.org/10.3390/MA12213481

van Vliet, J.A., Giller, K.E., 2017. Mineral Nutrition of Cocoa: A Review, in: Advances in Agronomy. https://doi.org/10.1016/bs.agron.2016.10.017

Vázquez-Ovando, A., Molina-Freaner, F., Nuñez-Farfán, J., Betancur-Ancona, D., Salvador-Figueroa, M., 2015. Classification of cacao beans (Theobroma cacao L.) of southern Mexico based on chemometric analysis with multivariate approach. European Food Research and Technology 240. https://doi.org/10.1007/s00217-015-2415-0

Venturelli, C., 2011. Heating Microscopy and its Applications. Micros. Today 19. https://doi.org/10.1017/s1551929510001185

Verné, E., Bretcanu, O., Balagna, C., Bianchi, C.L., Cannas, M., Gatti, S., Vitale-Brovarone, C., 2009. Early stage reactivity and in vitro behavior of silica-based bioactive glasses and glass-ceramics. J. Mater. Sci. Mater. Med. 20. https://doi.org/10.1007/s10856-008-3537-8

Viennet, C., Muret, P., 2015. Fibroblast Evaluation: Extracellular Matrix Synthesis. Measuring the Skin 1–5. https://doi.org/10.1007/978-3-319-26594-0_124-1

Vincken, J.P., Schols, H.A., Oomen, R.J.F.J., McCann, M.C., Ulvskov, P., Voragen, A.G.J., Visser, R.G.F., 2003. If homogalacturonan were a side chain of rhamnogalacturonan I.

Implications for cell wall architecture. Plant Physiol. 132, 1781–1789. https://doi.org/10.1104/PP.103.022350,

Vinoth, A., Dey, S., Datta, S., 2021. Designing UHMWPE hybrid composites using machine learning and metaheuristic algorithms. Compos. Struct. 267. https://doi.org/10.1016/j.compstruct.2021.113898

Volpini, V., Giubilini, A., Corsi, L., Nobili, A., Bondioli, F., 2022. Characterization of biocompatible scaffolds manufactured by fused filament fabrication of poly(3-hydroxybutyrate-co-3-hydroxyhexanoate). R. Soc. Open Sci. 9. https://doi.org/10.1098/RSOS.211485

Volzone, C., Stábile, F.M., 2013. Structural Changes by Thermal Treatment up to Glass Obtention of P2O5-Na2O-CaO-SiO2 Compounds with Bioglass Composition Types. New Journal of Glass and Ceramics 3.

Vriesmann, L.C., Teófilo, R.F., Lúcia de Oliveira Petkowicz, C., 2012. Extraction and characterization of pectin from cacao pod husks (Theobroma cacao L.) with citric acid. LWT 49, 108–116. https://doi.org/10.1016/J.LWT.2012.04.018

Vyas, A., Bandhu Ghosh, S., Bandyopadhyay-Ghosh, S., Agrawal, A.K., Khare, D., Dubey, A.K., 2022. Digital light processing mediated 3D printing of biocomposite bone scaffolds: Physico-chemical interactions and in-vitro biocompatibility. Polym. Compos. 43, 3175–3188. https://doi.org/10.1002/pc.26609

Walther, D.J., Peter, J.U., Bashammakh, S., Hörtnagl, H., Voits, M., Fink, H., Bader, M., 2003. Synthesis of serotonin by a second tryptophan hydroxylase isoform. Science (1979). 299, 76. https://doi.org/10.1126/SCIENCE.1078197,

Wang, C., Meng, C., Zhang, Z., Zhu, Q., 2022. 3D printing of polycaprolactone/bioactive glass composite scaffolds for in situ bone repair. Ceram. Int. 48. https://doi.org/10.1016/j.ceramint.2021.11.293

Wang, F., Semirumi, D.T., He, A., Pan, Z., Alizadeh, A., 2024. Physical, mechanical characterization, and artificial neural network modeling of biodegradable composite scaffold for biomedical applications. Eng. Appl. Artif. Intell. 136, 108889. https://doi.org/10.1016/J.ENGAPPAI.2024.108889

Wang, S., Cui, W., Bei, J., 2005. Bulk and surface modifications of polylactide. Anal. Bioanal. Chem. https://doi.org/10.1007/s00216-004-2771-2

Wang, W., Ma, X., Jiang, P., Hu, L., Zhi, Z., Chen, J., Ding, T., Ye, X., Liu, D., 2016. Characterization of pectin from grapefruit peel: A comparison of ultrasound-assisted and conventional heating extractions. Food Hydrocoll. 61, 730–739. https://doi.org/10.1016/J.FOODHYD.2016.06.019

Wang, W., Zhang, B., Li, M., Li, J., Zhang, C., Han, Y., Wang, L., Wang, K., Zhou, C., Liu, L., Fan, Y., Zhang, X., 2021. 3D printing of PLA/n-HA composite scaffolds with customized mechanical properties and biological functions for bone tissue engineering. Compos. B Eng. 224, 109192. https://doi.org/10.1016/J.COMPOSITESB.2021.109192

Wang, X., Zhao, L., Fuh, J.Y.H., Lee, H.P., 2019. Effect of Porosity on Mechanical Properties of 3D Printed Polymers: Experiments and Micromechanical Modeling Based on X-ray Computed Tomography Analysis. Polymers 2019, Vol. 11, Page 1154 11, 1154. https://doi.org/10.3390/POLYM11071154

Ward, L., Agrawal, A., Choudhary, A., Wolverton, C., 2016. A general-purpose machine learning framework for predicting properties of inorganic materials. NPJ Comput. Mater. 2. https://doi.org/10.1038/npjcompumats.2016.28

Waterman, P.G., Mole, S., 1994. Analysis of Phenolic Plant Metabolites, 1st ed. Wiley-Blackwell.

Watts, S.J., Hill, R.G., O'Donnell, M.D., Law, R. V., 2010. Influence of magnesia on the structure and properties of bioactive glasses. J. Non. Cryst. Solids 356. https://doi.org/10.1016/j.jnoncrysol.2009.04.074

Weininger, D., 1988. SMILES, a Chemical Language and Information System: 1: Introduction to Methodology and Encoding Rules. J. Chem. Inf. Comput. Sci. 28. https://doi.org/10.1021/ci00057a005

Weiß, T., Hildebrand, G., Schade, R., Liefeith, K., 2009. Two-photon polymerization for microfabrication of three-dimensional scaffolds for tissue engineering application. Eng. Life Sci. 9. https://doi.org/10.1002/elsc.200900002

Werner, K., Pommer, L., Broström, M., 2014. Thermal decomposition of hemicelluloses. J. Anal. Appl. Pyrolysis 110, 130–137. https://doi.org/10.1016/J.JAAP.2014.08.013

Willerth, S.M., Sakiyama-Elbert, S.E., 2019. Combining Stem Cells and Biomaterial Scaffolds for Constructing Tissues and Cell Delivery. StemJournal 1. https://doi.org/10.3233/stj-180001

Williams, D., Zhang, X., 2019. Definitions of Biomaterials for the Twenty-First Century, Definitions of Biomaterials for the Twenty-First Century. https://doi.org/10.1016/C2018-0-02529-3

Williams, D.F., 1999. The Williams Dictionary of Biomaterials, The Williams Dictionary of Biomaterials. https://doi.org/10.5949/upo9781846314438

Wu, C., Entezari, A., Zheng, K., Fang, J., Zreiqat, H., Steven, G.P., Swain, M. V., Li, Q., 2021. A machine learning-based multiscale model to predict bone formation in scaffolds. Nat. Comput. Sci. 1. https://doi.org/10.1038/s43588-021-00115-x

Wu, C., Luo, Y., Cuniberti, G., Xiao, Y., Gelinsky, M., 2011. Three-dimensional printing of hierarchical and tough mesoporous bioactive glass scaffolds with a controllable pore architecture, excellent mechanical strength and mineralization ability. Acta Biomater. 7. https://doi.org/10.1016/j.actbio.2011.03.009

Wu, C., Wan, B., Entezari, A., Fang, J., Xu, Y., Li, Q., 2024. Machine learning-based design for additive manufacturing in biomedical engineering. Int. J. Mech. Sci. 266. https://doi.org/10.1016/j.ijmecsci.2023.108828

Wu, H., Cheng, Y., Liu, W., He, R., Zhou, M., Wu, S., Song, X., Chen, Y., 2016. Effect of the particle size and the debinding process on the density of alumina ceramics fabricated by 3D printing based on stereolithography. Ceram. Int. 42. https://doi.org/10.1016/j.ceramint.2016.08.024

Wu, J., Shen, S., Gao, Q., Yu, C., Cheng, H., Pan, H., Chen, S., Ye, X., Chen, J., 2023. RG-I Domain Matters to the In Vitro Fermentation Characteristics of Pectic Polysaccharides Recycled from Citrus Canning Processing Water. Foods 2023, Vol. 12, Page 943 12, 943. https://doi.org/10.3390/FOODS12050943

Wu, C. Te, Chang, H.T., Wu, C.Y., Chen, S.W., Huang, S.Y., Huang, M., Pan, Y.T., Bradbury, P., Chou, J., Yen, H.W., 2020. Machine learning recommends affordable new Ti alloy with bone-like modulus. Materials Today 34. https://doi.org/10.1016/j.mattod.2019.08.008

Wu, Y., Lu, Y., Zhao, M., Bosiakov, S., Li, L., 2022. A Critical Review of Additive Manufacturing Techniques and Associated Biomaterials Used in Bone Tissue Engineering. Polymers (Basel). 14. https://doi.org/https://doi.org/10.3390/polym14102117

Xie, S., 2023. Perspectives on development of biomedical polymer materials in artificial intelligence age. J. Biomater. Appl. 37, 1355–1375. https://doi.org/10.1177/08853282231151822

Xie, T., Grossman, J.C., 2018. Crystal Graph Convolutional Neural Networks for an Accurate and Interpretable Prediction of Material Properties. Phys. Rev. Lett. 120. https://doi.org/10.1103/PhysRevLett.120.145301

Xu, F., Ren, H., Zheng, M., Shao, X., Dai, T., Wu, Y., Tian, L., Liu, Yu, Liu, B., Gunster, J., Liu, Yaxiong, Liu, Yanpu, 2020. Development of biodegradable bioactive glass ceramics by DLP printed containing EPCs/BMSCs for bone tissue engineering of rabbit mandible defects. J. Mech. Behav. Biomed. Mater. 103. https://doi.org/10.1016/j.jmbbm.2019.103532

Xu, J.-L., Lin, X., Gowen, A.A., 2022. Combining machine learning with meta-analysis for predicting cytotoxicity of micro- and nanoplastics. Journal of Hazardous Materials Advances 8. https://doi.org/10.1016/j.hazadv.2022.100175

Xu, P., Ji, X., Li, M., Lu, W., 2023. Small data machine learning in materials science. npj Computational Materials 2023 9:1 9, 1–15. https://doi.org/10.1038/s41524-023-01000-z

Xue, X., Hu, Y., Wang, S., Chen, X., Jiang, Y., Su, J., 2022. Fabrication of physical and chemical crosslinked hydrogels for bone tissue engineering. Bioact. Mater. 12, 327–339. https://doi.org/10.1016/J.BIOACTMAT.2021.10.029

Xynos, I.D., Hukkanen, M.V.J., Batten, J.J., Buttery, L.D., Hench, L.L., Polak, J.M., 2000. Bioglass ®45S5 stimulates osteoblast turnover and enhances bone formation in vitro: Implications and applications for bone tissue engineering. Calcif. Tissue Int. 67, 321–329. https://doi.org/10.1007/S002230001134/METRICS

Yamada, H., Liu, C., Wu, S., Koyama, Y., Ju, S., Shiomi, J., Morikawa, J., Yoshida, R., 2019. Predicting Materials Properties with Little Data Using Shotgun Transfer Learning. ACS Cent. Sci. 5. https://doi.org/10.1021/acscentsci.9b00804

Yan, C., Li, G., 2023. The Rise of Machine Learning in Polymer Discovery. Advanced Intelligent Systems. https://doi.org/10.1002/aisy.202200243

Yan, S., Zhang, Q., Wang, J., Liu, Y., Lu, S., Li, M., Kaplan, D.L., 2013. Silk fibroin/chondroitin sulfate/hyaluronic acid ternary scaffolds for dermal tissue reconstruction. Acta Biomater. 9. https://doi.org/10.1016/j.actbio.2013.02.016

Yang, C., Bai, J., Wang, G., Wang, H., Ma, S., 2023. Effect of Na2O content on wettability, crystallization and performances of sealing glass. Journal of Materials Research and Technology 23, 4117–4134. https://doi.org/10.1016/J.JMRT.2023.02.073

Yang, J., Hao, Z., Xu, J., Wang, J., Jiang, X., 2023. Fusion machine learning model predicts CAD-CAM ceramic colors and the corresponding minimal thicknesses over various clinical backgrounds. Dental Materials. https://doi.org/10.1016/j.dental.2023.11.013

Yang, Y., Wang, G., Liang, H., Gao, C., Peng, S., Shen, L., Shuai, C., 2019. Additive manufacturing of bone scaffolds. Int. J. Bioprint. https://doi.org/10.18063/IJB.v5i1.148

Yang, Y., Yuan, Y., Zhang, G., Wang, H., Chen, Y.C., Liu, Y., Tarolli, C.G., Crepeau, D., Bukartyk, J., Junna, M.R., Videnovic, A., Ellis, T.D., Lipford, M.C., Dorsey, R., Katabi, D., 2022. Artificial intelligence-enabled detection and assessment of Parkinson's disease using nocturnal breathing signals. Nat. Med. 28. https://doi.org/10.1038/s41591-022-01932-x

Yang, Z., Zhang, Y., Jin, G., Lei, D., Liu, Y., 2024. Insights into the impact of modification methods on the structural characteristics and health functions of pectin: A comprehensive review. Int. J. Biol. Macromol. 261, 129851. https://doi.org/10.1016/J.IJBIOMAC.2024.129851

Yao, A., Wang, D., Huang, W., Fu, Q., Rahaman, M.N., Day, D.E., 2007. In vitro bioactive characteristics of borate-based glasses with controllable degradation behavior. Journal of the American Ceramic Society 90, 303–306. https://doi.org/10.1111/j.1551-2916.2006.01358.x

Ye, S., Huang, W.Z., Li, M., Feng, X.Q., 2021. Deep learning method for determining the surface elastic moduli of microstructured solids. Extreme Mech. Lett. 44, 101226. https://doi.org/10.1016/J.EML.2021.101226

Ye, S., Li, M., Zhang, K., Zhao, H.P., Feng, X.Q., 2022. Extracting the properties of constituent phases from the overall response of composites: A deep neural network method. Compos. Struct. 293, 115707. https://doi.org/10.1016/J.COMPSTRUCT.2022.115707

Yeo, M., Kim, G.H., 2020. Micro/nano-hierarchical scaffold fabricated using a cell electrospinning/3D printing process for co-culturing myoblasts and HUVECs to induce myoblast alignment and differentiation. Acta Biomater. 107, 102–114. https://doi.org/10.1016/J.ACTBIO.2020.02.042

Yu, H., Peng, J., Xu, Y., Chang, J., Li, H., 2016. Bioglass Activated Skin Tissue Engineering Constructs for Wound Healing. ACS Appl. Mater. Interfaces 8, 703–715. https://doi.org/10.1021/ACSAMI.5B09853/ASSET/IMAGES/LARGE/AM-2015-09853K_0012.JPEG

Yu, J., Wang, Y., Dai, Z., Yang, F., Fallahpour, A., Nasiri-Tabrizi, B., 2021. Structural features modeling of substituted hydroxyapatite nanopowders as bone fillers via machine learning. Ceram. Int. 47. https://doi.org/10.1016/j.ceramint.2020.12.026

Yu, Z., Ye, S., Sun, Y., Zhao, H., Feng, X.Q., 2021. Deep learning method for predicting the mechanical properties of aluminum alloys with small data sets. Mater. Today Commun. 28, 102570. https://doi.org/10.1016/J.MTCOMM.2021.102570

Zarur, M., Seijo-Rabina, A., Goyanes, A., Concheiro, A., Alvarez-Lorenzo, C., 2023. pH-responsive scaffolds for tissue regeneration: In vivo performance. Acta Biomater. https://doi.org/10.1016/j.actbio.2023.07.025

Zeni, C., Pinsler, R., Zügner, D., Fowler, A., Horton, M., Fu, X., Shysheya, S., Crabbé, J., Sun, L., Smith, J., Nguyen, B., Schulz, H., Lewis, S., Huang, C.-W., Lu, Z., Zhou, Y., Yang, H., Hao, H., Li, J., Tomioka, R., Xie, T., 2023. MatterGen: a generative model for inorganic materials design. Nature 2025 639:8055 639, 624–632. https://doi.org/10.1038/S41586-025-08628-5

Zhang, C., Slegers, P.M., Wisse, J., Sanders, J.P.M., Bruins, M.E., 2018. Sustainable scenarios for alkaline protein extraction from leafy biomass using green tea residue as a model material. Biofuels, Bioproducts and Biorefining 12, 586–599. https://doi.org/10.1002/BBB.1870

Zhang, D., Leppäranta, O., Munukka, E., Ylänen, H., Viljanen, M.K., Eerola, E., Hupa, M., Hupa, L., 2010. Antibacterial effects and dissolution behavior of six bioactive glasses. J. Biomed. Mater. Res. A 93. https://doi.org/10.1002/jbm.a.32564

Zhang, J., Hu, Q., Wang, S., Tao, J., Gou, M., 2020. Digital light processing based three-dimensional printing for medical applications. Int. J. Bioprint. 6. https://doi.org/10.18063/ijb.v6i1.242

Zhang, J., Wang, P., Gao, R.X., 2019. Deep learning-based tensile strength prediction in fused deposition modeling. Comput. Ind. 107. https://doi.org/10.1016/j.compind.2019.01.011

Zhang, J., Zhao, S., Zhu, Y., Huang, Y., Zhu, M., Tao, C., Zhang, C., 2014. Three-dimensional printing of strontium-containing mesoporous bioactive glass scaffolds for bone regeneration. Acta Biomater. 10. https://doi.org/10.1016/j.actbio.2014.01.001

Zhang, P., Wang, Z., Li, J., Li, X., Cheng, L., 2020. From materials to devices using fused deposition modeling: A state-of-art review. Nanotechnol. Rev. https://doi.org/10.1515/ntrev-2020-0101

Zhang, W., Zhu, C., Ye, D., Xu, L., Zhang, Xiaochen, Wu, Q., Zhang, Xiuli, Kaplan, D.L., Jiang, X., 2014. Porous silk scaffolds for delivery of growth factors and stem cells to enhance bone regeneration. PLoS One 9. https://doi.org/10.1371/journal.pone.0102371

Zhang, X., Wei, C., Chueh, Y.H., Li, L., 2019. An integrated dual ultrasonic selective powder dispensing platform for three-dimensional printing of multiple material metal/glass objects in selective laser melting. Journal of Manufacturing Science and Engineering, Transactions of the ASME 141. https://doi.org/10.1115/1.4041427

Zhang, Y., Hu, M., Zhang, W., Zhang, X., 2022. Homology of selenium (Se) and tellurium (Te) endow the functional similarity of Se-doped and Te-doped mesoporous bioactive glass nanoparticles in bone tissue engineering. Ceram. Int. 48, 3729–3739. https://doi.org/10.1016/j.ceramint.2021.10.155

Zhang, Y., Wu, D., Zhao, X., Pakvasa, M., Tucker, A.B., Luo, H., Qin, K.H., Hu, D.A., Wang, E.J., Li, A.J., Zhang, M., Mao, Y., Sabharwal, M., He, F., Niu, C., Wang, H., Huang, L., Shi, D., Liu, Q., Ni, N., Fu, K., Chen, C., Wagstaff, W., Reid, R.R., Athiviraham, A., Ho, S., Lee, M.J., Hynes, K., Strelzow, J., He, T.C., El Dafrawy, M., 2020. Stem Cell-Friendly Scaffold Biomaterials: Applications for Bone Tissue Engineering and Regenerative Medicine. Front. Bioeng. Biotechnol. https://doi.org/10.3389/fbioe.2020.598607

Zhao, X., Liu, S., Yildirimer, L., Zhao, H., Ding, R., Wang, H., Cui, W., Weitz, D., 2016. Injectable Stem Cell-Laden Photocrosslinkable Microspheres Fabricated Using Microfluidics for Rapid Generation of Osteogenic Tissue Constructs. Adv. Funct. Mater. 26, 2809–2819. https://doi.org/10.1002/ADFM.201504943

Zhu, Y., Xu, T., Wei, Q., Mai, J., Yang, H., Zhang, H., Shimada, T., Kitamura, T., Zhang, T.Y., 2021. Linear-superelastic Ti-Nb nanocomposite alloys with ultralow modulus via high-throughput phase-field design and machine learning. npj Computational Materials 2021 7:1 7, 1–10. https://doi.org/10.1038/s41524-021-00674-7

Zhuang, F., Qi, Z., Duan, K., Xi, D., Zhu, Y., Zhu, H., Xiong, H., He, Q., 2021. A Comprehensive Survey on Transfer Learning. Proceedings of the IEEE. https://doi.org/10.1109/JPROC.2020.3004555

Ziemath, E.C., Aegerter, M.A., 1994. Raman and Infrared Investigations of Glass and Glass-Ceramics with Composition 2Na2O. 1CaO. 3SiO2. J. Mater. Res. 9, 216–225. https://doi.org/10.1557/JMR.1994.0216

Zreiqat, H., Howlett, C.R., Zannettino, A., Evans, P., Schulze-Tanzil, G., Knabe, C., Shakibaei, M., 2002. Mechanisms of magnesium-stimulated adhesion of osteoblastic cells to commonly used orthopaedic implants. J. Biomed. Mater. Res. 62, 175–184. https://doi.org/10.1002/JBM.10270

Zulkifli, M.Z.A., Nordin, D., Shaari, N., Kamarudin, S.K., 2023. Overview of Electrospinning for Tissue Engineering Applications. Polymers (Basel). https://doi.org/10.3390/polym15112418